A Computational Aeroelasticity Framework for Analyzing Flapping Wings

by

Satish Kumar Chimakurthi

A dissertation submitted in partial fulfillment
of the requirements for the degree of
Doctor of Philosophy
(Aerospace Engineering)
in The University of Michigan
2009

Doctoral Committee:

Professor Carlos E.S. Cesnik, Co-Chair
Professor Wei Shyy, Co-Chair
Professor Peretz P. Friedmann
Associate Professor Bogdan I. Epureanu
Senior Research Engineer Raymond E. Gordnier

Acknowledgements

My first and foremost thanks go to my advisor Prof. Carlos E.S. Cesnik. I would not have been able to accomplish anything I have, but for the tremendous amount of patience and understanding Prof. Cesnik had, especially during the initial years of my stint at UM. To pursue a PhD in Aerospace Engineering focused on aeroelasticity has always been a dream for me since my Master's at the University of Kentucky and I now really think that there would not have been either a better place than UM or a better advisor than Prof. Cesnik for me to do that. My learning curve in my PhD program had been unusually very steep and Prof. Cesnik undoubtedly helped me through it. Overall, I owe a lot to this multi-faceted professor and I shall spare no efforts from my side to scale up to his expectations wherever I am and in whichever setting I am in, in my life.

I have had the fortune of collaborating with Prof. Wei Shyy of the CFD group at UM during the last couple of years of my PhD program. I couldn't be more grateful to him for having shown tremendous interest in my research and for inspiring me to probe into issues related to fluid physics, amongst others, more deeply than ever. I do not have even an iota of hesitation to state that my interactions with him have helped a lot in accelerating the pace of my work further. I profusely thank him for that.

I would also like to acknowledge the guidance I received from Dr. Rafael Palacios (now working as Lecturer, Imperial College, London) who has been a constant source of

inspiration for me in different ways during the first few years of my PhD program. I have always been amazed by the huge body of knowledge he possessed. I thank him for being so strongly critical of my work without which I would not have learned to be constantly aware of my faults and fix them.

I would like to acknowledge the interactions (technical, comical, and personal) with my colleagues at the Active Aeroelasticity and Structures Research Laboratory which have been extremely useful: thanks go to Smith Thepvongs, Dr. Weihua Su, Ken Salas, Dr. Ajay Raghavan, Jiwon Mok, Dr. Chris Shearer, Dr. Jorge Morillo, Devesh Kumar, Kalyan Nadella, and Lindsey Ewing for being so jovial, friendly, and nice.

I am very grateful to all of my collaborators including Dr. Dragos Viieru (now with Aviation Partners Boeing, Seattle), Dr. Bret Stanford (AFRL, Dayton), Dr. Hikaru Aono, and Dr. Jian Tang. I would like to thank Dr. Viieru for helping with setting up of the CFD side of the interface in this dissertation and for being a very good friend. I would like to profusely thank Dr. Stanford for his help with the development of the nonlinear structural dynamics solution in this work. Undoubtedly, his valuable inputs, especially on code-related issues, have been greatly useful. I would like to thank Dr. Hikaru Aono (post-doctoral research fellow in the CFD group at UM) for being such a nice and responsible collaborator in the past year or so since we started working together. I acknowledge some of the results he processed for this work, especially those related to the highly flexible plunging wing. I would also like to thank for him for his help with the CFD grid generation for the elliptic Zimmerman wing. I would like to thank Prof. Ismet Gursul and Mr. Sam Heathcote (both at the University of Bath, UK) for providing me with the experimental data for the plunging wing cases. I would also like to thank Mr. Pin Wu (University of Florida, Gainesville) and Mr. Erik Sallstrom (University of Florida, Shalimar) for providing experimental data for the flapping wing cases in this work.

I would also like to thank my very intellectual friends outside my research group at UM: Matt Leach, Dr. Bryan Glaz, Ashwani Padthe, Abhijit Gogulapati, Pat Trizila, and Chang Kwon Kang. They have all been of great help to me on various occasions. I would like to particularly acknowledge Matt and Bryan who have perhaps been two of the nicest people I have ever come across in the last seven years of my graduate studies in the United States. I would like to particularly thank Bryan for being so comical and of course helpful too with everything (perhaps, he imbibed the former quality from me !).

My thanks also go to the staff at the University of Michigan: Ms. Denise Phelps, Mr. David Mclean (both with Aerospace Department), Dr. Amadi Nwanpka (CAEN), and Mr. Brock Palen (Center for Advanced Computing). All deserve praise for their great assistance with various things during my PhD program.

I would also like to thank my friends outside of UM for being so greatly inspiring during my program. Thanks go to Dr. Sai Doddi, Dr. Shankara Kuppa, Srikant Vallabhajosula, Sai Palaparthy, Arun Doradla, Kiran Pabbathi, and Karthik Laxminarayana in particular.

Although it goes without stating, I would like to thank my entire family for being so supportive through my seemingly everlasting journey of graduate school. I would like to particularly thank my sisters Dr. Roja Chimakurthi and Lavanya Chimakurthi for the constant source of support and encouragement that they have been especially during times when I felt low and down casted.

In addition, I would like to thank my dissertation committee members for their time and effort and the willingness to serve on my committee.

Last but not the least, I would like to acknowledge the financial support provided by the Air Force Office of Scientific Research/Multidisciplinary University Research Initiative (MURI) and the Michigan/AFRL/Boeing Collaborative Center in Aeronautical Sciences.

Table of Contents

List of Figures

Figure

List of Tables

Table

List of Appendices

Appendix

List of Symbols

a	Global acceleration vector
A	Stretching stiffness matrix
A_e	Area of a triangular finite element
A_r	Wing aspect ratio
B	Membrane-bending coupling stiffness matrix
B_b	Strain displacement matrix corresponding to the flexural strains and the bending degrees of freedom
B_m	Strain displacement matrix corresponding to the membrane strains and the membrane degrees of freedom
c	Mean chord length of the wing
C	Assembled damping matrix in the global frame
C^{bB}	Rotation matrix from the deformed frame B to the undeformed frame b
C_{el}	Element local damping matrix
C_{el-g}	Element global damping matrix
d_e	Vector of displacements of a material point with respect to the undeformed element frame
d^m_{pure}	6x1 vector of pure deformations at a node
d_{pure}	18x1 vector of pure deformations of an element
dt	Coupled time step used in the aeroelastic solution
D	Bending stiffness matrix
D_s	Plate stiffness
E_o	Element frame in the undeformed configuration
E	Element frame in the current configuration, Young's modulus, error metric used in the estimation of order of accuracy for interpolation schemes
f	Plunging/flapping frequency
f_o, f_1	Beam forces per unit length; first-order forces per unit length associated to the work needed to deform the cross-section

f_{so}, f_{s1}	Beam generalized forces corresponding to the finite section modes
f_{ij}, q_{ij}	Metrics of conversion from Cartesian coordinates to curvilinear coordinates
F	Assembled external force vector in the global frame
F_B	Beam sectional forces expressed in the deformed frame
F_{el}^{p}	Local force vector corresponding to inertial forces due to prescribed rigid body motion
F_{el-g}^{p}	Global force vector corresponding to inertial forces due to prescribed rigid body motion
G	Matrix containing derivatives of shape functions, Shear modulus
g	Global frame
h	Discretized grid spacing
h_{root}	Chord-normalized plunge amplitude at the root (ratio of plunge amplitude at the root and chord)
h_a	Stroke amplitude due to either prescribed plunge motion or flap rotation at the wing root
h_s	Plate thickness
H	Distribution function used in the thin plate spline interpolation
H_B	Column-matrix of beam angular momenta expressed in the deformed structural frame
I_m	Identity matrix of size 3x3
I	Inertial frame
j	Iteration number within the Newton-Raphson iteration loop
J	Jacobian matrix associated with transformation from Cartesian to curvilinear coordinates, torsional constant
J_t	Diagonal matrix containing inverse of finite element Jacobian matrix as its components
κ	Vector of beam curvatures in the undeformed frame
k	Beam curvature vector in the undeformed frame, reduced frequency
k_s	Shear correction factor
K	Beam curvature vector in the deformed frame
K_b	Stiffness matrix corresponding to plate bending degrees of freedom
K_{el}^{dyn}	Element local dynamic stiffness matrix
K_{el}^{shell}	Element shell stiffness matrix

$K_{el-g}^{shelldyn-p}$	Total element global stiffness matrix which includes projected shell stiffness matrix and element dynamic stiffness matrix
$K_{el}^{shell-p}$	Element shell stiffness matrix filtered through the projector matrix
K_{eff}	Effective stiffness matrix
K_m	Stiffness matrix corresponding to membrane degrees of freedom
K_{el}^{ss}	Element stress stiffening matrix
K_t	Assembled tangent stiffness matrix in the global frame
m	Node number in an element, master node used in CFD grid re-meshing
m_o, m_1	Beam moments per unit length; first-order moments per unit length associated to the work needed to deform cross-section
M	Assembled mass matrix in the global frame, typical point in the bilinear interpolation method
M_b	Inertia matrix of the beam cross-section
M_B	Beam sectional moments expressed in the deformed frame
M_{el}	Element local mass matrix
M_{el-g}	Element global mass matrix
n	Time level
$n_{\frac{s}{f}}$	Number of subcyles in the fluid solution in an explicit coupling method with subcycling
N	Matrix of shape functions of size 3x18, Number of points in the donor grid in the thin plate spline interpolation
N_1, N_2, N_3, N_4	Bilinear shape functions
N_e	Number of finite elements
N_{mf}	2x2 matrix of membrane forces
N_n	Number of finite element nodes
$\hat{p}$	Direction of rotation
$\hat{p}_x$, $\hat{p}_y$, $\hat{p}_z$	Components of the unit rotational pseudo vector
p	Distributed transverse load on the plate, Order of accuracy for the interpolation schemes
p_{int}	Interpolated solution at an arbitrary point in the bilinear interpolation
P	Typical material point
P_B	Column-matrix of beam linear momenta expressed in the deformed frame
P_r	Projector matrix

q	Vector of assembled nodal degrees of freedom, Vector of amplitudes of finite-section modes
q_{dg}^{m}	Vector of displacements at a node m with respect to the undeformed local element frame expressed in the global frame
q_e	Finite element nodal degree of freedom vector of size 18x1
Q_{s_0}	Column vector of generalized forces corresponding to finite-section modes
Q_{s_1}	Column vector of generalized moments corresponding to finite-section modes
Q_t	Vector of generalized momenta corresponding to finite-section modes
r_p	Position vector of a point on the undeformed beam reference line
r_{el}^{int}	Nonlinear local internal force vector
r_{el-g}^{int}	Nonlinear global internal force vector
r_{el}^{int-p}	Nonlinear internal force vector filtered through the projector matrix P_r
R	Assembled nonlinear internal force vector in the global frame, wing length, error ratio used in the estimation of order of accuracy for interpolation schemes
Re	Reynolds number
Rf	Residual force vector
R_p	Position vector of a point on the deformed beam reference line
R_h	Effective load vector
s	A slave node used in the CFD grid re-meshing
S	Current nodal coordinate system, Planform area of the wing
S_b	First-order asymptotic approximation to the beam stiffness matrix
S_o	Initial nodal coordinate system
S_r	Spectral radius parameter
St	Strouhal number
t	Time
T	Transformation matrix used in the computation of pure nodal rotations in the current element frame, time period of either plunge or flap
T_{EG}	Transformation matrix from global frame to the current element frame
T_{IG}	Transformation matrix from global frame to inertial frame
T_{GE}^{f}	Expanded form of the transformation matrix T_{GE}

T_{GE_o}	Transformation matrix from undeformed element frame to global frame
$T_{S_{new}}$	Rotation matrix corresponding to a nodal triad in the current Newton-Raphson iteration
$T_{S_{old}}$	Rotation matrix corresponding to a nodal triad in the previous Newton-Raphson iteration
$\bar{T}$	Rotation matrix used to update a nodal coordinate system
u_E^m	Pure nodal displacements at a node m
$u_{E_1}^m, u_{E_2}^m, u_{E_3}^m$	Pure nodal displacements at a node m in the current element coordinate system E along E_1, E_2, and E_3 directions respectively
U_s	Strain energy per unit length of beam
u, v, w	Flow velocities in the x, y, and z directions respectively
U_∞	Free stream velocity
U, V, W	Contravariant flow velocity components
v	Global velocity vector
v_{el}	Volume of a finite element
V_B	Beam inertial velocity column-matrix in the deformed frame
w	Column-matrix of three dimensional warping displacement components
x_e	Position vector of a material point with respect to the undeformed element frame
x_o	Position vector of the origin of an element frame in the undeformed configuration with respect to the global frame
x_m	Vector of coordinates of a master point m used in the CFD grid re-meshing
x_s	Vector of coordinates of a slave point s used in the CFD grid re-meshing
x_1	Coordinate along the beam span
x_2, x_3	Coordinates in the beam cross-section
X	Position vector of a material point with respect to the inertial frame
X_D	A point in the donor grid
X_I	A point in the receiver grid
X_R	Position vector of the flapping wing structure's actuation point with respect to the inertial frame
x_g	Position vector of a material point with respect to the global frame
z	Coordinate along the wing span
Ψ	Rotational pseudo vector

ψ	Magnitude of rotational pseudo vector
$\bar{\theta}_x, \bar{\theta}_y, \bar{\theta}_z$	Incremental rotations of a nodal triad computed in the global coordinate system during the previous Newton-Raphson iteration
$\theta_{E_1}, \theta_{E_2}, \theta_{E_3}$	Pure nodal rotations at a node about E_1, E_2, and E_3 directions respectively
$\bar{\omega}$	Angular velocity vector prescribed at the root
Ω	Skew symmetric matrix of the angular velocity vector $\bar{\omega}$
Ω_B	Beam inertial angular velocity vector at a point on the beam reference line in the deformed frame
Ω_{pn}	Anti-symmetric spin tensor corresponding to pure nodal rotations
ω_n	Column vector of incremental rotations of a nodal triad
$\alpha_f, \alpha_m, \gamma_{nm}, \beta$	Parameters related to the generalized-α method
α_k	Interpolation coefficients associated with the thin plate spline interpolation
β_c, f_m	Parameter used in the CFD grid re-meshing
γ	Vector of beam extensional and transverse shear strains
Δq	Incremental displacements in the Newton-Raphson iteration loop
Δt_f	Time step in the fluid solution
Δt_s	Time step in the structural solution
ζ_2, ζ_3	Area coordinates corresponding to a triangle finite element
ξ, η, γ	Time dependent curvilinear coordinates
θ	Decay function used in the CFD grid re-meshing
μ	Quantity that accounts for both laminar and turbulent viscosity, mass per unit length
ν	Poisson's ratio
Φ	Wing beat amplitude in radians
ρ_f	Fluid density
ρ_s	Structural density, density of plate/shell material
Π_1	Scaling parameter associated to the effective stiffness for an isotropic Kirchoff plate bending in a viscous fluid
Π_2	Scaling parameter associated to the mass moment of inertia for an isotropic Mindlin plate bending in a viscous fluid
ρ^*	Scaling parameter associated to the relative importance of structural and fluid densities for an isotropic Kirchoff or Mindlin plate bending in a viscous fluid

Acronyms

API	Application Programming Interface
BCIZ	Bazeley, Cheung, Irons, and Zienkiewicz
CFD	Computational Fluid Dynamics
COMP	Computation
CR	Co-rotational
CR-TL	Co-rotational-total Lagrangian
CR-UL	Co-rotational-updated Lagrangian
CSD	Computational Structural Dynamics
DKT	Discrete Kirchoff Triangle
DOF	Degrees of Freedom
DPIV	Digital Particle Image Velocimetry
EXP	Experiment
FBG	Fiber Bragg Gratings
FE	Finite Element
FWMAV	Flapping Wing Micro Air Vehicle
GCL	Geometric Conservation Law
LE	Leading Edge
LES	Large Eddy Simulation
LEV	Leading Edge Vortex
LST	Linear Strain Triangle
MAV	Micro Air Vehicle
NAFEMS	National Agency for Finite Element Methods and Standards
OPT	Optimal membrane Triangle
PDMS	Polydimethylsiloxane
PIV	Particle Image Velocimetry
RMS	Root Mean Square
TE	Trailing Edge
TPS	Thin Plate Spline
UM/NLABS	University of Michigan/Nonlinear Active Beam Solver
UM/NLAMS	University of Michigan/Nonlinear Membrane Shell Solver
UM/VABS	University of Michigan/Variational Asymptotic Beam Sectional Analysis Solver
URANS	Unsteady Reynolds Averaged Navier Stokes

Abstract

A Computational Aeroelasticity Framework for Analyzing Flapping Wings

by

Satish Kumar Chimakurthi

Co-Chairs: Carlos E.S. Cesnik and Wei Shyy

Flexible flapping wings have garnered a large amount of attention within the micro aerial vehicle (MAV) community: a critical component of MAV flight is the coupling of aerodynamics and structural dynamics. This dissertation presents a computational approach for simulating beam/shell-like wing structures flapping in incompressible flow at low Reynolds numbers in both hover and forward flight. Several nonlinear structural solutions of variable fidelity are coupled to an in-house developed pressure-based Navier-Stokes solution in a partitioned framework. In such an approach, the nonlinear partial differential equations modeling the dynamic behavior of the fluid and the structure are solved independently with boundary information (aerodynamic loads and structural displacements) shared between each other.

In the initial part of this dissertation, the development of a nonlinear structural dynamics solution suitable for flapping wings using the co-rotational approach is discussed. Next, the development of a suite of computational aeroelastic solutions using the partitioned approach is discussed. Verification and partial validation studies are presented for both the structural dynamics and the aeroelastic solvers using different wing configurations.

Case studies are presented for three different flexible wing configurations: rectangular wings with pure prescribed plunge motion, an elliptic wing with pure prescribed flap rotation, and a rectangular wing also prescribed with pure flap rotation. Numerical studies of the plunging wings showed that within the range of non-dimensional parameters considered, only a limited amount of spanwise flexibility is favorable for thrust generation. It was found that in the case of the most flexible plunging wing configuration, the instantantaneous angle of attack at most sections along the wing span decreased relative to other wings of lower flexibility. This was identified as being responsible for the decrease in the aerodynamic forces generated. Further, issues related to coupling strategies, fluid physics associated with rigid and flexible wings, and phase lag between prescribed motion and response were carefully examined.

Preliminary aeroelastic studies on the rectangular and elliptic flapping configurations indicated that within the range of parameters considered, aerodynamic forces could be enhanced due to wing flexibility.

The nonlinear aeroelastic framework developed will enable comprehensive analysis of flapping wings in support of future experimental tests and ultimately lead to identification of new MAV flapping wing concepts.

Chapter I

INTRODUCTION

Flapping Wing Micro Air Vehicles (FWMAVs) have the potential to revolutionize our capabilities of gathering information in environmental monitoring, homeland security, and other time sensitive areas [78, 79]. To fulfill that, they must have the ability to fly in urban settings, tunnels and caves, maintain forward and hovering flight, maneuver in constrained environments, and "perch" until needed. Due to their small size (maximum dimension on the order of 15 cm), flight regime (flight speeds of approximately 10-15 m/s operating in a low Reynolds number range of 10^3-10^5), and modes of operation, significant scientific advancement will be needed to create this revolutionary capability. The rise and growth of these vehicles have been stimulated by the long history of natural flight studies. From a biology-inspired viewpoint, aerodynamics, structural dynamics, and flight dynamics of birds, bats, and insects intersect with some of the richest problems in aerospace engineering which include:

- **Massively unsteady three-dimensional separation and vortical flows**: As an example, insect wings generate extra lift due to massive flow separation at the leading edge at large angles of attack which subsequently leads to the formation of a "leading edge vortex (LEV)" [31, 80].

- **Unsteady flight environment**: The flight environment around an insect wing is intrinsically unsteady due to wind gust and complex flapping motion. Therefore, insects utilize multiple unsteady aerodynamic mechanisms for lift and thrust enhancement [29, 95].

- **Aeroelasticity**: High speed cine and still photography and stroboscopy indicate that most biological flyers undergo orderly deformation in flight [102]. Further, there is substantial anisotropy in the wing structural characteristics between the chordwise and spanwise directions due to their venation patterns [23]. Although still being understood, it is possible that aeroelastic effects improve their aerodynamic performance since, for example, they seem to employ shape control to accommodate spatial and temporal flow structures [78].

- **Adaptive control:** Insects combine sensing, control, and wing maneuvering to maintain flight stability. For example, sensing an oncoming gust, feedback or adaptive control directs insect wings to flap asymmetrically compensating for the wind [80].

These are certain specific features found in natural flyers that may pose several challenges in a biologically inspired design of FWMAVs. In principle, one might like to first understand these biological systems, abstract certain desirable features and then apply them to the vehicle design. However, a challenge is that the scaling of both fluid dynamics and structural dynamics between a smaller natural flyer and practical flying hardware/lab experiment (larger dimension) is fundamentally difficult since a variety of scaling parameters (discussed later) have to be conserved in order to preserve the physics found in the former. Regardless, in order to develop a satisfactory flyer, the design needs to meet the following

objectives [77–79]:

- generate necessary lift which scales with the vehicle/wing length scale as l^3 (under geometric similitude); however, oftentimes, a flyer needs to increase or reduce lift to maneuver towards/avoid an object, resulting in the need for substantially more complicated considerations.

- minimize the power consumption.

In order to design optimal flyers within an entire flight envelope, there is a need to develop a knowledge base guiding future design of FWMAVs across a range of wind gust, flight speed, and time scales.

When wind gust adjustment, object avoidance, or station keeping become major factors, highly deformed wing shapes and coordinated wing-tail movement are often observed. Figure 1.1a illustrates such behavior for a hummingbird maneuvering around a potential threat, a chickadee adjusting its flight path to accommodate a target, and a finch making a precision landing. Understanding of the aerodynamic, structural, and control implications of these modes is essential for the development of high performance and robust micro air vehicles capable of performing desirable missions. The large deformations of animal wings lead to complex fluid-structure interactions, while the kinematics of flapping and the spectacular maneuvers performed by natural flyers result in coupled nonlinearities in fluid mechanics, aeroelasticity, flight dynamics, and control systems. Furthermore, as mentioned before, insect wings are generally anisotropic because of their structural construction: corrugated membrane skin, vein configuration, reinforced leading edge, etc. It was found that in a

majority of insect species the spanwise wing bending stiffness is about 1 to 2 orders of magnitude larger than the chordwise bending stiffness [23]. It was shown in literature [23] that, for certain species of insects, spanwise flexural stiffness scales with the third power of the wing chord while the chordwise stiffness scales with the second power of the wing chord. Figure 1.1b shows wings of a dragonfly, cicada, and a wasp. They exhibit substantial variation in aspect ratios and shapes but share the common feature of a reinforced leading edge. A dragonfly wing has more local variations in its structural composition and is more corrugated than the wing of a cicada or a wasp. It was shown in literature [75] that wing corrugation increases both warping rigidity and flexibility. Furthermore, specific characteristic features have been observed on the wing structure of a dragonfly which even help prevent fatigue fracture [75]. Moreover, the thin nature of the insect wing skin structure makes it unsuitable for taking compressive loads, which may result in skin wrinkling and/or buckling (i.e., large local deformations that will then interact with the flow). Consequently, several questions naturally arise in the analysis of flapping wings. Some of them are [79]:

- Can large flexible deformations provide a better interaction with the aerodynamics than if limited to the linear regimes ?
- If torsion stiffness along the wing span can be tailored, how can that affect the wing kinematics for optimum thrust generation ?
- How do these geometrically nonlinear effects and the anisotropy of the structure impact the aerodynamics characteristics of the flapping wing ?

All of these are issues that require detailed investigations and the understanding of which is

critical for the success of future FWMAV designs. Due to the foregoing reasons and many others, fluid-structure interaction studies are critical to FWMAV design.

While experimental techniques are extremely useful and much needed to support such studies, it is terribly difficult to measure airflow around actual insect wings [52] flapping at high frequencies due to their small size and the limitations of high speed photography techniques. Since quantifying the airflow and deformation patterns in three dimensions is critical for understanding the aerodynamic/aeroelastic mechanisms in insect flight, researchers have therefore resorted to dynamically scaled laboratory models [29, 95]. However, as already mentioned, the process of scaling is fundamentally very difficult and may lead to certain assumptions in the experimental models. For example, to date, robotic-model investigations have focused only on the flapping pattern of rigid wings without accounting for structural flexibility [80].

Computational aeroelasticity studies of flapping wings supported by experimental validation will therefore be of great advantage to surpass the limitations mentioned above [105]. As part of this dissertation, a suite of computational aeroelastic solutions have been developed to support the analyses of a variety of flapping wing structures. In order to give a perspective of the work done here, previous work in the areas including rigid wing aerodynamics of FWMAVs, experimental studies of flexible FWMAVs, and computational aeroelasticity of flapping wings is reviewed next.

1.1 Literature Review

1.1.1 Review of Experimental/Computational Studies in Aerodynamics of Rigid Flapping Wing Micro Air Vehicles

The aerodynamics of insect flight in relation to FWMAVs has been widely studied in the past several decades [6, 29, 31, 66, 81, 82, 100]. Most of the previous work focused on the unsteady lift and thrust generation mechanisms in flapping airfoils/wings. Excellent reviews [72, 92, 97] of the articles concerning these topics were done by several researchers in the past and so only a selected few such publications will be reviewed here.

The wing stroke of an insect is typically divided into four portions: two translational phases (upstroke and downstroke) when the wings sweep through the air with a high angle of attack, and two rotational phases (pronation and supination), when the wings rapidly rotate and reverse direction. The predictions of lift forces occuring during the wing stroke, computed using quasi-steady aerodynamic models have not been consistent with the physical measurements, especially when the hovering flight of insects was considered [80]. The lift coefficients estimated by direct force measurements in flying insects were found to be significantly larger than those predicted by the quasi-steady methods. Therefore, in the past decade or so, there has been a search for additional unsteady aerodynamic mechanisms to address this enigma of force production.

Ellington *et al.* [31], in their experimental effort, used a robotic laboratory model and visualized the airflow around the wings of the hawkmoth *Manduca Sexta* hovering at a chord-based Reynolds number of ≈ 2000 and found an intense leading-edge vortex (LEV)

in the downstroke of sufficient strength to explain the high-lift forces. It was mentioned that the LEV was created by a dynamic stall mechanism. The impact of spanwise flow on the stabilization of the LEV was also emphasized.

Liu and Kawachi [57] have conducted unsteady Navier-Stokes simulations around the hawkmoth wing in hover to probe the unsteady aerodynamics of hovering flight. Through their simulations, they confirmed the presence of a LEV at the end of pronation (the rotation that precedes the downstroke) previously observed in the experiments of Van Den Berg and Ellington [95]. They also observed spanwise axial flow consistent with what was observed in the robotic wing experiment of Ellington *et al.* [31].

Aono and Liu [6] used a multi-block and overset grid-based finite volume unsteady Navier-Stokes solver to study the force generation in the flapping flight of a hawkmoth in hover. One of the main conclusions of their study was that the structure of the LEV plays a key role in aerodynamic force-generation.

Birch and Dickinson [16] on the other hand performed experiments on a dynamically scaled robotic model of a *Drosophila* wing (a fruitfly) flapping in mineral oil at a Reynolds number of 160. The wing was equipped with sensors capable of directly measuring the time history of aerodynamic forces. They found from the measurements of spanwise velocity that the axial flow velocity within the core of the LEV was quite small and was only 2-5% of the average wing-tip velocity. The flow structure generated by the fruitfly wing was substantially different from that described for the model hawkmoth wing. No structure analogous to the spiral vortex of a delta-wing aircraft or the core of the LEV contained axial flow of very low velocity. In an attempt to find an answer to the stabilization of

the the LEV in the absence of spanwise flow in their fruitfly wing, they discovered that the prolonged attachment of LEV on insect wings may be due to the attenuating effect of the downwash induced by wake vorticity which decreases the strength of the vortex and provides stability to it. Because a spiral vortex was clearly present on the robotic model hawkmoth of Ellington *et al.* [31], their results suggest that the precise flow structure of a LEV may depend critically on Reynolds number. Further, they mentioned that, because the body length of a typical adult insect is in the range of 4-5 mm, fruitflies (body length $\approx$2.5-4 mm) might represent a better general model for the fluid mechanics of hovering flight than the much larger hawkmoths (body length $\approx$42 mm).

Recently, Shyy *et al.* [82] showed that for a low aspect-ratio flapping wing, tip vortices can increase lift both by creating a low-pressure region near the wing tip and by anchoring the leading-edge vortex to delay or even prevent it from shedding. Furthermore, it was also shown that, for certain flapping kinematics, the LEV remains attached along the spanwise direction and the tip effects are not prominent; in such situations, the aerodynamics is little affected by the aspect ratio of the wing.

Dickinson *et al.* [29] measured the time history of aerodynamic forces which were generated by a pattern of wing motion based on *Drosophila* kinematics. Results showed a transient peak in aerodynamic force at the start and end of each upstroke and downstroke. They determined that the peaks are due to a rotational mechanism akin to the Magnus effect [22], since they could not be accounted for, by a LEV which is a translational mechanism of unsteady lift (i.e., the LEV occurs during the translational phase of the wing stroke).

Lauder [52] provided a nice one page review of the work done by Ellington *et al.* [31]

and Birch and Dickinson [16]. He highlights the differences between the structure of the LEV observed in the robotic hawkmoth and the robotic fruitfly investigated by these biologists. He also emphasized the importance of DPIV (digital particle image velocimetry) for studying the mechanics of animal locomotion in fluids.

From their Navier-Stokes computations, Shyy and Liu [81] showed that while LEV is common to flapping wing aerodynamics at a Reynolds number (based on characteristic chord and flapping speed) of $O(10^4)$ or lower, its main characteristics and the implications on the lift generation change as the Reynolds number (wing sizing, flapping frequency) varies.

Ramamurti and Sandberg [66] used a finite element flow solver to compute unsteady flow past a *Drosophila* wing undergoing flapping motion. In their study, the effect of phasing between translational and rotational motions was studied by varying the rotational motion prior to the stroke reversal. It was observed that, when the wing rotation is advanced with respect to the stroke reversal, the peak in the thrust forces is higher than when the wing rotation is in phase with the stroke reversal and that the peak thrust is reduced further when the wing rotation is delayed.

Srygley and Thomas [88] trained red admiral butterflies *Vanessa atalanta* to fly freely to and from artificial flowers in a wind tunnel. They used high resolution, smoke-wire flow visualizations to obtain qualitative, high-speed digital images of the air flow around their wings. A motivating factor for their experiment was that previous researchers performed experiments with tethered insects, which may impact their flapping pattern. From their images, they showed that free-flying butterflies use a variety of unconventional aerodynamic

mechanisms to generate force: wake capture, two different types of leading-edge vortices, active and inactive upstrokes, in addition to the use of rotational mechanisms and the Weis-Fogh "clap-and-fling" mechanism. Further, they showed that free-flying butterflies often used different aerodynamic mechanisms in successive strokes. They mentioned that there is no one "key" to insect flight, instead insects rely on a wide array of aerodynamic mechanisms to take off, maneuver, maintain steady flight, and land.

Taylor *et al.* [91] showed that the cruise propulsive efficiency (defined as ratio of aerodynamic power output to mechanical power input) of birds, bats, and insects peaks within the interval $0.2 < St < 0.4$ (where St is Strouhal number). Previous studies show that this is also true for swimming animals like dolphins, sharks, and bony fish. The authors further mention that tuning cruise kinematics to optimize St seems to be a general principle of oscillatory lift-based propulsion. In order to show that St is tightly constrained in cruising flight, they provided two independent confirmations. As part of the first, they checked how St varies when an animal is forced to fly other than its preferred speed. They showed that it varied more in four individual zebra finches (*Taenopygia guttata*) forced to fly between 4 and 14 ms^{-1} than across all other 42 species flying at their preferred speeds. It means that flight speed affects St strongly because wing-beat frequency and amplitude are tightly constrained by physiology and morphology. A Monte Carlo analysis provided the second confirmation that St is tightly constrained in cruising flight. Further details of this are given in their work. Having provided independent confirmation that flying animals both operate within a narrow range of St when cruising and have converged on the optimum range $0.2 < St < 0.4$ expected for high propulsive efficiency, they mentioned that as a simple rule of

thumb, a cruising animal will move at a speed just over three times the product of its stroke frequency and amplitude (for $St \approx 0.3$). They conclude by predicting that for a flapping micro-air vehicle of 15-cm span cruising with a 90^o stroke angle (10-cm stroke amplitude) at 10 ms^{-1} should attain peak propulsive efficiency at a wingbeat frequency of just over 30 Hz.

Sallstrom and Ukeiley [70] investigated the flow over a rigid Zimmerman wing flapping at approximately +/-45 deg using stereoscopic particle image velocimetry. They have taken velocity snapshots at various phases of the wing for several chordwise locations while flapping in hover at two different frequencies (5 and 10 Hz) corresponding to Reynolds numbers of 230 and 450 respectively. Those snapshots have been divided into different phases and the flow at the same phase and location was averaged to create a three-dimensional average flow field. Results from the effort showed how vorticity is created by acceleration/deceleration of the wing and spread through diffusion and convection processes.

Bernal *et al.* [15] developed a new load cell for measuring force in a free-surface horizontal water tunnel. Fiber Bragg Gratings (FBG) were used to measure strain in the load cell flexures. The load cell was used to measure lift, drag, and pitching moment coefficients for a SD 7003 airfoil at Reynolds number 60x10^3 under steady and unsteady flow conditions considering both combined pitch/plunge and pure plunge. The unsteady measurement results show the large lift coefficients produced during mild and deep stall in the airfoil.

Shyy *et al.* [77, 80] have given an excellent review of flexible and flapping wing aerodynamics. In particular, they have reviewed aspects related to scaling and power implications, unsteady lift-enhancement mechanisms, thrust generation, effects of Reynolds number and

kinematics, amongst many others.

There are numerous other important articles and publications which discuss the aerodynamics of flapping wings which are not cited here but many of which could be found in Refs. [3, 53, 72, 92, 97].

1.1.2 Review of Experimental Studies in Aeroelasticity of Flapping Wing Micro Air Vehicles

The aeroelasticity of flapping wings has only recently been seriously addressed and a full picture of the basic aeroelastic phenomena in flapping flight is still not clear. Experimental efforts to study flexible FWMAVs are scarce in the literature. Some of these are discussed next.

Heathcote *et al*. [41] have experimentally investigated the effects of stiffness on thrust generation of airfoils undergoing a plunging motion under various free stream velocities. Direct force measurements showed that the thrust/input-power ratio (i.e. the propulsive efficiency) was found to be greater for flexible airfoils than for the rigid one. They also observed that at high plunging frequencies, the less flexible airfoil generates the largest thrust, while the more flexible airfoil generates the most thrust at low frequencies. To study the effect of spanwise stiffness on the thrust, lift, and propulsive efficiency of a plunging wing, a water tunnel study was conducted on a NACA 0012 uniform wing of aspect ratio 3. They observed that, introducing a degree of spanwise flexibility was found to be beneficial. For Strouhal numbers greater than 0.2, a degree of spanwise flexibility was found to yield a small increase in thrust coefficient, and a decrease in power-input requirement, resulting

in higher efficiency. In this case, a moderately stronger trailing-edge vortex system was observed. Introducing a far greater degree of spanwise flexibility, however, was found to be detrimental. They noted that the range of Strouhal numbers for which spanwise flexibility was found to offer benefits overlaps the range found in nature: $0.2<St<0.4$ [91].

Frampton *et al*. [33] have investigated a method of wing construction that results in an optimal relationship between flapping wing bending and twisting such that optimal thrust forces are generated. The thrust production of flapping wings was tested in an experimental rig. Results from this study indicated that the phase between bending and torsional motion is critical for the production of thrust. It was noted that a wing with bending and torsional motion in phase creates the largest thrust whereas a wing with the torsional motion lagging the bending motion by 90 deg results in the best efficiency.

Singh and Chopra [85, 86] and Singh [84] developed an experimental apparatus with a bio-inspired flapping mechanism to measure the thrust generated for a number of wing designs. The mechanism was operated at frequencies up to 12 Hz. The average air loads were measured using a custom built load cell with highly sensitive piezo-resistive strain gauges. The key conclusions that stemmed from this study are that the inertial loads constituted the major portion of the total loads acting on the flapping wings tested on the mechanism and that for all the wings tested, the thrust dropped at higher frequencies. Further, the author found that at such frequencies, the light-weight and highly flexible wings used in the study exhibited significant aeroelastic effects.

Sallstrom *et al.* [71] investigated air flow around three Zimmerman wings flapping in a simulated hover environment with varying flexibility using stereoscopic particle image ve-

locimetry. The wings were made from a carbon fiber skeleton and covered with a flexible membrane. Flexibility was varied by changing the number of layers of carbon fiber reinforcing the leading edge and hence it mainly affected the spanwise bending stiffness. Their study mainly showed how a wing that is too compliant in the spanwise direction suffers from poor performance producing thrust.

Wu *et al.* [103] presented a multidisciplinary experimental endeavor in correlating FW-MAVs aeroelasticity and thrust production, by quantifying and comparing elasticity, dynamic responses and air flow patterns of six different pairs of MAV wings (in each one, the membrane skin was reinforced with different leading edge and batten configurations) of the Zimmerman planform (two ellipses meeting at the quarter chord) with varying elastic properties. In their experiment, single degree-of-freedom flap motion was prescribed to the wings in both air and vacuum. A customized digital image correlation system was used to measure the wing deformation, a load sensor to record forces on the wings, and a stereo digital particle image velocimetry setup to capture flow structures. From the measurements of wing deformation and flow velocities, they have observed significant differences in aeroelastic behavior across the spectrum of tested wings. Amongst many conclusions, importantly, they found that only a suitable amount of flexibility is desirable for thrust generation.

Combes and Daniel [24] suggested that if inertial-elastic forces dominate wing bending, the dynamic shape of flapping wings could be predicted prior to calculations of aerodynamic force production avoiding the coupled aeroelastic problem. In their work, they used an experimental approach to examine the relative contributions of inertial-elastic and

fluid-dynamic forces to passive wing bending. Fresh *Manduca Sexta* wings were flapped (single degree-of-freedom rotation) at a realistic wingbeat frequency and stroke amplitude, mimicking the large amplitude motions of freely flying moths. High-speed video recording was done to compare instantaneous wing deformations of wings flapping in normal air versus helium (which has approximately 15% air density). They found that wings flapped in helium displayed similar spatial and temporal bending patterns and the same dominant frequencies of motion as wings flapped in normal air, despite the 85% reduction in fluid density. This demonstrated that the contribution of aerodynamic loading to instantaneous wing shape in *Manduca* is minor compared to the contribution of wing inertia. However, as they also mention, the kinematics prescribed to their wings were simple in that the wing rotated around only the dorsal-ventral axis of the wing hinge. Realistic wing kinematics which may include rapid wing rotations evident in some species during stroke reversal may involve increased aerodynamic forces and were not accounted for in their study. Further, the relative contributions of inertial-elastic and aerodynamic forces to wing bending will vary with flight conditions (hovering or forward-flight).

Most recently, Agrawal and Agrawal [1] attempted to expand the understanding of flexible wings in the context of flapping flight and translate the benefits of insect wing flexibility into a simple synthetic flexible wing design using both numerical and experimental approaches. To study the effects of flexibility on aerodynamic performance, the performance of two synthetic wings was compared: (i) a flexible wing based on a bio-inspired design of the hawkmoth (*Manduca Sexta*) wing and (ii) a rigid wing of similar geometry. The load-deformation characteristics of a real hawkmoth wing were first obtained through

static tests. The flexible synthetic wing was then designed in two steps - the structural model of the synthetic wing was analyzed using finite element analysis, followed by an optimization procedure to match the deflection profile of the synthetic wing with the real hawkmoth wing, using the diameter and modulus of veins as design variables. Since the matching for static load-deflection characteristics does not guarantee the performance of wings under dynamic flapping, they ensured a close match of the mass distribution of the flexible synthetic wing and the real insect wing. It is important to note that they have not recreated the venation pattern of the real hawkmoth wing for their synthetic wing design, but used a simpler venation pattern and matched the static load-deflection characteristics with the former. The FE model had 14 veins and their modulii were optimized by coupling the FE model with an optimization procedure. Finally, for the fabrication of the optimized wing, they considered a scaled-up version. For testing the aerodynamic performance of rigid and flexible wings, dynamic tests were performed on four wings: flexible wing with membrane, flexible wing without membrane, rigid wing with membrane, and rigid wing without membrane. The results from their tests showed that the aerodynamic performances of a bio-inspired flexible wing and a rigid wing are noticeably different. For example, more thrust was generated by the flexible wing compared to the rigid wing in all the three kinematic patterns considered. The authors emphasize that their results provide motivation for exploring the advantages of passive deformation through wing flexibility and that coupled fluid-structure simulations of flexible flapping wings are required to gain a fundamental understanding of the physics and to guide optimal FWMAV designs.

1.1.3 Review of Computational Studies in Aeroelasticity of Flapping Wing Micro Air Vehicles

While the previous subsections reviewed either computational/experimental studies in rigid flapping wing aerodynamics or experimental studies in aeroelasticity of flapping wings, this subsection presents a review of previous efforts in computational aeroelasticity. This will subsequently lead to the objectives of this dissertation whose focus is on the development of computational aeroelastic solutions suitable for flapping wing analyses.

Hamamoto *et al*. [38] have conducted finite element analysis based on the arbitrary Lagrangian-Eulerian method to perform fluid-structure interaction analysis on a deformable dragonfly wing in hover and examined the advantages and disadvantages of flexibility. No particular reference was made to the type of structural/fluid model used in the analysis. They tested three types of flapping flight: a flexible wing driven by dragonfly flapping motion, a rigid wing (stiffened version of the original flexible dragonfly wing) driven by dragonfly flapping motion, and a rigid wing driven by modified flapping based on tip motion of the flexible wing. They found that the flexible wing with nearly the same average energy consumption generated almost the same amount of lift force as the rigid wing with modified flapping motion, which realized the same angle of attack at the aerodynamically dominant sections of the wing. However, the rigid wing required 19% more peak torque and 34% more peak power, indicating the usefulness of wing flexibility.

Singh [84] and Singh and Chopra [86] have discussed a computational framework for the aeroelastic analysis of hover-capable, bio-inspired flapping wings. An in-house developed linear plate finite element solver was coupled with an in-house developed unsteady

aerodynamic solver based on indicial functions. Both of these solvers were validated with data available in literature. The structural model was validated with experiments conducted on an aluminium plate undergoing pure flapping motion and the aerodynamic model was validated with data available for a robotic insect. The authors considered two different light wings made out of mylar membrane and reinforced by aluminium frame. A bio-inspired combined flapping and pitching motion was prescribed. Frequencies up to 12 Hz were considered. Two different computational analyses were done on the wings: "uncoupled" aeroelastic analysis and "coupled" aeroelastic analysis. In the former, the assumption made was that wing bending in hovering insects is predominantly caused by inertial forces alone. So, in the calculation of wing deformations, the aerodynamic forces were neglected. However, no such assumption is made in the latter approach. The chord-based Reynolds number considered for all the analyses was in the 10^3 to 10^5 range. Results indicated that a "coupled" analysis did not have significant impact on the average thrust. But, the bending moment predictions were significantly altered. This shows that the aerodynamic loads cannot be neglected in computing the wing deformations.

Zhu [106] has performed a fully coupled fluid-structure interaction analyses to investigate the flapping motion of a flexible foil/wing. For the fluid dynamics solution, he used a three-dimensional boundary element method (model valid only up to Strouhal number 0.3 when the effect of leading edge separation is insignificant) and a two-dimensional nonlinear thin plate model for the structural dynamics solution. Therefore, the fluid flow is assumed to be irrotational, except for an infinitesimally thin wake shed from the trailing edge of the foil which is modeled as a shear layer. For the validation of his coupled fluid-structure

model, the author compared their computational results with experimental data obtained by Heathcote *et al.* [40] for a flexible airfoil in pure plunge. In this study, the author examined wings that can be bent in either the chordwise or the spanwise direction. To clarify the role of inertia in the deformation of the wing, the motion of it was studied in both water and air. Results showed that when the wing is immersed in air, the chordwise flexibility reduces both the thrust and the propulsion efficiency whereas spanwise flexibility (through equivalent plunge and pitch flexibility) increases the thrust without efficiency reduction within a small range of structural parameters. However, when the wing is immersed in water, the chordwise flexibility increased the efficiency and the spanwise flexibility reduced both the thrust and the efficiency.

Willis *et al.* [101] have presented a computational framework to design and analyze FWMAV flight. A series of different geometric and physical fidelity level representations of solution methodologies was described in the work. While a geometric nonlinear beam model is available in the framework for the structural solver, for the aerodynamics three different solvers were made available: lifting line aerodynamics, an unsteady boundary element method, and a high-order discontinuous Galerkin method for the solution of the Navier-Stokes equations. The authors emphasized that by using a multi-fidelity approach, design and analysis can be performed at an appropriate level of fidelity, in a moderate amount of time.

Liani *et al*. [56] coupled an unsteady panel method (where the airfoil may be of arbitrary shape and thickness but the flow is assumed to be attached) with the equations of motion for a two degree-of-freedom (pitch and plunge) typical wing section. They investigated the

elastic effect on the aerodynamic forces produced at different frequencies especially near its resonance. In the analysis, the airfoil was made infinitely rigid in pitch and the effect of aeroelastic oscillations was observed only when a plunge motion was prescribed. Computations were done for several frequencies and results showed that the forces on the airfoil (both lift and thrust) greatly increased while approaching the resonance frequency of the structure. They mentioned that this enhancement of aerodynamic forces may be beneficial for flapping wings so as to maximize aerodynamic efficiency. Apart from this analysis, the authors have also conducted experiments in a wind tunnel to investigate the forces acting on a carbon fibre flat rectangular wing undergoing root-flapping oscillations (Reynolds number: $24\text{x}10^3$ and tested reduced frequency range: 0.37 to 0.5). Numerical results were produced for this configuration with a linear finite element beam solver coupled with the aerodynamic model of Theodorsen. The authors found good agreement between computations and experiment over the frequency range examined and showed that flexibility can enhance aerodynamic forces on a flapping wing.

Tang *et al.* [90] explored a (two-dimensional) flexible airfoil by coupling a pressure based Navier-Stokes solver with a finite-element linear beam solver. In this work, the fluid flow around a plate of different thicknesses with a tear-drop shaped leading edge was computed at a Reynolds number of $9\text{x}10^3$. In addition to this, a flat plate with half cylinders at leading and trailing edges were investigated at a Reynolds number of 10^2 to probe the mechanism of thrust generation. In particular, they pointed out that the effect of the deformation (passive pitching) is similar to the rigid body motion (rigid pitching), meaning that the detailed shape of the airfoil is secondary to the equivalent angle of attack.

Kim *et al.* [51] presented a coupling method for the fluid-structure interaction analysis of a flexible flapping wing. The aerodynamic model was based on a modified strip theory improved to take into account a high relative angle of attack and dynamic stall effects induced by pitching and plunging motions. The details of the structural model are not furnished except that it considered large flapping motions and local elastic deformations. Their aeroelastic model was applied to a rectangular flapping wing and the results were validated with experimental data.

Unger *et al.* [94] coupled a density-based unsteady Reynolds-averaged Navier-Stokes (URANS) flow solver with a nonlinear finite element solver (shell and membrane FE) to perform aeroelastic analysis of a wing that is flexible in the chord-wise direction and rigid spanwise. The wing cross-section has a rigid leading edge region while the rest of the cross-section has flexible shell/membrane-like supports to mimic the foil of a real-life pigeon. The wing was prescribed with a combined sinusoidal plunging/pitching motion (Reynolds number: 10^5, reduced frequency: 0.2). The key conclusions from the study are that laminar separation bubbles on the upper and lower side of the airfoil move from trailing edge to the leading and back and that the computed deformations had good agreement with deformations measured in a wind tunnel.

Gogulapati *et al.* [35] coupled a commercial finite element solver (MSC.Marc) and a potential flow solution that uses a combined circulation/vorticity approach to compute unsteady aerodynamic loads. The aerodynamic model originally developed for rigid wings by Ansari *et al.* [3,4] was extended in this work to include spanwise flexibility. Preliminary aeroelastic response results indicated that, for the parameters considered in their study, the

effect of aerodynamic loads is relatively minor compared to the effect of the inertial loads; wing flexibility is found to have a favorable effect on lift generation.

In a successive effort, Gogulapati *et al.* [36] extended the aerodynamic model to include chordwise flexibility and showed preliminary aeroelastic results for flexible hawkmoth wings in hover. Preliminary aeroelastic results obtained for relatively stiff configurations suggested that spanwise flexibility may have a prominent role in flapping wings.

Ho *et al.* [42] used the two-way coupling feature of a commercially available flow solver (CFD-ACE+) and the structural dynamics solver FEMSTRESS to create their aeroelastic solution. Aeroelastic computations were validated against experimental results for flapping wings made of a parylene membrane skin reinforced with a titanium leading edge spar. They showed that stiffness distribution is a key parameter in determining vortex interaction and thrust production. Their results also showed that while higher stiffness is required in the outboard region of the wing to enhance lift, more flexibility is required in the inboard region for producing thrust.

Gopalakrishnan [37] coupled a linear elastic membrane solver with an unsteady LES (Large Eddy Simulation) flow solver to analyze flexible flapping wings. The focus of the study was on evaluating the effects of elastic cambering on flow structures and aerodynamic performance. No fluid-structure interpolation was used since the same grid distribution was used in both the solvers. Further, the inertial forces due to flapping were neglected in computing the deformations. The test wing chosen corresponds to a rectangular membrane prescribed with coupled torsional and single degree of freedom flap rotation. All simulations have been carried out at a chord-based Reynolds number of 10^3 for forward flight and

for an advance ratio of 0.5. Different membrane pre-stresses were investigated to give a desired camber in response to the aerodynamic loading. The results showed that the camber introduced by the wing flexibility increases the thrust and lift production considerably. Analysis of flow structures revealed that the leading edge vortex stays attached on the top surface of the wing, glides along the camber, and covers a major part of the wing, which results in high force production. On the other hand, for rigid wings (which were also considered) the leading edge vortex lifts off from the surface resulting in low force production.

Chandar and Damodaran [19] coupled an incompressible flow solver called "overBlown" provided by the Lawrence Livermore National Laboratory with an in-house developed thin-plate solver based on finite differences. They studied both a two-dimensional flexible airfoil and a spanwise-flexible wing prescribed with plunge motion and obtained good correlations with previous computations and experimental data. It was also shown in their work that a proper combination of time step, numerical relaxation, and damping yields stable numerical solutions.

Ishihara *et al.* [44] used a monolithic fluid-structure interaction approach to couple a set of nonlinear fluid and solid equations and studied the effect of passive pitching due to wing torsional flexibility and its impact on lift generation in Dipteran flight. They showed that given a sinusoidal flapping motion with a frequency below the wing torsion natural frequency, the resulting passive pitching in the steady state under fluid damping is approximately sinusoidal with the advanced phase shift. They also demonstrated that the lift generated can support the weight of some Diptera.

More recently, Attar and Gordnier [8] coupled a sixth-order Navier-Stokes solver to a

finite element solver of a two degree-of-freedom nonlinear string model to perform high fidelity aeroelastic computations. A low Reynolds number of 10^4 consistent with MAV flight was chosen and the effect of the plunging Strouhal number and reduced frequencies along with the static angle of attack of plunging was examined for both rigid and flexible wings.

1.2 Objectives of this Dissertation

Based on the literature review, it is clear that studies on the aeroelasticity of flapping wings are scarce and moreover, most of the computational aeroelasticity solutions previously developed have not been necessarily equipped with capabilities general enough to handle different types of wing structures and flight conditions. In some of those cases where CFD was used, only linear structural solvers were used in conjunction to it. And, in others where nonlinear structural dynamics solvers were used, they involved only simplified unsteady aerodynamics. Further, in the cases where both nonlinear structural dynamics and CFD solvers were used, the coupling algorithms have been of lower fidelity or the aeroelastic studies involved only two-dimensional structures. Overall, the coupling of high-fidelity nonlinear CFD and CSD solvers applicable to study of three-dimensional flapping wings has received very limited attention in literature. Keeping these shortcomings in view, the overall objectives of this dissertation are to:

- develop a suite of computational aeroelasticity solutions involving various nonlinear CSD and CFD solvers.

- develop a nonlinear structural dynamics shell finite element solution to address three-dimensional flapping wing investigations.
- investigate the physics of flexible plunging/flapping wings and examine the impact of wing flexibility on thrust generation.

(a)

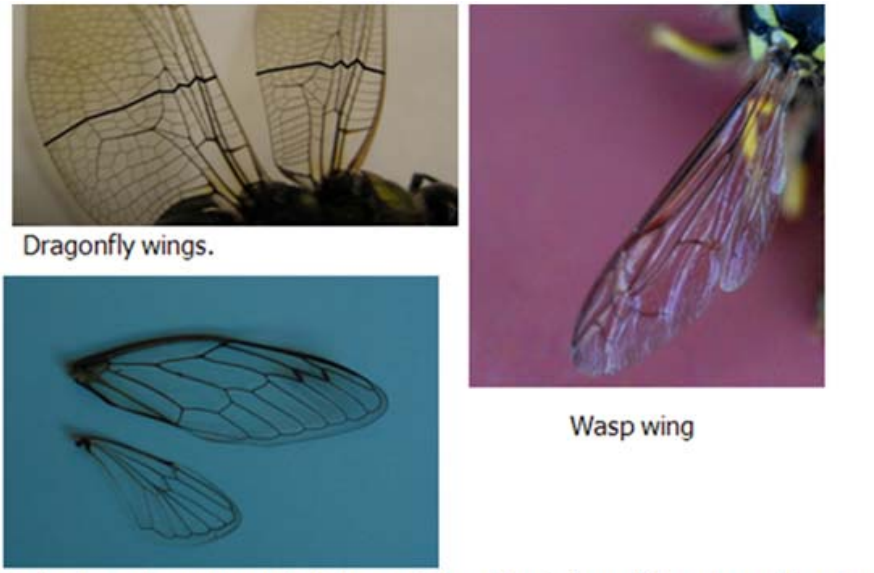

(b)

Figure 1.1: (a) Asymmetric flapping kinematics, involving wing-tail coordination, are displayed with a hummingbird avoiding a potential threat, a chickadee making adjustment while flying towards a target, and a finch during landing; (b) Wing structures of dragonfly, cicada and wasp with reinforced leading edge, anisotropic mechanical property distributions, and corrugated geometries [79].

Chapter II

CSD/CFD FORMULATIONS

This chapter presents the theoretical formulation for the structural dynamics solution (UM/NLAMS-"University of Michigan/Nonlinear Membrane Shell Solver") that was developed in this work and for some additional structural and fluid dynamics solutions used in conjunction with UM/NLAMS to develop multiple aeroelastic solutions. The CSD formulation developed in this work is discussed in the first section and then the additional CSD formulations (UM/NLABS-"University of Michigan/Nonlinear Active Beam Solver", MSC.Marc) and a CFD formulation ("UM/STREAM") are discussed in the second and third sections respectively. In the final section, scaling parameters are derived via the nondimensionalization of the CSD and CFD equations of motion presented in the initial sections.

2.1 CSD Formulation

2.1.1 UM/NLAMS (total Lagrangian co-rotational geometrically nonlinear shell solution)

The geometrically nonlinear shell finite element formulation developed here is based on a co-rotational approach and has the capability to handle time-dependent boundary conditions suitable for a flapping wing problem. The nonlinear structural dynamics solution is based on a flexible multi-body type finite element analysis [98, 99] of a flapping wing. It relies on the use of a body-fixed floating frame of reference to describe the prescribed rigid body motion and on a co-rotational (CR) form of the total Lagrangian approach [10] to account for geometric nonlinearities. The solution is implemented in the "University of Michigan's Nonlinear Membrane Shell Solver (UM/NLAMS)", written in Fortran 90. The CR formulation has generated a great amount of interest in the last couple of decades. A comprehensive list of references that discuss this formulation is available in [99]. The idea of this approach is to decompose the motion into rigid body and pure deformational parts through the use of a local frame at each finite element which translates and rotates with the element [13]. The components of the element's internal force vector are first calculated relative to the CR frame and are then transformed to a "global" frame using a CR transformation matrix. The CR frame transformation eliminates the element rigid body motion so that a linear deformation theory can be used [99] as long as the flexible deformations are small with respect to the element dimensions. Hence, the main advantage of it is its effectiveness for problems with small strains but large rotations [93].

The co-rotational formulation can be applied in two different forms as listed below:

1. **total Lagrangian (CR-TL)**: In this approach, the reference configuration is taken as the initial configuration, but translated and rotated in accordance with the motion of the co-rotating local system.

2. **updated Lagrangian (CR-UL)**: In this approach, the translated and rotated configuration at the previous time-step is taken as the reference configuration during the current time-step [58].

The CR-TL approach is used in this work. Co-rotational formulations involving shell elements for flexible multi-body systems applications are scarce and are discussed in Refs. [59, 98]. Application of this method to problems concerning flapping wing aeroelasticity are not available, however, recent studies by Relvas and Suleman [68, 69] reported the development of a method involving the application of co-rotational theory to nonlinear aeroelasticity problems. Reference [68] discusses the coupling of a vortex-ring method with a co-rotational structural solution of a four-noded shell FE and studied the stability of a nonlinear clamped plate subjected to low speed airflow to illustrate the fluid-structure interaction procedure. In a subsequent effort, the authors [69] presented the coupling of an Euler flow solver with a nonlinear co-rotational beam FE solver and demonstrated it by studying the dynamic response of two-dimensional NACA 0012 airfoil section that is resting on a Winkler foundation. Two types of analyses were performed: first assuming that the airfoil is rigid and second assuming it to be flexible and discretizing the airfoil surface with co-rotational beam elements.

The three key issues identified during a literature survey concerning the use of a co-rotational formulation are:

1. the choice of a suitable local element frame

2. the choice of a suitable anisotropic element (this is especially important for triangular shells since they are obtained as a superposition of membrane and plate models and several combinations are possible)

3. parameterization of local and global rotations

The first issue is discussed in Refs. [13, 27, 61]. While several alternatives have been proposed for the choice of the local element frame, for most problems where only small strains are involved this issue is not important. However, in such a case, it is critical that the local element deformational displacements are small relative to the element dimensions. In the current work, triangular elements will be used for the finite element discretization. The specific issues involved in choosing local element frames concerning the use of trianglular shell elements are discussed in Ref. [12], and the choice of a suitable linear element in Ref. [14]. The development of flapping wing dynamic finite-element equations of motion for thin shell structures is discussed next. The formulation is a proposed extension for flapping wing dynamics of the static co-rotational analysis of shell structures presented in Refs. [49, 50, 67].

The derivation of flapping wing equations of motion using nonlinear shell finite elements via a co-rotational approach to accommodate prescribed time-dependent boundary conditions involves several key steps discussed next:

2.1.1.1 Definition of coordinate systems in the analysis

Several coordinate systems are required to fully describe the geometry and deformation of the shell structure. Fig. 2.1 shows a schematic of a typical triangular shell finite element in its initial (undeformed) and the deformed (current) configurations. A total of 2+N_e+N_n (where N_e is the number of finite elements and N_n is the number of nodes in the discretized structure) coordinate systems are used in the analysis:

- an inertial frame that is always fixed in time (I in Fig. 2.1)
- a floating(global) frame whose motion is known in the inertial frame by virtue of the prescribed rigid body motion of the structure (g in Fig. 2.1)
- N_e co-rotational frames (one for each element) that translate and rotate with the element as it deforms ("E_o" and "E" in Fig. 2.1)
- N_n nodal coordinate frames (one for each node) that are rigidly tied to their respective nodes and rotate with them ("S_o" and "S" in Fig. 2.1).

The final equations of motion are written with respect to the global frame, g.

2.1.1.2 Computation of inertial velocities and accelerations of a material point

The position (in the inertial frame) of a material point P (see Fig. 2.1) in the structure is given by

$$X = X_R + T_{IG}\, x_g \tag{2.1}$$

where X is the position vector in the inertial frame, X_R is the position vector of the structure's actuation point (or the origin of the flapping/global frame) in the inertial frame, x_g is the position vector of P in the global frame, and T_{IG} is a transformation matrix from global frame to the inertial frame. This matrix is a nonlinear function of the components of the rotational pseudo vector Ψ (a unit vector that defines a finite rotation in space) [7], which defines the orientation of the global frame with respect to the inertial frame. The pseudo vector is defined as:

$$\Psi = \psi\, \hat{p} \tag{2.2}$$

where ψ is the magnitude of rotation and $\hat{p}$ is the direction of rotation, defined as:

$$\hat{p} = \frac{\Psi}{\psi} = \left\{ \begin{array}{c} \hat{p}_x \\ \\ \hat{p}_y \\ \\ \hat{p}_z \end{array} \right\} \tag{2.3}$$

In general, both the magnitude ψ and the direction of rotation $\hat{p}$ could be time dependent. In the case where the direction of rotation is constant, the resultant motion of the tip of the pseudo vector will be in a plane. If the direction of rotation changes with time, the motion of the tip will be in three dimensions. The former case is two-dimensional and the latter is three-dimensional rotation [7, 9]. The transformation matrix T_{IG} is defined as in [34]:

$$T_{IG} = I_m + \tilde{\hat{p}}\, sin\psi + 2\, (\tilde{\hat{p}})^2\, sin^2 \frac{\psi}{2} \tag{2.4}$$

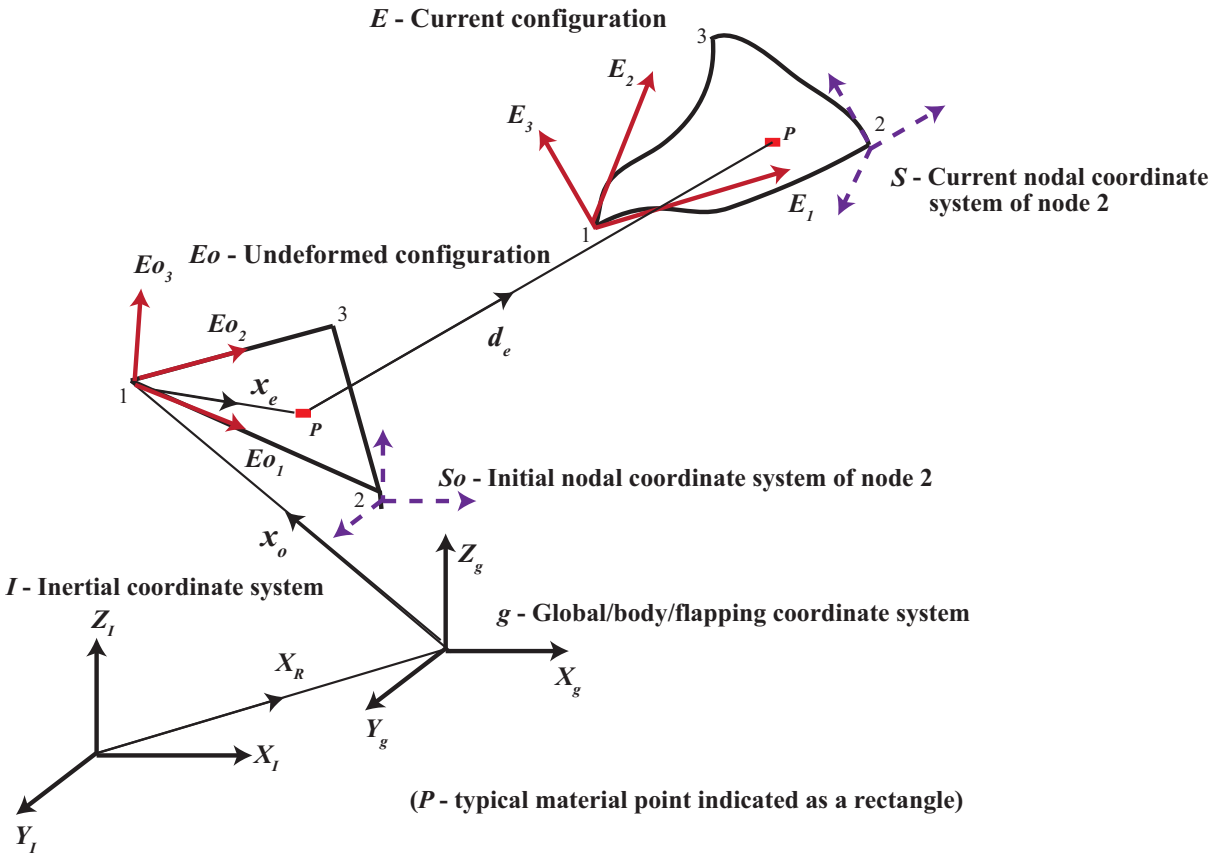

Figure 2.1: A schematic showing the undeformed (initial) and deformed configurations of a typical shell element and the various coordinate systems involved in the analysis.

where I_m is a 3×3 identity matrix and the tilde indicates a skew-symmetric matrix. The position vector of the material point with respect to the global coordinate system x_g given in Eq. 2.1 can be written as:

$$x_g = x_o + T_{GE_o}\,(x_e + d_e) \tag{2.5}$$

where x_o is the position vector of the origin of an element frame in the undeformed configuration with respect to the global frame expressed as components in the global frame,

T_{GE_o} is the transformation matrix from undeformed element frame to the global frame, x_e is the position vector of the point with respect to the undeformed element frame, and d_e is the vector of displacements of the point with respect to the same. The position vector of the material point in the inertial frame given in Eq. 2.1 then becomes:

$$X = X_R + T_{IG}\, x_o + T_{IG}\, T_{GE_o}\, x_e + T_{IG}\, T_{GE_o}\, d_e \tag{2.6}$$

The time derivative of the transformation matrix in Eq. 2.4 is [73]:

$$\dot{T}_{IG} = \Omega\, T_{IG} \tag{2.7}$$

where Ω is a skew symmetric matrix of the angular velocity vector $\bar{\omega}$ prescribed at the wing root. The velocity and acceleration of the material point can then be computed by successive differentiation of the position vector in Eq. 2.6 and are given as:

$$\dot{X} = \dot{X}_R + \Omega\, T_{IG}\, x_o + \Omega\, T_{IG}\, T_{GE_o}\, x_e + \Omega\, T_{IG}\, T_{GE_o}\, d_e + T_{IG}\, T_{GE_o}\, \dot{d}_e \tag{2.8}$$

$$\ddot{X} = \ddot{X}_R + (\dot{\Omega} + \Omega\,\Omega)\, T_{IG}\, (x_o + T_{GE_o}\, x_e + T_{GE_o}\, d_e) + 2\,\Omega\, T_{IG}\, T_{GE_o}\, \dot{d}_e + T_{IG}\, T_{GE_o}\, \ddot{d}_e \tag{2.9}$$

2.1.1.3 Computation of virtual work due to inertial forces

The virtual work due to inertial forces for an element is given by:

$$\delta W = \rho_s \int_{v_{el}} \delta X^T \ddot{X} dv_{el} \tag{2.10}$$

where δX is the variation of the position vector, i.e.,

$$\delta X = T_{IG}\, T_{GE_o}\, \delta d_e \tag{2.11}$$

and v_{el} is the volume of the element. The vector of displacements d_e can be approximated as:

$$d_e = N q_e \tag{2.12}$$

where N is a matrix of shape functions of size 3×18 and q_e is the finite element nodal degree of freedom vector of size 18×1 with respect to the undeformed element frame. The variation of the position vector now becomes:

$$\delta X = T_{IG}\, T_{GE_o}\, N\, \delta q_e \tag{2.13}$$

The acceleration vector can be written as:

$$\begin{aligned} \ddot{X} = \ddot{X}_R + (\dot{\Omega} + \Omega\, \Omega)\, T_{IG}\, (x_o + T_{GE_o}\, x_e + T_{GE_o}\, N\, q_e) + \\ 2\, \Omega\, T_{IG}\, T_{GE_o}\, N\, \dot{q_e} + T_{IG}\, T_{GE_o}\, N\, \ddot{q_e} \end{aligned} \tag{2.14}$$

Using the above terms, the virtual work expression in Eq. 2.10 now becomes:

$$\delta W = \rho_s \int_{v_{el}} \left\{ \begin{array}{c} \delta q_e^T \; N^T \; T_{GE_o}^T \; T_{IG}^T \; \ddot{X}_R + \\ \delta q_e^T \; N^T \; T_{GE_o}^T \; T_{IG}^T \; (\dot{\Omega} + \Omega \; \Omega) \; T_{IG} \; x_o + \\ \delta q_e^T \; N^T \; T_{GE_o}^T \; T_{IG}^T \; (\dot{\Omega} + \Omega \; \Omega) \; T_{IG} \; T_{GE_o} \; x_e + \\ \delta q_e^T \; N^T \; T_{GE_o}^T \; T_{IG}^T \; (\dot{\Omega} + \Omega \; \Omega) \; T_{IG} \; T_{GE_o} \; N \; q_e + \\ 2 \; \delta q_e^T \; N^T \; T_{GE_o}^T \; T_{IG}^T \; \Omega \; T_{IG} \; T_{GE_o} \; N \; \dot{q}_e + \\ \delta \; q_e^T \; N^T \; T_{GE_o}^T \; T_{IG}^T \; T_{IG} \; T_{GE_o} \; N \; \ddot{q}_e \end{array} \right\} dv_{el} \tag{2.15}$$

From this expression, the element local mass matrix, gyroscopic damping matrix, dynamic stiffness matrix, and the inertial contribution to the force vector are given by:

$$M_{el} = \rho_s \int_{v_{el}} \left\{ N^T \; T_{GE_o}^T \; T_{IG}^T \; T_{IG} \; T_{GE_o} \; N \right\} dv_{el} \tag{2.16}$$

$$C_{el} = 2\rho_s \int_{v_{el}} \left\{ N^T \; T_{GE_o}^T \; T_{IG}^T \; \Omega \; T_{IG} \; T_{GE_o} \; N \right\} dv_{el} \tag{2.17}$$

$$K_{el}^{dyn} = \rho_s \int_{v_{el}} \left\{ N^T \; T_{GE_o}^T \; T_{IG}^T \; (\dot{\Omega} + \Omega \; \Omega) \; T_{IG} \; T_{GE_o} \; N \right\} dv_{el} \tag{2.18}$$

$$F_{el}^p = -\rho_s \int_{v_{el}} \{ N^T \; T_{GE_o}^T \; T_{IG}^T \; \ddot{X}_R + N^T \; T_{GE_o}^T \; T_{IG}^T \; (\dot{\Omega} + \Omega \; \Omega) \; T_{IG} \; x_o + \tag{2.19}$$

$$N^T \; T_{GE_o}^T \; T_{IG}^T \; (\dot{\Omega} + \Omega \; \Omega) \; T_{IG} \; T_{GE_o} \; x_e \} dv_{el} \tag{2.20}$$

These equations are numerically integrated using a 7 point Gauss quadrature [107]. The element mass matrix in Eq. 2.16 is consistent. The damping matrix in Eq. 2.17 is a

skew-symmetric matrix arising from Coriolis forces. The stiffness matrix in Eq. 2.18 is a dynamic term representing the coupling effect between the large rigid body motions and the elastic motions. The elastic portion of the stiffness matrix will be discussed subsequently. The force vector in Eq. 2.19 is due to the prescribed rigid body motion. The first term arises from rigid body translational motion. The second and the third terms arise from rigid body angular and centrifugal accelerations. A fourth term in the forcing vector will arise due to aerodynamic loading (discussed later). The key steps involved in the computation of the virtual work due to inertial forces are highlighted in a flowchart shown in Fig. 2.2.

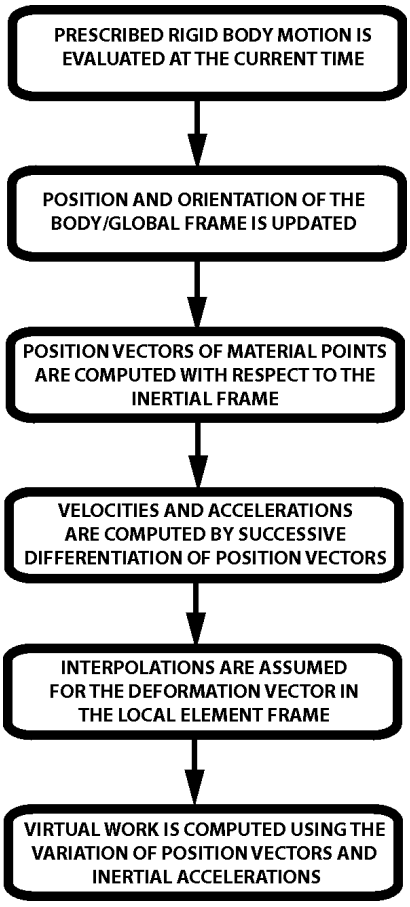

Figure 2.2: Procedure for computation of virtual work due to inertial forces

2.1.1.4 Element local deformations (co-rotational approach)

As mentioned above, the static co-rotational formulation of a shell element as described in Refs. [49, 50, 67] is used in this work. While full details of the approach are provided in those references, a brief overview of it is presented here, while extensively quoting from Ref. [49]. Referring to Fig. 2.1, the origin of the undeformed element frame E_o is chosen at node 1 of the element and the axis E_{o_1} (i.e., the local x-axis) is chosen as the line joining nodes 1 and 2. The axis E_{o_3} (the local z-axis) is the normal to the element mid-plane containing the nodes 1, 2, and 3. The axis E_{o_2} (the local y-axis) then defines a Cartesian right-handed coordinate system. The coordinate system denoted by E is the element co-rotational system defined in a similar fashion but in the current or deformed configuration. The nodal coordinate systems are denoted by S_o and S in the undeformed and deformed configurations, respectively (shown only for node 2 in Fig. 2.1 for clarity). The orientation of S_o is arbitrary and is chosen to be parallel to the inertial frame in this work. The coordinate system S in the current configuration is obtained by updating its transformation matrix, which defines the current orientation of the node in the global system. This is done after every Newton-Raphson iteration using the following expression:

$$T_{S_{new}} = \bar{T}\, T_{S_{old}} \tag{2.21}$$

where

$$\bar{T} = I_m + \frac{\tilde{\omega}_n + 0.5\tilde{\omega}_n^2}{1 + 0.25 \mid \omega_n \mid^2} \tag{2.22}$$

$$\omega_n = \begin{bmatrix} \bar{\theta}_x & \bar{\theta}_y & \bar{\theta}_z \end{bmatrix}^T \tag{2.23}$$

$$\tilde{\omega}_n = \begin{bmatrix} 0 & -\bar{\theta}_z & \bar{\theta}_y \\ \bar{\theta}_z & 0 & -\bar{\theta}_x \\ -\bar{\theta}_y & \bar{\theta}_x & 0 \end{bmatrix} \tag{2.24}$$

The $\bar{\theta}$ quantities are the incremental rotations of triad S computed in the global coordinate system during the previous iteration. Once the nodal coordinate systems in the current configuration are obtained, the next step is the computation of the pure deformations (both displacements and rotations) in the local coordinate system E. Pure nodal displacements at a node "m" in E may be expressed by the relation:

$$u_E^m = \begin{Bmatrix} u_{E_1}^m \\ u_{E_2}^m \\ u_{E_3}^m \end{Bmatrix} = T_{EG}\left(q_{dg}^m + x_o^m - q_{dg}^1 - x_o^1\right) - x_e^m \tag{2.25}$$

where m=1, 2, 3. T_{EG} is a transformation matrix from global frame to the current element frame, q_{dg}^m is the displacement vector of a node m in the global frame, x_o^m is the position vector of node m in the undeformed element configuration expressed in the global frame. x_o^1 is equal to x_o introduced in Eq. 2.5. Pure nodal rotations expressed in E are equal to the components of an anti-symmetric matrix spin tensor defined as:

$$\Omega_{pn} = \begin{bmatrix} 0 & -\theta_{E_3} & \theta_{E_2} \\ \theta_{E_3} & 0 & -\theta_{E_1} \\ -\theta_{E_2} & \theta_{E_1} & 0 \end{bmatrix} \tag{2.26}$$

This tensor is found by using the following expressions:

$$\Omega_{pn} = 2(T - I_m)(T + I_m)^{-1} \tag{2.27}$$

$$T = T_{EG}\, T_{S_{new}}\, T_{GE_o} \tag{2.28}$$

where the matrices T_{EG} and $T_{GE_o}^T$ transform the components of a vector in the global frame into those in deformed co-rotational and undeformed co-rotational frames respectively. The vector of pure deformations at a node is given by:

$$d_{pure}^m = \begin{bmatrix} u_{E_1}^m & u_{E_2}^m & u_{E_3}^m & \theta_{E_1}^m & \theta_{E_2}^m & \theta_{E_3}^m \end{bmatrix}^T \tag{2.29}$$

The vector of pure element deformations is obtained by combining such vectors at all three nodes of the element and is given by:

$$d_{pure} = \begin{pmatrix} d_{pure}^1 \\ d_{pure}^2 \\ d_{pure}^3 \end{pmatrix} \tag{2.30}$$

2.1.1.5 Element stiffness matrix / Nonlinear internal force vector

A three-node triangular shell element involving an optimal membrane element (OPT) [32] and a discrete Kirchoff triangle (DKT) plate bending element [11] presented in Refs. [49, 50] is used in this work. Both of these elements are described briefly below:

- **DKT**: In the process of deriving the stiffness matrix for this element, unlike in many

triangular plate elements, a complete quartic polynomial (15 terms) is used to represent the out-of-plate displacement [25]. However, the usual nine degrees of freedom (DOF) (two rotations and a displacement at each node) are initially supplemented by extra degrees of freedom at the vertices and mid-sides. The constraint of zero transverse shear strain is then enforced at selected locations. With these constraints imposed, a nine DOF element is obtained at the end with two rotations and a displacement at each of the element nodes. As a consequence of the process by which the element is derived, the transverse displacement is not explicitly defined in the interior of the element. Hence, the shape functions required to form either the mass matrix or the stress stiffening matrix (discussed later) are not available. This problem may be overcome by borrowing shape functions from other similar elements. Following Ref. [49], for the displacement interpolation, the shape functions corresponding to a "BCIZ (Bazeley, Cheung, Irons, and Zienkiewicz)" [107] plate element are used. The stiffness matrix corresponding to the plate bending DOF can be written as [49]:

$$K_b = \int B_b^T \; D \; B_b \; dA_e \tag{2.31}$$

where B_b is the strain-nodal displacement matrix corresponding to bending deformation, D is the bending stiffness matrix, and A_e is the area of the triangular finite element.

- **OPT**: The OPT element is termed "optimal" because, for any arbitrary aspect ratio, its response for in-plane pure bending is exact. Like the DKT element, the OPT element is based on an assumption on strains and so the shape functions are borrowed

from another triangular membrane element ("LST-Ret") with the same degrees of freedom as that of the OPT element. The stiffness matrix corresponding to the membrane DOF are [49]:

$$K_m = \int B_m^T \, A \, B_m \, dA_e \tag{2.32}$$

where B_m is the strain-nodal displacement matrix corresponding to membrane deformation, and A is the stretching stiffness matrix.

The DKT and the OPT element stiffness matrices are combined to form the final shell stiffness matrix of the element and further modified to include the membrane-bending coupling effect for laminated composite plates:

$$K_{el}^{shell} = \begin{bmatrix} K_m & \int B_m^T \, B \, B_b \, dA_e \\ \int B_b^T \, B \, B_m \, dA_e & K_b \end{bmatrix} \tag{2.33}$$

where B is the membrane-bending coupling stiffness matrix. More details of the stiffness matrices including the definition of the individual terms are presented in Ref. [49].

The effect of nonlinear stress stiffening is added to the co-rotational formulation by including a geometric stiffness matrix [25]. The expression for stress stiffening is obtained by considering the work done by the membrane forces as they act through displacements associated with small lateral and in-plane deflections. The final expression for the stress

stiffening matrix is given by:

$$K_{el}^{ss} = \int_{A_e} G^T J_t^T \begin{bmatrix} N_{mf} & 0_{2\times2} & 0_{2\times2} \\ 0_{2\times2} & N_{mf} & 0_{2\times2} \\ 0_{2\times2} & 0_{2\times2} & N_{mf} \end{bmatrix} J_t \, G \, d\zeta_2 \, d\zeta_3 \tag{2.34}$$

The sub-matrix N_{mf} of size 2×2 whose components are the membrane forces, is the same as $\tilde{N}$ defined in Ref. [49]. More details on the derivation of this expression along with a definition of the individual terms are given in Refs. [25, 49].

Using the pure element deformations in Eq. 2.30, the nonlinear internal force vector is computed using the local element shell and dynamic stiffness matrices (after re-arranging them according to desired order of degrees of freedom as in Eq. 2.30) as:

$$r_{el}^{int} = (K_{el}^{shell} + K_{el}^{dyn}) \, d_{pure} \tag{2.35}$$

Since the pure deformations obtained in Eq. 2.30 may not be really pure, a projector matrix P_r can be introduced to bring the non-equilibrated internal force vector into equilibrium. More details about the idea of projection are given in Ref. [60]. The local element stiffness matrix computed in Eq. 2.33 and the internal force vector computed in Eq. 2.35 are filtered through the projector matrix as follows:

$$K_{el}^{shell-p} = P_r^T K_{el}^{shell} \, P_r \tag{2.36}$$

$$r_{el}^{int-p} = P_r^T \, K_{el}^{shell} \, d_{pure} \tag{2.37}$$

In computing the projection of the internal force vector, as shown in Eq. 2.37, the contribution due to the dynamic stiffness matrix is excluded. At this point, if the membrane forces are expected to be significant, the stress stiffness matrix obtained in Eq. 2.34 should be added to the projected local element stiffness matrix in Eq. 2.36.

Having obtained the stiffness and mass matrices along with the internal force vector in the element frame, they are all transformed into the global frame before the finite element assembly process. The transformation of the element local stiffness matrix which includes both the elastic and the dynamic stiffness terms is given as:

$$K_{el-g}^{shelldyn-p} = (T_{GE}^{f})(K_{el}^{shell-p} + K_{el}^{dyn})(T_{GE}^{f})^{T} \tag{2.38}$$

where the transformation matrix T_{GE}^{f} above is an expanded form of T_{GE} (which is transpose of T_{EG} defined earlier) used to accommodate the transformation of all the 18 degrees of freedom of the element. The subscript " $-\ g$" indicates that the corresponding element matrix operates on the global degrees of freedom. The superscript "f" indicates "full/expanded". Similarly, the element mass and the gyroscopic matrices given in Eqs. 2.16 and 2.17, respectively, are transformed into the global frame as follows:

$$M_{el-g} = T_{GE_o} M_{el} T_{GE_o}^{T} \tag{2.39}$$

$$C_{el-g} = T_{GE_o} C_{el} T_{GE_o}^{T} \tag{2.40}$$

Further, the element internal force and the prescribed motion force vectors given in Eqs. 2.37 and 2.19, respectively, are transformed to the global frame as:

$$r_{el-g}^{int} = T_{GE}^{f} r_{el}^{int-p} \tag{2.41}$$

$$F_{el-g}^{p} = T_{GE_o}^{f} F_{el}^{p} \tag{2.42}$$

The global element mass, stiffness, gyroscopic damping matrices given in Eqs. 2.39, 2.38, 2.40, respectively, and the element global internal force and the prescribed-motion force vectors given in Eqs. 2.41 and 2.42, respectively, are assembled for the entire structure to form global matrices/vectors. The global mass, tangent stiffness, and damping matrices are denoted as M, K_t (assembled form of $K_{el-g}^{shelldyn-p}$ matrix for the entire structure) , and C, respectively, while the global internal and the total force vectors are denoted as R and F. The total force vector F also includes the aerodynamic forces expressed in the global frame that are computed from a CFD analysis in this work (discussed later).

2.1.1.6 Direct time integration of UM/NLAMS governing equations

The nonlinear structural dynamics finite element governing equations of motion can be written as:

$$Ma + Cv + R(q) = F \tag{2.43}$$

where q is the nodal degree of freedom vector in the global frame, v and a are the global velocity and acceleration vectors, respectively. In this work, the numerical integration of the governing equations was performed using either the Newmark or the generalized-α

methods [21, 74]. Ref. [21] discussed the application of the generalized-α scheme for linear problems. In this work, it is extended to solve the nonlinear equations of motion in a predictor-corrector type of framework similar to the one described for the Newmark method in Ref. [89]. The generalized-α method discussed in Ref. [21] solves second-order differential equations for a discrete time-step, n, using the standard Newmark relations to update the displacements and velocities as shown below:

$$q_{n+1} = q_n + \Delta t_s \, v_n + \Delta t_s^2 \, [(\frac{1}{2} - \beta) \, a_n + \beta \, a_{n+1}] \tag{2.44}$$

$$v_{n+1} = v_n + \Delta t_s \, [(1 - \gamma_{nm}) \, a_n + \gamma_{nm} \, a_{n+1}] \tag{2.45}$$

The balance equation is given by:

$$M a_{n+1-\alpha_m} + C v_{n+1-\alpha_f} + R_{n+1-\alpha_f} = F(t_{n+1-\alpha_f}) \tag{2.46}$$

where

$$\begin{aligned} a_{n+1-\alpha_m} &= (1 - \alpha_m) a_{n+1} + \alpha_m a_n \\ v_{n+1-\alpha_f} &= (1 - \alpha_f) v_{n+1} + \alpha_f v_n \\ R_{n+1-\alpha_f} &= (1 - \alpha_f) R_{n+1} + \alpha_f R_n \\ F(t_{n+1-\alpha_f}) &= (1 - \alpha_f) F_{n+1} + \alpha_f F_n \end{aligned} \tag{2.47}$$

Substituting the relations in Eq. 2.47 into the balance equation in Eq. 2.46 gives:

$$\begin{aligned} M[(1 - \alpha_m) a_{n+1} + \alpha_m a_n] + C[(1 - \alpha_f) v_{n+1} + \alpha_f v_n] + (1 - \alpha_f) R_{n+1} + \\ \alpha_f R_n = (1 - \alpha_f) F_{n+1} + \alpha_f F_n \end{aligned} \tag{2.48}$$

Using the Newmark update relation of displacements Eq. 2.44, the accelerations become:

$$a_{n+1} = \frac{1}{\beta \Delta t_s^2}[q_{n+1} - q_n - \Delta t_s v_n - \Delta t_s^2(\frac{1}{2} - \beta)a_n] \tag{2.49}$$

$$a_{n+1} = \frac{1}{\beta \Delta t_s^2}[\delta q - \Delta t_s v_n - \Delta t_s^2(\frac{1}{2} - \beta)a_n] \tag{2.50}$$

Substituting this into the velocity update relation Eq. 2.45 gives:

$$v_{n+1} = v_n + \Delta t_s(1 - \gamma_{nm})a_n + \frac{\gamma_{nm}}{\beta \Delta t_s}\delta q - \frac{\gamma_{nm}}{\beta}v_n - \frac{\gamma_{nm}\Delta t_s}{\beta}(\frac{1}{2} - \beta)a_n \tag{2.51}$$

Substituting the previous two relations Eqs. 2.50, 2.51 in the velocity and acceleration relations of Eq. 2.47, gives:

$$a_{n+1-\alpha_m} = (1 - \alpha_m)\frac{1}{\beta \Delta t_s^2}[\delta q - \Delta t_s v_n - \Delta t_s^2(\frac{1}{2} - \beta)a_n] + \alpha_m a_n \tag{2.52}$$

$$v_{n+1-\alpha_f} = (1-\alpha_f)[v_n + \Delta t_s(1-\gamma_{nm})a_n + \frac{\gamma_{nm}}{\beta \Delta t_s}\delta q - \frac{\gamma_{nm}}{\beta}v_n - \frac{\gamma_{nm}\Delta t_s}{\beta}(\frac{1}{2}-\beta)a_n] + \alpha_f v_n \tag{2.53}$$

Using the tangent stiffness method [89], the internal forces at time step $n + 1$ (i.e., R_{n+1}) can be written as:

$$R_{n+1} = R_n + K_t \delta q \tag{2.54}$$

$$R_{n+1-\alpha_f} = (1 - \alpha_f)(R_n + K_t \delta q) + \alpha_f R_n \tag{2.55}$$

Substituting the previous set of equations in the balance equation, Eq. 2.46 becomes:

$$K_{eff}\delta q = R_h \tag{2.56}$$

where K_{eff} and R_h are the effective stiffness matrix and the effective load vector, and are given as:

$$K_{eff} = \frac{1-\alpha_m}{\beta\Delta t_s^2}M + \frac{1-\alpha_f}{\beta\Delta t_s}C + (1-\alpha_f)K_t \tag{2.57}$$

$$\begin{aligned} R_h = {} & \tfrac{1-\alpha_m}{\beta\Delta t_s}Mv_n + \tfrac{1-\alpha_m}{\beta}(\tfrac{1}{2}-\beta)Ma_n - \alpha_m Ma_n - C(1-\alpha_f)V_n - \\ & ... - C(1-\alpha_f)\Delta t_s(1-\gamma_{nm})a_n + C(1-\alpha_f)\tfrac{\gamma_{nm}}{\beta}v_n + C(1-\alpha_f)\tfrac{\gamma_{nm}\Delta t_s}{\beta}(\tfrac{1}{2} \\ & -\beta)a_n - C\alpha_f v_n - (1-\alpha_f)R_n - \alpha_f R_n + (1-\alpha_f)F_{n+1} + \alpha_f F_n \end{aligned} \tag{2.58}$$

A step-by-step solution procedure to solve the system of equations using the quantities computed in Eqs. 2.57 and 2.58 is given as follows:

1. Initialize q_o and its time derivatives.

2. Select a time-step size Δt_s and a spectral radius parameter S_r ($0 \leq S_r \leq 1$): this parameter is inversely proportional to the high frequency dissipation.

3. Compute parameters α_f = $-S_r$/(1+S_r) and α_m = (1-2S_r)/(1+S_r).

4. Compute parameters $\gamma_{nm} = 0.5 + \alpha_m - \alpha_f$ and $\beta = 0.25(1+\alpha_m-\alpha_f)^2$

5. Form the effective stiffness matrix from the individual mass, damping, and tangent stiffness matrices using Eq. 2.57.

6. Form the effective load vector Eq. 2.58.

7. Solve for the displacement increments using Eq. 2.56.

To improve the solution accuracy and to avoid the development of numerical instabilities, it is generally necessary to employ iterations within each time step in order to maintain equilibrium [89]. The following are the steps to be followed in a typical iteration (j) within the iterative loop.

- Evaluate the $(j-1)^{th}$ approximation to the acceleration, velocities, and displacements using:

$$\begin{gathered} a_{co} = \frac{1-\alpha_m}{\beta \Delta t_s^2}, a_{c1} = \frac{\gamma_{nm}}{\beta \Delta t_s} \\ a_{c2} = \frac{1}{\beta \Delta t_s}, a_{c3} = \frac{1}{2\beta} - 1 \\ a_{c4} = \frac{\gamma_{nm}}{\beta} - 1, a_{c5} = \frac{\Delta t_s}{2}(\frac{\gamma_{nm}}{\beta} - 2) \end{gathered} \tag{2.59}$$

$$\begin{aligned} a_{n+1}^{j-1} &= a_{co}\delta q^{j-1} - a_{c2}\dot{q}_n - a_{c3}\ddot{q}_n \\ v_{n+1}^{j-1} &= a_{c1}\delta q^{j-1} - a_{c4}\dot{q}_n - a_{c5}\ddot{q}_n \\ q_{n+1}^{j-1} &= q_n + \delta q^{j-1} \end{aligned} \tag{2.60}$$

- Update nodal rotation matrices using the new approximation to the solution q (last of Eq. 2.60) and Eq. 2.21.

- Evaluate the $(j-1)^{th}$ residual force with:

$$\begin{aligned} Rf_{n+1}^{j-1} = (1-\alpha_f)F(t_{n+1}) + \alpha_f F(t_n) - M(1-\alpha_m)a_{n+1}^{j-1} - M\alpha_m a_n - \\ ...C(1-\alpha_f)v_{n+1}^{j-1} - C\alpha_f v_n - (1-\alpha_f)R_{n+1}^{j-1} - \alpha_f R_n \end{aligned} \tag{2.61}$$

- Solve for the j^{th} corrected displacements using:

$$K_{eff}\Delta q^{j} = Rf_{n+1}^{j-1} \tag{2.62}$$

- Evaluate the corrected displacement increments with:

$$\delta q^{j} = \delta q^{j-1} + \Delta q^{j} \tag{2.63}$$

- Check for convergence of the iteration:

$$\frac{\mid \Delta q^{j} \mid}{\mid q_t + \delta q^{j} \mid} \leq tol \tag{2.64}$$

  where "*tol*" is convergence tolerance for the iteration.

- If the solution is not converged, return to the first step; if it does, proceed to the next time-step.

For a specific choice of the parameters involved in the generalized-α method, other integration schemes could be obtained. For example, if α_f = 0 and α_m = 0, the method reduces to the standard Newmark scheme. The primary goal of the generalized-α method is to provide the user with control over high frequency dissipation while limiting the impact on the low frequency dynamics. In aeroelastic simulations, this method could prove to be very beneficial in dissipating non-physical high frequency oscillations which result due to poor spatial resolution.

The generalized-α method was extended to systems of first-order differential equations by Jansen *et al.* [45] and later applied by Shearer and Cesnik [74] in the flight dynamic analysis of a highly flexible aircraft.

Fig. 2.3 highlights the key steps involved in the solution process of UM/NLAMS.

2.2 Additional CSD Formulations

Two additional CSD formulations used in the development of the aeroelastic solutions in this work are discussed next. First, an in-house developed quasi-$3D$ slender structural solver called UM/NLABS is discussed followed by a brief discussion of a commercial finite element solver called MSC.Marc.

2.2.1 UM/NLABS (total Lagrangian geometrically nonlinear beam/linear plate solution)

The geometrically-nonlinear structural dynamic solution in UM/NLABS is based on an asymptotic approach to the equations governing the dynamics of a general 3-D anisotropic slender solid [63, 64]. It is implemented in the "University of Michigan's Nonlinear Active Beam Solver (UM/NLABS)" computer code. Assuming the presence of a small parameter (the inverse of the wing aspect ratio) allows for a multi-scale solution process, in which the problem is decomposed into separate cross-sectional (small-scale) and longitudinal (long-scale) analyses. The longitudinal problem solves for average measures of deformation of the reference line under given external excitations. The cross-sectional problem solves the

local deformation for given values of the long-scale variables. Both problems are tightly coupled and together provide an efficient approximation to the displacement field in the original 3-D domain. A flow diagram of the process is shown in Fig. 2.4. The structural formulation follows the variational-asymptotic method for the analysis of composite beams [18]: the equations of motion for a slender anisotropic elastic 3-D solid are approximated by the recursive solution of a linear 2-D problem at each cross section [63], and a 1-D geometrically-nonlinear problem along the reference line [64]. This procedure allows the asymptotic approximation of the 3-D warping field in the beam cross sections, which are used with the 1-D beam solution to recover a 3-D displacement field. The warping is approximated for the elastic degrees of freedom of a Timoshenko-beam model (extension and transverse shear, γ, and twist, bending about two directions, κ) and augmented with an arbitrary set of functions approximating the sectional deformation field (amplitude, q, and its derivative along the spanwise direction, q'). These capture "non-classical" deformations, which are referred to as *finite-section modes*. And these new deformation modes are not restricted to be as small as the fundamental warping field. The solution of a variational problem yields the warping field corresponding to 1-D beam strains [γ, κ, q, q']. In its first order approximation, it can be written as [63]:

$$\begin{aligned} w(x_1, x_2, x_3) = w_\gamma\left(x_2, x_3\right)\gamma(x_1) + w_\kappa\left(x_2, x_3\right)\kappa(x_1) + w_{q_n}\left(x_2, x_3\right) q_n(x_1) \\ + w_{q_n'}\left(x_2, x_3\right) q_n'(x_1) + H.O.T. \end{aligned} \tag{2.65}$$

where [w_γ, w_κ, w_{q_n}, $w_{q_n'}$] are the first-order warping influence coefficients, x_1 is the curvilinear coordinate along the beam reference line, x_2 and x_3 are curvilinear coordinates in

the beam cross-section. Using this approximation for the warping field, the cross-section problem gives the strain energy per unit length of the beam which is given by:

$$U_s = \frac{1}{2}\left\{ \begin{array}{cccc} \gamma^T & \kappa^T & q^T & q'^T \end{array} \right\} [S_b] \left\{ \begin{array}{c} \gamma \\ \kappa \\ q \\ q' \end{array} \right\} + H.O.T. \tag{2.66}$$

Here, the constant matrix S_b is the first-order asymptotic approximation to the stiffness matrix. The integration of the kinetic energy can be directly done as function of the 1-D variables, yielding:

$$K_e = \frac{1}{2}\left\{ \begin{array}{ccc} V_B^T & \Omega_B^T & \dot{q_n}^T \end{array} \right\} [M_b] \left\{ \begin{array}{c} V_B \\ \Omega_B \\ \dot{q_n} \end{array} \right\} \tag{2.67}$$

where the constant matrix M_b is the inertia matrix for the cross section. From the resulting 1-D problem, the geometrically-nonlinear dynamic equations of equilibrium along the reference line (as presented in Ref. [64]) are written as:

$$\dot{P}_B + \tilde{\Omega}_B P_B = {F'}_B + \tilde{K}_B F_B - {f'}_1 - \tilde{K}_B f_1 + f_0 \tag{2.68}$$

$$\dot{H}_B + \tilde{\Omega}_B H_B + \tilde{\mathrm{V}}_B P_B = {M'}_B + \tilde{K}_B M_B - {m'}_1 - \tilde{K}_B m_1 + \left(\tilde{e}_1 + \tilde{\gamma}\right) F_B + m_0 \tag{2.69}$$

$$\dot{Q}_t = \left(Q'_{s_1} - {f'}_{s_1}\right) - \left(Q_{s_0} - f_{s_0}\right) \tag{2.70}$$

where the generalized forces and momenta are all expressed in their components in a reference frame attached to the deformed beam reference line. The first two equations above imply equilibrium of forces and moments. The last set of equations includes the equilibrium equations corresponding to the finite-section modes. The $(\bullet)'$and $(\dot{\bullet})$ mean the partial derivative with respect to the beam axial coordinate x_1 and time t, respectively. In the equations above, P_B and H_B are the sectional linear and angular momenta, F_B and M_B are the column vectors of sectional internal forces and moments per unit length on the reference line expressed in the deformed frame, f_0 and m_0 are the column vectors of conventional (zero-order) applied force and moment per unit length on the reference line expressed in the deformed frame, f_1 and m_1 are the first-order loads associated to the work needed to deform the beam cross-section, Q_{s_0} and Q_{s_1} are the column vectors of the generalized forces and moments corresponding to the finite-section modes, and Q_t is the vector of the corresponding generalized momenta. The last three magnitudes are vectors of dimension N_{fs}, the number of finite section modes.

The constitutive relations of the beam in the deformed frame can be written as:

$$\begin{Bmatrix} F_B \\ M_B \\ Q_{s_0} \\ Q_{s_1} \end{Bmatrix} = [S_b] \begin{Bmatrix} \gamma \\ \kappa \\ q \\ q' \end{Bmatrix} \tag{2.71}$$

where

$$\gamma = \begin{Bmatrix} \gamma_1 & 2\gamma_{12} & 2\gamma_{23} \end{Bmatrix}^T = C^{bB}\, R_p' - r_p' \tag{2.72}$$

is the vector of non-linear force strains in which R_p and r_p are the position vectors of the deformed and undeformed reference lines respectively, C^{bB} is the rotation matrix from the deformed frame B to the undeformed frame b. The vector of non-linear beam curvatures κ is given by:

$$\kappa = \left\{ \begin{array}{ccc} \kappa_1 & 2\kappa_2 & \kappa_3 \end{array} \right\}^T = C^{bB}\, K - k \tag{2.73}$$

K and k are the curvature vectors in the deformed and undeformed frames, respectively. Similarly, the generalized momentum-velocity relations are given by:

$$\left\{ \begin{array}{c} P_B \\ H_B \\ Q_t \end{array} \right\} = [M_b] \left\{ \begin{array}{c} V_B \\ \Omega_B \\ \dot{q} \end{array} \right\} \tag{2.74}$$

Assuming there is only one finite section mode, the constitutive relations in Eq. 2.71 can be explicitly written as:

$$\left\{ \begin{array}{c} F_{B_1} \\ F_{B_2} \\ F_{B_3} \\ M_{B_1} \\ M_{B_2} \\ M_{B_3} \\ Q_{s_0}^{(1)} \\ Q_{s_1}^{(1)} \end{array} \right\} = \left[\begin{array}{cccccccc} S_{11} & S_{12} & S_{13} & S_{14} & S_{15} & S_{16} & S_{17} & S_{18} \\ S_{21} & S_{22} & S_{23} & S_{24} & S_{25} & S_{26} & S_{27} & S_{28} \\ S_{31} & S_{32} & S_{33} & S_{34} & S_{35} & S_{36} & S_{37} & S_{38} \\ S_{41} & S_{42} & S_{43} & S_{44} & S_{45} & S_{46} & S_{47} & S_{48} \\ S_{51} & S_{52} & S_{53} & S_{54} & S_{55} & S_{56} & S_{57} & S_{58} \\ S_{61} & S_{62} & S_{63} & S_{64} & S_{65} & S_{66} & S_{67} & S_{68} \\ S_{71} & S_{72} & S_{73} & S_{74} & S_{75} & S_{76} & S_{77} & S_{78} \\ S_{81} & S_{82} & S_{83} & S_{84} & S_{85} & S_{86} & S_{87} & S_{88} \end{array} \right] \left\{ \begin{array}{c} \gamma_{11} \\ 2\gamma_{12} \\ 2\gamma_{23} \\ \kappa_1 \\ \kappa_2 \\ \kappa_3 \\ q^{(1)} \\ q'^{(1)} \end{array} \right\} \tag{2.75}$$

In a similar fashion, the generalized momentum-velocity relations in Eq. 2.74 can be written as:

$$\begin{Bmatrix} P_{B_1} \\ P_{B_2} \\ P_{B_3} \\ H_{B_1} \\ H_{B_2} \\ H_{B_3} \\ Q_t^{(1)} \end{Bmatrix} = \begin{bmatrix} M_{11} & M_{12} & M_{13} & M_{14} & M_{15} & M_{16} & M_{17} \\ M_{21} & M_{22} & M_{23} & M_{24} & M_{25} & M_{26} & M_{27} \\ M_{31} & M_{32} & M_{33} & M_{34} & M_{35} & M_{36} & M_{37} \\ M_{41} & M_{42} & M_{43} & M_{44} & M_{45} & M_{46} & M_{47} \\ M_{51} & M_{52} & M_{53} & M_{54} & M_{55} & M_{56} & M_{57} \\ M_{61} & M_{62} & M_{63} & M_{64} & M_{65} & M_{66} & M_{67} \\ M_{71} & M_{72} & M_{73} & M_{74} & M_{75} & M_{76} & M_{77} \end{bmatrix} \begin{Bmatrix} V_{B_1} \\ V_{B_2} \\ V_{B_3} \\ \Omega_{B_1} \\ \Omega_{B_2} \\ \Omega_{B_3} \\ \dot{q}^{(1)} \end{Bmatrix} \tag{2.76}$$

The implementation of this formulation in UM/NLABS follows the approach described in Ref. [64], where the solution to Eqs. 2.68, 2.69, and 2.70 is obtained by means of a finite-element discretization on a mixed-variational form of the equations. Therefore, although they are analyzed independently, the small and long-scale problems are intimately linked in the detailed approximation to the solution. This is particularly important in the generation of the solid side of an aeroelastic model: the interface of the structural model consists of the actual wetted surfaces of the vehicle, without extrapolations from the motion of a reduced-dimension structural model, nor the assumption of rigid cross sections utilized by beam theories.

2.2.2 MSC.Marc (total/updated Lagrangian geometrically nonlinear shell solution)

MSC.Marc [2] is a general-purpose, commercial, implicit, and nonlinear finite-element solver that can be used to analyze a wide range of structural configurations. It is capable of handling nonlinearities either due to material behavior, large deformation, or boundary conditions. It contains three isoparametric, doubly curved, thin shell elements: 3-, 4-, and 8-node elements based on Koiter-Sanders theory [2] amongst many others. Some of the shell elements in the solver could be used in conjunction with selected beam elements to model built-up structural wing constructions. Furthermore, the elements support a variety of constitutive laws to accommodate both isotropic and anisotropic structural modeling. Results for several demonstration problems obtained with MSC.Marc were validated against standard reference solutions, e.g., those from "National Agency for Finite Element Methods and Standards (NAFEMS)" [2].

MSC.Marc provides a coupling interface to external CFD solvers available through user subroutine programming. Such an interface was developed in this work to perform aeroelastic simulations and is discussed in the next chapter.

2.3 CFD Formulation - UM/STREAM (Pressure-based Incompressible Navier-Stokes solver)

UM/STREAM is an incompressible RANS (Reynolds-Averaged Navier-Stokes) solver capable of handling multi-block structured and moving grids. As to its basic formulation, the continuity equation and the u-momentum equation in curvilinear coordinates are writ-

ten as follows (the v and w-momentum equations can be written along similar lines) [76]:

$$\frac{\partial(J\rho_f)}{\partial t} + \frac{\partial\left(\rho_f U\right)}{\partial \xi} + \frac{\partial\left(\rho_f V\right)}{\partial \eta} + \frac{\partial\left(\rho_f W\right)}{\partial \gamma} = 0 \tag{2.77}$$

$$\begin{aligned}\tfrac{\partial(J\rho_f u)}{\partial t} + \tfrac{\partial\left(\rho_f U u\right)}{\partial \xi} + \tfrac{\partial\left(\rho_f V u\right)}{\partial \eta} + \tfrac{\partial\left(\rho_f W u\right)}{\partial \gamma} &= \tfrac{\partial}{\partial \xi}[\tfrac{\mu}{J}(q_{11}u_\xi + q_{12}u_\eta + q_{13}u_\gamma)] \\ &+ \tfrac{\partial}{\partial \eta}[\tfrac{\mu}{J}(q_{21}u_\xi + q_{22}u_\eta + q_{23}u_\gamma)] \\ &+ \tfrac{\partial}{\partial \gamma}[\tfrac{\mu}{J}(q_{31}u_\xi + q_{32}u_\eta + q_{33}u_\gamma)] \\ &- [\tfrac{\partial}{\partial \xi}(f_1 p) + \tfrac{\partial}{\partial \eta}(f_4 p) + \tfrac{\partial}{\partial \gamma}(f_7 p)]\end{aligned} \tag{2.78}$$

where (x, y, z) are Cartesian coordinates and (ξ, η, γ) are time dependent curvilinear coordinates which are functions of the Cartesian coordinates i.e. ξ = ξ(x, y, z, t), η = η(x, y, z, t), γ = γ(x, y, z, t). u, v, and w are the flow velocity components in the x, y, and z directions respectively. The quantities f_1, f_4, and f_7 are defined as:

$$\begin{aligned} f_1 &= (y_\eta\, z_\gamma - y_\gamma\, z_\eta) \\ f_4 &= (y_\gamma\, z_\xi - y_\xi\, z_\gamma) \\ f_7 &= (y_\xi\, z_\eta - y_\eta\, z_\xi) \end{aligned} \tag{2.79}$$

Also, ρ_f is the fluid density, p is the pressure, μ is a quantity that accounts for both laminar and turbulent viscosity. Further, a subscript variable to u, x, y, or z implies a derivative of the latter with respect to the former. U, V, and W are the contravariant velocity components given by:

$$\begin{aligned} U &= f_{11}(u - \dot{x}) + f_{12}(v - \dot{y}) + f_{13}(w - \dot{z}) \\ V &= f_{21}(u - \dot{x}) + f_{22}(v - \dot{y}) + f_{23}(w - \dot{z}) \\ W &= f_{31}(u - \dot{x}) + f_{32}(v - \dot{y}) + f_{33}(w - \dot{z}) \end{aligned} \tag{2.80}$$

where f_{ij}, q_{ij} (i=1 to 3, j=1 to 3) are the metrics of the conversion from Cartesian coordinates to curvilinear coordinates, and $\dot{x}$, $\dot{y}$, and $\dot{z}$ are the grid velocities evaluated as follows:

$$\dot{x}_{n+1} = \frac{x_{n+1} - x_n}{\Delta t_f}, \dot{y}_{n+1} = \frac{y_{n+1} - y_n}{\Delta t_f}, \dot{z}_{n+1} = \frac{z_{n+1} - z_n}{\Delta t_f} \tag{2.81}$$

Here, Δt_f is the fluid solver time step. The determinant of the transformation matrix between Cartesian and curvilinear coordinates is given by:

$$J = x_\xi y_\eta z_\zeta + x_\zeta y_\xi z_\eta + x_\eta y_\zeta z_\xi - x_\xi y_\zeta z_\xi - x_\zeta y_\eta z_\xi - x_\eta y_\xi z_\zeta \tag{2.82}$$

where, as before, the subscripts to x, y, and z denote a derivative.

A detailed discussion about the discretization of these equations can be found in Refs. [76] and [83]. When performing computations on a fixed grid, the grid velocities are non-existent, though this is not the case while performing computations on a grid that moves with respect to time. In such cases, two major issues need to be considered:

- Kinematic conditions should be enforced at the interface or the moving boundary (i.e., $u = \dot{x}$, $v = \dot{y}$, and $w = \dot{z}$: these can be imposed as boundary conditions).
- The geometric conservation law must be invoked to evaluate the Jacobian values in order to enforce volume conservation.

The numerical solution in UM/STREAM is obtained using a pressure-based algorithm, with combined cartesian and contravariant velocity variables to facilitate strong conservation law formulations and consistent finite volume treatment. The convection terms are

discretized using a second-order upwind scheme, while the pressure and viscous terms with a second-order central difference scheme.

2.4 Nondimensionalization and Scaling Parameters

Nondimensionalization of equations is generally useful to reduce the number of parameters in a problem, to identify characteristic properties of the system under consideration, and to indicate which combination of parameters may be important. From the viewpoint of fluid-structure interaction, several dimensionless parameters may naturally arise during the nondimensionalization process of the fluid and structural dynamics equations using a set of suitable reference scales. Depending upon the problem at hand and the type of equations used to model the physical phenomena involved, the resultant set of scaling parameters could vary.

As an example, in the previous section, on the CSD side, two "plate/shell" element formulations were presented along with the one for a "beam." Nondimensionalizing each of these equations in conjunction with the "incompressible Navier-Stokes" equations also presented previously, will result in two different sets of scaling parameters. Depending upon which structural model is used in an aeroelastic simulation, the associated scaling parameters should be considered.

In the next three sub-sections, the governing equations of motion for UM/STREAM, UM/NLAMS, and UM/NLABS presented previously will be shown in nondimensional form and the resulting scaling parameters will be highlighted. It may be noted that a nondimensional variable is indicated by an asterisk superscript.

2.4.1 Nondimensionalization of UM/STREAM equations

If the free stream velocity U_∞, the mean chord length c, and the ratio of mean chord length to the free stream velocity, i.e., $\frac{c}{U_\infty}$ are chosen as the reference scales for the velocity, length, and time, respectively, the nondimensional form of the u-momentum equation given in Eq. 2.78 becomes:

$$\begin{aligned}\frac{\partial(Ju^*)}{\partial t^*} + \frac{\partial(U^*u^*)}{\partial \xi^*} + \frac{\partial(V^*u^*)}{\partial \eta^*} + \frac{\partial(W^*u^*)}{\partial \gamma^*} = \frac{\partial}{\partial \xi^*}[\frac{1}{Re\ J}(q_{11}\frac{\partial u^*}{\partial \xi^*} + q_{12}\frac{\partial u^*}{\partial \eta^*} + q_{13}\frac{\partial u^*}{\partial \gamma^*})] \\ + \frac{\partial}{\partial \eta^*}[\frac{1}{Re\ J}(q_{21}\frac{\partial u^*}{\partial \xi^*} + q_{22}\frac{\partial u^*}{\partial \eta^*} + q_{23}\frac{\partial u^*}{\partial \gamma^*})] + \frac{\partial}{\partial \gamma^*}[\frac{1}{Re\ J}(q_{31}\frac{\partial u^*}{\partial \xi^*} + q_{32}\frac{\partial u^*}{\partial \eta^*} + q_{33}\frac{\partial u^*}{\partial \gamma^*})] \\ -[\frac{\partial}{\partial \xi^*}(f_3 p^*) + \frac{\partial}{\partial \eta^*}(f_6 p^*) + \frac{\partial}{\partial \gamma^*}(f_9 p^*)]\end{aligned} \tag{2.83}$$

In a similar manner, if the free stream velocity U_∞, the mean chord length c, and the inverse flapping/plunging frequency ($\frac{1}{f}$) are chosen as the velocity, length, and time scales, respectively, the nondimensional form of Eq. 2.78 now becomes:

$$\begin{aligned}\frac{k}{\pi}\ \frac{\partial(Ju^*)}{\partial t^*} + \frac{\partial(U^*u^*)}{\partial \xi^*} + \frac{\partial(V^*u^*)}{\partial \eta^*} + \frac{\partial(W^*u^*)}{\partial \gamma^*} = \frac{\partial}{\partial \xi^*}[\frac{1}{Re\ J}(q_{11}\frac{\partial u^*}{\partial \xi^*} + q_{12}\frac{\partial u^*}{\partial \eta^*} + q_{13}\frac{\partial u^*}{\partial \gamma^*})] \\ + \frac{\partial}{\partial \eta^*}[\frac{1}{Re\ J}(q_{21}\frac{\partial u^*}{\partial \xi^*} + q_{22}\frac{\partial u^*}{\partial \eta^*} + q_{23}\frac{\partial u^*}{\partial \gamma^*})] + \frac{\partial}{\partial \gamma^*}[\frac{1}{Re\ J}(q_{31}\frac{\partial u^*}{\partial \xi^*} + q_{32}\frac{\partial u^*}{\partial \eta^*} + q_{33}\frac{\partial u^*}{\partial \gamma^*})] \\ -[\frac{\partial}{\partial \xi^*}(f_3 p^*) + \frac{\partial}{\partial \eta^*}(f_6 p^*) + \frac{\partial}{\partial \gamma^*}(f_9 p^*)]\end{aligned} \tag{2.84}$$

The dimensionless quantities common to both equations shown above are:

$$\begin{aligned} u^* = \frac{u}{U_\infty} \qquad U^* = \frac{U}{U_\infty} \quad V^* = \frac{V}{U_\infty} \quad W^* = \frac{W}{U_\infty} \\ \xi^* = \frac{\psi}{c} \qquad \eta^* = \frac{\eta}{c} \qquad \gamma^* = \frac{\gamma}{c} \\ Re = \frac{\rho_f\ U_\infty\ c}{\mu} \quad p^* = \frac{p}{\rho_f\ U_\infty^2} \end{aligned} \tag{2.85}$$

where Re is the chord-based Reynolds number. Apart from the parameters above, the parameter specific to Eq. 2.83 is:

$$t^* = \frac{t\ U_\infty}{c} \tag{2.86}$$

And those specific to Eq. 2.84 are:

$$\begin{aligned} t^* &= t\ f \\ k &= \frac{\pi\ f\ c}{U_\infty} \end{aligned} \tag{2.87}$$

where k is the reduced frequency. Another dimensionless parameter Strouhal number denoted by St given by a ratio between the oscillating (flapping) speed and the forward speed is a measure of propulsive efficiency in flying and swimming animals [80]. It is normally defined as:

$$St = \frac{2\ f\ h_a}{U_\infty} \tag{2.88}$$

where h_a is the stroke amplitude due to either prescribed plunge motion or flap rotation at the root. In the case of a wing of length R flapping with an amplitude Φ (measured in radians), the stroke amplitude h_a is the product $R\Phi$.

In hovering flight, for which there is no forward speed, the reference speed U_∞ is defined as the mean wing tip velocity $2f\Phi R$. The reduced frequency then becomes:

$$k = \frac{\pi}{\Phi\ A_r} \tag{2.89}$$

where A_r is the wing aspect ratio.

The nondimensional form of the v and w momentum equations could be written in a

similar fashion and many more dimensionless parameters will arise from them.

2.4.2 Nondimensionalization of UM/NLAMS equations

As mentioned previously, in the structural dynamics solution UM/NLAMS, a linear plate deformation theory is used in the local co-rotational frame. For nondimensionalization purposes, the classical Kirchoff equations of motion for a transversely loaded laminated composite plate are considered. They can be written as [47]:

$$\begin{aligned} A_{11}\,\frac{\partial^2 u^0}{\partial x^2} + 2\,A_{16}\,\frac{\partial^2 u^0}{\partial x \partial y} + A_{66}\,\frac{\partial^2 u^0}{\partial y^2} + A_{16}\,\frac{\partial^2 v^0}{\partial x^2} + (A_{12} + A_{66})\,\frac{\partial^2 v^0}{\partial x \partial y} + A_{26}\,\frac{\partial^2 v^0}{\partial y^2} - \\ B_{11}\,\frac{\partial^3 w}{\partial x^3} - 3\,B_{16}\,\frac{\partial^3 w}{\partial x^2 \partial y} - (B_{12} + 2\,B_{66})\,\frac{\partial^3 w}{\partial x \partial y^2} - B_{26}\,\frac{\partial^3 w}{\partial y^3} = 0 \end{aligned} \tag{2.90}$$

$$\begin{aligned} A_{16}\,\frac{\partial^2 u^0}{\partial x^2} + (A_{12} + A_{66})\,\frac{\partial^2 u^0}{\partial x \partial y} + A_{26}\,\frac{\partial^2 u^0}{\partial y^2} + A_{66}\,\frac{\partial^2 v^0}{\partial x^2} + 2\,A_{26}\,\frac{\partial^2 v^0}{\partial x \partial y} + A_{22}\,\frac{\partial^2 v^0}{\partial y^2} - \\ B_{16}\,\frac{\partial^3 w}{\partial x^3} - (B_{12} + 2\,B_{66})\,\frac{\partial^3 w}{\partial x^2 \partial y} - 3\,B_{26}\,\frac{\partial^3 w}{\partial x \partial y^2} - B_{22}\,\frac{\partial^3 w}{\partial y^3} = 0 \end{aligned} \tag{2.91}$$

$$\begin{aligned} D_{11}\,\frac{\partial^4 w}{\partial x^4} + 4\,D_{16}\,\frac{\partial^4 w}{\partial x^3 \partial y} + 2\,(D_{12} + 2\,D_{66})\,\frac{\partial^4 w}{\partial x^2 \partial y^2} + 4\,D_{26}\,\frac{\partial^4 w}{\partial x \partial y^3} + D_{22}\,\frac{\partial^4 w}{\partial y^4} - \\ B_{11}\,\frac{\partial^3 u^0}{\partial x^3} - 3\,B_{16}\,\frac{\partial^3 u^0}{\partial x^2 \partial y} - (B_{12} + 2\,B_{66})\,\frac{\partial^3 u^0}{\partial x \partial y^2} - B_{26}\,\frac{\partial^3 u^0}{\partial y^3} - B_{16}\,\frac{\partial^3 v^0}{\partial x^3} - \\ (B_{12} + 2\,B_{66})\,\frac{\partial^3 v^0}{\partial x^2 \partial y} - 3\,B_{26}\,\frac{\partial^3 v^0}{\partial x \partial y^2} - B_{22}\,\frac{\partial^3 v^0}{\partial y^3} + \rho_s\,h_s\,\ddot{w} = p \end{aligned} \tag{2.92}$$

Where u^o, v^o, and w are the displacements in the x, y, and z directions respectively, of a point on the mid-surface of the plate considered in the x-y plane. Further, the coefficients A_{ij}, B_{ij}, and D_{ij} are the elements of matrices A, B, and D which correspond to the extensional, the bending-extension coupling, and the bending stiffnesses respectively, all defined in detail in Ref. [47]. ρ_s is the density of the plate material, h_s is the thickness of the plate, and p is the distributed transverse load on the plate.

The first two equations presented above correspond to the in-plane equilibrium and the last one corresponds to the out-of-plane motion. For the purpose of scaling, only Eq. 2.92 is considered next.

Choosing the same reference scales as in the case of nondimensionalization of UM/STREAM equations will be equivalent to dividing Eq. 2.92 throughout by the factor "$\rho_f \; U_\infty^2$" which will then be nondimensionalized in the following manner:

$$\begin{gathered} D_{11}^* \; \frac{\partial^4 w^*}{\partial x^{*4}} + 4 \; D_{16}^* \; \frac{\partial^4 w^*}{\partial x^{*3} \partial y^*} + 2 \; (D_{12}^* + 2 \; D_{66}^*) \; \frac{\partial^4 w^*}{\partial x^{*2} \partial y^{*2}} + 4 \; D_{26}^* \; \frac{\partial^4 w^*}{\partial x^* \partial y^{*3}} + D_{22}^* \; \frac{\partial^4 w^*}{\partial y^{*4}} - \\ B_{11}^* \; \frac{\partial^3 u^{0*}}{\partial x^{*3}} - 3 \; B_{16}^* \; \frac{\partial^3 u^{0*}}{\partial x^{*2} \partial y^*} - (B_{12}^* + 2 \; B_{66}^*) \; \frac{\partial^3 u^{0*}}{\partial x^* \partial y^{*2}} - B_{26}^* \; \frac{\partial^3 u^{0*}}{\partial y^{*3}} - B_{16}^* \; \frac{\partial^3 v^{0*}}{\partial x^{*3}} - \\ (B_{12}^* + 2 \; B_{66}^*) \; \frac{\partial^3 v^{0*}}{\partial x^{*2} \partial y^*} - 3 \; B_{26}^* \; \frac{\partial^3 v^{0*}}{\partial x^* \partial y^{*2}} - B_{22}^* \; \frac{\partial^3 v^{0*}}{\partial y^{*3}} + \rho^* \; h_s^* \; \frac{\partial^2 w^*}{\partial t^{*2}} = p^* \end{gathered} \tag{2.93}$$

where the nondimensional parameters that naturally arose are furnished below:

$$\begin{gathered} D_{11}^* = \frac{D_{11}}{\rho_f \; U_\infty^2 \; c^3} \quad D_{16}^* = \frac{D_{16}}{\rho_f \; U_\infty^2 \; c^3} \quad D_{12}^* = \frac{D_{12}}{\rho_f \; U_\infty^2 \; c^3} \\ D_{66}^* = \frac{D_{66}}{\rho_f \; U_\infty^2 \; c^3} \quad D_{26}^* = \frac{D_{26}}{\rho_f \; U_\infty^2 \; c^3} \quad D_{22}^* = \frac{D_{22}}{\rho_f \; U_\infty^2 \; c^3} \\ B_{11}^* = \frac{B_{11}}{\rho_f \; U_\infty^2 \; c^2} \quad B_{16}^* = \frac{B_{16}}{\rho_f \; U_\infty^2 \; c^2} \quad B_{12}^* = \frac{B_{12}}{\rho_f \; U_\infty^2 \; c^2} \\ B_{66}^* = \frac{B_{66}}{\rho_f \; U_\infty^2 \; c^2} \quad B_{26}^* = \frac{B_{26}}{\rho_f \; U_\infty^2 \; c^2} \qquad \rho^* = \frac{\rho_s}{\rho_f} \end{gathered} \tag{2.94}$$

The rest of the dimensionless quantities in Eq. 2.93 are:

$$\begin{gathered} p^* = \frac{p}{\rho_f \; U_\infty^2} \\ w^* = \frac{w}{c} \\ h_s^* = \frac{h_s}{c} \end{gathered} \tag{2.95}$$

As a special case, for an isotropic plate, B_{11}, B_{16}, B_{12}, B_{66}, and B_{26} will vanish since there

is no bending-stretch coupling and further, due to the isotropic constitutive relations, the following conditions will hold:

$$\begin{aligned} D_{11} &= D_s \\ D_{12} &= \nu\, D_s \\ D_{16} &= 0 \\ D_{22} &= D_s \\ D_{26} &= 0 \\ D_{66} &= (\tfrac{1-\nu}{2})\, D_s \end{aligned} \tag{2.96}$$

where

$$D_s = \frac{E\, h_s^3}{12\,(1-\nu^2)} \tag{2.97}$$

Eq. 2.93 then reduces to:

$$D_s^*(\tfrac{\partial^4 w^*}{\partial x^{*4}} + 2\,\tfrac{\partial^4 w^*}{\partial x^{*2}\partial y^{*2}} + \tfrac{\partial^4 w^*}{\partial y^{*4}}) + \rho^*\, h_s^*\, \tfrac{\partial^2 w^*}{\partial t^{*2}} = p^* \tag{2.98}$$

The only two scaling parameters that arise for a transversely loaded isotropic Kirchoff plate are then:

$$\begin{aligned} \Pi_1 = D_s^* &= \tfrac{D_s}{\rho_f\, U_\infty^2\, c^3} \\ \rho^* &= \tfrac{\rho_s}{\rho_f} \end{aligned} \tag{2.99}$$

In this manner, several other scaling parameters could be obtained by nondimensionalizing the other two governing equations (Eqs. 2.90, 2.91) of the composite Kirchoff plate.

As another special case for the composite plate, if shear deformation is also included,

then two additional equations of equilibrium will be included and more parameters will arise. For example, in the case of an isotropic shear deformable plate, one of the scaling parameters will be:

$$\Pi_2 = \frac{I_B}{\rho_f \, c^5} \tag{2.100}$$

where I_B is the mass moment of inertia associated with shear degrees of freedom about either the x or y directions.

2.4.3 Nondimensionalization of UM/NLABS equations

With the same choice of the scaling parameters as made in the non-dimensionalization of the Navier-Stokes equations, the non-dimensional form of the Euler-Lagrange equations of motion for the beam highlighted in Eqs. 2.68, 2.69, and 2.70 is written as:

$$\dot{P}_B^* + \tilde{\Omega}_B^* P_B^* = {F'}_B^* + \tilde{K}_B^* F_B^* - {f'}_1^* - \tilde{K}_B^* f_1^* + f_0^* \tag{2.101}$$

$$\dot{H}_B^* + \tilde{\Omega}_B^* H_B^* + \tilde{\mathrm{V}}_B^* P_B^* = {M'}_B^* + \tilde{K}_B^* M_B^* - {m'}_1^* - \tilde{K}_B^* m_1^* + (\tilde{e}_1^* + \tilde{\gamma}^*) \, F_B^* + m_0^* \tag{2.102}$$

$$\dot{Q}_t^* = ({Q'}_{s_1}^{\ *} - {f'}_{s_1}^*) - (Q_{s_0}^* - f_{s_0}^*) \tag{2.103}$$

The nondimensional form of the constitutive law relating the internal forces/moments and the generalized strains/curvatures shown in Eq. 2.71 can be written as:

$$\begin{Bmatrix} F^*_{B_1} \\ F^*_{B_2} \\ F^*_{B_3} \\ M^*_{B_1} \\ M^*_{B_2} \\ M^*_{B_3} \\ Q^{*(1)}_{s_0} \\ Q^{*(1)}_{s_1} \end{Bmatrix} = \begin{bmatrix} S^*_{11} & S^*_{12} & S^*_{13} & S^*_{14} & S^*_{15} & S^*_{16} & S^*_{17} & S^*_{18} \\ S^*_{21} & S^*_{22} & S^*_{23} & S^*_{24} & S^*_{25} & S^*_{26} & S^*_{27} & S^*_{28} \\ S^*_{31} & S^*_{32} & S^*_{33} & S^*_{34} & S^*_{35} & S^*_{36} & S^*_{37} & S^*_{38} \\ S^*_{41} & S^*_{42} & S^*_{43} & S^*_{44} & S^*_{45} & S^*_{46} & S^*_{47} & S^*_{48} \\ S^*_{51} & S^*_{52} & S^*_{53} & S^*_{54} & S^*_{55} & S^*_{56} & S^*_{57} & S^*_{58} \\ S^*_{61} & S^*_{62} & S^*_{63} & S^*_{64} & S^*_{65} & S^*_{66} & S^*_{67} & S^*_{68} \\ S^*_{71} & S^*_{72} & S^*_{73} & S^*_{74} & S^*_{75} & S^*_{76} & S^*_{77} & S^*_{78} \\ S^*_{81} & S^*_{82} & S^*_{83} & S^*_{84} & S^*_{85} & S^*_{86} & S^*_{87} & S^*_{88} \end{bmatrix} \begin{Bmatrix} \gamma^*_{11} \\ 2\gamma^*_{12} \\ 2\gamma^*_{23} \\ \kappa^*_1 \\ \kappa^*_2 \\ \kappa^*_3 \\ q^{*(1)} \\ q'^{*(1)} \end{Bmatrix} \tag{2.104}$$

Several dimensionless parameters involving both the fluid and the structural parameters arise as a result of the nondimensionalization. They are highlighted next:

$$S^*_{ij} = \frac{S_{ij}}{\rho_f U^2_\infty c^2} \tag{2.105}$$

for i, j = 1 to 3, i = 7 and j= 4 to 6, or i=8 and j=1 to 3

$$S^*_{ij} = \frac{S_{ij}}{\rho_f U^2_\infty c^3} \tag{2.106}$$

for either i=1 to 3 and j=4 to 6, i = 4 to 7 and j=1 to 3, or i=8 and j=4 to 6

$$S^*_{ij} = \frac{S_{ij}}{\rho_f U^2_\infty c^4} \tag{2.107}$$

for i = 4 to 6 and j = 4 to 6, where each S_{ij} is a component of the stiffness matrix which depends upon both the geometry and material properties.

Similarly, the non-dimensional form of the momentum-velocity relations in 2.74 is given by:

$$\begin{Bmatrix} P^*_{B_1} \\ P^*_{B_2} \\ P^*_{B_3} \\ H^*_{B_1} \\ H^*_{B_2} \\ H^*_{B_3} \\ Q^{*(1)}_t \end{Bmatrix} = \begin{bmatrix} M^*_{11} & M^*_{12} & M^*_{13} & M^*_{14} & M^*_{15} & M^*_{16} & M^*_{17} \\ M^*_{21} & M^*_{22} & M^*_{23} & M^*_{24} & M^*_{25} & M^*_{26} & M^*_{27} \\ M^*_{31} & M^*_{32} & M^*_{33} & M^*_{34} & M^*_{35} & M^*_{36} & M^*_{37} \\ M^*_{41} & M^*_{42} & M^*_{43} & M^*_{44} & M^*_{45} & M^*_{46} & M^*_{47} \\ M^*_{51} & M^*_{52} & M^*_{53} & M^*_{54} & M^*_{55} & M^*_{56} & M^*_{57} \\ M^*_{61} & M^*_{62} & M^*_{63} & M^*_{64} & M^*_{65} & M^*_{66} & M^*_{67} \\ M^*_{71} & M^*_{72} & M^*_{73} & M^*_{74} & M^*_{75} & M^*_{75} & M^*_{77} \end{bmatrix} \begin{Bmatrix} V^*_{B_1} \\ V^*_{B_2} \\ V^*_{B_3} \\ \Omega^*_{B_1} \\ \Omega^*_{B_2} \\ \Omega^*_{B_3} \\ \dot{q}^{*(1)} \end{Bmatrix} \tag{2.108}$$

where

$$M^*_{ij} = \frac{M_{ij}}{\rho_f \, c^2} \tag{2.109}$$

for i, j=1 to 3, i=7 and j=1 to 3, i=7 and j=7

$$M^*_{ij} = \frac{M_{ij}}{\rho_f \, c^3} \tag{2.110}$$

for either i=1 to 3 and j=4 to 6, i=4 to 6 and j=1 to 3, or i=7 and j=4 to 6

$$M^*_{ij} = \frac{M_{ij}}{\rho_f \, c^4} \tag{2.111}$$

for i=4 to 6 and j=4 to 6. The rest of the non-dimensional quantities involved in Eqs. 2.101, 2.102, and 2.103 are:

$$x_1^* = \frac{x_1}{c} \tag{2.112}$$

$$t^* = \frac{U_\infty}{c} t \tag{2.113}$$

$$V_B^* = \frac{V_B}{U_\infty} \tag{2.114}$$

$$\Omega_B^* = \frac{c}{U_\infty} \Omega_B \tag{2.115}$$

$$\tilde{K}_B^* = c\tilde{K}_B \tag{2.116}$$

$$F_B^* = \frac{F_B}{\rho_f U_\infty^2 c^2} \tag{2.117}$$

$$M_B^* = \frac{M_B}{\rho_f U_\infty^2 c^3} \tag{2.118}$$

$$f_0^* = \frac{f_0}{\rho_f U_\infty^2 c} \tag{2.119}$$

$$f_1^* = \frac{f_1}{\rho_f U_\infty^2 c^2} \tag{2.120}$$

$$m_0^* = \frac{m_0}{\rho_f U_\infty^2 c^2} \tag{2.121}$$

$$m_1^* = \frac{m_1}{\rho_f U_\infty^2 c^3} \tag{2.122}$$

$$\gamma^* = \gamma \tag{2.123}$$

$$\kappa^* = c\kappa \tag{2.124}$$

$$P_B^* = \frac{P_B}{\rho_f U_\infty c^2} \tag{2.125}$$

$$H_B^* = \frac{H_B}{\rho_f U_\infty c^3} \tag{2.126}$$

$$Q_t^* = \frac{Q_t}{\rho_f \, U_\infty c^2} \tag{2.127}$$

$$Q_{s_0}^* = \frac{Q_{s_0}}{\rho_f U_\infty c} \tag{2.128}$$

$$Q_{s_1}^* = \frac{Q_{s_1}}{\rho_f U_\infty c^2} \tag{2.129}$$

$$f_{s_0}^* = \frac{f_{s_0}}{\rho_f U_\infty c} \tag{2.130}$$

$$f_{s_1}^* = \frac{f_{s_1}}{\rho_f U_\infty c^2} \tag{2.131}$$

As a special case, in the event the beam is prismatic and the reference line is at the mass centroid and also assuming no finite section modes, the stiffness and the mass matrices shown in Eqs. 2.104 and 2.108 become diagonal. The reduced non-dimensional stiffness matrix in its diagonal form then becomes as shown in Eq. 2.132.

$$\begin{Bmatrix} F_{B_1}^* \\ F_{B_2}^* \\ F_{B_3}^* \\ M_{B_1}^* \\ M_{B_2}^* \\ M_{B_3}^* \end{Bmatrix} = \begin{bmatrix} S_{11}^* & 0 & 0 & 0 & 0 & 0 \\ 0 & S_{22}^* & 0 & 0 & 0 & 0 \\ 0 & 0 & S_{33}^* & 0 & 0 & 0 \\ 0 & 0 & 0 & S_{44}^* & 0 & 0 \\ 0 & 0 & 0 & 0 & S_{55}^* & 0 \\ 0 & 0 & 0 & 0 & 0 & S_{66}^* \end{bmatrix} \begin{Bmatrix} \gamma_{11}^* \\ 2\gamma_{12}^* \\ 2\gamma_{23}^* \\ \kappa_1^* \\ \kappa_2^* \\ \kappa_3^* \end{Bmatrix} \tag{2.132}$$

where

$$\begin{aligned} S_{11}^* &= \tfrac{EA}{\rho_f \, U_\infty^2 \, c^2} \quad S_{22}^* = \tfrac{k_s GA}{\rho_f \, U_\infty^2 \, c^2} \quad S_{33}^* = \tfrac{k_s GA}{\rho_f \, U_\infty^2 \, c^2} \\ S_{44}^* &= \tfrac{GJ}{\rho_f \, U_\infty^2 \, c^4} \quad S_{55}^* = \tfrac{EI_2}{\rho_f \, U_\infty^2 \, c^4} \quad S_{66}^* = \tfrac{EI_3}{\rho_f \, U_\infty^2 \, c^4} \end{aligned} \tag{2.133}$$

EA, k_sGA, GJ, EI_2, and EI_3 are the extensional, shear, torsion, and bending stiffness constants.

Similarly, the reduced non-dimensional form of the mass matrix Eq. 2.108 in its non-dimensional form becomes:

$$\begin{Bmatrix} P^*_{B_1} \\ P^*_{B_2} \\ P^*_{B_3} \\ H^*_{B_1} \\ H^*_{B_2} \\ H^*_{B_3} \end{Bmatrix} = \begin{bmatrix} M^*_{11} & 0 & 0 & 0 & 0 & 0 \\ 0 & M^*_{22} & 0 & 0 & 0 & 0 \\ 0 & 0 & M^*_{33} & 0 & 0 & 0 \\ 0 & 0 & 0 & M^*_{44} & 0 & 0 \\ 0 & 0 & 0 & 0 & M^*_{55} & 0 \\ 0 & 0 & 0 & 0 & 0 & M^*_{66} \end{bmatrix} \begin{Bmatrix} V^*_{B_1} \\ V^*_{B_2} \\ V^*_{B_3} \\ \Omega^*_{B_1} \\ \Omega^*_{B_2} \\ \Omega^*_{B_3} \end{Bmatrix} \tag{2.134}$$

where

$$M^*_{11} = M^*_{22} = M^*_{33} = \frac{\mu}{\rho_f \, c^2} \tag{2.135}$$

$$M^*_{44} = \tfrac{I_{22}+I_{33}}{\rho_f \, c^4} \quad M^*_{55} = \tfrac{I_{22}}{\rho_f \, c^4} \quad M^*_{66} = \tfrac{I_{33}}{\rho_f \, c^4} \tag{2.136}$$

μ is the mass per unit length, and I_{22}, I_{33}, and I_{23} are the cross-sectional mass moments and product of inertia respectively.

2.4.4 Examples of dimensionless parameters applied to natural flyers

Table 2.1 shows selected structural and flow properties of three natural flyers. Table 2.2 shows several dimensionless parameters for the three natural flyers listed in Table 2.1. For the calculation of the dimensionless parameters Π_1, Π_2, and ρ^*, it was assumed that

the corresponding wing is a thin homogeneous isotropic plate. In the table, A_r denotes the wing aspect ratio. Specifications for the hummingbird were obtained from Ref. [26], whereas, those for the Bumblebee and Hawkmoth were obtained from Fig. 4 of Ref. [23].

Table 2.1: Selected structural and flow properties of three natural flyers [80]

	BumbleBee	**Hawkmoth**	**Hummingbird**
Mean chord length c (cm)	0.4	1.8	2.0
Wing mass (mg)	0.45	47	294
Forward velocity (m/s)	4.5	5.0	8.0
Mean wing thickness (cm)	$7\text{x}10^{-4}$	$3.4\text{x}10^{-3}$	0.1
Wing semi-span (cm)	1.3	4.9	8.5

Table 2.2: Dimensionless parameters for the natural flyers listed in Table 2.1

Parameter	**BumbleBee**	**Hawkmoth**	**Hummingbird**
A_r	6.6	5.3	8.2
Re	$1.2\text{x}10^3$ - $3\text{x}10^3$	$4.2\text{x}10^3$ - $5.3\text{x}10^3$	$1.1\text{x}10^4$
St	1.82	0.98	1.27
k	0.42	0.28	0.18
Π_1	510	61	$1.56\text{x}10^3$
Π_2	20	12.7	170
ρ^*	1560	1230	172

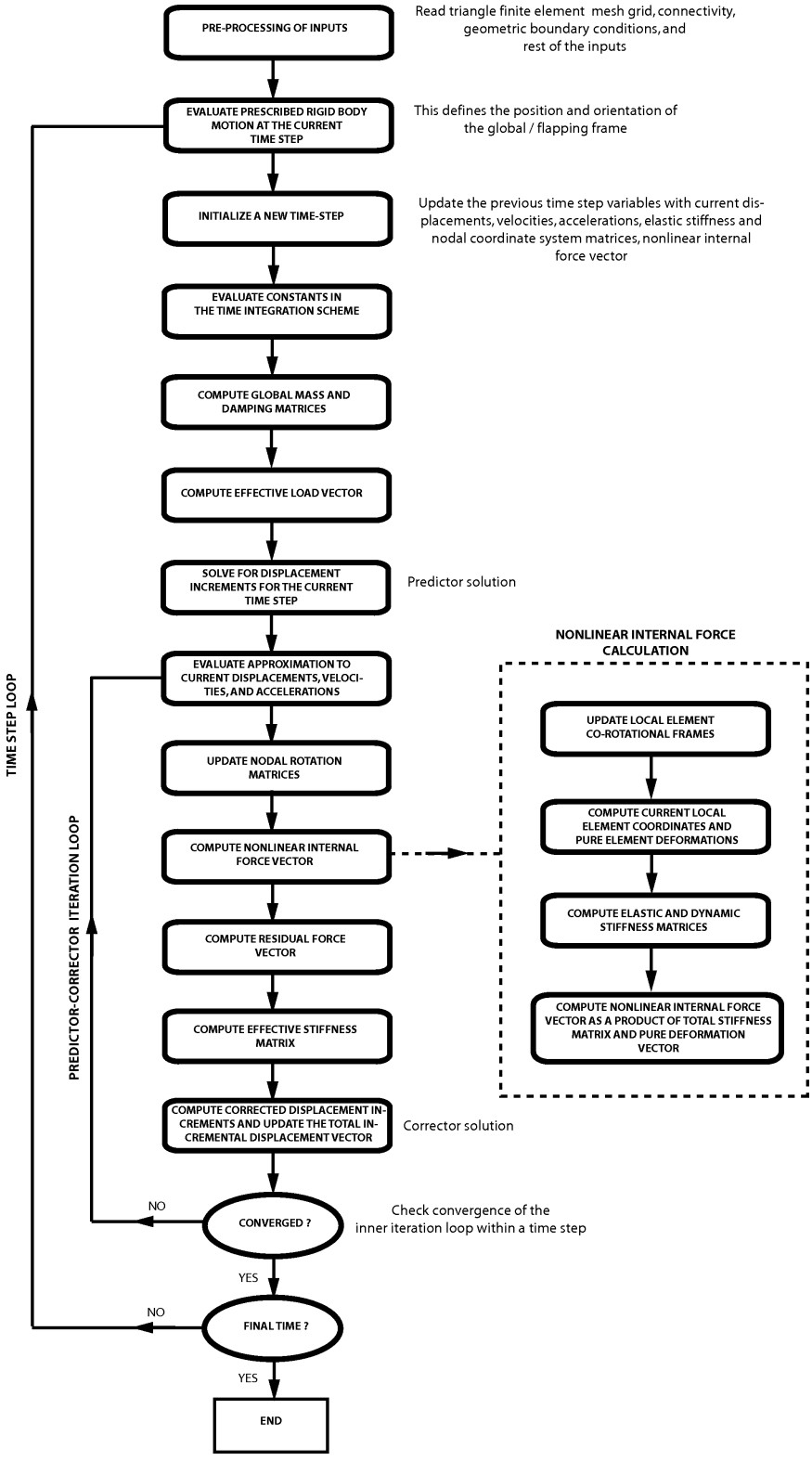

Figure 2.3: Nonlinear finite element solution process for flapping wing shell structures implemented in UM/NLAMS

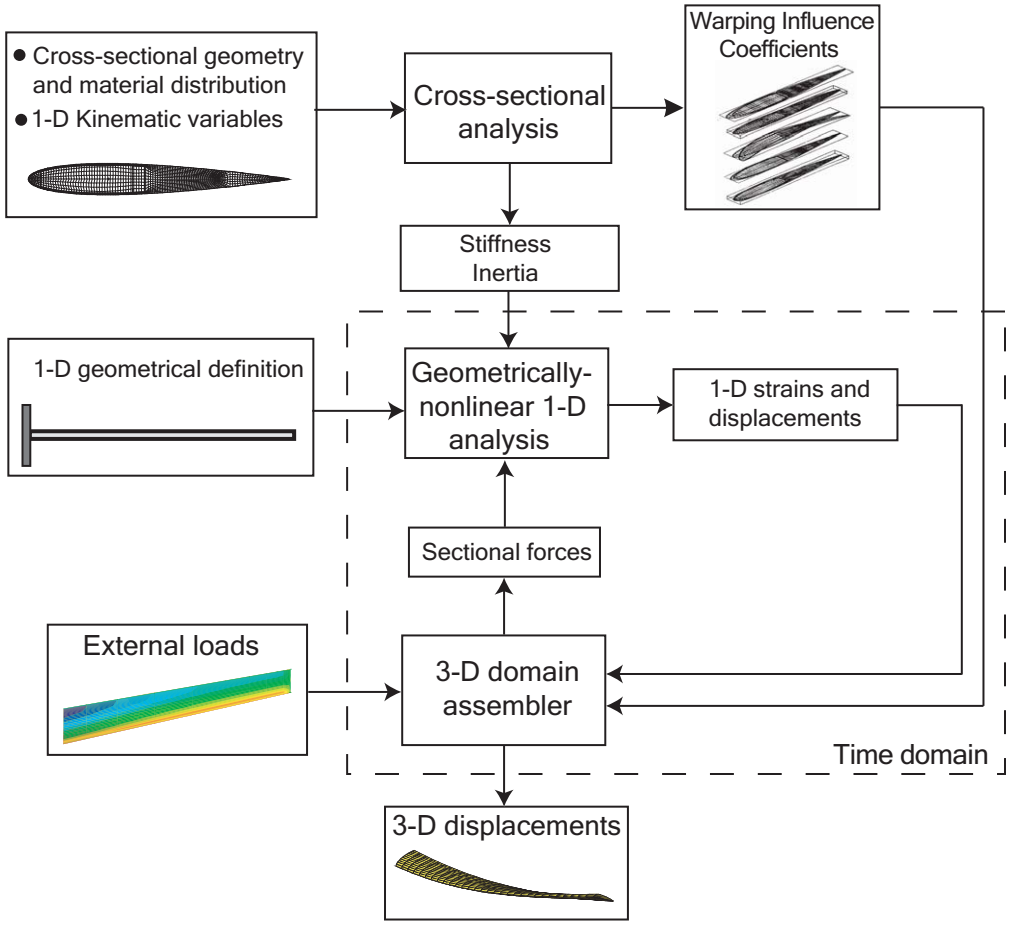

Figure 2.4: Asymptotic solution process for 3-D slender structures implemented in UM/NLABS [62, 64]

Chapter III

AEROELASTIC INTERFACE

With the use of the stand-alone CFD/CSD formulations presented previously, in this chapter, a suite of computational aeroelastic solutions of variable fidelity levels are developed. Depending upon the problem at hand, one of the solution approaches could be adopted to solve it. Furthermore, such a variety of tools will enable cross-validation of aeroelastic solutions in the absence of experimental data or more established computational solutions.

3.1 Coupling Strategies

There are several ways in which an aeroelastic solution could be implemented for the coupled flapping wing problem. Based on a literature survey, it was found that the coupling schemes could be classified as shown in Fig. 3.1. In a *Monolithic method* [96], the discretized fluid and structural equations are solved simultaneously in a single iteration loop. The governing equations are reformulated to get one combined set of equations and integrated in time simultaneously. The advantage of this method is that it ensures stability and convergence of the whole coupled problem [96]. And, there is no need for interpo-

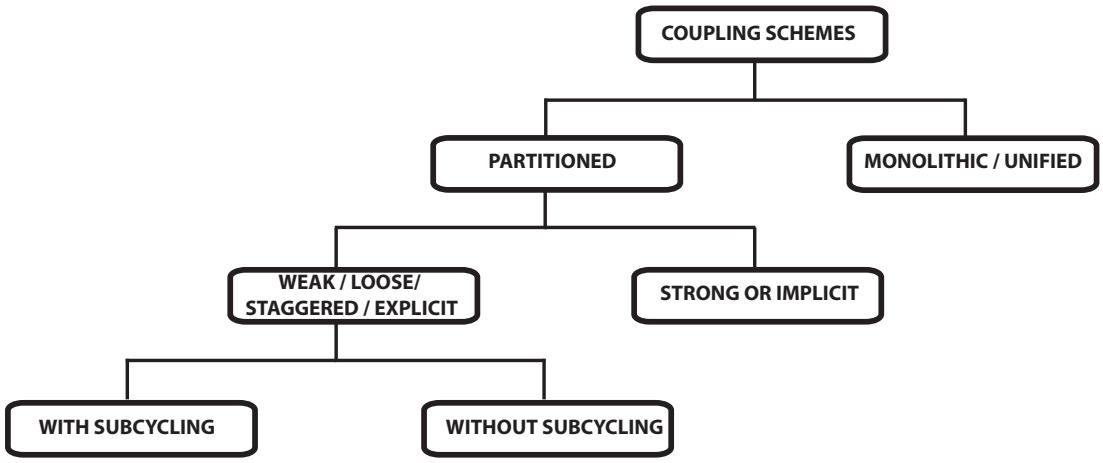

Figure 3.1: A schematic showing the classification of the available coupling schemes to solve aeroelasticity problems.

lation of solution between the fluid and the structure. However, the approach may suffer from ill-conditioning of the combined finite element matrices due to the large difference in the stiffness of the fluid and the structure [30]. Further, the time-step has to be equal for both the fluid and the structure which may be inefficient if different time scales are involved in a problem which is generally the case. In fact, since each of the disciplines may be solved more efficiently with a unique time integration scheme, combining the solutions and marching them with one common scheme may become a compromise on the best possible solution that the individual solvers would have obtained otherwise in a partitioned framework. The monolithic approach is therefore computationally challenging and may not be useful in all situations.

In *Partitioned methods*, the nonlinear partial differential equations modeling the dynamic behavior of the fluid and the structure are solved independently with boundary information (aerodynamic loads and structural displacements) shared between each other

alternately. A schematic of such a framework is shown in Fig. 3.2. The key motivating

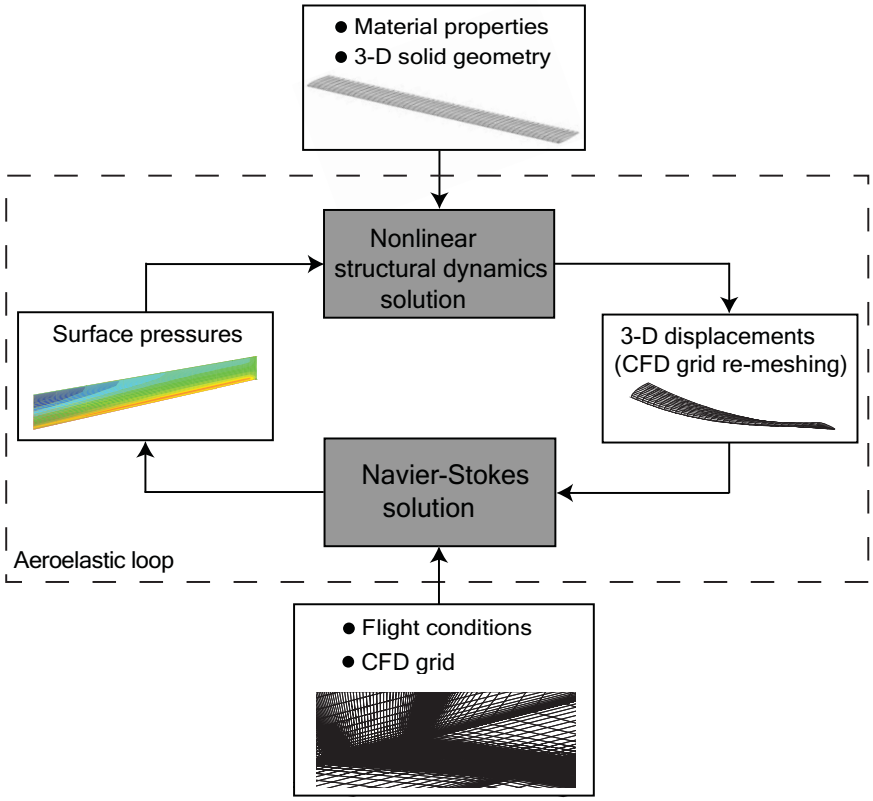

Figure 3.2: A schematic of a typical aeroelastic solution process [20].

factor for the use of these methods is that the existing state-of-the-art fluid and structure codes could be re-used with minor modifications to allow for the coupling of the individual solvers. These methods are further classified into:

1. **Strong or implicit**: In this approach, both the fluid and the structural solvers exchange more than once per coupled time-step (see Fig. 3.3). Each such iteration meant for exchange of data between the flow and the structure is called a "subiteration." The number of such fluid-structure subiterations is determined by a specified convergence criterion. Between any two fluid-structure subiterations, the step initial

conditions in the solvers are not updated and hence a new solution is obtained for the same time-step at the end of a subiteration. However, between the last fluid-structure subiteration of a coupled time-step and the first fluid-structure subiteration of the subsequent coupled time-step, the step initial conditions in the solvers are updated and the solution is time-marched.

2. **Weak or explicit**: This method is also called *staggered* or *loose* coupling. In this coupling approach, both solvers are called once per coupled time-step to exchange data at the fluid-structure interface. It is important to note that numerical instabilities have been encountered [17] due to added-mass effects when explicit coupling methods were used to study the interaction of thin-elastic structures with incompressible, viscous flows. Such algorithms exhibit numerical instabilities for a given geometry as soon as the density of the structure is lower than a certain threshold.

The *explicit* methods are further classified into those:

1. **With subcycling**: This method originated from the fact that the fluid and the structure fields are generally governed by different time scales. More commonly, time-step in the fluid, say Δt_f is several orders smaller than that used in the structural solution Δt_s. Once these time-steps are chosen based on stability/accuracy requirements of the individual solvers, the fluid solution is then subcycled with a factor $n_{\frac{s}{f}} = \frac{\Delta t_f}{\Delta t_s}$ before exchanging information with the structural solution. Although there are computational advantages with this scheme, previous efforts in this area proves that this scheme has a low order of accuracy, and also that subcycling of the fluid solution may amplify the errors in the aeroelastic solution.

2. **Without subcycling**: In this method no such subcycling of fluid solution as discussed above is done. The flow and the structure march with equal time-steps and exchange data at every time instant.

3.2 Aeroelasticity Framework

Figure 3.4 shows an overview of the aeroelastic solutions that were developed in this work. Three combinations of coupled solutions of the "partitioned type" are highlighted which are between:

- the in-house geometrically nonlinear beam / linear plate finite element solver UM/NLABS and the pressure-based incompressible Navier-Stokes solver UM/STREAM;
- the commercially available geometrically nonlinear plate/shell finite element solver MSC.Marc and UM/STREAM;
- the in-house developed geometrically nonlinear plate/shell finite element solver UM/NLAMS and UM/STREAM.

Both *explicit* and *implicit* coupling algorithms have been adopted for the simulation codes involving UM/NLABS and UM/NLAMS. However, only the *explicit* method was possible in the case of the code involving MSC.Marc since it does not support exchanges with an external CFD solver more than once within a coupled time-step. A reason for this is given in subsection 3.3.2. Table 3.1 furnishes more details of all the simulation codes already

highlighted in Fig. 3.4. A brief overview of the process by which each of the different coupled simulation codes is produced is discussed next.

Table 3.1: List of computational aeroelasticity codes developed in this work

coupled code	**fidelity level**	**source availability**	**coupling scheme**
UM/NLABS+STREAM	quasi-3D slender structure CSD, CFD	in-house	implicit/explicit
MSC.Marc+UM/STREAM	shell FE, CFD	commercial CSD and in-house CFD	explicit
UM/NLAMS+STREAM	shell FE, CFD	in-house	implicit

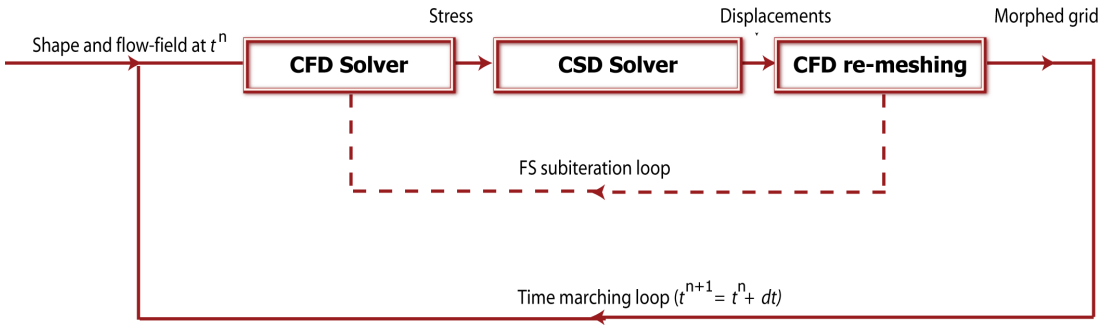

Figure 3.3: A schematic of the implicit coupling approach involving fluid-structure subiterations

3.3 Coupling Procedures

A dedicated interface module is developed to enable communication between the flow and the structure at the 3-D wetted surface (fluid-structure interface) for each of the coupled simulation codes. In the interface module, both the fluid and the structural modules are called one after the other according to the coupling method adopted for the problem. The coupling algorithm (*explicit* or *implicit*) is determined by the capability of the individual simulation code as already shown in Table 3.1. Several interface subroutines have been

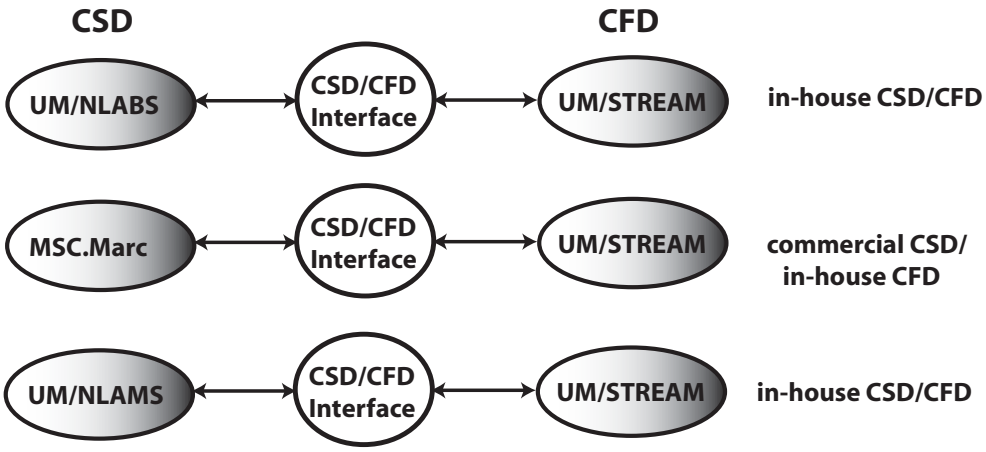

Figure 3.4: A schematic of the aeroelastic framework involving different structural and fluid dynamics solvers and their coupling as developed in this work

written to control the coupled solution and to perform interpolation of physical quantities between the fluid and the structural grids via the thin-plate spline [87] or the bilinear [65] interpolation methods. For the CFD grid re-meshing at each iteration, a master-slave approach [39] was used. A coupled code was achieved simply by compiling the object files of the individual solvers along with those of the interface routines to produce a shared executable file. More details of these aspects are discussed in the next few sub-sections separately for each coupled simulation code.

3.3.1 UM/NLABS and UM/STREAM

The codes UM/NLABS and UM/STREAM were developed at the University of Michigan and so their sources were accessible. There are several advantages to this, which include the ability to adopt a coupling method of choice and also access to the aeroelastic jacobians which facilitate any design sensitivity analysis.

For the coupling, as already mentioned above, an interface module was created from which calls were made to the subroutines of the individual solvers along with those needed for the interpolation of data across the fluid-structure interface and the re-meshing of the CFD grid due to wing deformation. While the calls to the structural and fluid solvers include those needed for pre-processing, solution, and post-processing, the other calls include the ones needed to pass pressures from the CFD analysis at the fluid-structure interface, interpolate them on to the CSD side of the interface, integration of the pressures to get resultant forces vectors at the CSD mesh centers, a subsequent transformation of those force vectors to get resultant forces and moments along the beam reference line conducted by considering the flexibility of the cross-section [64], and pass displacements from the CSD to the CFD side. Figure 3.5 highlights these calls in detail. The procedure for a typical aeroelastic simulation is discussed next by stepping through the interface module in detail.

The first step in the interfacing process is that the top and bottom surfaces of the wing are "flagged" using appropriate input cards at the time of creation of the computational models in both CFD and CSD. The interface code operates on these surfaces separately but identically for the interpolation of data across the fluid-structure interface (i.e., the top surface of the wing on the CFD side interfaces with the one on the CSD side and similarly the corresponding bottom surfaces). Once basic information about the interface mesh on either sides is obtained, the interface program starts two different loops (the *time-step* and the *subiteration* ones). Inside these loops, several subroutines are called which perform the following:

1. the CFD solution is computed with the current grid configuration.

2. pressures are extracted at the face centers and boundary points of the top and bottom surfaces of the CFD interface mesh separately in two different arrays.

3. pressures from each of the surfaces are then interpolated onto the face centers of the corresponding surface of the CSD interface mesh. In this work, the *bilinear* interpolation method (discussed later) was used to do this, the choice of which was arbitrary.

4. the pressures at the face centers of the CSD interface mesh are then integrated to get three-dimensional force vectors at the same locations.

5. the force vectors at each station of nodes along the beam reference line are then used to compute the resultant forces and moments at the corresponding beam node.

6. the CSD solution is then computed with the current set of loads.

7. three-dimensional displacement solution is obtained at the CSD interface mesh nodes which is compared to the one computed during the previous subiteration or time-step to get incremental displacements at each node.

8. incremental displacements at the CSD interface nodes are then interpolated onto the CFD grid nodes using the *thin plate spline* scheme (discussed later), the choice of which was arbitrary.

9. incremental displacements obtained at the CFD interface nodes are then used to perturb the rest of the CFD grid, the procedure for which is discussed later.

Figure 3.6 shows a sample interface mesh for UM/NLABS along with the discretized beam reference line (shown along the leading edge of a flat plate wing). Each black dot on the reference line indicates a finite element node. As part of the initial input to the structural solver UM/NLABS, a surface station of interface nodes along the chord is defined at each of those beam nodes. The nodes at all such surface stations constitute the fluid-structure interface which communicate with the corresponding interface mesh nodes of the CFD side. The interface mesh on the CSD side is updated at each iteration using the one-dimensional displacements and rotations computed at the beam reference line.

3.3.2 MSC.Marc and UM/STREAM

MSC.Marc supports coupling with an external CFD solver using a set of code coupling API (application programming interface) routines and the concept of "Coupling Regions." A "Coupling Region" is that part of the surface or volume of the structural model where the interaction with the external solver takes place [2]. A surface region consists of a list of edges or geometric curves in 2-D and a list of faces or geometric surfaces in 3-D. A volumetric region consists of a list of elements or contact bodies. "Coupling regions" are defined by the **COUPLING REGION** model definition option in MSC.Marc [2].

The first step in the development of the coupled code involving MSC.Marc and UM/STREAM is the preparation of a main driver program. The program involves calls to several of MSC.Marc's API and UM/STREAM's routines. While the subroutines related to UM/STREAM are the same as those discussed in the previous subsection, the MSC.Marc's API calls importantly include three user subroutines and then a set of utility routines that are

called from these user subroutines. The three user subroutines correspond to the following:

1. **CPLREG_INIT** (Initialization): This subroutine is called once at the start of the analysis and can be used to extract the connectivity and coordinates of the coupling regions defined in the structural model. Further, the pre-processing routines related to the CFD solver UM/STREAM are also called from this subroutine.

2. **CPLREG_EXCHANGE** (Data Exchange): This subroutine is called twice per coupling time step, once at the start and once at the end. This is a limitation of MSC.Marc versions 2005r3 and 2008r1. If this subroutine can be called more than twice per coupled time-step, an implicit coupling approach will become possible. The call at the start can be used to set the new values of physical quantities that are received from the external solver for the next coupling time step. The call at the end can be used to extract the new values of physical quantities that must be sent to the external solver. This means that, in the current setup, at the start, pressures from UM/STREAM are obtained and are interpolated onto the structural interface mesh in MSC.Marc. At the end of the call, displacements are obtained from MSC.Marc and are interpolated onto the fluid interface mesh in the CFD model.

3. **CPLREG_FINALIZE** (Finalization): This subroutine is called once at the end of the analyis and can be used to inform the external solver that the MSC.Marc analysis has ended.

Several utility routines can be called from the user subroutines to obtain the connectivity and coordinates of the coupling region, the current values of physical quantities in the

coupling regions, to set the new values of physical quantities for the next coupling time step, etc. Figure 3.7 shows a flow chart of the driver program which indicates all the three user subroutines discussed above along with the various utility routines used. The main driver program, the individual object and the archive files (ending with ".o" and ".a" respectively) that make up the stand-alone MSC.Marc distribution are compiled along with those used to build the stand-alone CFD solver UM/STREAM to obtain a single binary executable file that contains the entire coupled code. This can then be executed as a custom MSC.Marc program using specific commands available in the MSC.Marc manuals [2].

In order to prepare the input file for an aeroelastic analysis using this coupled code, the structural model of the wing structure is prepared in MSC.Marc/Mentat exactly as is done in the case of a stand-alone structural dynamics model in MSC.Marc. The resultant input file is then adapted for an aeroelastic analysis with UM/STREAM by including the **COUPLING REGION** model definition option which specifies the coupling regions in the analysis. As an example, in the case where a wing structure is meshed with shell elements, the top and bottom faces of each shell element are independent surface entities, as far as the coupling regions are concerned. Therefore, the top faces of all the shell elements will be flagged as "TOP" and the bottom ones as "BOTTOM."

3.3.3 UM/NLAMS and UM/STREAM

The coupling procedure used to couple the in-house geometrically nonlinear shell FE solver UM/NLAMS and UM/STREAM is similar to the one in the case of the coupled code involving UM/NLABS. However, since the structure here is discretized with shell

elements, the interface mesh is not explicitly defined as part of the inputs. The undeformed initial mesh configuration of the discretized shell structure naturally becomes the interface mesh definition.

3.4 Convergence Criteria for Implicit Aeroelastic Simulations

As mentioned previously, in an *implicit* coupling method, the number of fluid-structure subiterations is determined by a specified convergence criterion. This could be judiciously chosen based on the problem at hand. Possible criteria include a check on the Euclidean or any other suitable norm of the entire solution vector either on the CFD or the CSD side, a check on the energy conservation at the fluid-structure interface, etc. The convergence criterion chosen in the current work where the coupled code involving UM/NLABS is used is a check on the absolute difference of vertical displacement at the wing tip node computed in two consecutive subiterations. In the case of the coupled code involving UM/NLAMS, it is a check on the absolute difference in the Euclidean norm of the entire CSD solution vector computed in two consecutive subiterations. It is important to note that the smoothness or possibly the accuracy of the coupled solution could depend upon the criterion chosen.

3.5 CFD/CSD Interpolation Techniques

Since the surface discretization for the fluid and structure is generally different due to different accuracy requirements in the resolution of individual solution features, it is necessary to perform interpolation of physical quantities between the fluid and the structural

meshes. To enable this, in this work, the *thin-plate spline* [87] and the *bilinear interpolation* methods [65] are included in the aeroelastic framework. Both the methods are briefly presented below:

1. **Thin plate spline method**: The thin-plate spline is a global interpolation approach meaning that the entire surface is fitted with a set of functions. Its distribution function is given by:

$$\begin{gathered} H(X_I) = \sum_{k=1}^{N} \alpha_k |X_I - X_D|^2 log|X_I - X_D| \\ X = x\hat{i} + y\hat{j} \end{gathered} \tag{3.1}$$

   where X_I is a point in the receiver grid and X_D is a point in the donor grid and the interpolation coefficients α_k are known. N is the number of points in the donor grid. $\hat{i}$ and $\hat{j}$ are the unit vectors in the x and y directions respectively. Details of this scheme are available in Ref. [87].

2. **Bilinear method:** The bilinear interpolation is a local scheme meaning that only a subset of the surface is fitted with appropriate functions. Figure 3.8 provides a schematic that shows how the solution at an interpolating point is obtained from the solution at the four supporting points around it. Assuming that (x_1, y_1), (x_2, y_1), (x_2, y_2), and (x_1, y_2) are the coordinates of nodes 1, 2, 3, and 4 respectively, the interpolated solution p_{int} at an arbitrary point (x, y) within the rectangle is given by the interpolation function below:

$$p_{int} = N_1 p_1 + N_2 p_2 + N_3 p_3 + N_4 p_4 \tag{3.2}$$

where

$$N_1 = \frac{(x_2 - x)(y_2 - y)}{(x_2 - x_1)(y_2 - y_1)}, N_2 = \frac{(x - x_1)(y_2 - y)}{(x_2 - x_1)(y_2 - y_1)},$$
$$N_3 = \frac{(x - x_1)(y - y_1)}{(x_2 - x_1)(y_2 - y_1)}, N_4 = \frac{(x_2 - x)(y - y_1)}{(x_2 - x_1)(y_2 - y_1)} \tag{3.3}$$

and p_1, p_2, p_3, and p_4 are the field information given at nodes 1, 2, 3, and 4 respectively. This scheme applies only to cases where the donor grids are structured into four-noded quads.

In this work, the *thin-plate spline* method is used for the interpolation of displacements and the *bilinear method* for the pressure loads, the choice of which was arbitrary. Velocities at the structural nodes are not interpolated onto the CFD mesh, as they are calculated by the CFD solver itself based on the displacements at two consecutive subiterations/time-steps by using a first-order backward difference scheme to satisfy the geometric conservation law (GCL) [48].

In Appendix A, the order of accuracy for both the interpolation schemes is estimated by interpolating assumed pressure distribution functions from a CFD source grid on to a CSD receiver grid.

3.6 CFD Grid Re-meshing/Morphing Technique

As mentioned previously, the CFD solver STREAM employs multi-block structured grids. For the grid morphing in the aeroelastic simulations, a master/slave strategy is used to establish a relationship between the moving surface points (master points) and vertices

located at the grid blocks (slave points). The movement of the master points is based on the displacements obtained from the structural solver, while the movement of the slave points is in turn based on that of the master points. For this purpose, a simple but effective formula suggested by Hartwich and Agrawal [39], based on a spring analogy, is used and is given by:

$$\bar{x}_s = x_s + \theta(\bar{x}_m - x_m) \tag{3.4}$$

The subscripts m and s represent master and slave, respectively, the overbar indicates the new position. x_s is a vector of the coordinates (x_v, y_v, z_v) of a slave point and x_m is that of a master point (x_p, y_p, z_p). In this work, a Gaussian distribution function as suggested by Hartwich and Agrawal [39] is used for the decay function, θ, given by:

$$\theta = exp[-\beta_c \, min[f_m, \frac{\sqrt{(x_v - x_p)^2 + (y_v - y_p)^2 + (z_v - z_p)^2}}{\epsilon + \sqrt{(\bar{x}_p - x_p)^2 + (\bar{y}_p - y_p)^2 + (\bar{z}_p - z_p)^2}}]] \tag{3.5}$$

where ϵ is an arbitrary small number to eliminate divisions by zero. The coefficient β_c affects the stiffness: a larger value causes the block to behave more like a rigid body and a smaller value makes the mesh behave in a pliant fashion. Similarly, the factor f_m in Eq. 3.5 also plays an important role in the re-meshing: for a fixed value of β_c, a smaller f_m will make the mesh behave in a more pliant fashion and vice-versa. Once the displacements of the slave points are obtained, they are propagated throughout the entire grid using a transfinite interpolation technique. More details about the moving mesh algorithm can be obtained in Refs. [39, 48, 55].

3.7 Generation of the Coupled Aeroelastic Code

A coupled code was achieved simply by compiling the object files of the individual solvers along with those of the interface routines (interpolation, morphing, etc.) to produce a single shared executable file. This would then be ported to Linux workstations without having to re-compile the code (unless certain machine-specific libraries are needed). This was possible in the current work due to the availability of the individual source codes. In cases where this is not possible, a relatively less efficient way of data transfer is obtained by reading and writing data files from one solver to the other at every iteration/time-step.

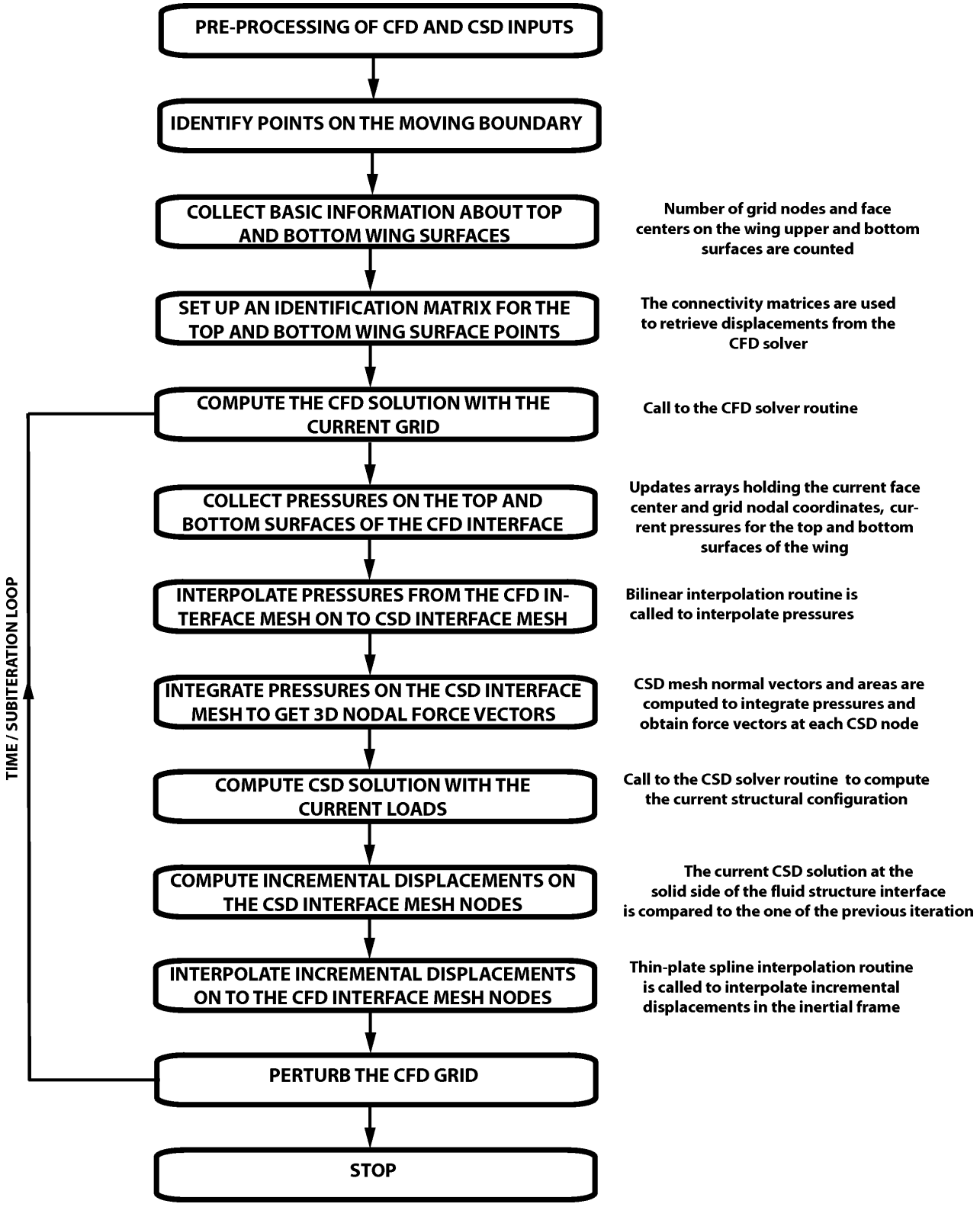

Figure 3.5: Interface program for UM/NLABS and UM/STREAM

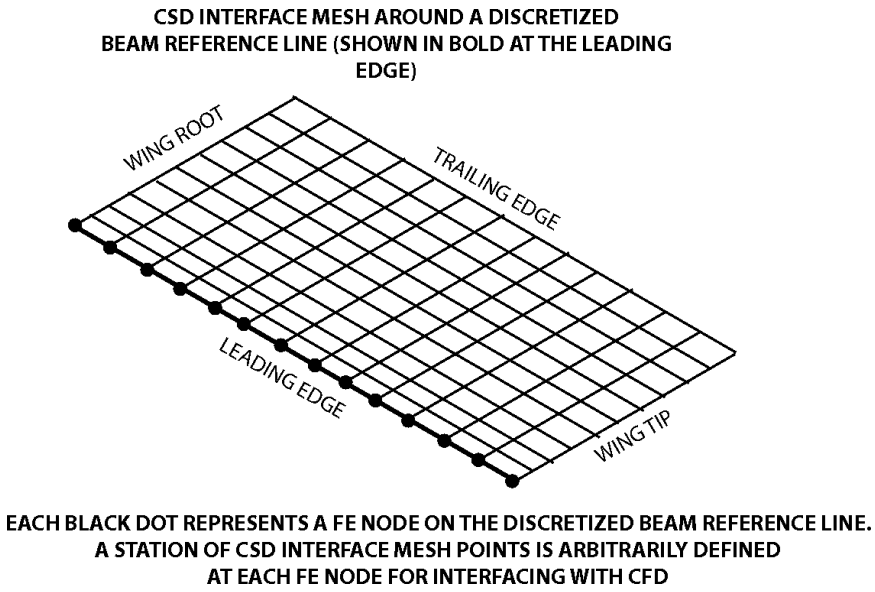

Figure 3.6: Sample UM/NLABS interface mesh for a flat plate rectangular wing including the beam reference line

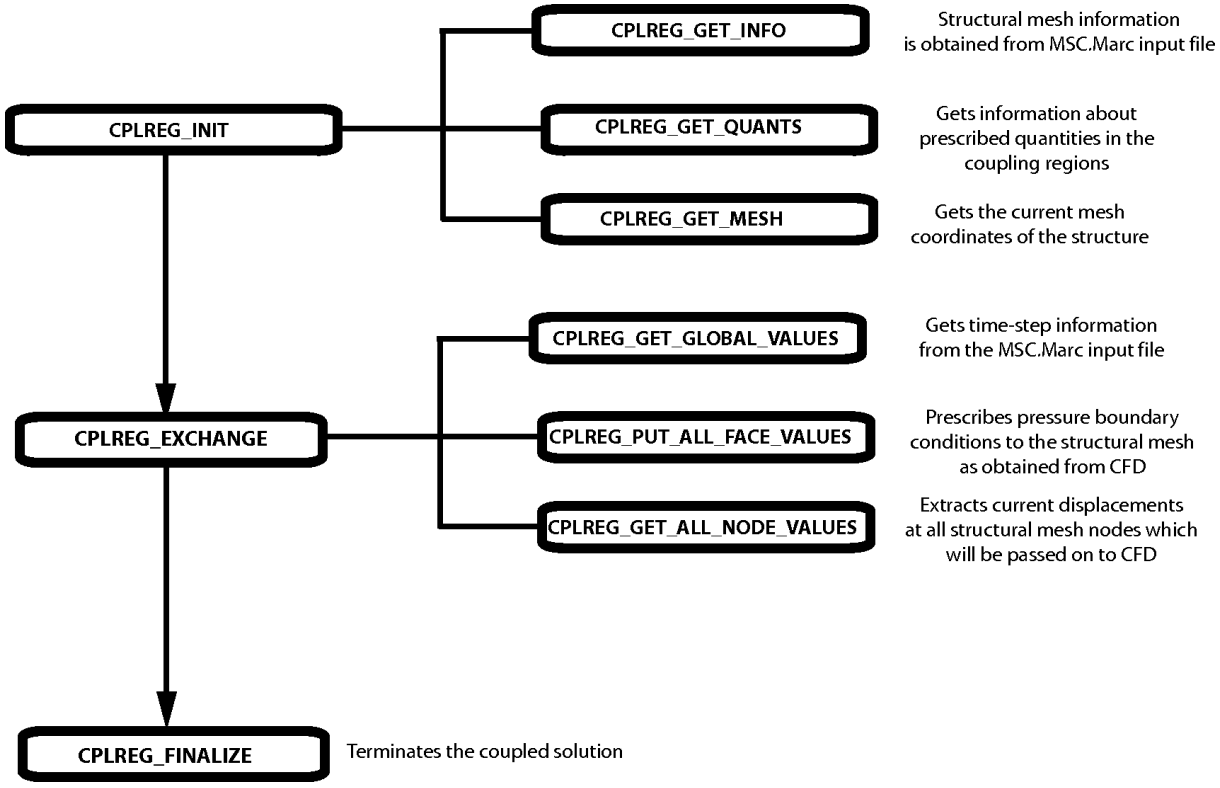

Figure 3.7: Interface program for MSC.Marc and UM/STREAM only showing the MSC.Marc's API calls

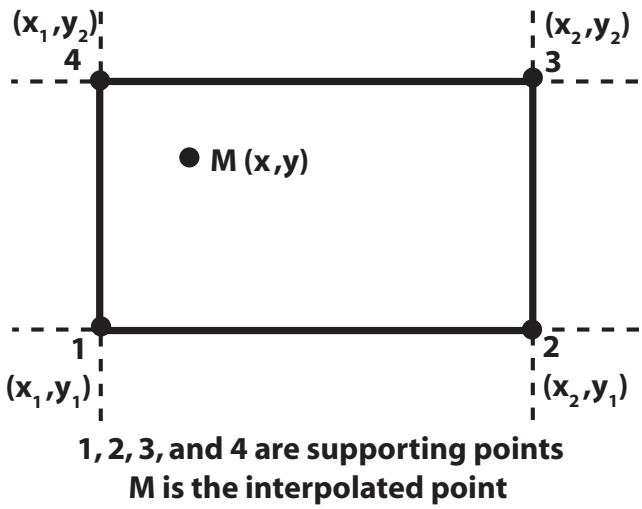

Figure 3.8: Bilinear interpolation geometric arrangement

Chapter IV

NUMERICAL INVESTIGATIONS OF THE GEOMETRICALLY NONLINEAR SHELL SOLUTION

This chapter presents selected verification and validation studies for the nonlinear structural dynamics solver UM/NLAMS developed as part of this work. Test cases are presented to evaluate the rigid body kinematics, geometrically nonlinear statics, and dynamics capability of the code.

4.1 Rigid Body Kinematics

As a check for the rigid body kinematics implementation in the solver UM/NLAMS, a simple test was conducted on a rigid rectangular plate shown in Fig. 4.1 actuated at point "A" with prescribed large amplitude rotation functions in three dimensions. The amplitudes of rotation are 30, 45, and 80 degrees about X (along span), Y (along chord), and Z (vertical) directions, respectively. Three dimensional displacements and velocities were extracted at an arbitrary point "B" (also shown in Fig. 4.1) and are plotted in Figs. 4.2 and 4.3. The results from UM/NLAMS have an excellent correlation with the exact solution computed in a MATLAB routine using the rotation tensor corresponding to the

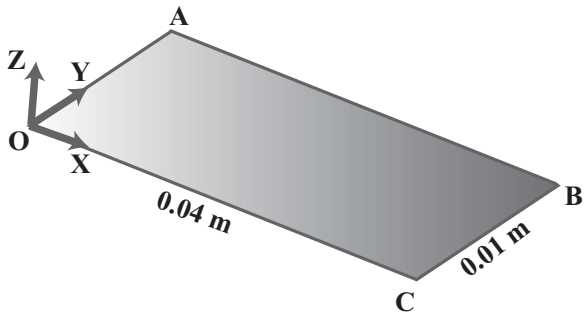

Figure 4.1: Rectangular plate configuration used to check rigid body kinematics implementation in UM/NLAMS and MSC.Marc.

rotation vector [7] and also with those computed in MSC.Marc.

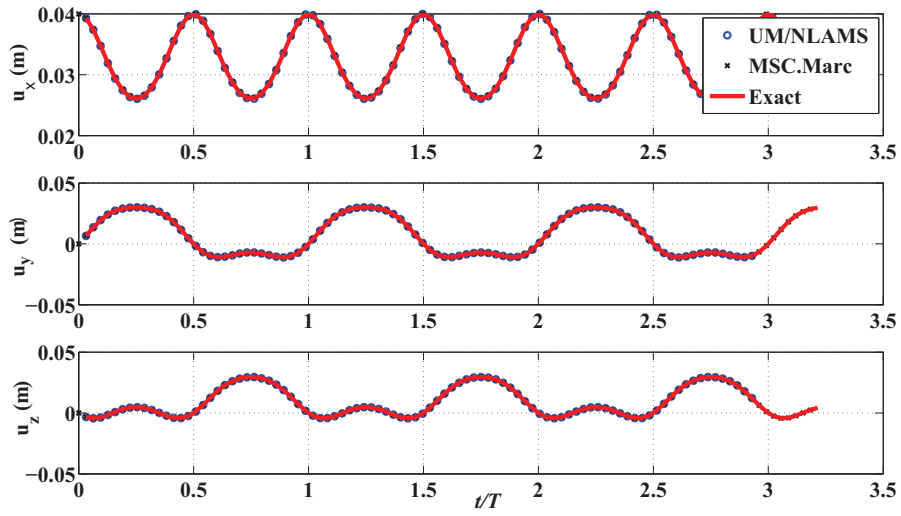

Figure 4.2: Displacements extracted at point "B" in Fig. 4.1 based on rigid body kinematics prescribed at point "A" in the same figure.

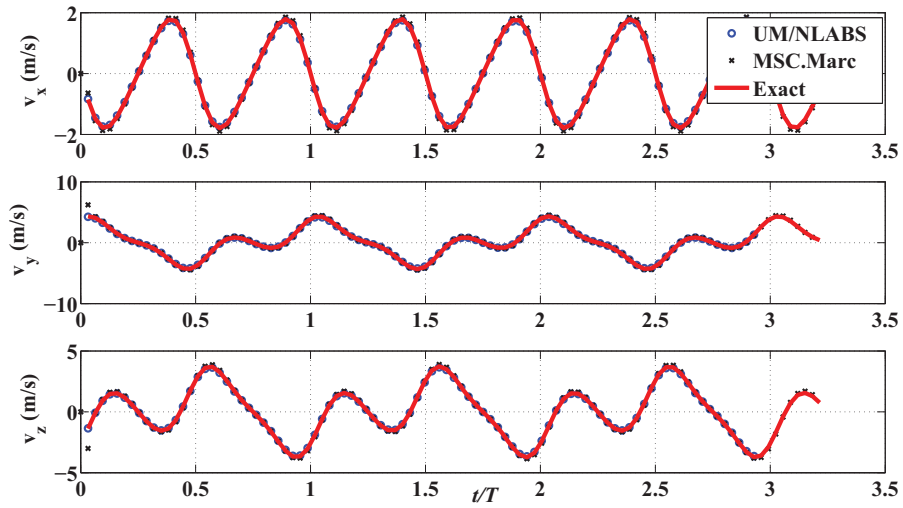

Figure 4.3: Translational velocities extracted at point "B" in Fig. 4.1 based on rigid body kinematics prescribed at point "A" in the same figure.

4.2 Nonlinear Static Structural Response

Three cantilever plate configurations subjected to different static loads (previously studied in Refs. [43, 49]) are considered in this subsection. Results presented include tip displacement as a function of the applied load in all the cases discussed.

4.2.1 Case 1: Cantilever plate subjected to uniform end moments

This case is used as one of the reference test cases to evaluate the geometrically nonlinear static capability of UM/NLAMS. It corresponds to a cantilevered isotropic plate of aspect ratio 2 subjected to uniform applied moments along the tip edge. The key parameters related to this case are included in Table 4.1. The analytical solution for the case is given in Ref. [49] and is used for comparison with results obtained from UM/NLAMS.

Table 4.1: Parameters associated with Case 1

plate length	0.6 m	Poisson's ratio	0.3
plate width	0.3 m	number of finite elements	512
plate thickness	0.001 m	number of load steps	25
Young's modulus	196.2 GPa	error limit	10^{-3}

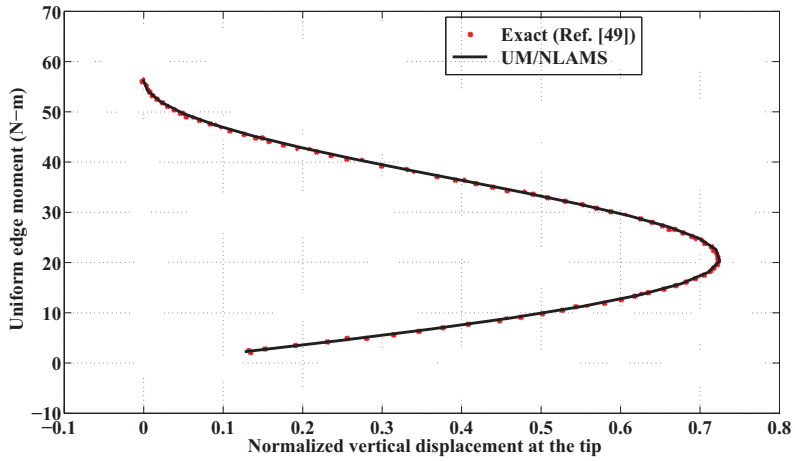

Figure 4.4: Normalized tip displacement as a function of the applied moment for the plate in Case 1 (displacement is normalized with respect to plate length)

Fig. 4.4 shows the normalized vertical displacement at a point on the tip (point "A" in Fig. 4.5) versus the applied moment. The displacement is normalized with respect to the length of the plate (also for all the cases discussed next unless specified otherwise). The plot compares the solution computed in UM/NLAMS with those provided in the reference paper [49] (which also discusses validation with analytical solutions). As seen in Fig. 4.4, there is an excellent match between the two results. The maximum tip deflection obtained in this case is 0.4 m which corresponds to 73% of the plate length. Due to the applied moment, the cantilever plate forms a circular arc as shown in Fig. 4.5. In order to compute the solution as a function of the applied load, a load control approach was followed in this work: the maximum load in the analysis was broken into several load steps and applied in

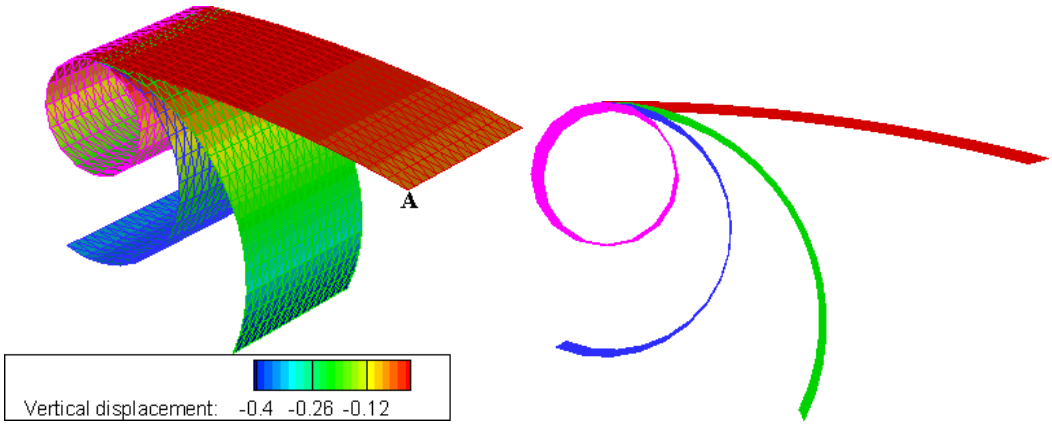

Figure 4.5: Snapshots of static wing deformation for the plate in Case 1 (legend in m)

increments. For each load increment, nonlinear static equilibrium was sought to compute the corresponding static response. The convergence criterion within each load step loop was chosen as the absolute difference in the Euclidean norm of the entire solution vector computed in any two consecutive Newton-Raphson iterations. For the current case, the tolerance for it was set to 10^{-3}.

4.2.2 Case 2: Cantilever plate subjected to an end lateral load

This case corresponds to an isotropic cantilever plate subjected to a lateral load at one of its free corners (node "A" of Fig. 4.6). The key parameters related to this case are included in Table 4.2. The results obtained from UM/NLAMS are compared to those published in Ref. [43]. Fig. 4.7 shows the normalized vertical displacement at the tip (node "B" of Fig. 4.6) versus the applied load. As before, the displacement is normalized with respect to the length of the plate. The maximum displacement found in this case was 45% of the plate length. Fig. 4.8 shows snapshots of the static wing deformation for three different load

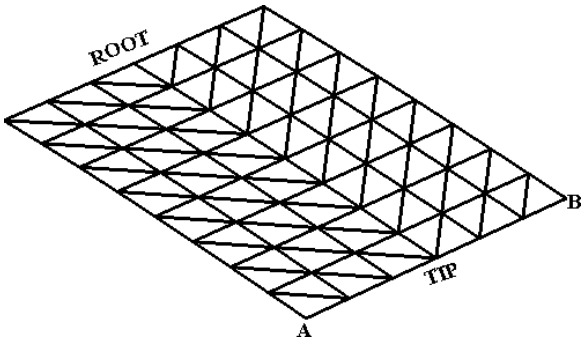

Figure 4.6: Finite element mesh configuration for the plate in Case 2

steps. The maximum difference in the static displacement computed in UM/NLAMS and that found in Ref. [43] is up to 1% of the plate length. A reason for this is the difference in the solution formulation of UM/NLAMS and that of Ref. [43]. While the former is based on co-rotational form of the total Lagrangian method, the latter is that of the updated Lagrangian method.

Table 4.2: Parameters associated with Case 2

plate length	40 m	Poisson's ratio	0.3
plate width	30 m	number of finite elements	96
plate thickness	0.4 m	number of load steps	25
Young's modulus	0.12 GPa	error limit	10^{-4}

4.2.3 Case 3: Cantilever plate subjected to an end shear force

This case corresponds to isotropic cantilever plate subjected to shear forces at the three nodes of the tip (nodes "A," "B," and "C" in Fig. 4.9). The load at nodes "A" and "C" is 10 N, whereas at node "B" it is 20 N. Similar to previous two cases, the load is applied incrementally in several load steps. The key parameters related to this case are included in Table 4.3. The solution obtained from UM/NLAMS in this case is compared to the analyt-

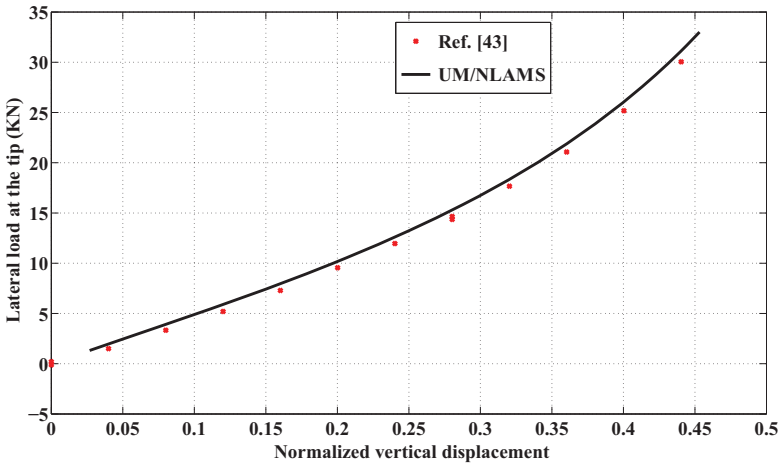

Figure 4.7: Normalized tip displacement as a function of applied load for the plate in Case 2 (displacement is normalized with respect to plate length)

ical solution published in Ref. [49]. Fig. 4.10 shows the normalized vertical displacement at the tip (node "A" in Fig. 4.9) versus the total applied load (sum of the loads on points "A", "B", and "C"). The maximum displacement found in this case was approximately 68% of the plate length. The agreement is very good up to 60% deformation, after which UM/NLAMS has difficulties to converging within the maximum number of subiterations (200) within a load step. This presents itself as a softer behavior than that of Ref. [49]. The cause for this behavior is unknown and requires further investigation. However, it is expected that increasing the number of load steps or the number of subiterations within a load step depending upon its size will help accelerate convergence.

Table 4.3: Parameters associated with Case 3

plate length	0.1 m	Poisson's ratio	0.
plate width	0.01 m	number of finite elements	128
plate thickness	0.001 m	number of load steps	25
Young's modulus	117.72 GPa	error limit	10^{-4}

4.3 Dynamic Structural Response

In this subsection, both rectangular and elliptic plate configurations are actuated with different types of prescribed dynamic motions. In all the cases considered, responses computed using UM/NLAMS are verified against those from MSC.Marc. Results presented include tip displacement as a function of time and also snapshots of three-dimensional wing deformation contours.

4.3.1 Case 4: A rectangular plate prescribed with single degree-of-freedom flap rotation

A rectangular aluminum plate shown in Fig. 4.11 was prescribed with a single degree-of-freedom large amplitude flap rotation about an axis running through the chord. In the figure, the square block at the wing root is constrained in all degrees of freedom with respect to the global frame, and the rotation was prescribed as a "1-cosine" variation. This enabled the simulation to start from zero initial displacement and velocity, obviating the need for a special starting procedure as would have been the case if a sine variation was prescribed. The key parameters related to this case are included in Table 4.4. Figs. 4.12,

Table 4.4: Parameters associated with Case 4

plate length	80 mm	prescribed flap rotation profile	1-cosine
plate width	27 mm	flapping frequency	5, 10, and 30 Hz
plate thickness	0.2 mm	flapping amplitude	17 deg
Young's modulus	70 GPa	time-step sizes	1.5x10^{-4} and 10^{-5} s
Poisson's ratio	0.3	number of finite elements	512
material density	2700 kg/m^3	error limit	10^{-4}

4.13, and 4.14 show the normalized vertical displacement at the tip (point "A" in Fig. 4.11) as a function of non-dimensional time (time normalized with respect to the period of the flap rotation) for three different flapping frequencies: 5 Hz, 10 Hz, and 30 Hz, respectively. These results are compared to those obtained from the commercial finite element solver MSC.Marc. The bilinear thin-triangular shell element no.138 is used to discretize the wing in MSC.Marc (also for all the MSC.Marc cases discussed here). The time-integration schemes used are the non-dissipative form of the Newmark and the generalized-α methods. The former was used in the 5 Hz and the 10 Hz cases whereas the latter in the 30 Hz case with a spectral radius value set to 0.4. The time-step size used in the 5 Hz and 10 Hz cases was 1.5x10^{-4} s and in the 30 Hz case was 10^{-5} s. The convergence criterion for the Newton-Raphson convergence loop is a check on the absolute difference in the Euclidean norm of the entire solution vector computed in any two consecutive iterations, set to 10^{-4} in the three cases considered here. As seen from the results in Fig. 4.12, the agreement between UM/NLAMS and MSC.Marc for lower frequencies is very good. With increase in frequency, differences start to become apparent (Fig. 4.14). There are noticeable discrepancies in the highest frequency (30 Hz) response, which is presumably due to the stronger geometric nonlinearities, as well as the increased effect of the transient terms in Eq. 2.43. The exact cause for the discrepancies will require further investigation. Due to these reasons, for the aeroelastic response studies in this work, only the lower frequencies up to 10 Hz are considered. Future studies should be conducted to address which solution is more accurate under higher frequency regimes.

4.3.2 Case 5: A rectangular cantilever plate prescribed with pure plunge motion

A rectangular cantilever steel plate was prescribed with a pure plunge motion at the root. The key parameters related to this case are included in Table 4.5. Fig. 4.15 shows the normalized vertical displacement at the tip versus the normalized time, with a comparison between UM/NLAMS and the commercial finite element solver MSC.Marc. The displacements and time are normalized with respect to the plunge amplitude and the period of plunge respectively. The time integration method used is the Newmark scheme. As seen in Fig. 4.15, there is an excellent match between the results computed in both the codes.

Table 4.5: Parameters associated with Case 5

plate length	0.3 m	prescribed plunge profile	1-cosine
plate width	0.1 m	plunge frequency	1.78 Hz
plate thickness	0.001 m	plunge amplitude	0.0175 m
Young's modulus	210 GPa	time-step size	10^{-3} s
Poisson's ratio	0.3	number of finite elements	1150
material density	7800 kg/m^3	error limit	10^{-4}

4.3.3 Case 6: An elliptic cantilever plate prescribed with rotations about all axes

An elliptic isotropic plate of the Zimmerman planform (shown in Fig. 4.16) is cantilevered along the root with respect to the global frame and is actuated at its leading edge point on the root with prescribed rotation functions about all three coordinate axes. The Zimmerman planform is simply formed by two ellipses intersecting at the quarter chord

point. Mathematically, it is defined by

$$\begin{aligned} (\tfrac{x}{R})^2 + (\tfrac{y}{c_1})^2 = 1 \begin{cases} 0 \le x \le R \\ 0 \le y \le c_1 \end{cases} \\ (\tfrac{x}{R})^2 + (\tfrac{y}{c_2})^2 = 1 \begin{cases} 0 \le x \le R \\ -c_2 \le y \le 0 \end{cases} \end{aligned} \tag{4.1}$$

where

$$\begin{aligned} c_1 = 0.75c \qquad c_2 = 0.75c \\ S = \tfrac{c_1 R\pi}{2} + \tfrac{c_2 R\pi}{2} = \tfrac{cR\pi}{2} \quad A_r = \tfrac{4R^2}{S} = \tfrac{8R}{c\pi} \end{aligned} \tag{4.2}$$

In Eq. 4.2, c is the chord length at the root, R is the length of the wing defined as the length of the quarter chord line along the wing span, and A_r is the aspect ratio of the full wing which is 7.65 in this case. The key parameters related to this case are included in Table 4.6. Fig. 4.17 shows the normalized vertical displacement at the tip (quarter chord point) versus the normalized time, with a comparison between UM/NLAMS and MSC.Marc. As seen from the figure, overall, there is a very good correlation between them barring some discrepancies at specific time instants. Figs. 4.18 and 4.19 show snapshots of wing deformation computed in both UM/NLAMS and MSC.Marc for three different time instants ("A", "B", and "C" of Fig. 4.17). As seen from the snapshots, there is an excellent agreement between the three-dimensional wing deformation computed in UM/NLAMS and MSC.Marc at points "A" and "C", but, there is a slight discrepancy (approximately 3% of plate length) at point "B" which is also seen from Fig. 4.17.

Table 4.6: Parameters associated with Case 6

plate length at quarter chord	0.075 m	prescribed rotation profile	1-cosine
plate width at the root	0.025 m	flap frequency	10 Hz
plate thickness	$0.2\text{x}10^{-3}$ m	flap amplitudes	5, 15, and 5 deg about x, y, and z axes respectively
Young's modulus	7.34 GPa	time-step size	$1.5\text{x}10^{-4}$ s
Poisson's ratio	0.3	number of finite elements	244
material density	1740 kg/m^3	error limit	10^{-4}

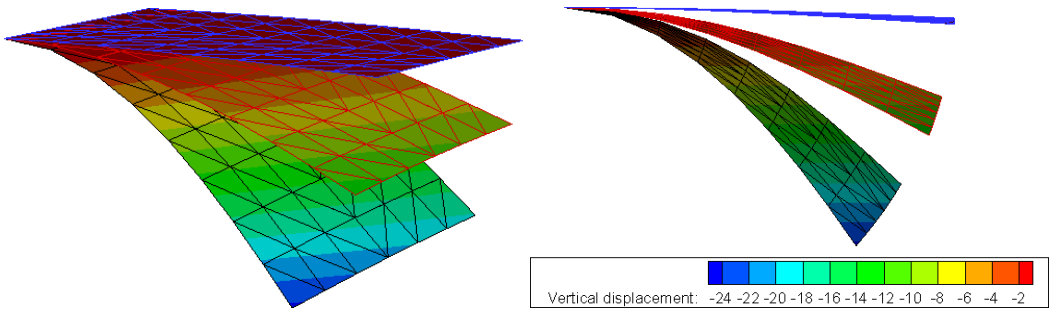

Figure 4.8: Snapshots of wing deformation for the plate in Case 2 (legend in m)

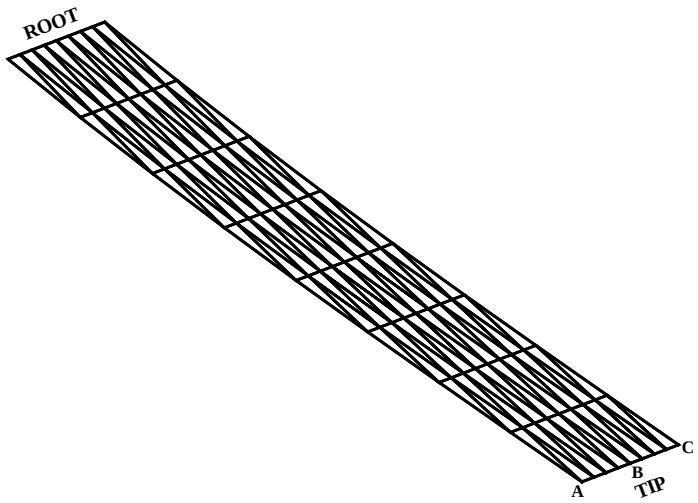

Figure 4.9: Finite element mesh configuration for the plate in Case 3

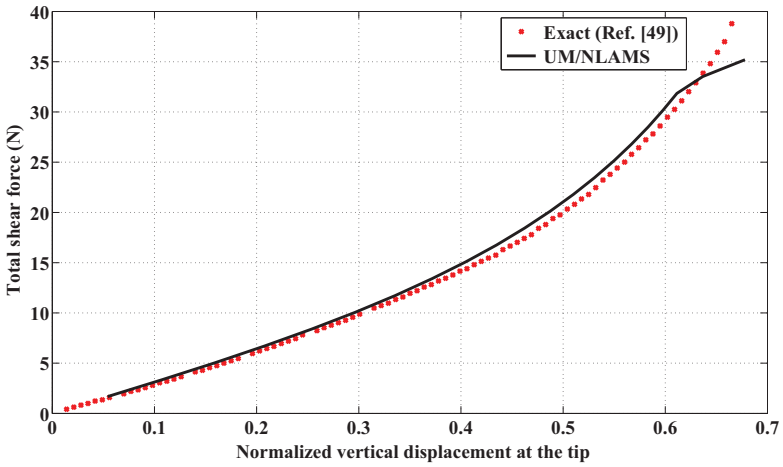

Figure 4.10: Normalized tip displacement as a function of the magnitude of the total applied load for the plate in Case 3 (displacement is normalized with respect to plate length)

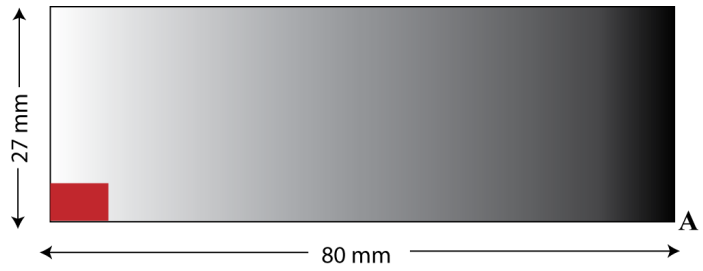

Figure 4.11: Rectangular flat plate flapping wing configuration for Case 4.

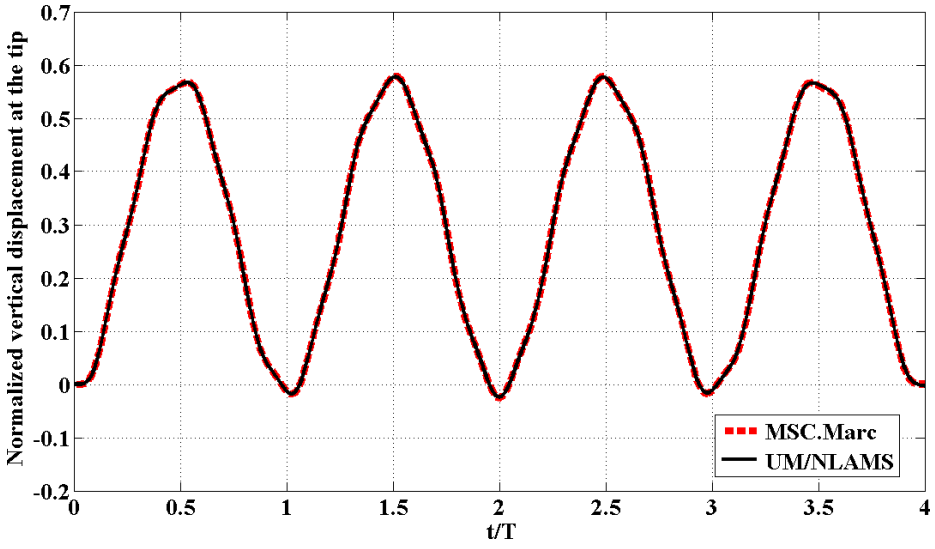

Figure 4.12: Rectangular flat plate response due to flapping excitation (5 Hz) in Case 4 (displacement is normalized with respect to plate length).

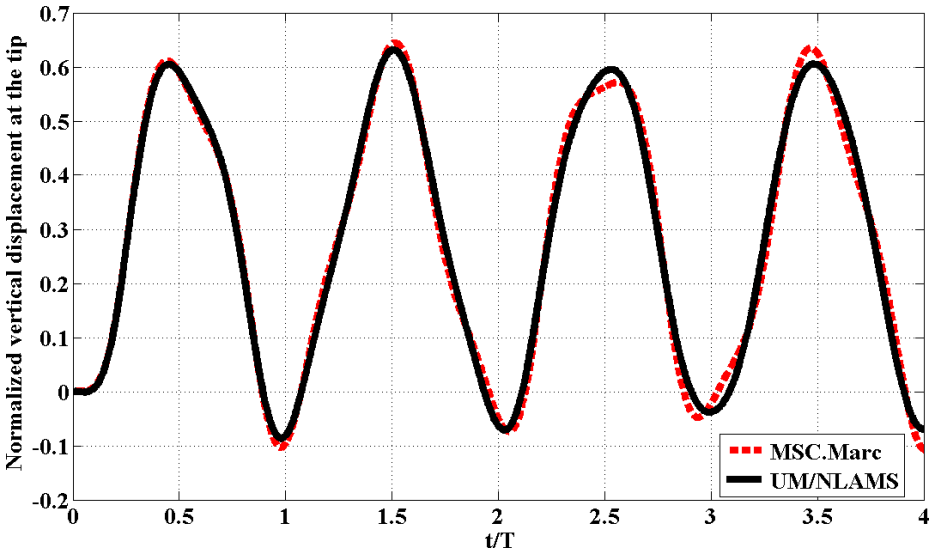

Figure 4.13: Rectangular flat plate response due to flapping excitation (10 Hz) in Case 4 (displacement is normalized with respect to plate length).

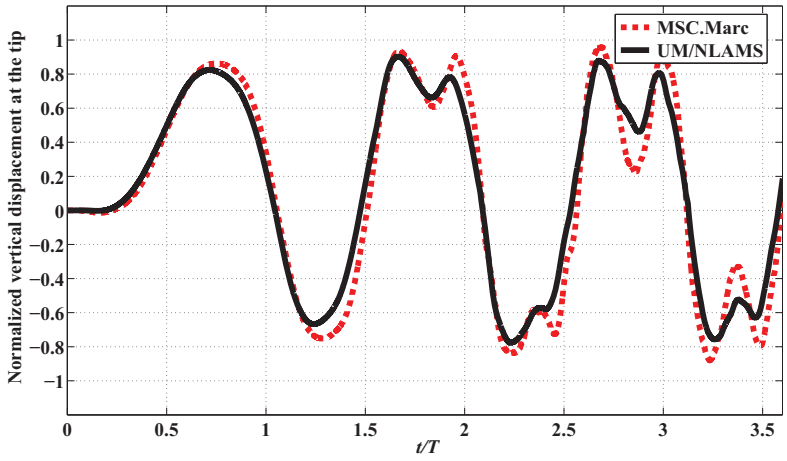

Figure 4.14: Rectangular flat plate response due to flapping excitation (30 Hz) in Case 4 (displacement is normalized with respect to plate length).

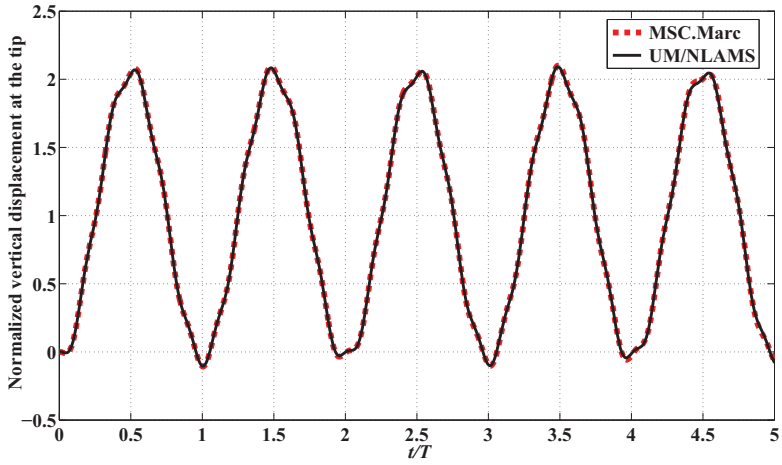

Figure 4.15: Rectangular plate response due to plunge excitation in Case 5 (displacement is normalized with respect to the amplitude of plunge).

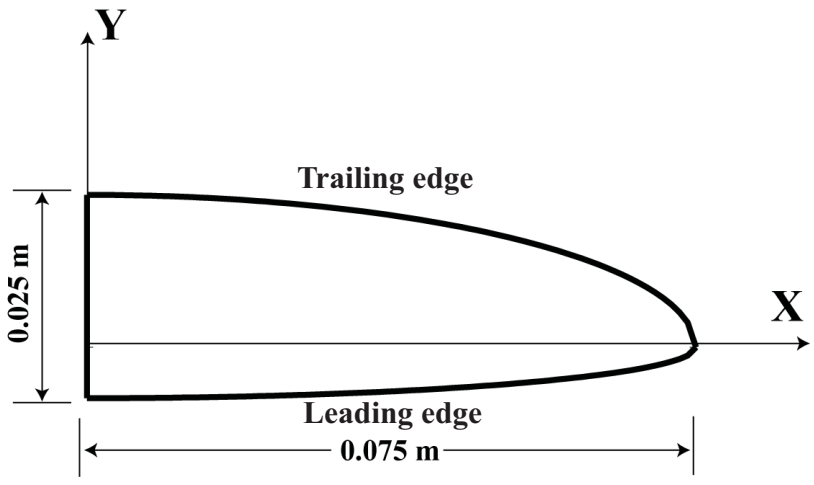

Figure 4.16: Zimmerman elliptic plate flapping wing configuration.

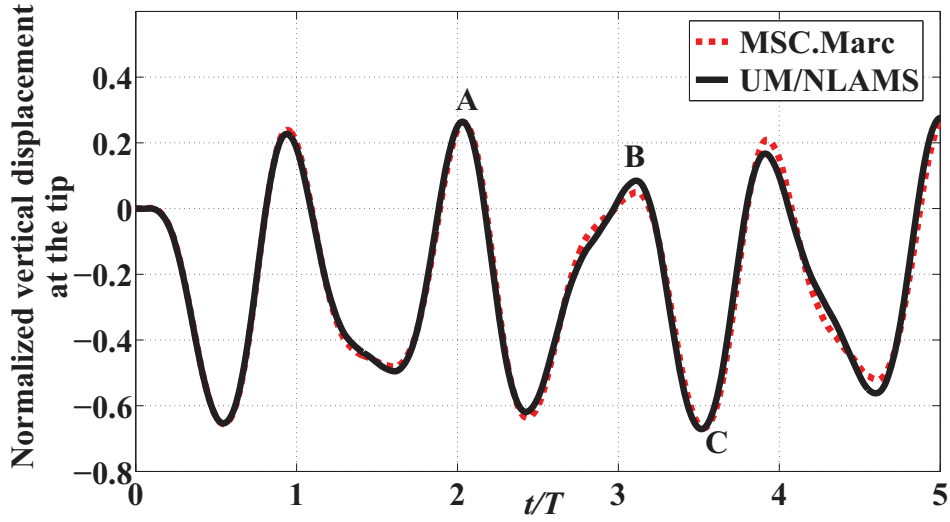

Figure 4.17: Elliptic flat plate response to prescribed flap rotations in Case 6 (displacement is normalized with respect to plate length).

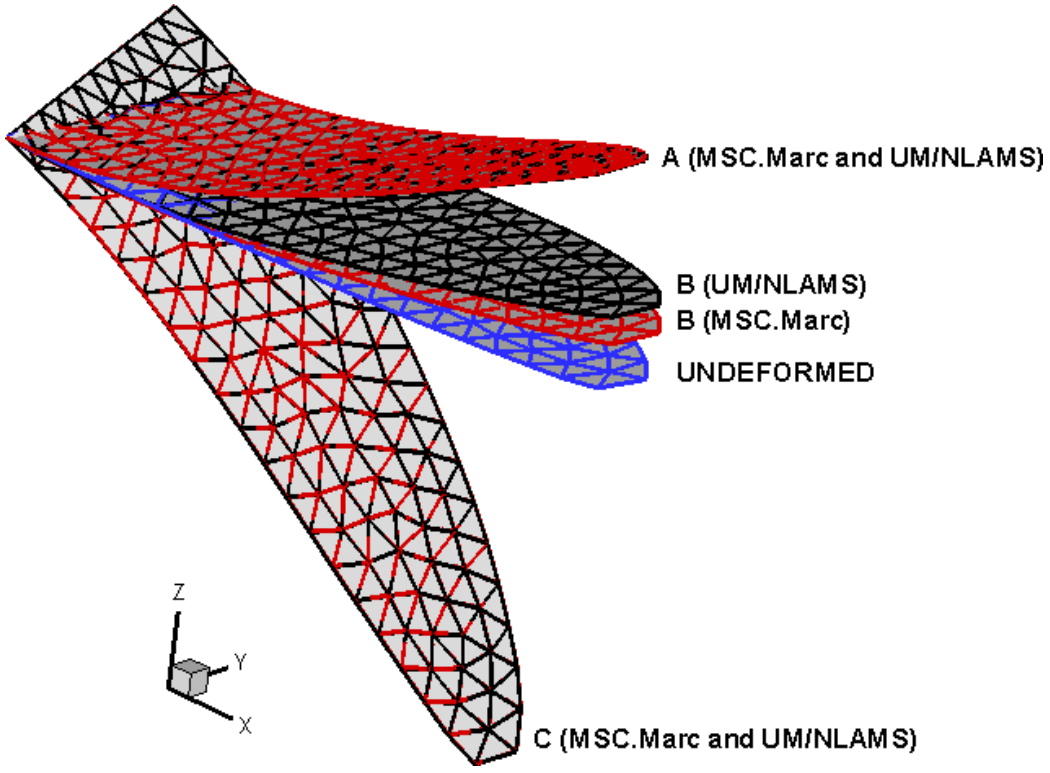

Figure 4.18: Snapshot of dynamic wing deformation in Case 6 (perspective)

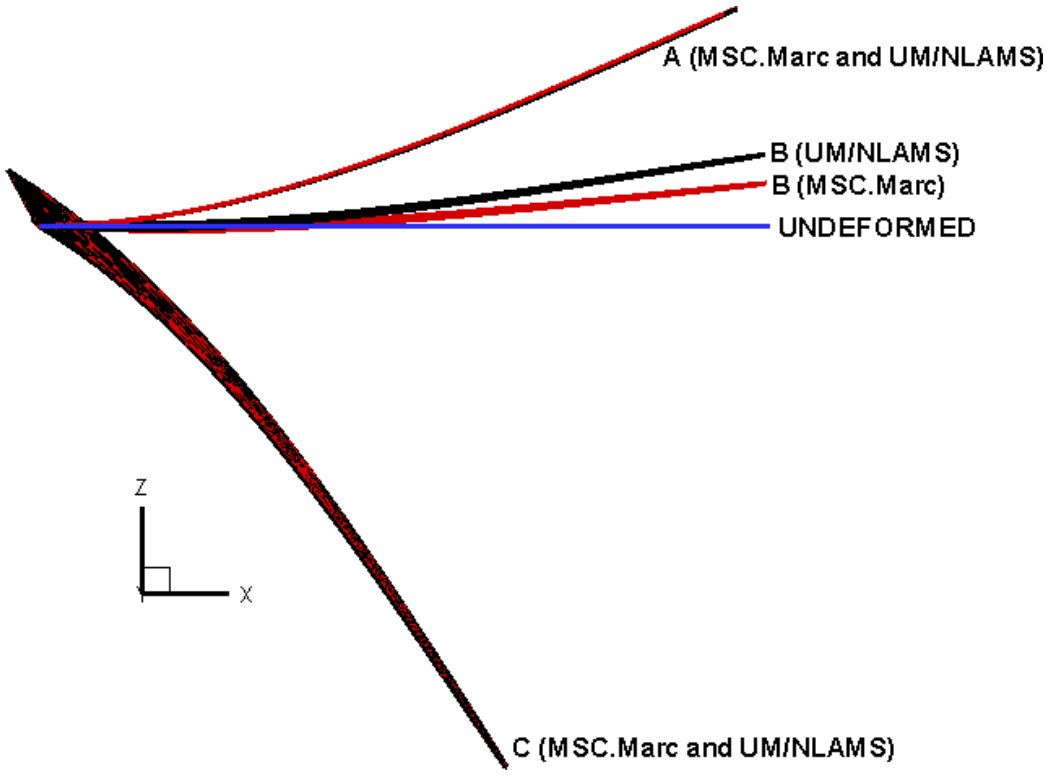

Figure 4.19: Snapshot of dynamic wing deformation in Case 6 (side view)

Chapter V

NUMERICAL INVESTIGATION OF PLUNGING/FLAPPING WINGS

The goal of this chapter is twofold. First is the verification and/or validation of the proposed aeroelastic formulations presented previously and second is the investigation of the effect of flexibility on the aerodynamics of simplified plunging/flapping wing configurations. For this purpose, three different flexible wings listed below have been chosen whose choice has been mainly motivated by the availability of experimental data:

- A rectangular wing prescribed with pure plunge motion.
- An elliptic wing of the Zimmerman planform prescribed with large amplitude single degree-of-freedom pure flap rotation.
- A rectangular wing prescribed with large amplitude single degree-of-freedom pure flap rotation.

In two of these testcases, results from the coupled codes involving UM/NLAMS and MSC.Marc are verified against each other. Further, the impact of aeroelastic interactions on lift and/or thrust generation with varying reduced frequency, and/or flexibility is studied.

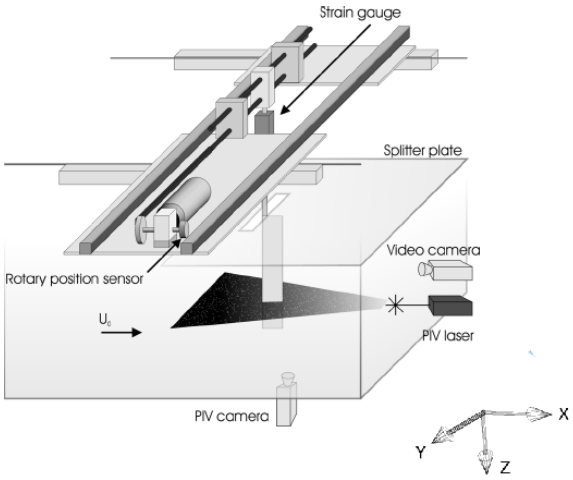

Figure 5.1: Water-tunnel experimental setup (from Heathcote *et al.* [41])

Also, the fluid physics associated with aeroelastic wing deformations is discussed with the help of flow structures and pressure distributions. In the next three sections, aeroelastic studies conducted on the wing configurations mentioned above are presented in detail, one after the other, starting from the rectangular plunging wing case.

5.1 A Rectangular Wing Prescribed With Pure Plunge Motion at the Root

5.1.1 Description of the Test Case

Water tunnel studies have been performed by Heathcote *et al.* [41] to study the effect of spanwise flexibility on the thrust, lift, and propulsive efficiency on a rectangular wing (NACA 0012 cross section) configuration. A schematic of the experimental setup is shown in Fig. 5.1. Three wings of 0.3-m span and 0.1-m chord with varying levels of flexibility

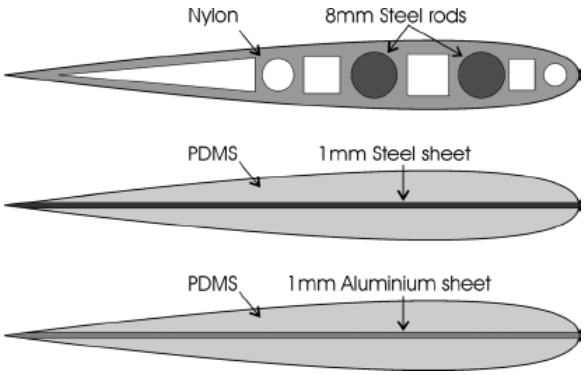

Figure 5.2: "Inflexible/Rigid," "Flexible," and "Highly Flexible" wing cross-sections (top to bottom in that order) used in the experiments of Heathcote *et al.* [41]

were constructed. The representations of the cross-section constructions are reproduced in Fig. 5.2. The leading edge at the wing root was actuated by a prescribed cosine plunge displacement profile as shown in Fig. 5.3 in all three cases. The overall wing thrust coefficient, tip displacement response, and trailing edge vorticity measured in the experiment are used for correlations with computations in this work.

5.1.2 Computational Models

A structured multi-block O-type grid around a NACA 0012 wing of aspect ratio 3 was used for the CFD simulations. Grid sensitivity studies have been performed to identify a grid suitable (based on a convergence check of overall lift and thrust coefficient response) for the computations in this work. The number of points in the final grid configuration is 0.3 million approximately. The CFD model setup including the boundary conditions is shown in Fig. 5.4. The fluid solution is based on laminar flow assumption. The wing structures of progressively increasing spanwise flexibility are labeled as "Rigid," "Flexible-1," "Flexible-2," and "Flexible-3" in this document. While the "Rigid," "Flexible-1," and

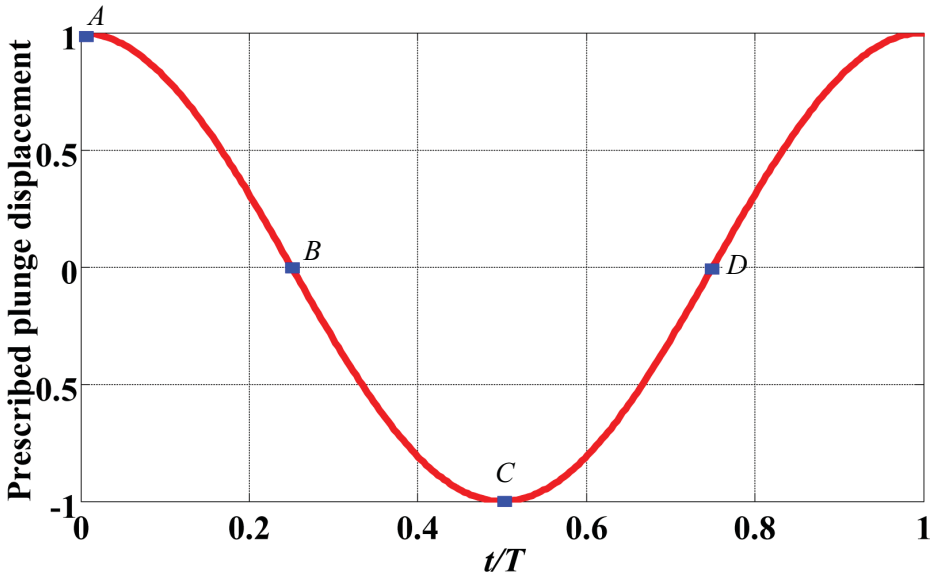

Figure 5.3: Prescribed plunge motion for the rectangular plunging wing (displacement normalized w.r.t. amplitude) (Points A, B, C, and D are representative time instants corresponding to 0, $T/4$, $T/2$, and $3T/4$ respectively where T is the period of plunge motion. These are used at several places for referencing purpose.)

"Flexible-2" configurations correspond to "Inflexible/Rigid," "Flexible," and "Highly Flexible" ones of the experiment, the "Flexible-3" configuration was considered as a special case only in the computations due to reasons which will be discussed subsequently in this section. For the structural analysis of these wing configurations, different models were developed using the previously presented CSD solvers UM/NLABS, MSC.Marc, and UM/NLAMS. The first (Figs. 5.5 and 5.6) one in UM/NLABS is based on a 1-D beam finite-element discretization with 39 elements along the semi-span. Chordwise deformation was reported as being negligible in the experiment, therefore, a beam model with six elastic degrees of freedom, corresponding to extension, twist, and shear and bending in two directions could be chosen. The beam reference line (cantilevered to a plunging frame of reference) is chosen along the leading edge of the wing (highlighted in black in Fig. 5.5)

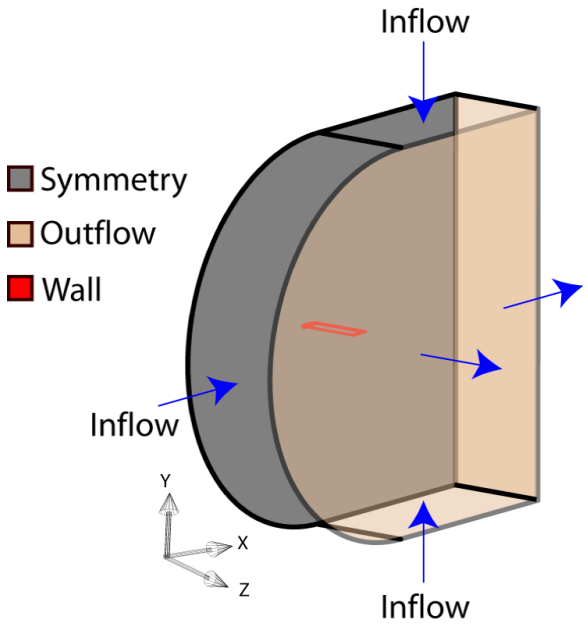

Figure 5.4: CFD computational model setup for the rectangular plunging wing.

and cross-sectional properties are evaluated with respect to the leading edge point. Furthermore, the properties are uniform throughout the semi-span. The contribution of the PDMS rubber material (used in the experimental "Flexible" and "Highly Flexible" wing constructions) to the overall mass and stiffness properties was found to be negligible compared to either Steel or Aluminium (the mass density of PDMS was assumed to be 0.97 kg/m^3 whereas in reality it is 970 kg/m^3 which was not considered in this work): therefore, only the stainless steel stiffener (rectangular thin strip) was used for the evaluation of cross-sectional properties (Fig. 5.6). The mass and stiffness property matrices (computed in UM/VABS) for all the flexible plunging wing configurations are furnished in Appendix B. The 3-D structural solution is obtained by using 75 recovery nodes on each cross section resulting in a structured grid of 3000 interface points which define the solid side of the aeroelastic interface. The second structural model (Fig. 5.7) is a rectangular plate and it

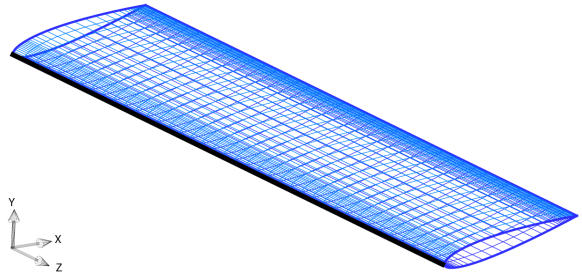

Figure 5.5: UM/NLABS computational models (CSD-CFD interface grid with the beam reference line indicated in black).

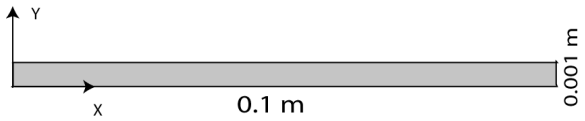

Figure 5.6: UM/NLABS computational models (rectangular thin-strip cross section used to evaluate structural stiffness and mass properties.)

was created in MSC.Marc using four-noded thick shell elements (MSC.Marc element number 75). The wing is actuated by prescribing motion to a pivot point which is connected to the structure via a rigid link. The third structural model is also a rectangular plate created in UM/NLAMS using triangular finite elements. The wing was defined in the global frame which was prescribed with the plunge motion like in the previous two cases. A summary of the wing geometrical and mechanical properties common to all the three models discussed above is included in Table 5.1. Table 5.2 provides information about the flow properties (dimensional). In Table 5.3, the key dimensionless parameters related to either the structure, the flow, or to both are furnished.

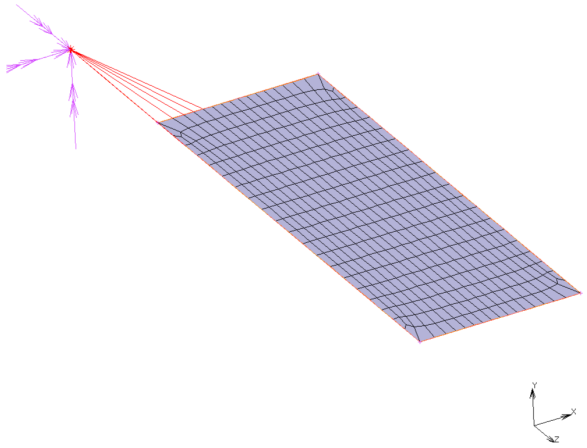

Figure 5.7: Shell finite element model of the thin rectangular steel strip in MSC Marc.

5.1.3 Evaluation of Computational Parameters

5.1.3.1 Time-Step for Aeroelastic Computations

As mentioned above, to assess the independence of the numerical solution to grid refinement, a grid convergence study was performed on a rigid wing and a suitable grid was subsequently chosen. A time-step sensitivity study was performed with that grid at a reduced frequency of 1.82 and chord-based Reynolds number of $3\text{x}10^{4}$. Three different non-dimensional time-steps $3\text{x}10^{-3}$ ($1\text{x}10^{-3}$ s), $6\text{x}10^{-3}$ ($2\text{x}10^{-3}$ s), and $15\text{x}10^{-3}$ ($5\text{x}10^{-3}$ s) as defined in Eq. 2.113 were tested. The corresponding thrust coefficient of the rigid wing as a function of time is shown in Fig. 5.8. Based on this analysis, a time-step of $6\text{x}10^{-3}$ ($2\text{x}10^{-3}$ s) was chosen as being adequate to ensure asymptotic convergence and it was used in all cases discussed in this section unless otherwise stated.

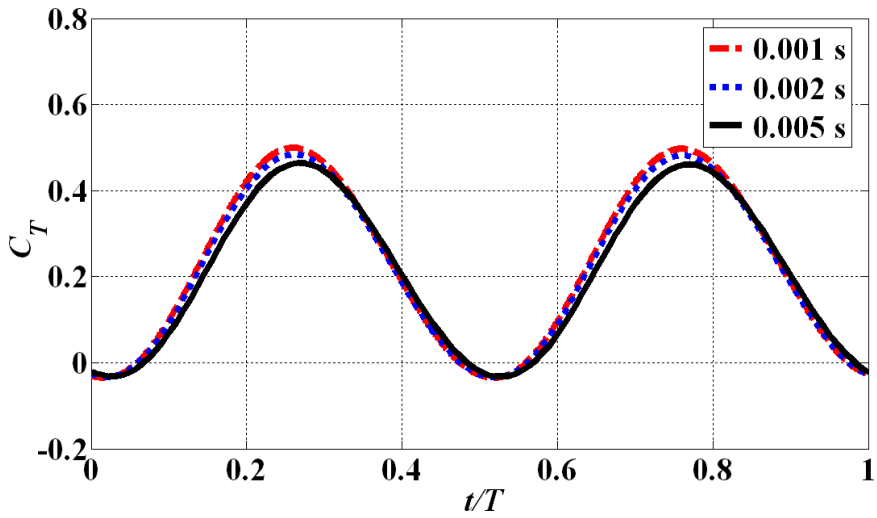

Figure 5.8: Rigid wing computation (time step sensitivity).

Table 5.1: Geometric and mechanical properties of the plunging wing configurations

	"Flexible-1"	"Flexible-2"	"Flexible-3"
semi-span [m]	0.3	0.3	0.3
chord length [m]	0.1	0.1	0.1
Poisson's ratio	0.3	0.3	0.3
structural thickness [m]	0.001	0.001	0.001
material density [kg/m^3]	7.8x10^3	2.7x10^3	2.7x10^3
Young's modulus [GPa]	210	70	40

5.1.3.2 Convergence Criterion for Aeroelastic Computations

In the case of the coupled code involving MSC.Marc, the issue of a convergence criterion does not arise since, as previously mentioned, it supports only an explicit coupling. Two different convergence criteria were used in the aeroelastic computations for the implicit convergence within a coupled time-step in the coupled code involving UM/NLAMS. They are:

Table 5.2: Flow properties

flow velocity	0.3 m/s	water density	1000 kg/m^3

- a check on the absolute difference of vertical displacement at the node corresponding to the tip of the wing leading edge in two consecutive fluid-structure subiterations (namely "Newmark-C1"), and

- a check on the Euclidean norm of the entire solution vector computed in two consecutive fluid-structure subiterations (namely "Newmark-C2")

Fig. 5.9 shows the mean lift coefficient on the wing computed using the Newmark method independently considering both the convergence criteria. As seen in the figure, though expected, it is interesting to see that high frequency oscillations (of approximately 500 Hz) are seen in the response computed using the convergence criterion just based on the tip displacement ("Newmark-C1"). However, these are not seen in the case where a convergence criterion based on the entire solution vector was used ("Newmark-C2"). This is an example of a case in which the smoothness of the aeroelastic response has a dependence on the chosen convergence criterion in an implicit coupling. In all the cases involving UM/NLABS and UM/NLAMS in this section and also in others, the "Newmark-C2" convergence criterion listed above is used unless otherwise stated.

Table 5.3: Dimensionless parameters associated with wing model

	"Flexible-1"	"Flexible-2"	"Flexible-3"
chord-Reynolds number: *Re*	3x10^4	3x10^4	3x10^4
Strouhal number: *St*	0.04 to 0.202	0.202	0.202
reduced frequency: *k*	0.4 to 1.82	1.82	1.82
chord-normalized plunge amplitude: h_{root}	0.175	0.175	0.175
Π_1	213	73.8	42.2
Π_2	6.5x10^{-9}	2.25x10^{-9}	2.25x10^{-9}
ρ^*	7.8	2.7	2.7

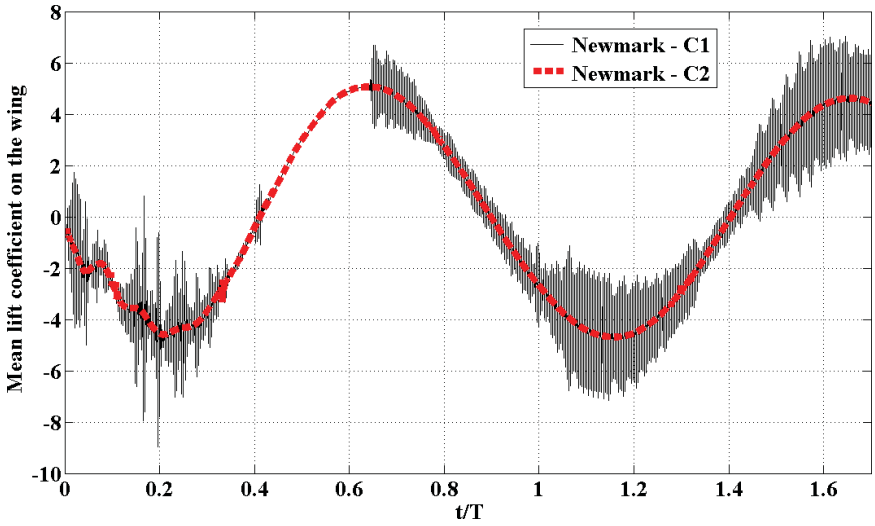

Figure 5.9: Lift coefficient of the "Flexible-1" plunging wing computed in UM/NLAMS with two different convergence criteria.

5.1.4 Explicit and Implicit Coupling Methods

To demonstrate the impact of the fluid-structure subiterations within a time-step (implicit computation) on the coupled response, two different computations were performed.

The first computation was done with the "Flexible-1" plunging wing for a chord Reynolds number of $3\text{x}10^4$ and reduced frequency of 1.74 with both explicit and implicit coupling methods in UM/NLABS. Figs. 5.10 and 5.11 include the computed lift coefficient response on the wing. In general, as seen in Fig. 5.10, there is little difference in the peak amplitudes between the two solutions for the selected time steps. The implicit method, however, as seen in Fig. 5.11, eliminates most of the high-frequency error through forced convergence within each time step, a feature not present in the explicit approach.

The second computation was done with the "Flexible-2" plunging wing for a chord Reynolds number of $3\text{x}10^4$ and reduced frequency of 1.82 once again with both explicit and

implicit coupling methods but in MSC.Marc and UM/NLAMS, respectively. The Newmark time integration scheme was used in both the codes. Fig. 5.12 shows the aeroelastic lift coefficient response focusing only on a portion of the response during the first cycle. While the response computed using the coupled code involving UM/NLAMS is stable, the one in the case of MSC.Marc diverges within the first few coupled time-steps. This behavior persists even for prohibitively small time-steps, e.g., 10^{-5} s (5750 steps per period). Fig. 5.13 shows the Euclidean norm of the error within the first coupled time-step as a function of the fluid-structure subiteration number as computed in the implicit aeroelastic code involving UM/NLAMS. As can be seen, in order to achieve convergence in the first time-step, approximately 30 subiterations were needed for the error to be less than 10^{-6}. The absence of the fluid-structure subiteration scheme in the coupled code involving MSC.Marc explains why the response is unstable. Since the coupling in that case is controlled by MSC.Marc, there is no correct option for an implicit coupling of the code for aeroelastic analysis. Due to the foregoing reasons, in this work, only results based on the implicit coupling method are focused on, while still presenting those of the explicit coupling wherever MSC.Marc is involved.

5.1.5 Cross Validation of Rectangular Plunging Wing Aeroelastic Solutions

Fig. 5.14 shows the vertical displacement at the tip (in the inertial frame) normalized with respect to the plunge amplitude for the "Flexible-1" wing computed with all three coupled simulation codes involving UM/NLAMS, UM/NLABS, and MSC.Marc including the experimental data. Excellent correlation is obtained between the three computational

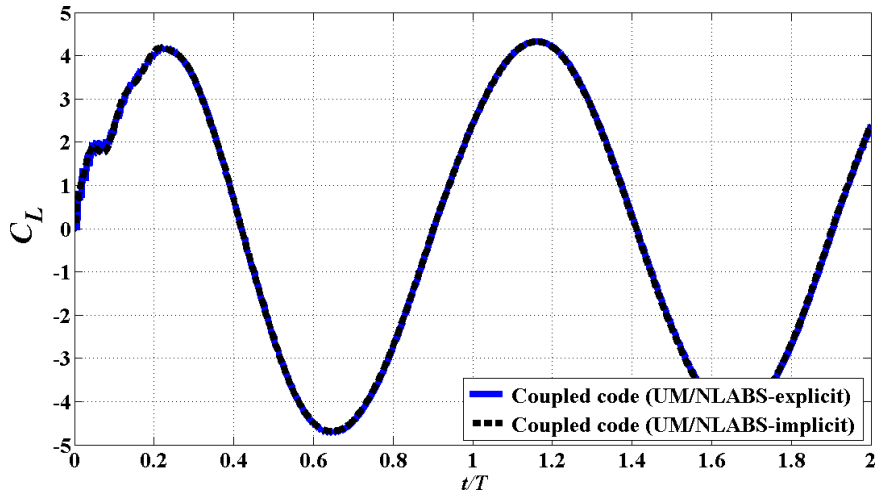

Figure 5.10: Lift coefficient response of the "Flexible-1" wing for reduced frequency of 1.74: explicit and implicit coupling methods in UM/NLABS.

solutions and also the experimental response. This indicates that the frameworks using UM/NLABS (more efficient) and UM/NLAMS / MSC.Marc (more general) work similarly for bend/twist dominated flexible wings and that their integration with the CFD is verified. The UM/NLAMS and MSC.Marc frameworks will be used to develop plate/shell-like structural dynamic models of insect wing-like structures useful for other aeroelastic computations in this work. But for the results that follow in this section, only the UM/NLABS-based framework is used for the detailed analysis of this wing configuration.

5.1.6 Correlations between "Rigid" and "Flexible-1" Wing Computations With Experiment

For the case of chord Reynolds number $3x10^4$ and reduced frequency of 1.82, the thrust coefficient response of both the "Rigid" and "Flexible-1" wings in pure plunge is shown in Figs. 5.15 and 5.16. The experimental data of Heathcote *et al.* [41] is also included

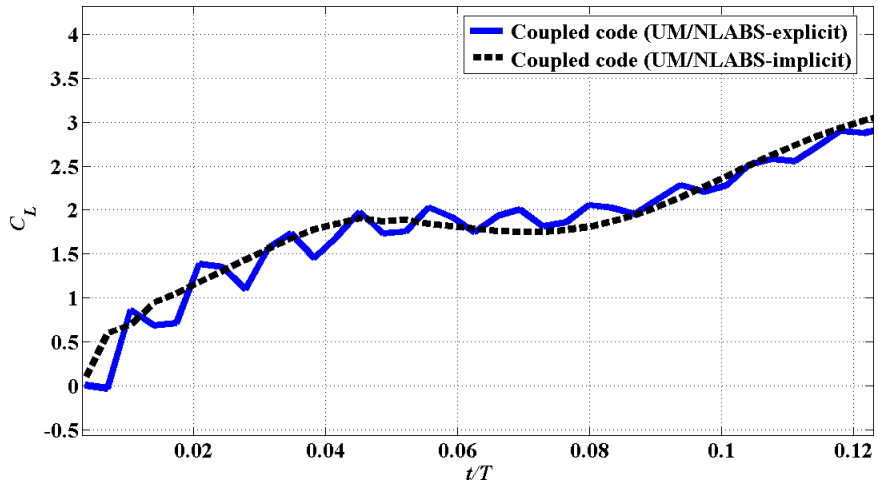

Figure 5.11: Lift coefficient response of the "Flexible-1" wing for reduced frequency of 1.74: explicit and implicit coupling methods in UM/NLABS (zoomed view highlighting high frequency oscillations).

for comparison in both the figures. The computational response correlates well with that of the experiment. It may be noted that the results presented in this subsection and all others related to the rectangular wing case are those obtained from the coupled code involving UM/NLABS. So, the word "Computation" in the plot legends refers to the coupled code involving UM/NLABS unless otherwise stated. Furthermore, only in this subsection, the word "rigid" in any of the plots refers to the "Rigid" configuration and "flexible" refers to "Flexible-1" one. As found in the experiment, the frequency of the thrust coefficient response is twice that of the plunge frequency as the maximum thrust occurs twice in a period as the wing passes through the neutral (zero) position (points B and D of Fig. 5.3). There are, however, missing parts of the troughs corresponding to the "Rigid" wing at the end of downstroke (point C of Fig. 5.3) and both the troughs and the peaks corresponding to the "Flexible-1" wing at points B and C. Figs. 5.15 and 5.16 also show that the thrust coefficient of the "Flexible-1" wing is greater than that of the "Rigid" wing. This indicates

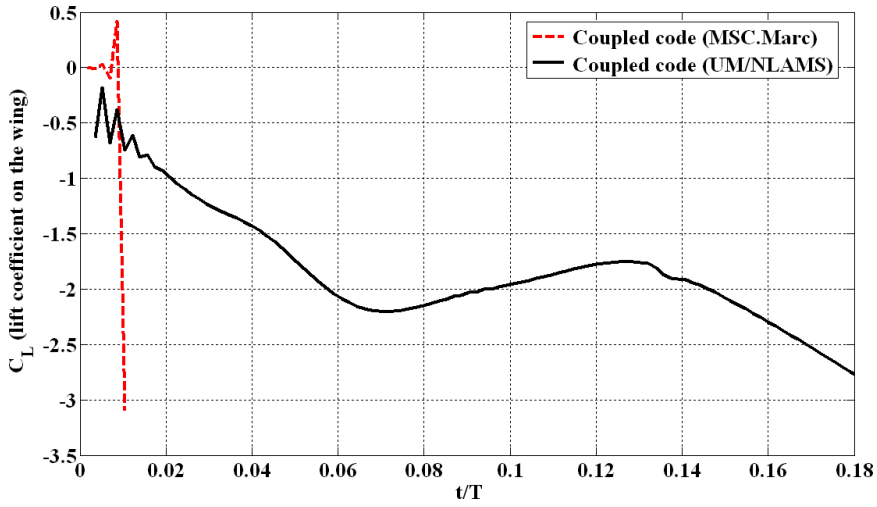

Figure 5.12: Lift coefficient response of the "Flexible-2" plunging wing (the response computed with MSC.Marc is scaled by a factor of 100 for visualization purposes.

that some spanwise flexibility can have a favorable impact on the thrust response. It is worth noticing, however, that this result is not monotonic. As will be shown later in this section, the thrust generated in the "Flexible-3" plunging wing case is reduced when compared to the "Rigid" case due to a larger spanwise flexibility of the wing ($\Pi_1 = 42.2$, which is approximately 1/5 th of the value for the "Flexible-1" wing). Although different in many ways, Ref. [106] also attempts to study the effect of wing flexibility on the thrust generation. Similar result was numerically obtained for a wing with $\Pi_1 = 57.2$. Simulations were done for both plunge and combined pitch/plunge in water. The author observed from the numerical simulation that the thrust loss is associated with a decrease in heave amplitude along the span of the wing when compared to the prescribed motion.

To assess the dependence of thrust production on the reduced frequency of oscillation, a parametric study was conducted on both the "Rigid" and "Flexible-1" wings. Figs. 5.17, 5.18, and 5.19 show the computational results and their comparison with the experiment,

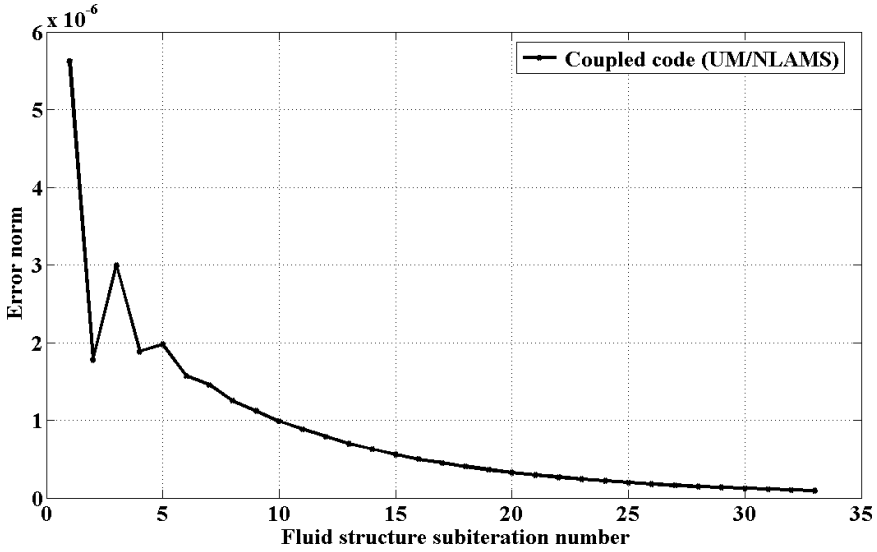

Figure 5.13: Aeroelastic convergence within the first coupled time step for the "Flexible-2" wing computed in UM/NLAMS.

showing good correlation between them. As shown from the experiment, the thrust coefficient response increases gradually at low reduced frequencies and more rapidly at higher reduced frequencies. This trend is captured well by the model. It may be noted here that time-steps of 6x10^{-3} (2x10^{-3} s) and 15x10^{-3} (5x10^{-3} s) were used for the "Rigid" and the "Flexible-1" wing simulations, respectively. Fig. 5.20 shows the elastic tip displacement response as a function of reduced frequency for the "Flexible-1" wing. As seen in the figure, the amplitude of deformation increases with the oscillation frequency in a similar fashion as the thrust coefficient. While the overall agreement between the computation and the experiment is good, it is much better at lower frequencies than at the higher ones.

Trailing-edge vortical structures from both the computation and the experiment are shown in Fig. 5.21 at two selected time instants (A and B of Fig. 5.3) for the "Rigid" and "Flexible-1 (E= 210 GPa)" wing cases. In the figure, the individual subfigures are identi-

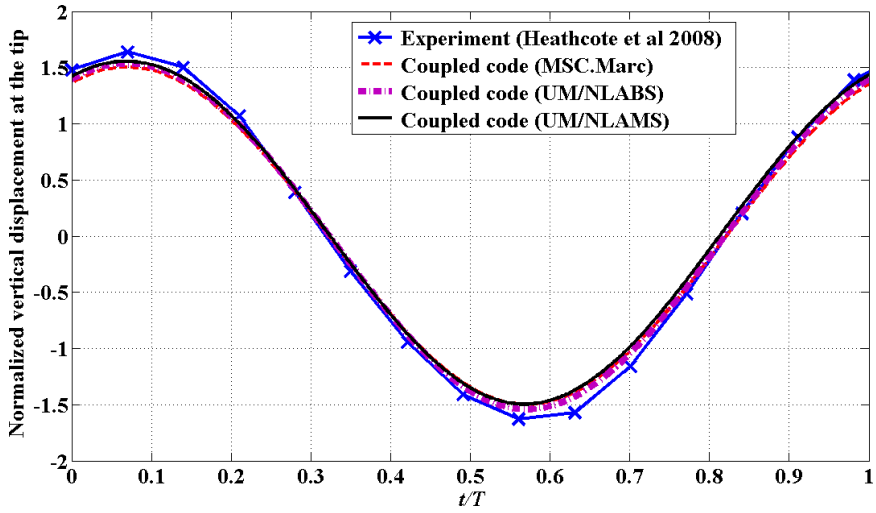

Figure 5.14: "Flexible-1" wing tip displacement response as computed in the coupled codes involving UM/NLAMS, UM/NLABS, and MSC.Marc along with experimental data of Heathcote *et al* [41] (displacement is normalized with respect to amplitude of plunge).

fied by either α or β and hyphenated by a number. The computed tailing-edge normalized vorticity contours at both time instants show an overall qualitatively good agreement with the experimental data in terms of location and rotational direction. As to the strength of the vorticity, it is weaker in the computation than in the experiment. Moreover, some small scale vortices are not captured in the computed vortical structures.

5.1.7 Correlations between "Flexible-2" and "Flexible-3" Wing Computations With Experiment

Data corresponding to vertical displacement at the wing tip from the computation for "Rigid", "Flexible-1 (E=210 GPa)", "Flexible-2 (E= 70 GPa)", and "Flexible-3 (E=40 GPa)" wing cases and the experiment for "Inflexible", "Flexible", and "Highly flexible" are shown over one plunge cycle in Fig. 5.22. As before, the displacement is normalized

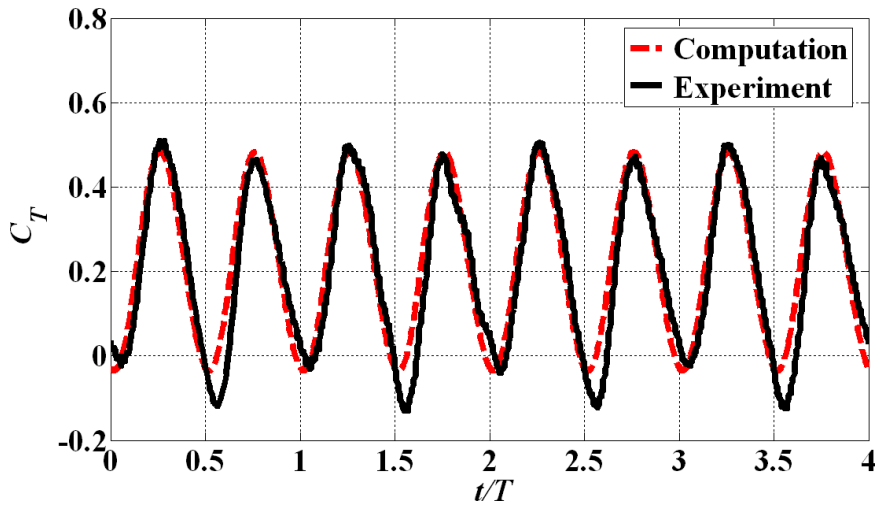

Figure 5.15: Time history of thrust coefficient for the "Rigid" plunging wing.

with respect to the amplitude of prescribed wing motion. In the "Rigid" and "Flexible-1 (E= 210 GPa)" wing cases (Rigid (COMP) and Flexible-1 (COMP, E=210 GPa) in Fig. 5.22), the computed displacement response shows good agreement with the experiment data (Inflexible (EXP) and Flexible (EXP) in Fig. 5.22) both qualitatively and quantitatively as was already shown in the previous subsection. However, in the case of "Flexible-2 (COMP, E=70 GPa)" wing, both the amplitude and the phase lag at the tip are different from those of the experimental data (Highly flexible (EXP) in Fig. 5.22). Interestingly, the response in the case of the "Flexible-3 (COMP, E=40 GPa)" wing has a much better match with the experiment. The time histories of thrust and lift coefficients for only the "Flexible-2 (E=70 GPa)", "Flexible-3 (E=40 GPa)", and "Highly flexible (EXP)" wing cases are presented in Fig. 5.23. Again, just like in the case of the tip displacement, the time responses of aerodynamic force coefficients in the "Flexible-3 (E= 40 GPa)" wing case show a closer agreement with the experimental data ("Highly flexible") than those of the "Flexible-2 (E=70 GPa)" wing case. Also, it is interesting to see that the thrust coefficient

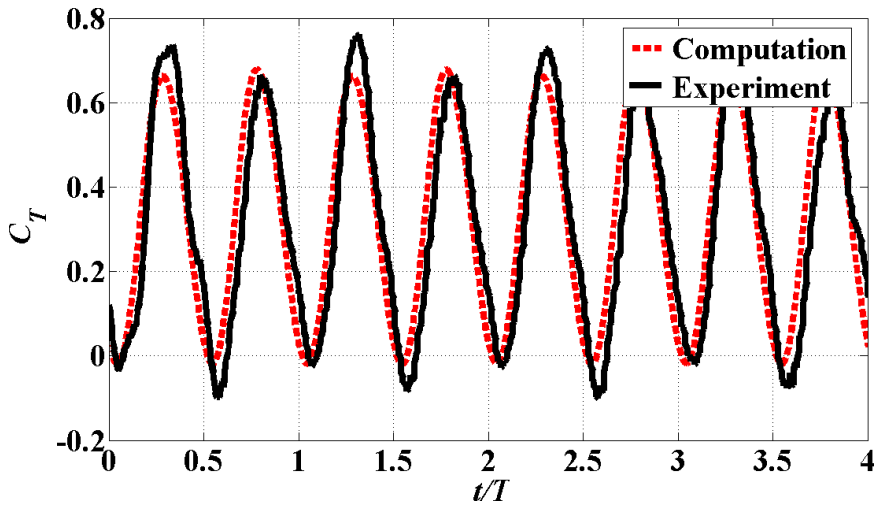

Figure 5.16: Time history of thrust coefficient for the "Flexible-1" plunging wing.

in the case of the experiment presents higher frequency content in it which is not present in the computational response. From the above, it is clear that the 43% drop in Young's modulus (from E=70 GPa to E=40 GPa) of "Flexible-2 (E=70 GPa)" case was found to provide the correct amount of equivalent flexibility encountered in the experimental results.

Trailing-edge vortical structures from both the computation and the experiment are shown in Fig. 5.24 at two selected time instants (A and B of Fig. 5.3) for the "Flexible-2 (E=70 GPa)" and "Flexible-3 (E=40 GPa)" wing cases. In the "Flexible-2 (E=70 GPa)" wing case, at the beginning of downstroke (t/T=0), the size of computed trailing-edge vortical structures is slightly larger than those of the experiment ((α-1, α-2) and (β-1, β-2) in Fig. 5.24a). Furthermore, the vorticity magnitude in the computation is weaker and is less fragmented than in the case of the experiment. In the "Flexible-3 (E= 40 GPa)" wing case, at the beginning of downstroke, the computed trailing-edge vortical structures show a much better agreement with those of the experiments ((α-1, α-2) and (β-1, β-2) in Fig.

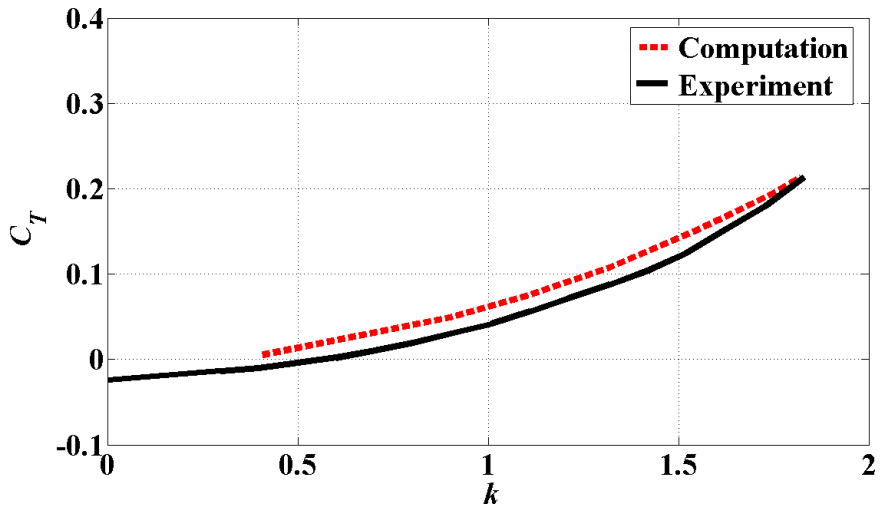

Figure 5.17: Thrust coefficient as a function of reduced frequency for the "Rigid" plunging wing.

5.24b) both qualitatively and quantitatively. Similar trends were observed even at the middle of downstroke (t/T = 0.25) which corresponds to the maximum plunging velocity of the wing root. At this time instant, in the computed results of the "Flexible-2 (E= 70 GPa)" wing case, a counter-clockwise vortex is seen near the trailing-edge ((α-3) and (α-4) in 5.24a) at both mid-span and tip stations. However, in the case of the experiment (β-3) and (β-4) in both Figs. 5.24a and 5.24b, the vortex is counter-clockwise only at the mid-span station and and is clockwise at the tip. Such a trend is observed in the "Flexible-3 (E= 40 GPa)" wing case as shown in (α-4) and (β-4) in Fig. 5.24b. Overall, there is a good qualitative correlation of the vortical structures with the experimental data barring the fact that the computed vorticity is weaker in all of the cases. Importantly, the correlations of the "Flexible-3 (E= 40 GPa)" wing case with the experiment are much better than those of "Flexible-2 (E=70 GPa)" case.

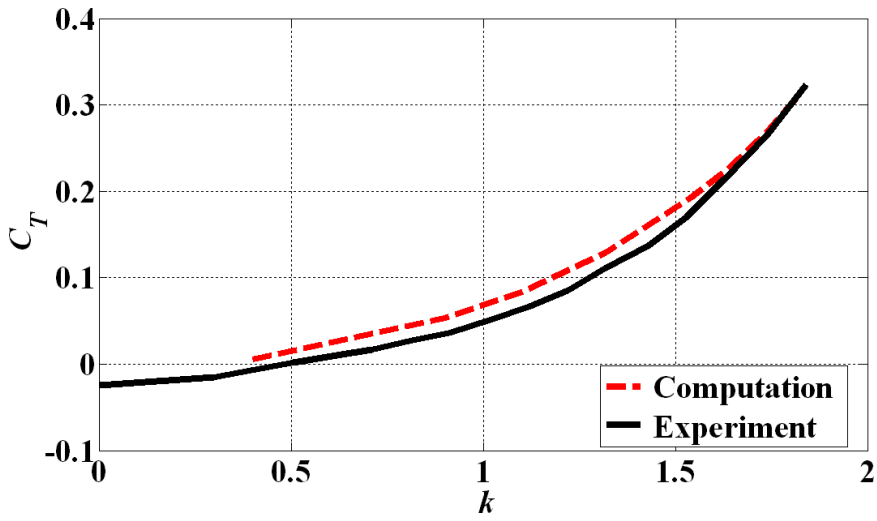

Figure 5.18: Thrust coefficient as a function of reduced frequency for the "Flexible-1" plunging wing.

5.1.8 Effect of Structural Flexibility on Aerodynamics - Flow Structures

To better understand the implications of wing flexibility on the aerodynamics, detailed flow structure and pressure distributions need to be investigated. Results are shown for selected wing span locations and representative time instants for all wing configurations. The "Rigid" and "Flexible-1" cases are discussed first followed by a discussion of the "Flexible-2" and "Flexible-3" ones.

In Fig. 5.25, streamlines (as viewed from the reference frame moving with the prescribed motion) and pressure contours around the airfoil at 50% semi-span location are plotted for both "Rigid" and "Flexible-1" wings at four different time instants (A, B, C, and D of Fig. 5.3) within a stroke period T. It may be observed from the figure that the streamlines in the case of the flexible wing hit the wing surface because the reference frame with respect to which they were plotted does not take into account the surface speed due to

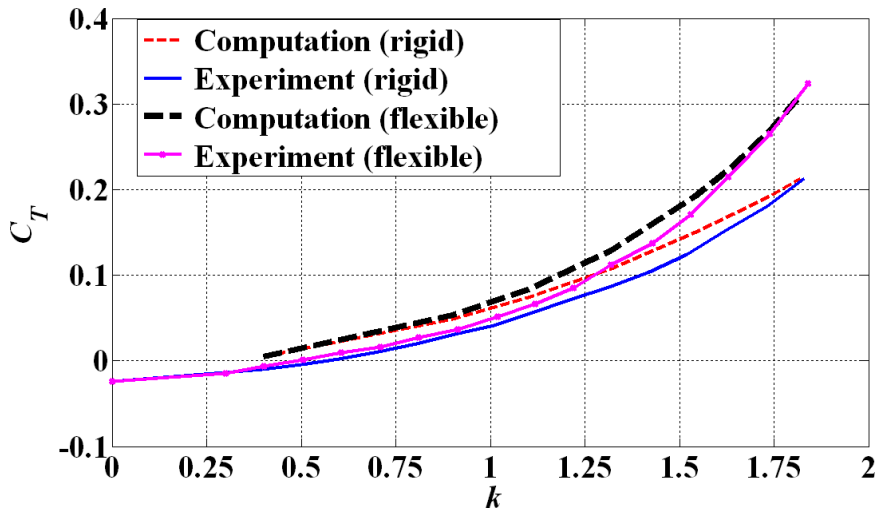

Figure 5.19: Thrust coefficient as a function of reduced frequency for both "Rigid" and "Flexible-1" plunging wings together.

deformation. The following features can be observed:

1. At point A (t = 0), i.e., at the beginning of the downstroke, in the case of the "Rigid" wing, a strong vortex is seen on the bottom surface close to the leading edge and a weaker one on the top surface near the mid-chord. Whereas in the case of the "Flexible-1" wing, no vortex is seen on the top surface and the one on the bottom surface is stronger than its counterpart on the "Rigid" wing.

2. At point B (t = T/4), i.e., at the middle of the down-stroke, in both "Rigid" and "Flexible-1" wings, the vortex on the bottom surface becomes weaker and moves downstream. Furthermore, only for the "Rigid" wing, the smaller vortex on the top surface grows in size and also moves downstream towards the trailing edge. This is the point at which maximum thrust is generated in both the "Rigid" and the "Flexible-1" cases.

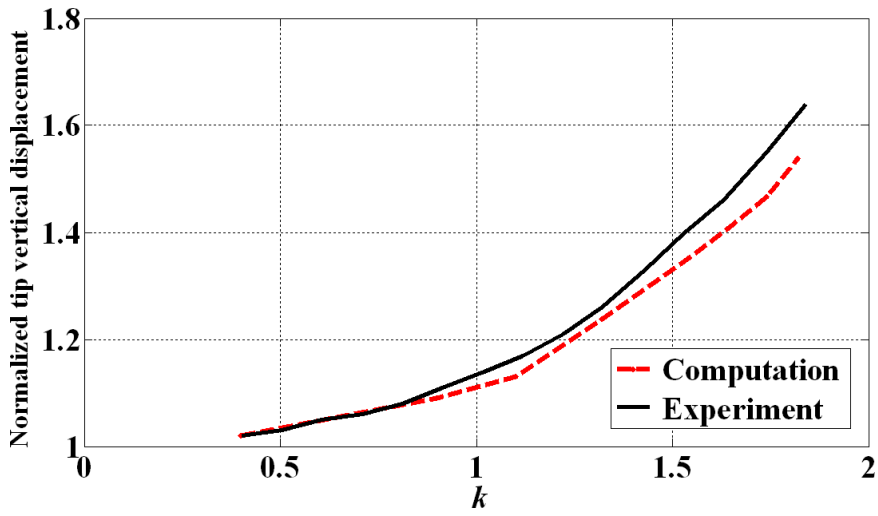

Figure 5.20: Computed and experimental tip elastic vertical displacement response normalized with respect to the amplitude of prescribed motion ("Flexible-1" wing).

3. At point C (t = T/2), i.e., at the beginning of the upstroke, in the case of the "Rigid" wing, a large vortical structure is now seen on the top surface closer to the leading edge and a smaller sized vortex on the bottom surface closer to the trailing edge. For the "Flexible-1" wing, a much stronger vortex is seen on the top surface.

4. At point D (t = 3T/4), in the case of the "Rigid" wing, both the vortices seen at time T/2 become weaker and move towards the trailing edge. The one on the top surface moves downstream much less than the one on the bottom. Whereas in the "Flexible-1" wing case, the weakening of the vortex is seen but it does not convect downstream as much as its counterpart on the "Rigid" wing.

Figs. 5.26 and 5.27 show the spanwise distribution of pressure contours for both top and bottom surfaces of the "Rigid" and "Flexible-1" wings corresponding to point B of Fig. 5.3. In general, most of the top surface presents suction for both cases. However,

the effect is more pronounced in the case of the "Flexible-1" wing. Leading edge suction plays a critical role in determining the level of the thrust generated [28]. While the pressure contours presented in Figs. 5.26 and 5.27 provide a global picture of the spanwise variation, in order to focus on the effect of leading edge suction and its enhancement in the case of the "Flexible-1" wing, Fig. 5.28 shows the pressure field distributions at four stations along the wing semi-span (15%, 50%, 83%, 97%) for two different time instants (points B and C of Fig. 5.3). It is seen in the figure that the effect of leading-edge suction is enhanced in the "Flexible-1" wing case (higher suction peak near the leading edge) which helps explain the increase in thrust with increase in flexibility.

The structural flexibility results in higher instantaneous effective angles of attack, which, in turn, promote larger streamline curvatures around the wing. As a consequence, from the momentum equations, streamline curvatures induce pressure gradients correspondingly. The instantaneous effective angle of attack is defined as:

$$\alpha_{inst} = tan^{-1}(-\frac{1}{U_\infty}\frac{dh(t)}{dt}) \tag{5.1}$$

where $\frac{dh(t)}{dt}$ is the wing velocity component normal to the uniform flow in the case of the "Rigid" wing and, in the case of the "Flexible-1" wing, it is the sum of that and the velocity due to elastic deformation. In order to corroborate the impact of flexibility on thrust generation, Fig. 5.29 shows the time response of the instantaneous angle of attack for both "Rigid" and "Flexible-1" wings. For the "Flexible-1" wing case, two different stations along the semi-span (50% and 97%) are considered since each station sees a different effective angle of attack due to wing bending and spanwise variation of velocities induced

due to deformation. As seen in the figure, the amplitude of the effective angle of attack in the case of the "Flexible-1" wing (for 97% semi-span station) is at least 35% higher than that of the "Rigid" wing. This reinforces the fact shown in Fig. 5.16 that there is a thrust enhancement due to wing flexibility. Also, it is important to note here that flexible wings can yield favorable performance at quite high instantaneous angles of attack (50 deg) and large streamline curvatures without stalling.

In order to discern the effects of flexibility on the flow structure further, streamlines at several stations along the semi-span for both the "Rigid" and the "Flexible-1" wings are plotted in Fig. 5.30. They are placed next to each other for comparison. These represent the wing when it is at its mean position (point B of Fig. 5.3). The left column corresponds to the "Rigid" wing and the right to the "Flexible-1" one. Each row in the figure corresponds to a location along the semi-span.

From these results, the following observations can be made:

- For the "Rigid" wing, a smaller separation bubble is observed on the top surface near the inboard region of the wing and closer to the wing trailing edge in addition to a bigger one on the bottom surface closer to the leading edge. The smaller bubble is not seen on the "Flexible-1" wing in any region.

- On the "Rigid" wing, the separation bubble exists until around 83% semi-span, whereas on the "Flexible-1" wing, it exists until 60% semi-span. In general, the size of the separation bubble in the case of the "Flexible-1" wing is smaller than its counterpart on the "Rigid" wing. This may also be observed from the "Rigid" and "Flexible-1" pressure distributions presented in Fig. 5.27.

- Streamlines are shown to be hitting the wing surface in the case of the "Flexible-1" wing (similar to Fig. 5.25). Again, this is because the reference frame with respect to which they were plotted does not take the surface speed due to deformation into account.

Finally, to gain better understanding of the impact of variation in Young's modulus (as a resulting Π_1) on the aerodynamics and also understand the difference in the aerodynamic force generation in the "Flexible-2" and "Flexible-3" cases, flow structure and pressure (Cp) distribution around the wing for those cases at t/T of 0.25 are illustrated in Fig. 5.31. The wing tip of the "Flexible-2 (E= 70 GPa)" wing case is in-phase with the root at this time instant, whereas the tip of the "Flexible-3 (E= 40 GPa)" wing case is in out-of-phase motion. Spanwise vorticity contours for both of these cases are shown in Fig. 5.31(a) (i.e., the first row) at two different stations along the semi-span ("middle" and "near the tip"). In the "Flexible-2 (E= 70 GPa)" wing case, the contours near the mid semi-span show larger sized trailing-edge vortex than that seen in the "Flexible-3 (E= 40 GPa)" wing case (compare α-1 and β-1 of Fig. 5.31(a)). A small leading-edge vortex (LEV) is observed on the lower surface whereas none is seen in the "Flexible-3 (E= 40 GPa)" wing case. At the section near the wing tip, in both the "Flexible-2 (E= 70 GPa) and Flexible-3 (E= 40 GPa)" wing cases a LEV is observed on the lower surface (α-2 and β-2 in Fig. 5.31(a)). Also, looking at Figs. 5.31(b) and (c), considerable differences may be found between the flow field velocity results of these two cases. In the normalized horizontal velocity contours of the "Flexible-2 (E= 70 GPa)" wing case (i.e., α-1 and α-2 in Fig. 5.31(b)), the area of accelerated flow is larger than those of the "Flexible-3 (E= 40 GPa)" wing case (i.e.

β-1 and β-2 in Fig. 5.31(b)) especially near the leading and trailing edges, and the flow is separated near the leading edge of the lower surface. Further, the normalized vertical velocity contours of the "Flexible-3 (E= 40 GPa)" wing case around the mid semi-span section show smaller area of induced flow than those of the "Flexible-2 (E= 70 GPa)" wing case, although, that is not the case near the wing tip. The flow features discussed so far correspond to velocity distributions on the wing surface and hence the aerodynamic force generation. Basically, the area of pressure curve of the "Flexible-2 (E= 70 GPa)" wing case is larger than that of the "Flexible-3 (E= 40 GPa)" wing case (for example, compare α-1 and β-1 in Fig. 5.31(d)). Moreover, it is clear from the flow structures discussed thus far that the acceleration and separation of flow near the leading and trailing edges are responsible for peak pressure on the wing surface (compare α-1 of Fig. 5.31(b) and α-1 of Fig. 5.31(d) for example). From the law of conservation of momentum, the magnitude of velocity contours of the "Flexible-2 (E= 70 GPa)" wing case shows that it could produce larger aerodynamic forces than in the case of the "Flexible-3 (E= 40 GPa)" wing case which supports what is shown in Fig. 5.23. This fact is reinforced further in the next sub-section.

5.1.9 Effect of Structural Flexibility on Aerodynamics - Role of Phase Lag and Effective Angle of Attack

In order to corroborate the decrease in the aerodynamic force (lift and thrust) generation in the "Flexible-3" case over the other three cases, the role of phase lag and instantaneous effective angle of attack is discussed here. Figures 5.32 and 5.33 below show the lift and thrust coefficient as a function of time for all four wing configurations. It is clear from

them that there is a non-monotonic trend in the mean aerodynamic forces as the flexibility is increased starting from the "Rigid" wing case. While the "Flexible-1" wing produces the largest aerodynamic forces, the "Flexible-3" wing produces the smallest. This is primarily due to the phase lag between the prescribed root motion and tip response which affects the effective angle of attack that a wing section sees through the span and subsequently the pressure gradients along with the leading edge suction. Figure 5.34 illustrates this fact with a plot of the effective angle of attack as a function of time at four different stations along the wing span for all four wing configurations in each case.

The plot has four sub-plots in it labeled as A, B, C, and D. Each sub-plot corresponds to the time response of the instantaneous angle of attack at a section along the span as indicated underneath, for all four wing configurations (A -"Rigid," B -"Flexible-1," C - "Flexible-2," and D - "Flexible-3"). It can be deduced from these figures that:

- The angle of attack variation of the rigid wing (shown in bold black) is obviously identical in all four sub-plots due to the absence of elastic deformation.
- The amplitude of angle of attack in the case of the "Flexible-1" wing is generally larger than that of the other three wings at all sections except the one at the tip.
- The amplitude of angle of attack in the case of the " Flexible-3" wing is smaller at all sections.

The trends discussed above have been observed to be generally applicable to other sections along the wings too. Even though the angle of attack in the "Flexible-1" wing is lower than that in the "Flexible-2" and "Flexible-3" wings at the tip section, it is not the case at

other sections. Since it is the cumulative effect of the angle of attack seen by the flow at all sections through the span that is important in total force generation on the wing, the forces in the "Flexible-1" case are still the largest. In a similar manner, the decrease in the angle of attack in the case of the "Flexible-3" wing (at several sections through the wing) over that of the others led to a decrease in the leading edge suction which in turn caused a loss of total thrust and of course total lift on the wing too. Sample pressure contours for all four wing configurations at mid-span at t/T = 0.25 are shown in Fig. 5.35. The dominance of leading edge suction in the "Flexible-1" case and the reduction of it in the "Flexible-3" case are clearly seen in the figure.

Figure 5.36 is a plot of the instantaneous angle of attack along the span position at the time instant corresponding to the maximum thrust position for all four wing configurations which illustrates the diminishment of thrust in "Flexible-3" wing further. As seen from the plot, clearly, the area under the "Flexible-1" curve is the largest and the one under the "Flexible-3", the smallest.

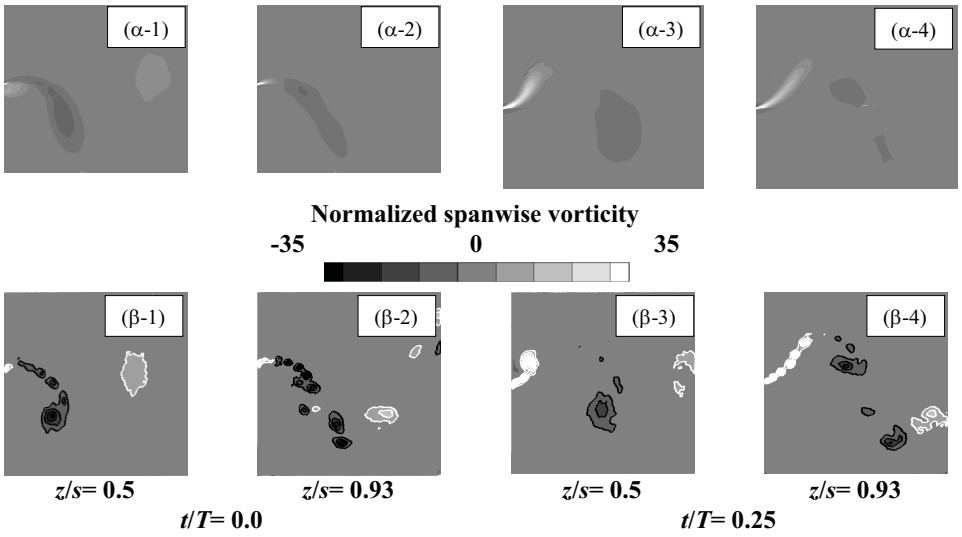

(a) Rigid, Upper: COMP, Lower: EXP (*Inflexible*)

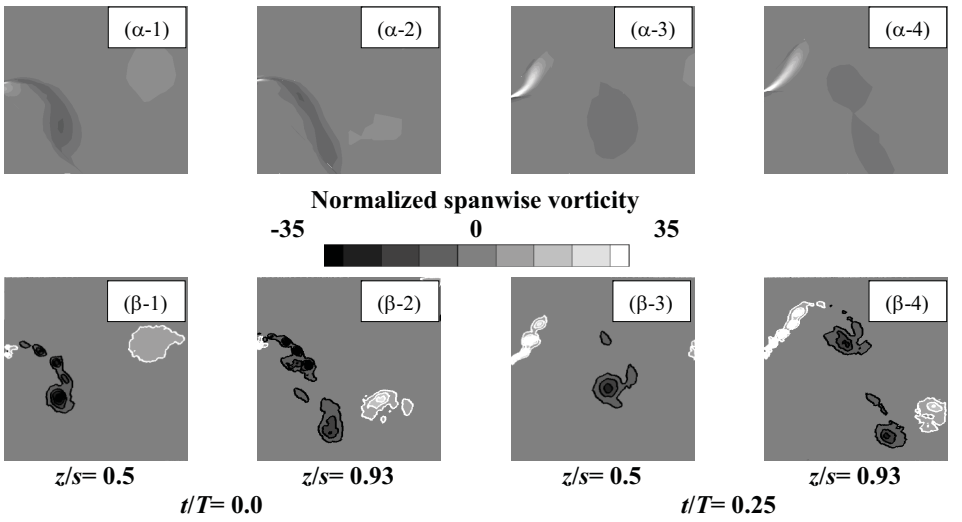

(b) Flexible-1, Upper: COMP (*E*= 210 GPa), Lower: EXP (*Flexible*)

Figure 5.21: Spanwise vortical structures beyond the trailing-edge at selected time instants [5]. (a) Rigid; (b) Flexible-1 (E= 210 GPa). Note that spanwise vorticity is normalized by a factor of c/U_∞ where U_∞ is freestream velocity and c is wing chord. Counter-clockwise (from the viewpoint of an observer looking into the plot) vorticity is shown light and clockwise vorticity is shown dark.

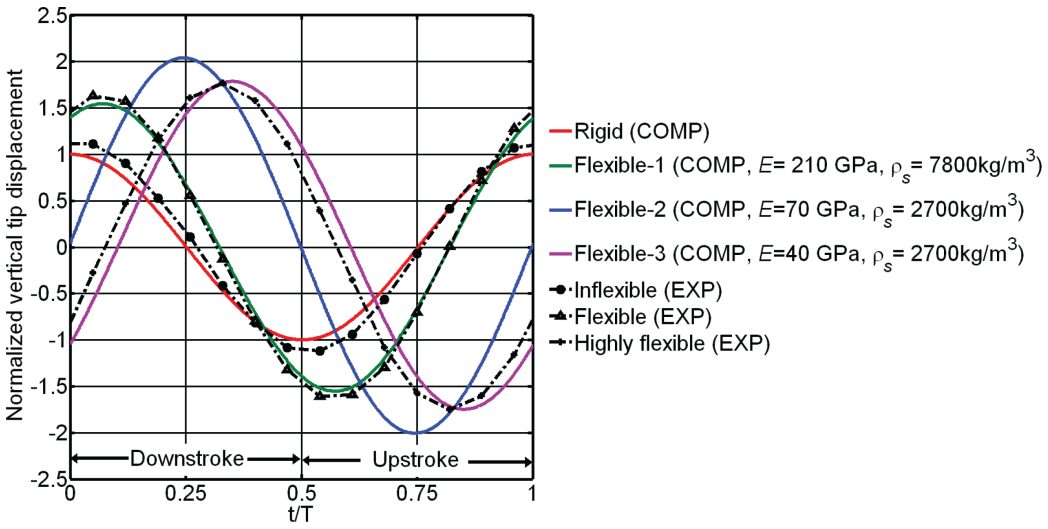

Figure 5.22: Comparison of experimental and computational results for vertical displacement at the tip for four variations of spanwise flexibility over one cycle of plunge [5] (displacement is normalized with respect to amplitude of plunge).

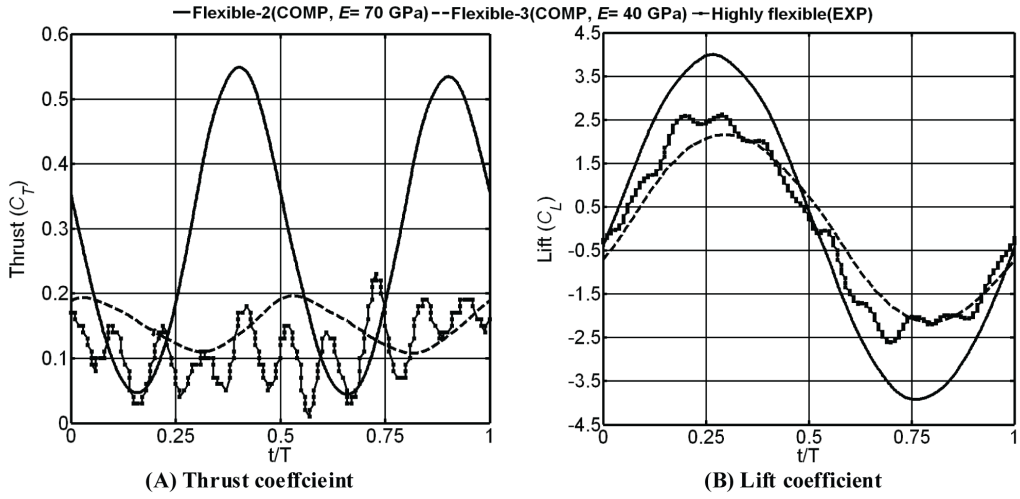

Figure 5.23: Effect of structural flexibility on instantaneous aerodynamic force generation [5]. (A) Thrust; (B) Lift.

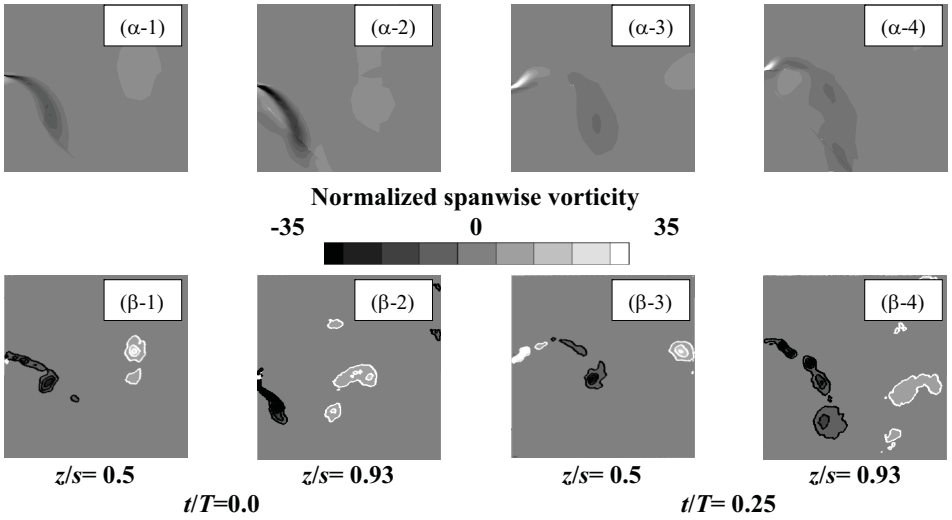

(a) Flexible-2, Upper: COMP (*E*= 70 GPa), Lower: EXP (*Highly Flexible*)

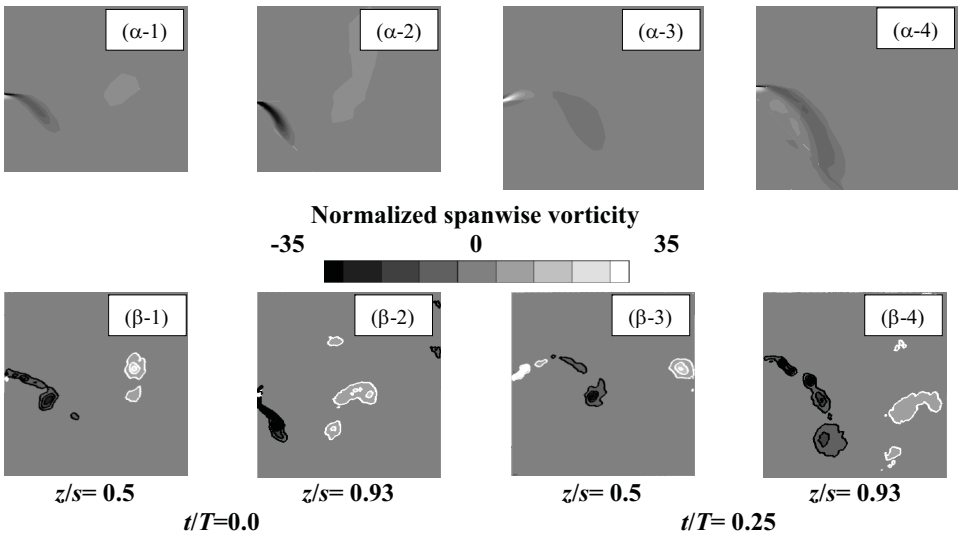

(b) Flexible-3, Upper: COMP (*E*= 40 GPa), Lower: EXP (*Highly Flexible*)

Figure 5.24: Spanwise vortical structures beyond the trailing-edge at selected time instants [5]. (a) Flexible-2 (E= 70 GPa); (b) Flexible-3 (E= 40 GPa). Note that spanwise vorticity is normalized by a factor of c/U_∞ where U_∞ is freestream velocity and c is wing chord. Counter-clockwise (from the viewpoint of an observer looking into the plot) vorticity is shown light and clockwise vorticity is shown dark.

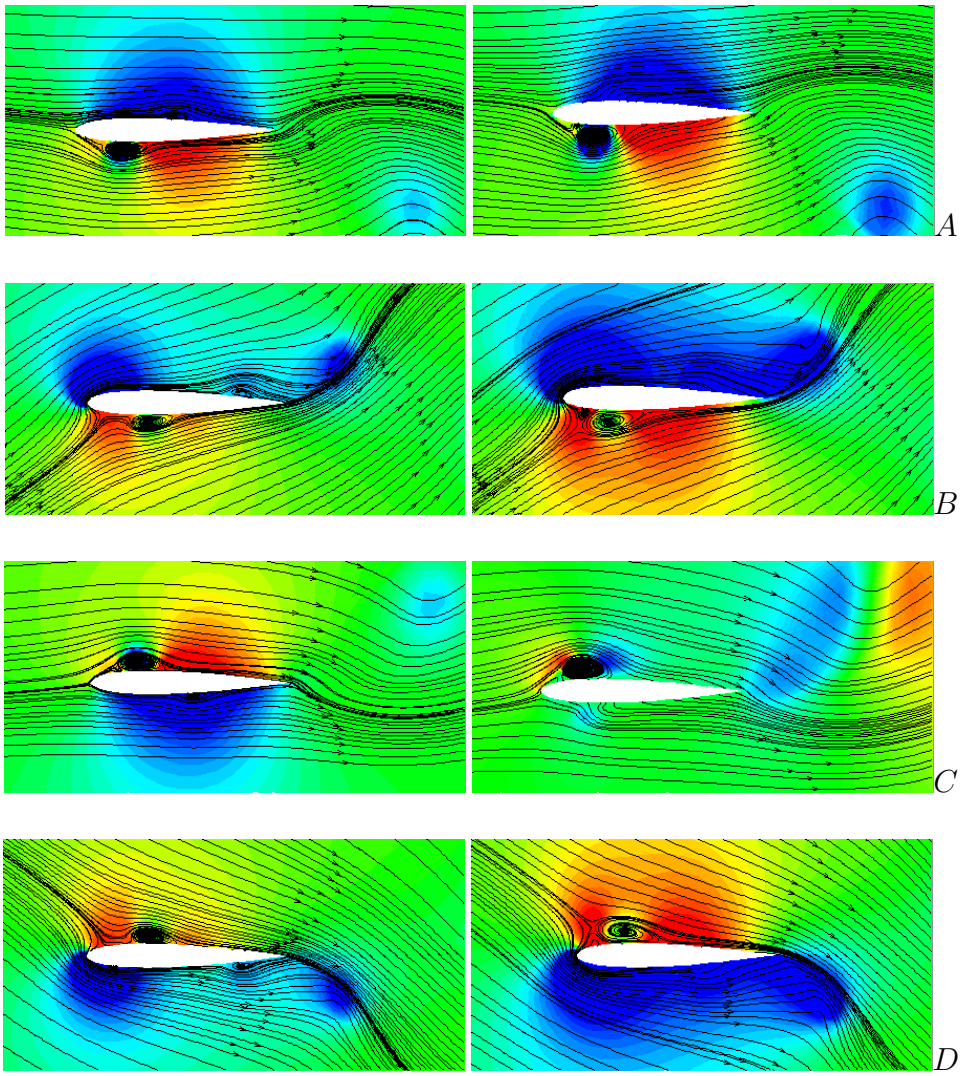

Figure 5.25: Pressure contours and streamlines at four different time instants in a stroke period around the airfoil at 50% semi-span section (as viewed from the reference frame moving with prescribed motion) (left) “Rigid”; (right) “Flexible-1” [20]

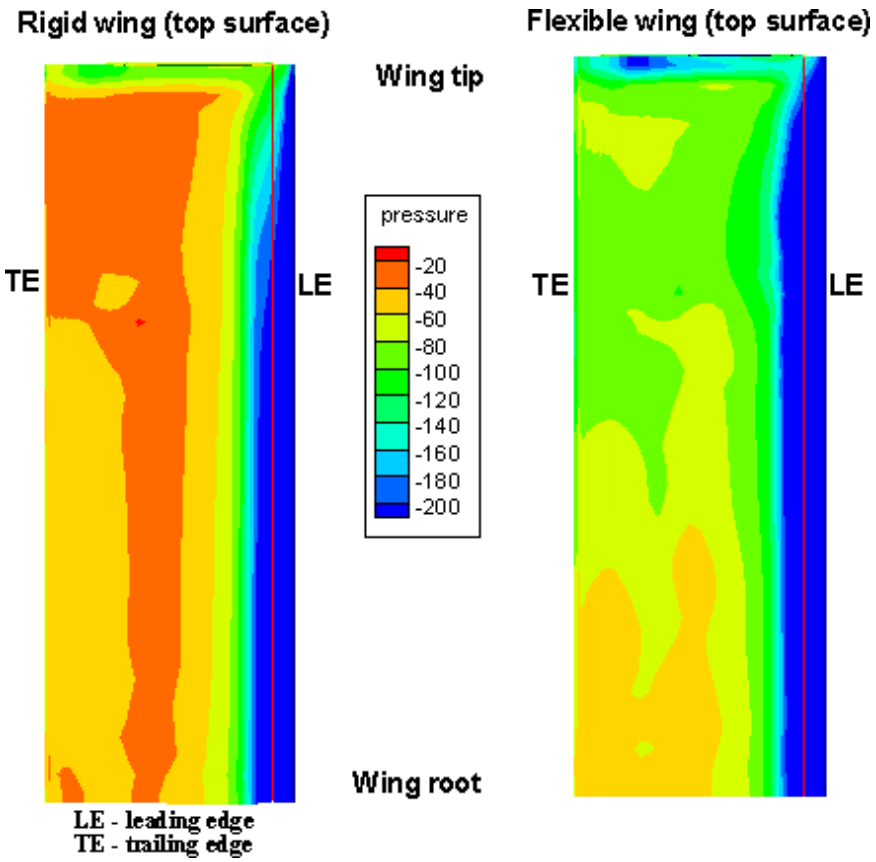

Figure 5.26: Pressure distribution on the "Rigid" and "Flexible-1" wings at point B of Fig. 5.3: top surface.

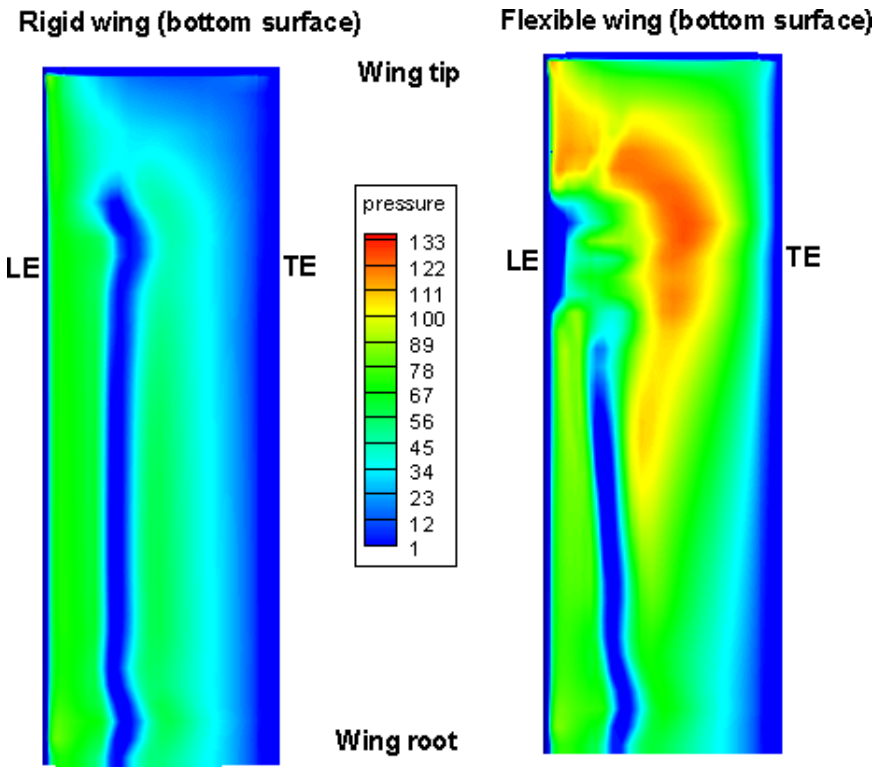

Figure 5.27: Pressure distribution on the "Rigid" and "Flexible-1" wings at point B of Fig. 5.3: bottom surface.

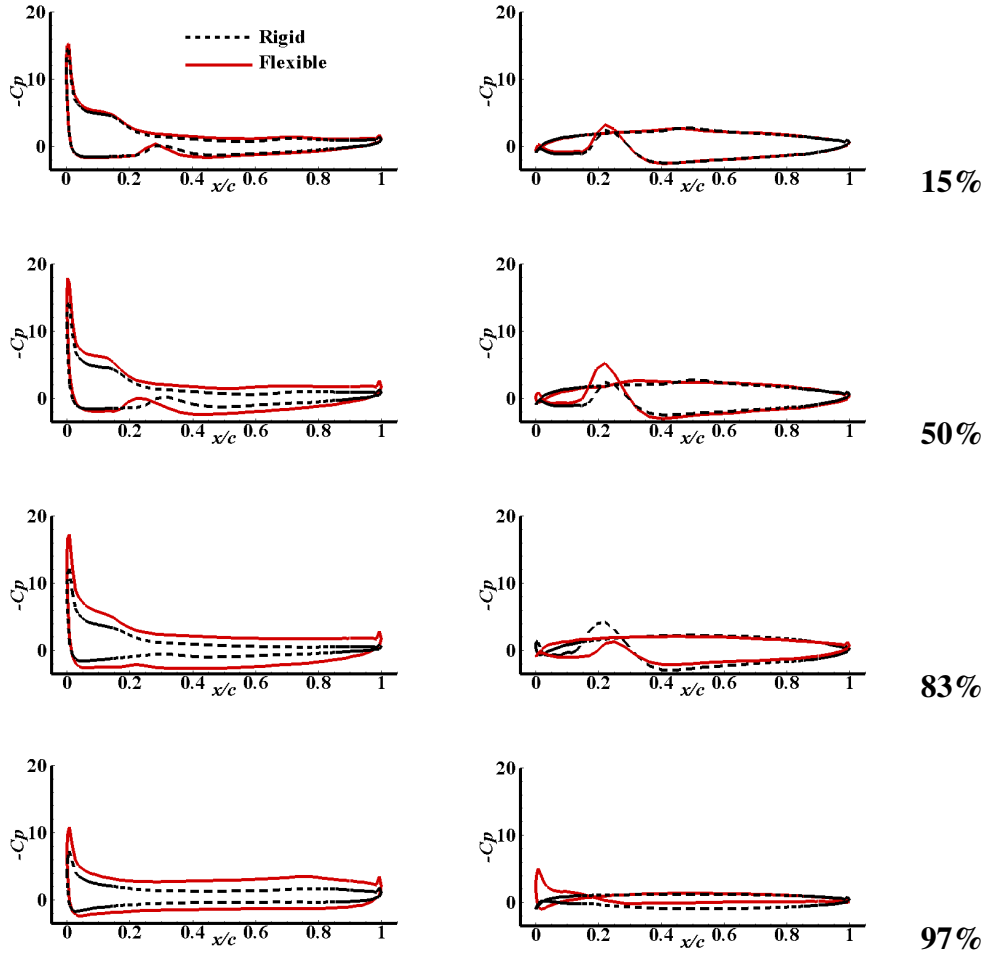

Figure 5.28: Pressure field distribution at several stations along the wing semi-span (for time instants corresponding to B and C of Fig. 5.3) for "Rigid" and "Flexible-1" wings

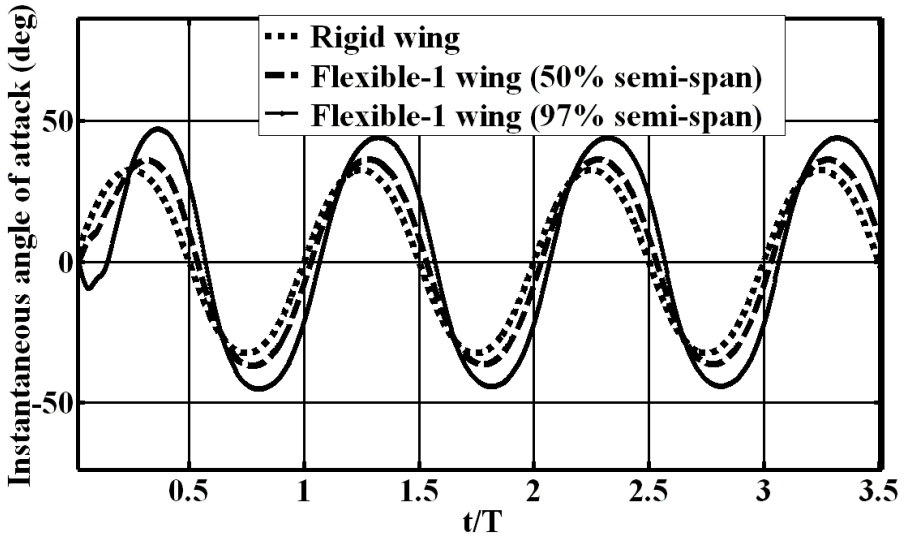

Figure 5.29: Time response of the instantaneous angle of attack for the plunging wing ("Rigid" and "Flexible-1").

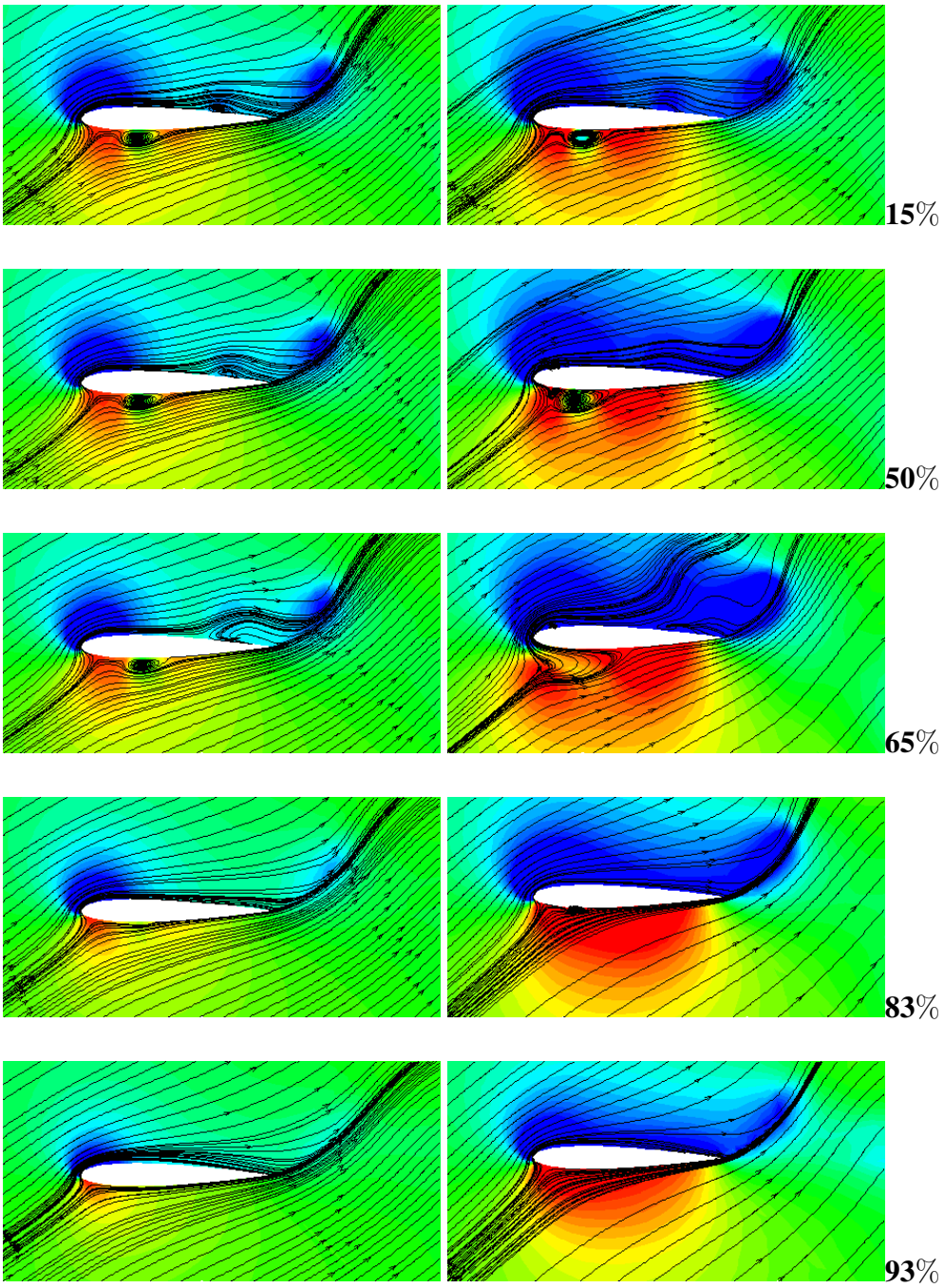

Figure 5.30: Pressure contours and streamlines on the wing at time instant B of Fig. 5.3 through the semi-span (as viewed from the reference frame moving with prescribed motion) (left -"Rigid" and right - "Flexible-1").

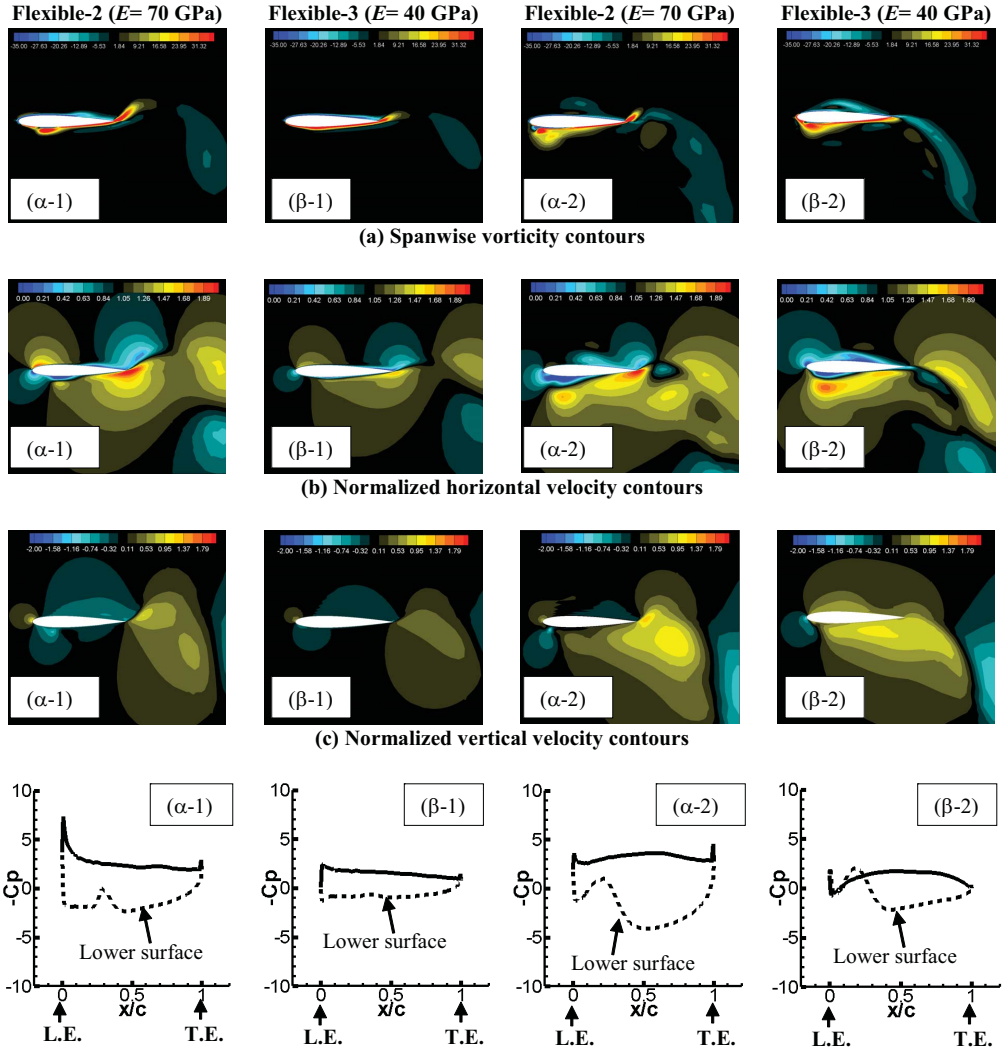

Figure 5.31: Comparison of computed vorticity, flow velocity, and pressure distribution results at *t/T*=0.25 between the "Flexible-2 (E=40 GPa)" and "Flexible-3 (E=70 GPa)" wing cases [5]. Note that vorticity is normalized by a factor of c/U_∞ where U_∞ is freestream velocity and c is wing chord. (a) Normalized spanwise vorticity contours; (b) Normalized horizontal velocity contours (with respect to U_∞); (c) Normalized vertical velocity contours (with respect to U_∞); (d) Pressure coefficient distributions.

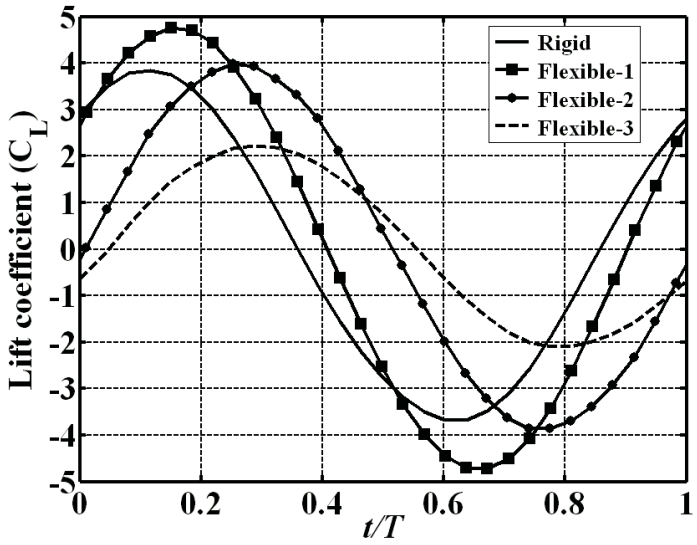

Figure 5.32: Lift coefficient on the wing as a function of normalized time for all four plunging wing configurations

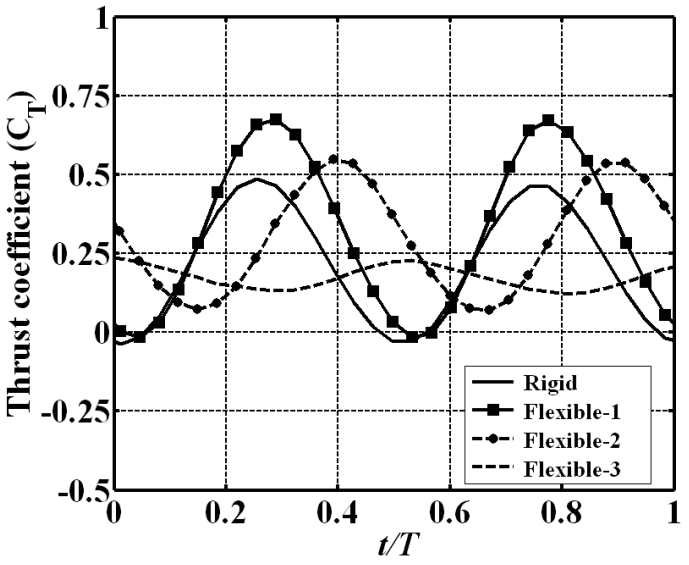

Figure 5.33: Thrust coefficient on the wing as a function of normalized time for all four plunging wing configurations

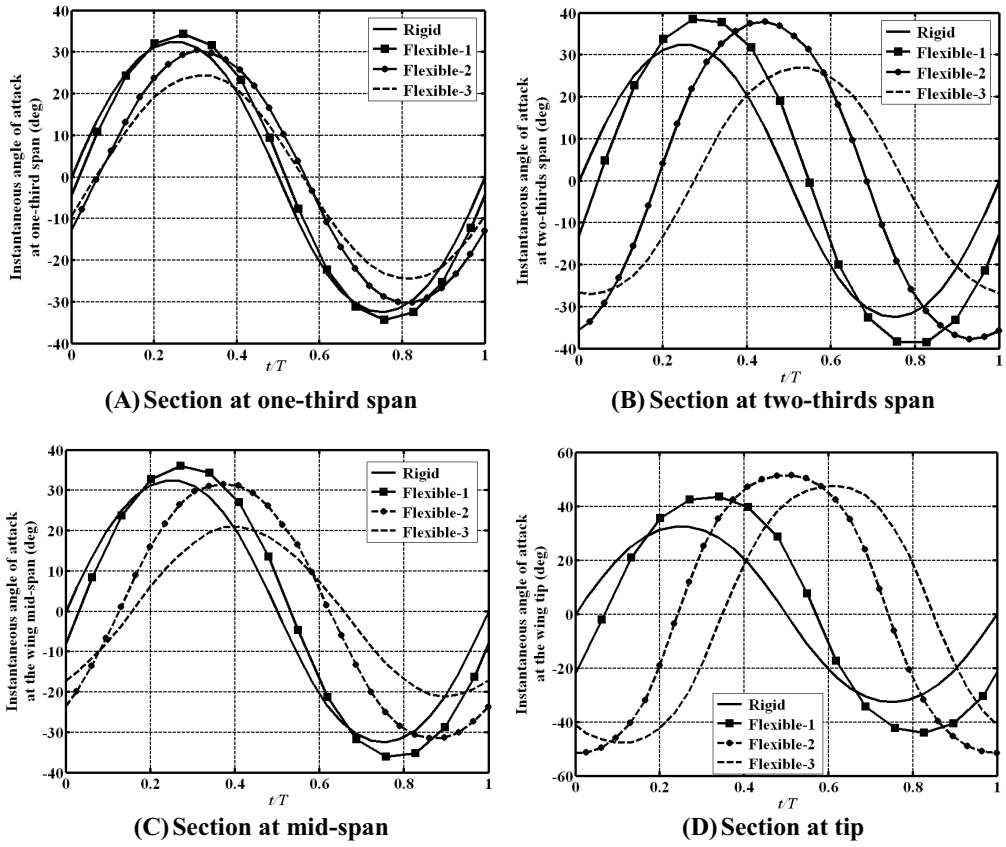

Figure 5.34: Effective/Instantaneous angle of attack as a function of time at four different sections along the wing span for all four flexible plunging wing configurations

Figure 5.37 shows a plot of the thrust coefficient as a function of the non-dimensional parameter Π_1 (first of Eq. 2.99) in the "Rigid", "Flexible-2", and "Flexible-3" cases. It should be noted that the other non-dimensional parameter ρ^* (second of Eq. 2.99) is fixed in both the flexible wing computations. The data corresponding to the wing "Flexible-1" is not shown in the plot since ρ^* is different in its case than in the other two configurations. A non-monotonic trend in the thrust production is clearly seen in the figure.

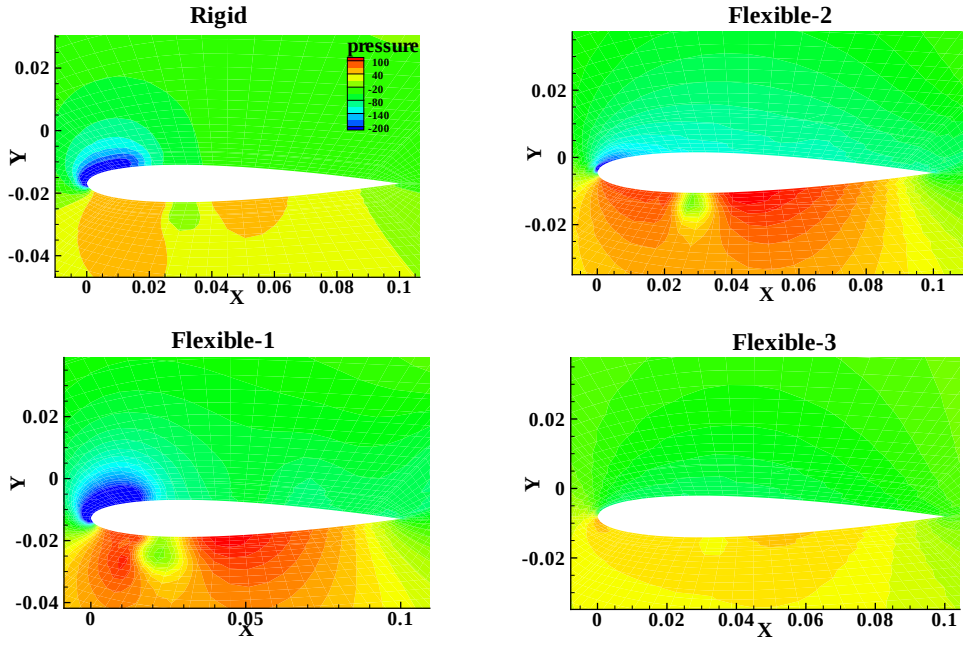

Figure 5.35: Pressure contours at mid-span at t/T = 0.25 for all four plunging wing configurations

5.2 An Elliptic Wing (Zimmerman planform) Prescribed With Pure Single Degree-of-Freedom Flap Rotation

5.2.1 Description of the Test Case

Experimental studies have been conducted on an aluminium wing of the Zimmerman planform (Fig. 5.38) at the University of Florida to support the validation efforts of the aeroelastic solutions in this work. Single degree-of-freedom large amplitude sinusoidal flap rotation (+/- 21 deg) about an axis through the chord was prescribed to the wing at the root. Full details of the experimental setup are given in Ref. [103]. Results obtained in the experiment include wing tip deformation as a function of time and phase averaged flow velocities from PIV measurements at selected stations along the chord. Computational

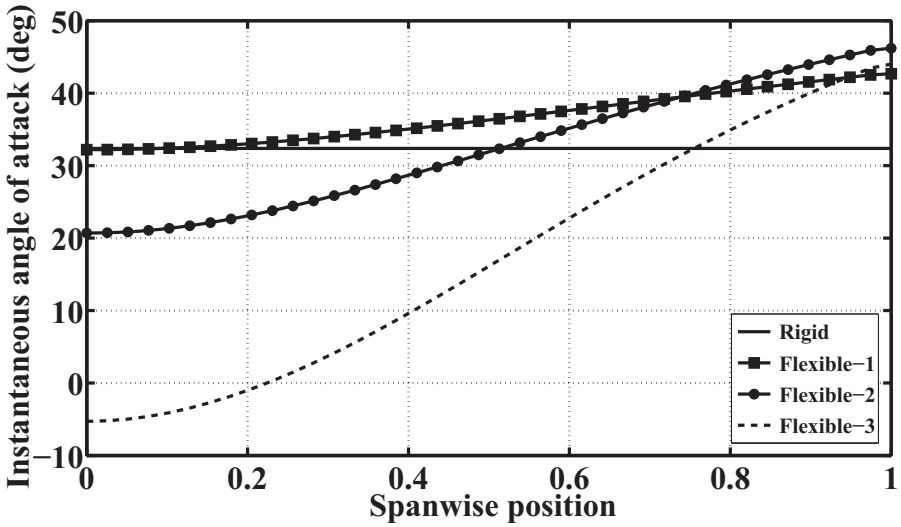

Figure 5.36: Instantaneous angle of attack along the wing span at the first thrust peak position corresponding to all four flexible plunging wing configurations (Rigid: t/T = 0.25, Flexible-1: t/T = 0.28, Flexible-2: t/T = 0.40, Flexible - 3: t/T = 0.53)

analysis of this wing configuration and correlation with experimental data were performed as part of this dissertation. A summary of the geometric and mechanical properties of this baseline configuration are included in Table 5.4. Table 5.5 provides information about the flow properties (dimensional). In Table 5.6, the key dimensionless parameters related to either the structure, the flow, or to both for the baseline Aluminium wing configuration are furnished.

Considering this as the baseline case, a series of hypothetical wing configurations were numerically studied to better understand the impact of flexibility on aerodynamics. They were chosen by keeping all parameters corresponding to the baseline aluminium flapping wing case in Table 5.4 fixed and only varying the flapping amplitude and the Young's modulus (effectively varying Π_1). The former is set to 5 deg and for the latter, five different

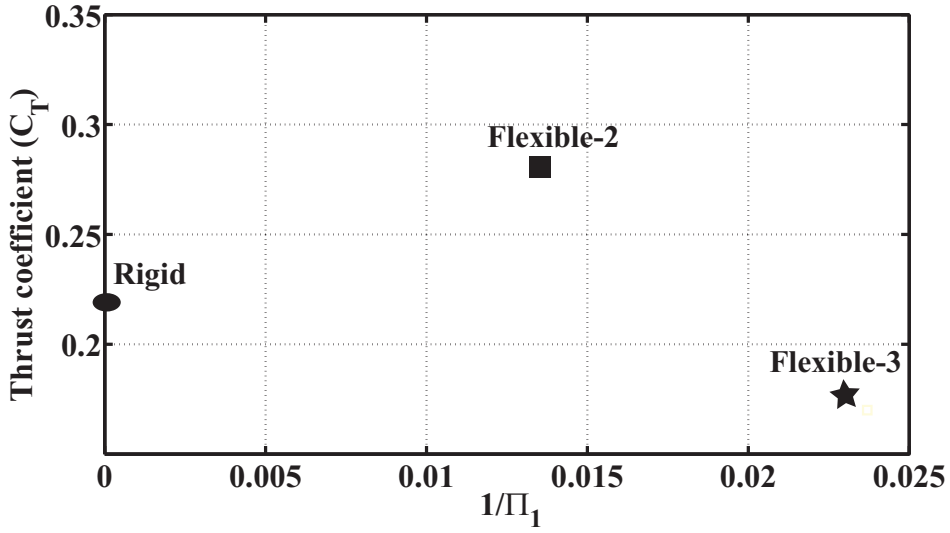

Figure 5.37: Mean thrust coefficient as a function of the inverse of non-dimensional parameter Π_1 for the plunging wing configurations. Density ratio ρ^* = 2.7 in both "Flexible-2" and "Flexible-3" cases.).

variations are considered (0.1 GPa, 10 GPa, 30 GPa, 50 GPa, 70 GPa) apart from the rigid one. For these configurations, the parameter Π_1 varies between 938 (E = 0.1 GPa) and 6.6x10^5 (E = 70 GPa). Table 5.7 shows the dimensionless parameters corresponding to the hypothetical flapping wing configurations.

Table 5.4: Geometric and mechanical properties of the Zimmerman aluminium flapping wing configuration

semi-span at quarter chord [m]	0.075
chord length at the root [m]	0.025
mean chord length [m]	0.0196
Poisson's ratio	0.3
structural thickness [m]	0.4x10^{-3}
material density [kg/m^3]	2700
Young's modulus [GPa]	70

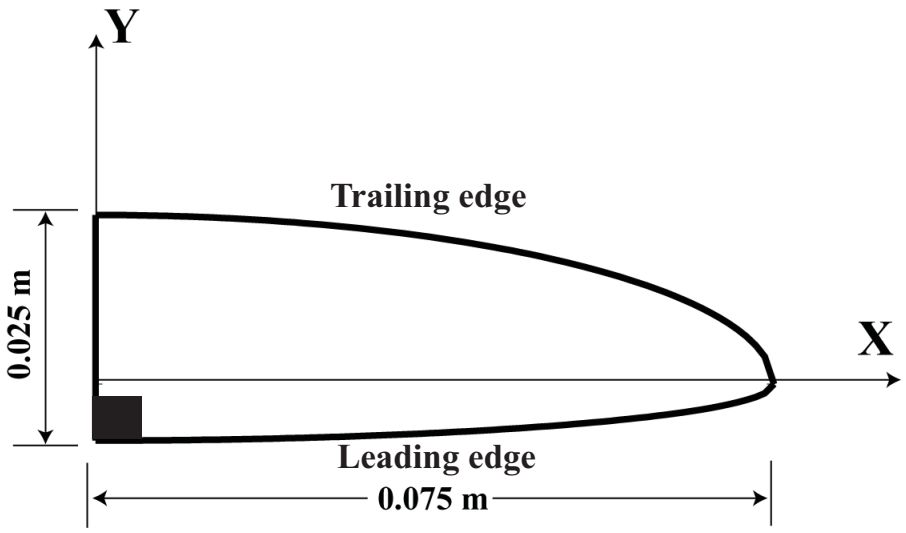

Figure 5.38: Zimmerman wing geometry (the black square at the leading edge of the wing root is the region on the wing that is in contact with the flapping mechanism and is of dimensions 5 mm x 5 mm).

Table 5.5: Flow properties associated with the Zimmerman aluminium flapping wing configuration

flow velocity	hover (1.1 m/s)	air density	1.209 kg/m^3

5.2.2 Computational Models

A structured multi-block grid around the Zimmerman wing of aspect ratio 7.65 was used for the CFD simulations. Based on a grid sensitivity study (discussed in 5.2.3), the grid configuration has 0.7 million points. The CFD grid configuration is shown in Fig. 5.39. It has an "O-type" topology around the wing. The fluid solution is based on laminar flow assumption. The computational aeroelastic analysis of this wing configuration was done using the coupled code involving UM/NLAMS. The finite element mesh configuration developed for UM/NLAMS is shown in Fig. 5.40. A 5 mm x 5 mm square region near the

Table 5.6: Dimensionless parameters associated with Zimmerman aluminium flapping wing configuration

chord-Reynolds number: *Re*	2605
Strouhal number: *St*	1.0
reduced frequency: *k*	0.56
aspect ratio	7.65
Π_1	$38\text{x}10^3$
ρ^*	2233

Table 5.7: Dimensionless parameters associated with hypothetical Zimmerman flapping wing configurations

chord-Reynolds number: *Re*	620
Strouhal number: *St*	1.0
reduced frequency: *k*	2.35
aspect ratio	7.65
Π_1	$938 - 6.6\text{x}10^5$
ρ^*	2233

root at the leading edge was constrained in all degrees of freedom (with respect to the global frame) in the structural solver, since the flapping mechanism in the experiment was used to actuate that region on the wing. A total of 480 elements (275 nodes) were used in the finite element discretization.

5.2.3 Evaluation of Computational Parameters

To assess the independence of the numerical solution to CFD grid refinement, a grid convergence study was performed and a suitable grid was subsequently chosen. Figs. 5.41 and 5.42 show the time history of lift coefficient on the wing and normalized vertical displacement (with respect to wing span) at the tip, respectively, for three different CFD grid configurations: coarse (0.6 million points, first grid spacing: $2.5\text{x}10^{-3}$), medium (0.7 million points, first grid spacing: $1.0\text{x}10^{-3}$), and fine (1.2 million points, first grid spacing:

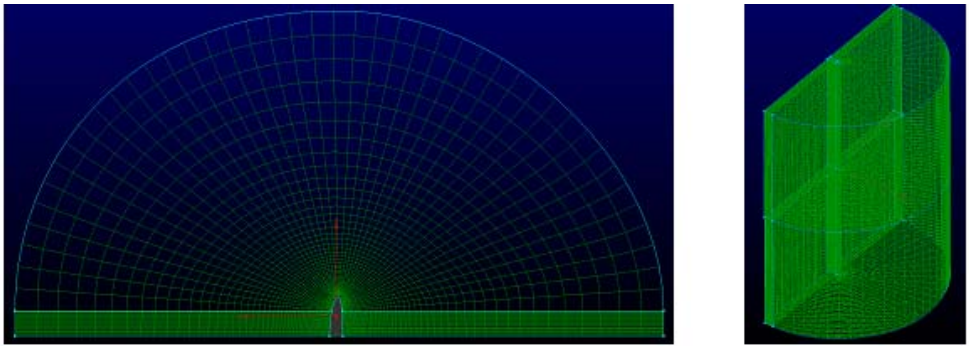

Figure 5.39: CFD computational grid for the Zimmerman flapping wing configurations.

5.0x10^{-4}). It is interesting to see that there is little or no sensitivity of the response to the grid refinements. This practically means that even the coarse grid configuration considered here is converged enough for the case studied. Notwithstanding this, the "medium" CFD grid configuration was chosen for all computations in this section specially keeping in view the relatively smaller first grid spacing in its case than in the "coarse" one which may become important for certain cases. Further, approximately 650 time-steps per period of computation were used in all the cases considered in this section, which were found to be sufficient for asymptotic convergence of the dynamic response. The convergence criterion for the aeroelastic convergence is chosen as a check on the Euclidean norm of the entire solution vector computed in two consecutive fluid-structure subiterations.

5.2.4 Correlations with Experimental Data

Figs. 5.43 and 5.44 show a comparison of the velocity magnitude and vorticity between computation and the experiment for two different time instants (t/T = 0.3 and 0.48). The flow field in these plots is shown on a slice that is cut at the quarter chord station going

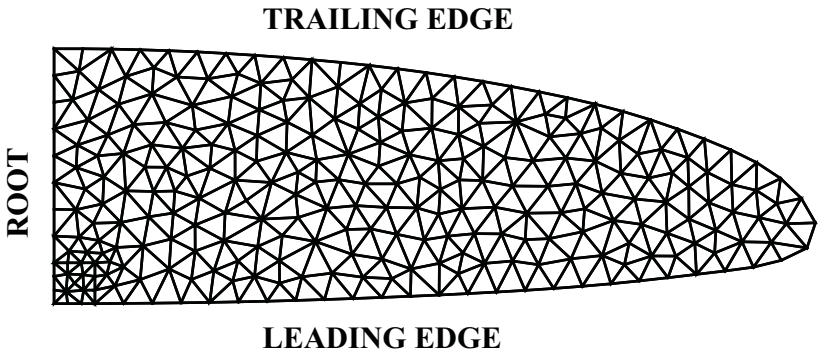

Figure 5.40: Triangular finite element mesh configuration of the CSD computational model used for the Zimmerman flapping wing configurations.

through the span. It must be noted that experimental data could not be measured above the wing in the white "cone-like" region which is outside the laser sheet. As seen from the correlations, there is good overall agreement in the flow structures between the computation and the experiment at both time instants. However, at the first time instant, the vorticity is weaker and more fragmented in the experiment than in the computation. Also, in general, there is more discrepancy near the wing tip than in the rest of the wing. A similar trend is observed even at the other time instant. This is confirmed from the comparison of velocity distributions between the computation and experiment shown in Fig. 5.45. Each of those plots is obtained by considering a line of points vertically above the wing which are obtained by intersecting a slice going through the quarter chord all along the span and another slice at either a section near the mid-span or the tip that goes through the entire chord. For

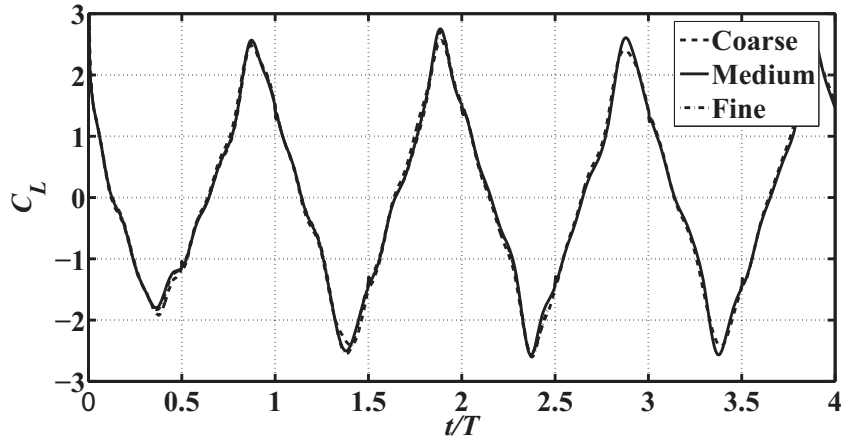

Figure 5.41: CFD grid sensitivity results for the Zimmerman Aluminium flapping wing case (lift coefficient).

example, Figs. 5.45a and 5.45b show such velocity magnitude distributions corresponding to a line of points obtained by intersecting the chordwise slice at mid-span and tip respectively one after the other with the slice going through the span at quarter chord, both for the time instant t/T=0.3. Then, Figs. 5.45c and 5.45d correspond to the same line of points but now for time instant t/T=0.48. Part of the reason for the discrepancies in the correlations is due the fact that the experimental data is phase averaged whereas the computation data is instantaneous and is based on the flow after a periodic solution was reached. In Fig. 5.45, there is missing experimental data at several locations due to limitations of the laser sheet in PIV setup. Fig. 5.46 shows a comparison of the normalized tip displacement (with respect to inertial frame) between computation and experiment. As in the results disussed above, there is an overall agreement in amplitude barring some disagreement in the phase.

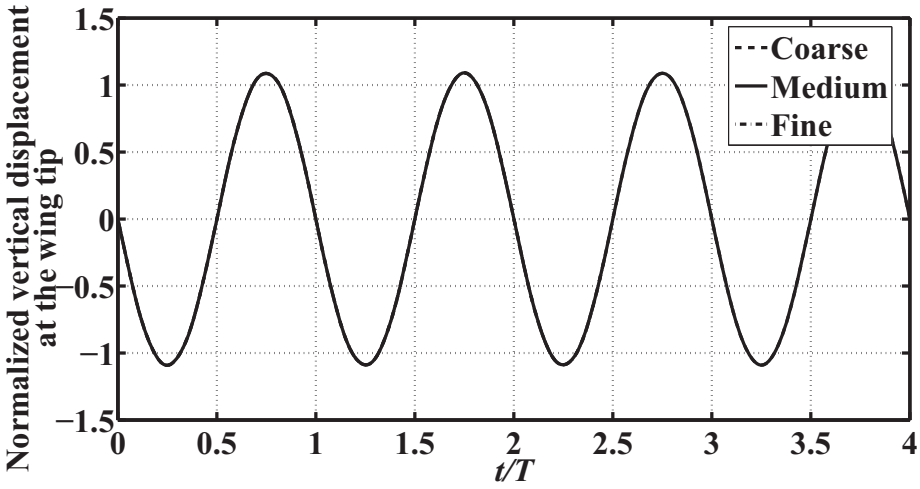

Figure 5.42: CFD grid sensitivity results for the Zimmerman Aluminium flapping wing case (displacement at the tip normalized with respect to the wing length).

5.2.5 Correlations Between Aerodynamic Force Production and Flow Field Around the Aluminium Flapping Wing

Figure 5.47 shows the time histories of lift and thrust coefficients on the wing for a single period after obtaining a periodic response. Points A and B in the figure correspond to minimum and maximum lift coefficient, respectively. These points are also associated with the maxima for the thrust coefficient. Fig. 5.48 shows contours of normalized vorticity in the plane of the paper along with streamlines for three different stations along the wing for the time instant corresponding to point B of Fig. 5.47. From the figure, it is clear that the spanwise distribution of vorticity is dominated by a pair of counter-rotating vortices at both leading and trailing edges. Furthermore, they are clearly growing in size from the root to the tip. A significant portion of the wing at this time instant (as shown in Fig. 5.49) is dominated by suction which explains the large lift coefficient of the wing at this time instant. On the contrary, at time instant A of Fig. 5.47, the lift coefficient is minimum and

is supported by the spanwise distribution of vorticity shown in Fig. 5.50 and further by the pressure distribution on the top and bottom surfaces of the wing shown in Fig. 5.51.

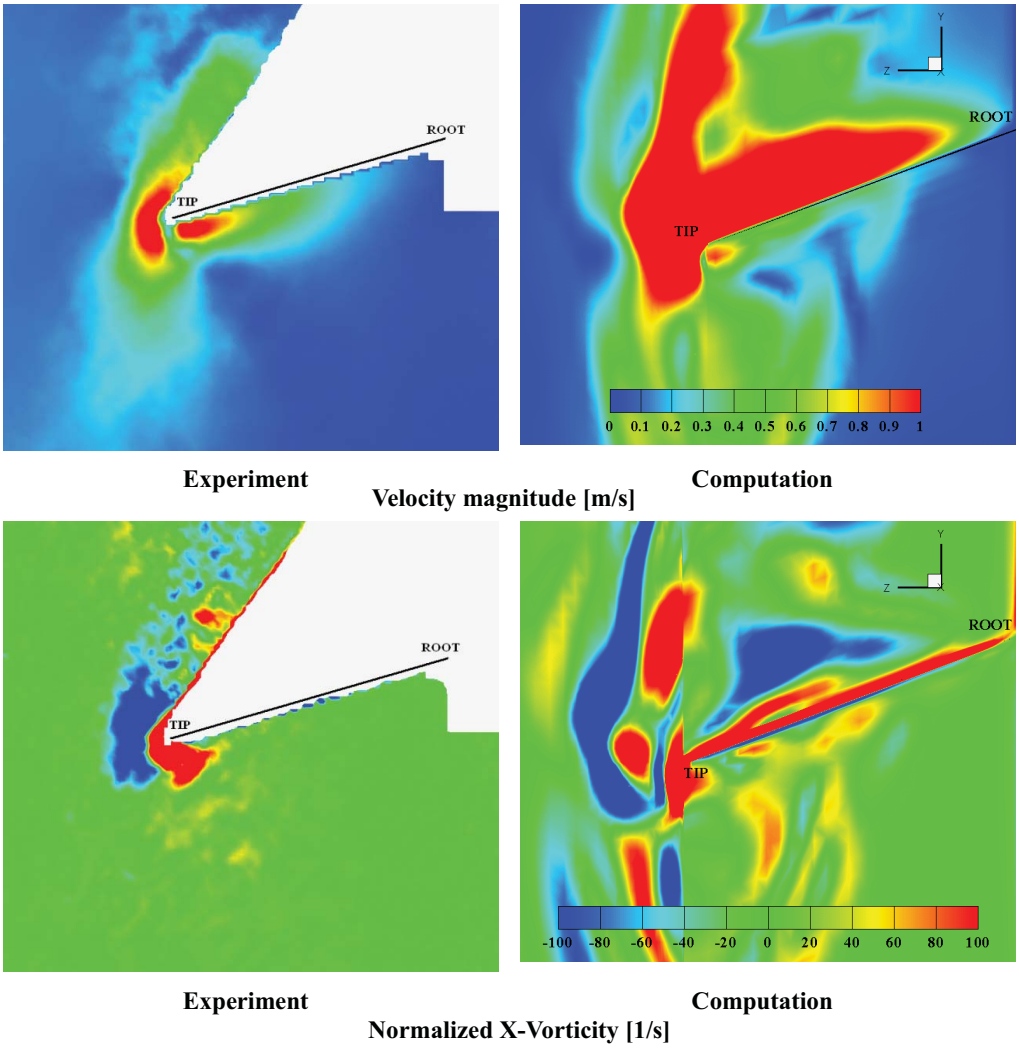

Figure 5.43: Comparison of velocity magnitude and vorticity at t/T = 0.3 for a slice at the quarter chord of the wing going through the entire span (left-experiment, right-computation). Note that vorticity is normalized by a factor of c/U_∞ where U_∞ is freestream velocity and c is wing root chord.

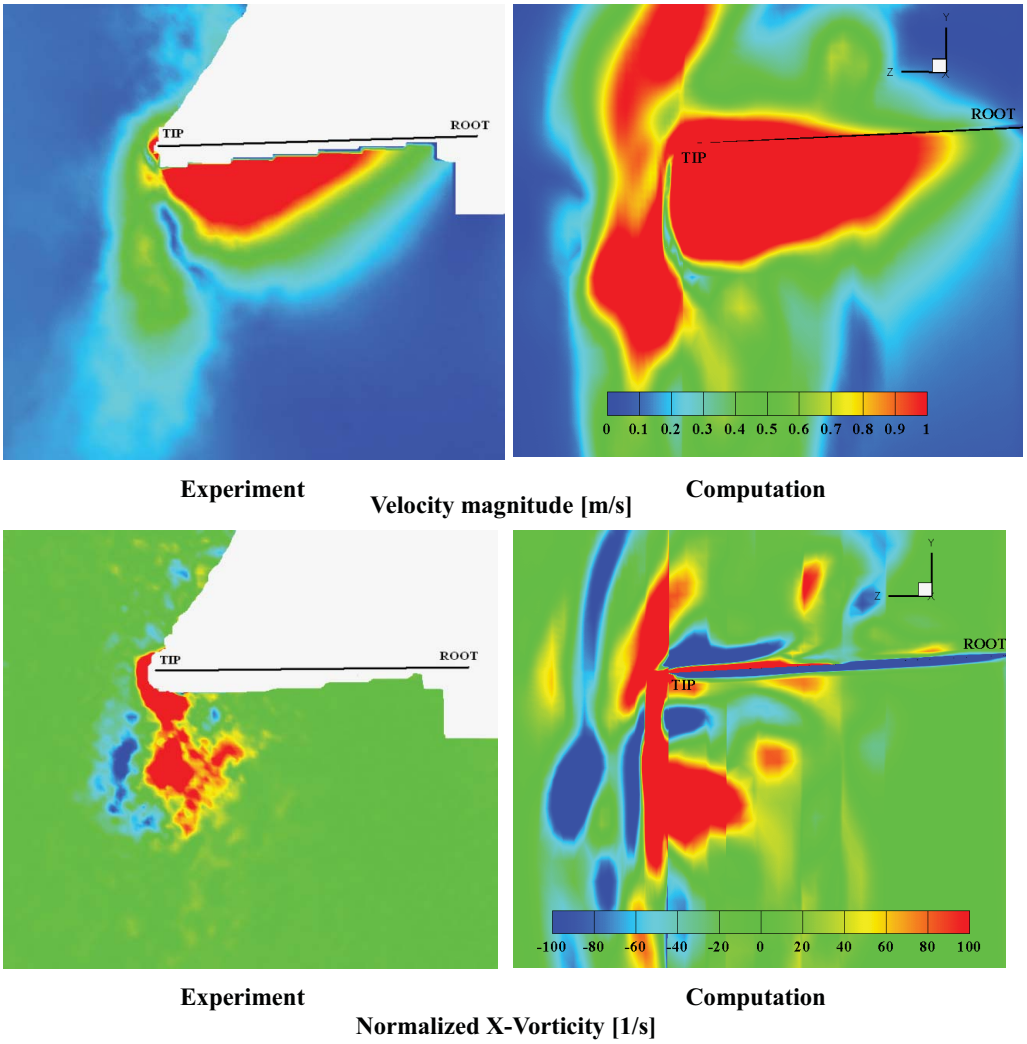

Figure 5.44: Comparison of velocity magnitude and vorticity at t/T = 0.48 for a slice at the quarter chord of the wing going through the entire span (left-experiment, right-comptation). Note that vorticity is normalized by a factor of c/U_∞ where U_∞ is freestream velocity and c is wing root chord.

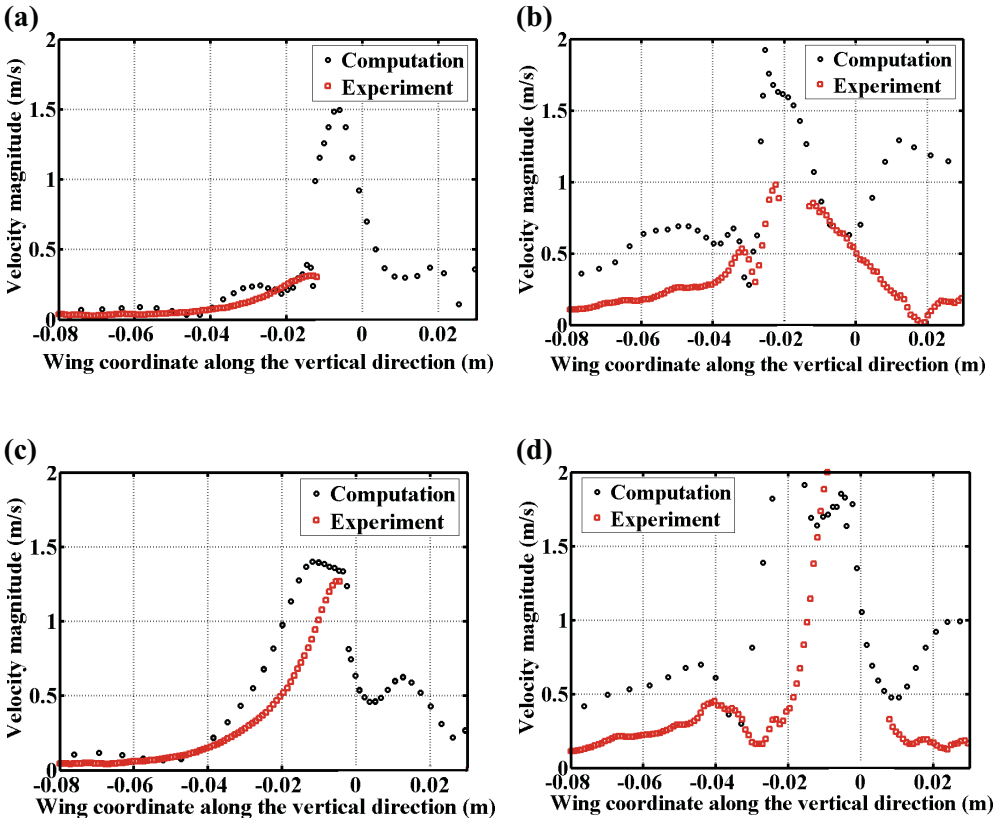

Figure 5.45: Comparison of velocity magnitude between computation and experiment at two different time instants and for two different slices along the wing span: plots (a) and (b) above correspond to time instant t/T = 0.3 and plots (c) and (d) to t/T = 0.48

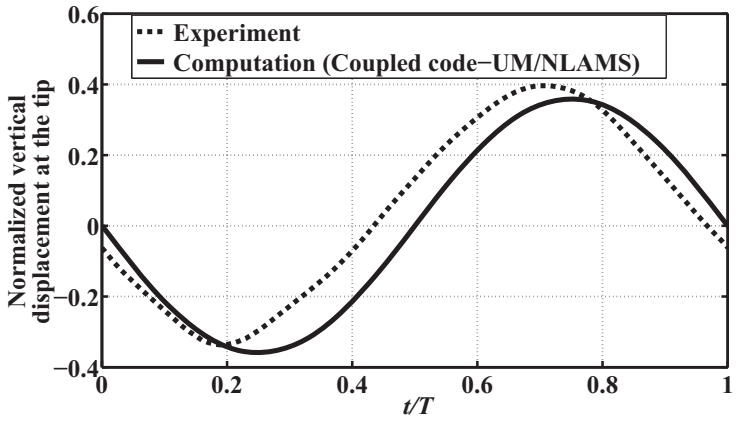

Figure 5.46: Comparison of normalized vertical displacement response at the wing tip of Zimmerman Aluminium flapping wing between computation and experiment (displacement is normalized with respect to the wing length).

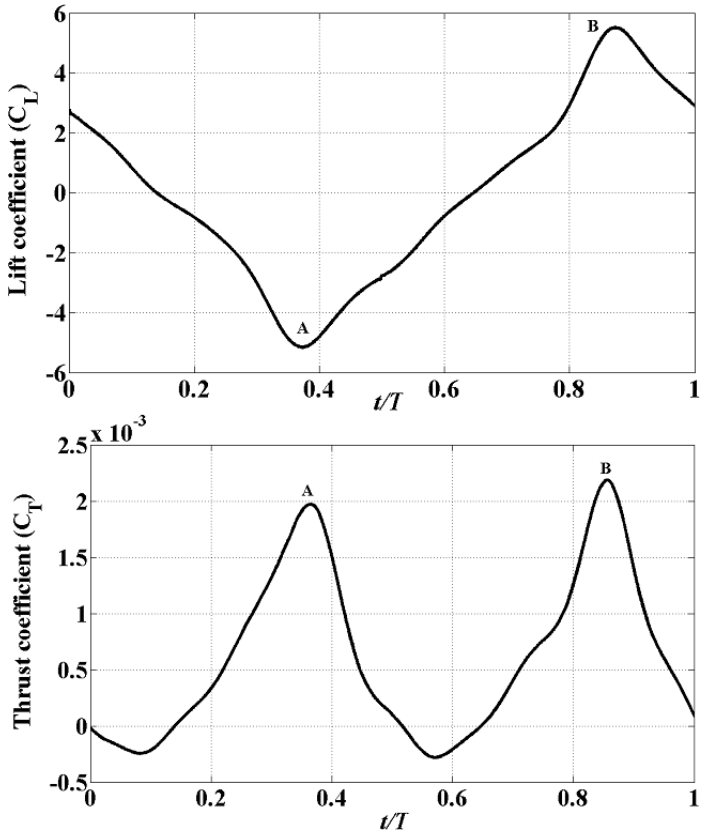

Figure 5.47: Lift and thrust coefficient response for the aluminium Zimmerman flapping wing.

5.2.6 Effect of Flexibility on Aerodynamics

The experimental data is available only for the case of aluminium (E = 70 GPa and Π_1 = 38 x 10^3), which is very close to being rigid (tip deformation of only 2% span was observed when measured with respect to the global frame in UM/NLAMS). Several variations in Young's modulus (effectively Π_1) are considered only in the computations to assess the impact of flexibility on aerodynamic force generation. Figs. 5.52 and 5.53 show the lift and thrust coefficient response, respectively, for four cycles of computation for all cases of flexibility. It should be noted that for better clarity only data points skipping every ten time

instants are considered in the plotting. As seen from the plots, the response corresponding to all wing configurations except the one with "E = 0.1 GPa" seems to be close to periodic. Figs. 5.54 and 5.55 give more insight into this by showing the mean lift and thrust coefficient, respectively, for all five cases. The standard deviation in the "E = 0.1 GPa" case is so large for the mean lift/thrust coefficients that it was omitted from the plots. A reason for the aperiodicity in this case is the absence of enough aerodynamic damping which would reduce the structural dynamics general solution to the particular solution, which represents the steady-state vibration. Two key observations can be made from Figs. 5.54 and 5.55:

- Within the range of flexibility considered, the mean thrust coefficient varies monotonically with increasing flexibility (due to the uncertainty in the mean values particularly for the "E = 10 GPa" and "E = 0.1 GPa" cases, no similar statement can be made for the mean lift coefficient).

- While the increase in the thrust coefficient from "Rigid" to "E = 10 GPa" is only minimum, it is more rapid from the latter to "E = 0.1 GPa" case, as more flexibility is added to the system.

From this point, only the two extreme cases corresponding to "Rigid" and "E = 0.1 GPa" are considered to study the effects of flexibility on aerodynamic force generation. Figs. 5.56 and 5.57 show the lift and thrust coefficient response corresponding to these two cases for several cycles of computation. As seen from the plots, while the instantaneous lift coefficient on the "Rigid" wing configuration is much greater than that of "E = 0.1 GPa" wing configuration, the trend is clearly opposite in the case of the thrust coefficient. Figs. 5.58 and 5.59 correspond to the pressure distribution contour plots on the top and bottom

surfaces of the "Rigid" and "E = 0.1 GPa" wings, respectively, at time instant D indicated in Figs. 5.56 and 5.57. It is seen from these plots that the top surface of the "Rigid" wing is dominated by suction more than that of the "E = 0.1 GPa" wing and so, it was found that the total resultant force of the "Rigid" wing is more than that of the "E = 0.1 GPa" at this time instant (and also at all others). Moreover, in the former, it is all in the form of lift whereas in the latter, due to the elastic twisting of the wing, there is also an effective horizontal force component (thrust). Fig. 5.60 illustrates this by showing the geometric twist angle at several stations along the span for both wing configurations. The geometric twist computed is the slope of the line joining the leading and trailing edge points corresponding to each station. In the figure, the data for the "E = 0.1 GPa" case is shown for four different time instants A, B, C, and D indicated in Fig. 5.57. The data for the "Rigid wing" is shown only for one time instant since in that case the twist angle is zero at all time instants due to the absence of prescribed pitch. As seen in the figure, for the case of the "E = 0.1 GPa" wing, the twist angle gradually increases from root to the tip at three time instants: A, C, and D. For time B, the behavior is non-monotonic.

From the results presented above it seems that it is possible to tailor wing flexibility to alter the aerodynamics of a flapping wing. It will be interesting to conduct further studies by considering local variations in flexibility, which may better reflect the structural characteristics of the wings of an actual insect.

Table 5.8: Parameters associated with rectangular flapping wing case

flow velocity [m/s]	0.95 (hover)	air density[kg/m^3]	1.209
chord-based Reynolds number	2565	Strouhal number	1.0
reduced frequency	0.89	Π_1	2400
aspect ratio	5.9	ρ^*	2233

5.3 A Rectangular Wing Prescribed With Pure Single Degree-of-Freedom Flap Rotation

Experimental studies have also been conducted at the University of Florida on a rectangular aluminium wing prescribed with large amplitude (+/- 17 deg) single degree-of-freedom flap rotation about an axis through its root chord. The frequency of flapping is 10 Hz. However, unlike in the previously presented Zimmerman wing study, only the displacements have been measured in this case and not flow velocities. The experimental setup used is similar to what is described in Ref. [104]. The aeroelastic response is computed for that wing (geometry shown in Fig. 4.11) using both of the coupled codes involving UM/NLAMS and MSC.Marc. For this case, the key parameters include those in Table 4.4 that are related to the 10 Hz vacuum case and the ones included in Table 5.8. A structured multi-block H-H type grid around a flat-plate rectangular wing of aspect ratio 5.93 was used for the CFD simulations. The total number of grid points is 0.6 million with close to 300 points on the wing surface. The CFD grid configuration including the boundary conditions is shown in Fig. 5.61. The boundaries on all sides of the wing/wall are 18 chord lengths away from the wing.

Fig. 5.62 shows the variation of displacement at the tip (point A in Fig. 4.11) versus non-dimensional time computed in the coupled codes involving UM/NLAMS and

MSC.Marc and measured in the experiment. As seen from the figure, there is an overall good agreement between the coupled codes and the experiment. Some noticeable discrepancy in the amplitude should be investigated in greater detail in a future effort, once more experimental data will become available for this configuration.

Figs. 5.63 and 5.64 show the lift and thrust coefficient response computed in the coupled code involving UM/NLAMS. Although small, the thrust produced is enhanced in the case of the flexible wing while it is again zero in the case of the rigid wing just like in the "Rigid" Zimmerman wing case due to the absence of any prescribed pitch rotation.

5.4 Summary of Numerical Investigations

The goal of this section is to briefly summarize the numerical investigations presented in all previous sections of this chapter. Several conclusions could be drawn based on the results obtained in them using the aeroelastic solutions developed as part of this dissertation.

Importantly, it was found that within the range of non-dimensional parameters considered, spanwise flexibility of a plunging wing can have a favorable impact on thrust generation. Furthermore, only certain amount of flexibility was found to be desirable for it. The importance of leading-edge suction, instantaneous angle of attack, and phase lag between wing root and tip was emphasized with a number of flow structures and pressure distributions for several plunging wing configurations. It was also shown that leading-edge suction is important to generate thrust in plunging wings with leading edge curvature. In the elliptic Zimmerman and rectangular single degree-of-freedom flapping wing cases, it

was shown that aerodynamic force generation could be enhanced due to wing flexibility. In particular, in the elliptic wing case it was shown that elastic twisting of the wing could produce larger mean thrust and also instantaneous thrust that is several orders of magnitude greater than that produced in other relatively rigid configurations (for example, compare Figs. 5.57 and 5.47). Notwithstanding the fact that the last two studies were preliminary, they were demonstrative of the effect of passive deformations on aerodynamic force generation. While the validation of a computational framework is an ongoing process, the numerical studies in this chapter have demonstrated preliminary validation of the aeroelastic solutions developed as part of this dissertation. In the process, the sensitivity of solutions to the aeroelastic coupling scheme with particular emphasis on the advantages of the implicit scheme and the aeroelastic convergence criterion were studied.

Apart from the above, the cross-validation of aeroelastic solutions produced with coupled codes involving UM/NLAMS, UM/NLABS, and MSC.Marc was demonstrated too.

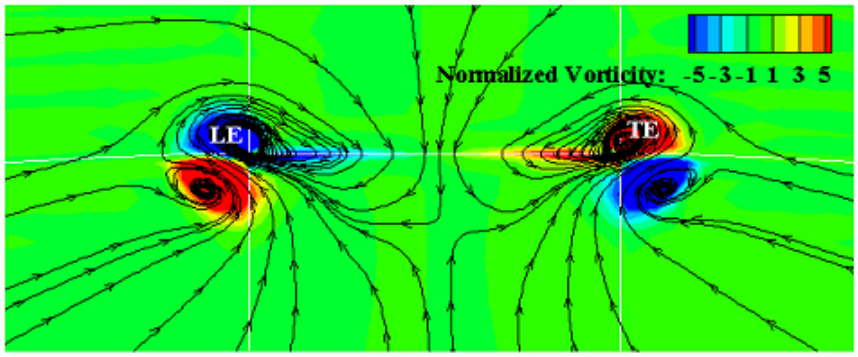

(5% semi-span)

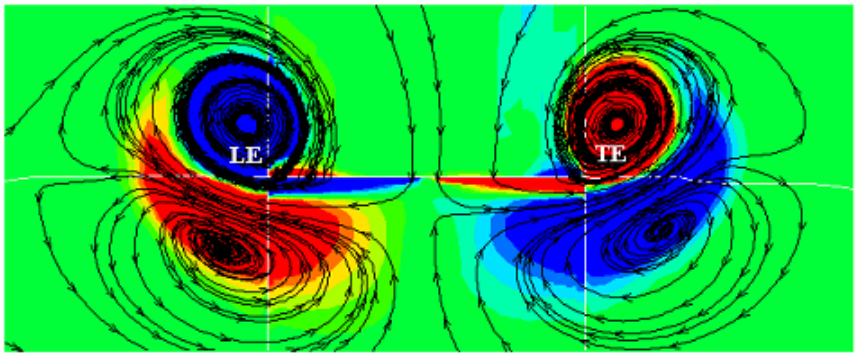

(50% semi-span)

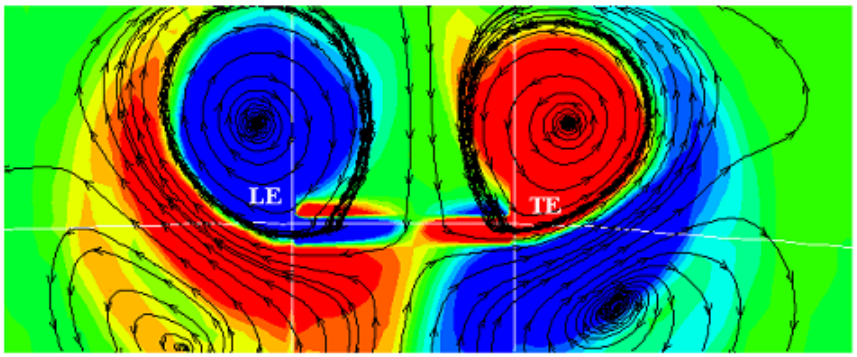

(80% semi-span)

Figure 5.48: Normalized vorticity contours for three different stations along the aluminium Zimmerman flapping wing at time instant indicated as B in Fig. 5.47 (LE - Leading edge, TE - Trailing edge). Note that vorticity is normalized by a factor of c/U_∞ where U_∞ is freestream velocity and c is wing root chord.

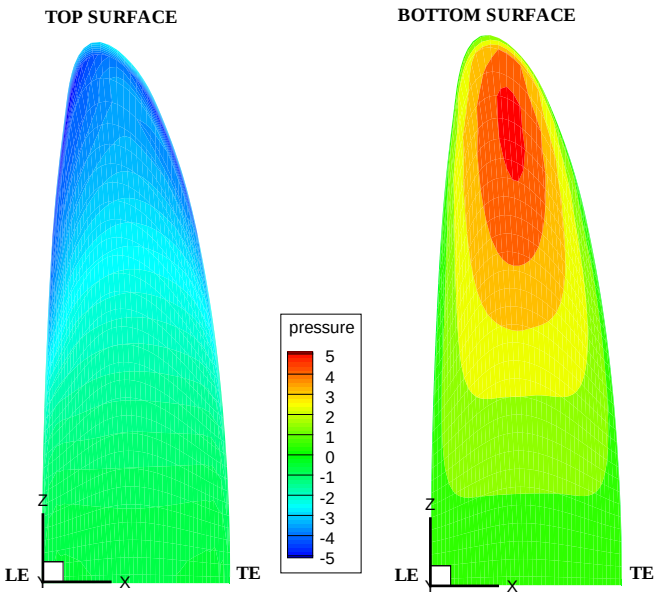

Figure 5.49: Pressure distribution contours on the top and bottom surfaces of the aluminium Zimmerman flapping wing at time instant indicated as B in Fig. 5.47

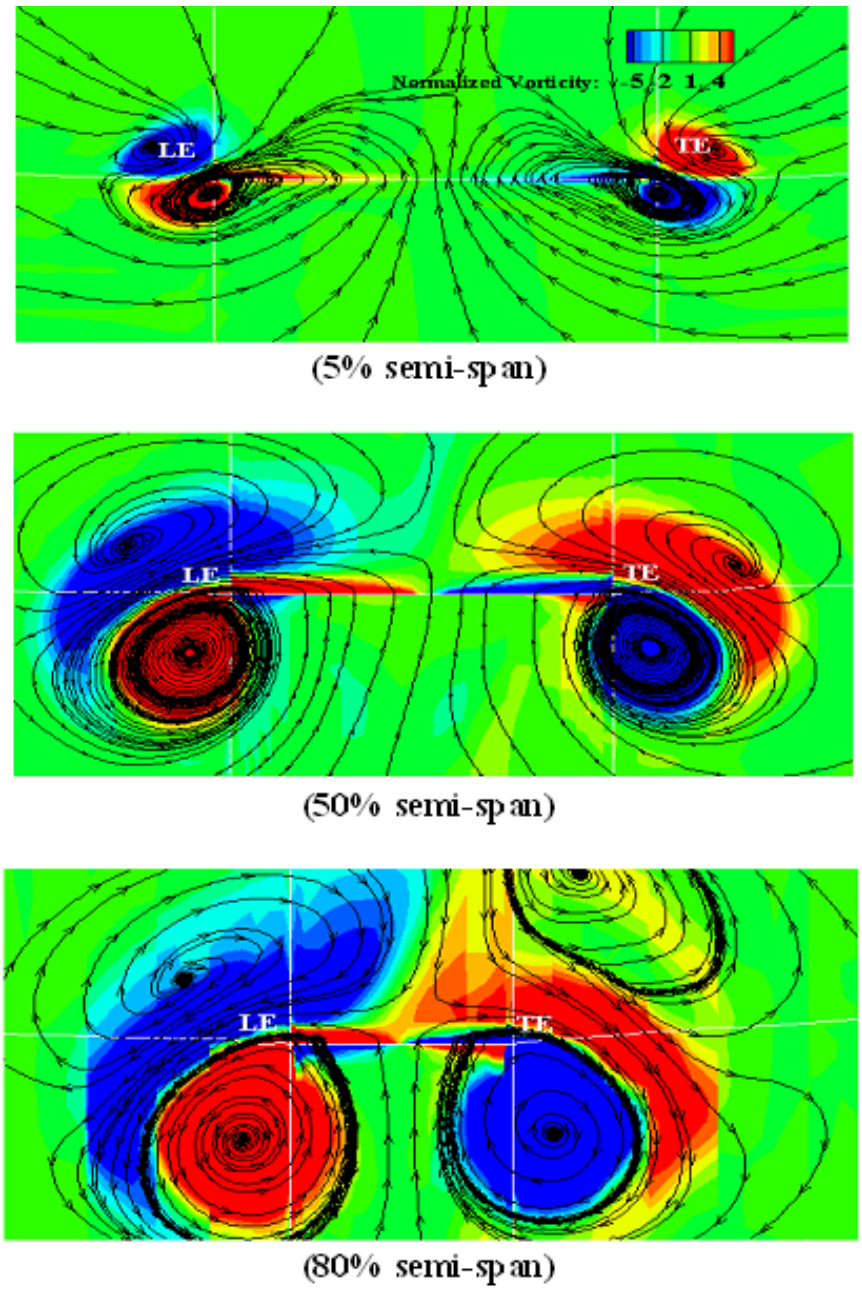

Figure 5.50: Normalized vorticity contours for three different stations along the aluminium Zimmerman flapping wing at time instant indicated as A in Fig. 5.47 (LE - Leading edge, TE - Trailing edge). Note that vorticity is normalized by a factor of c/U_∞ where U_∞ is freestream velocity and c is wing root chord.

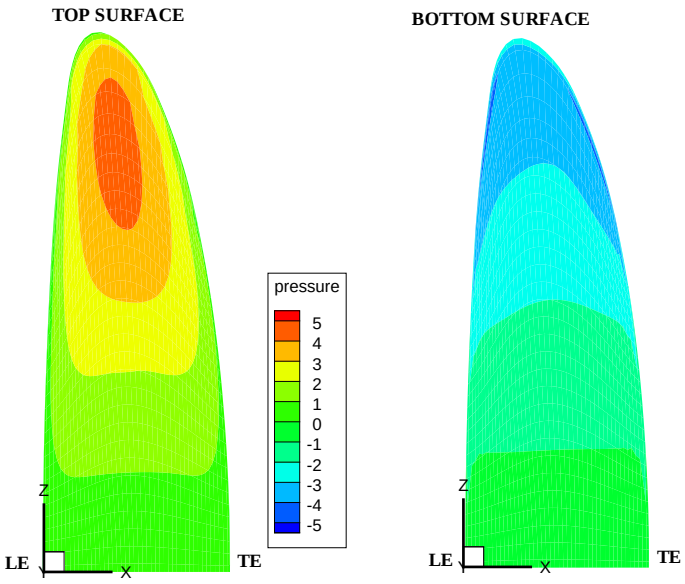

Figure 5.51: Pressure distribution contours on the top and bottom surfaces of the aluminium Zimmerman flapping wing at time instant indicated as A in Fig. 5.47.

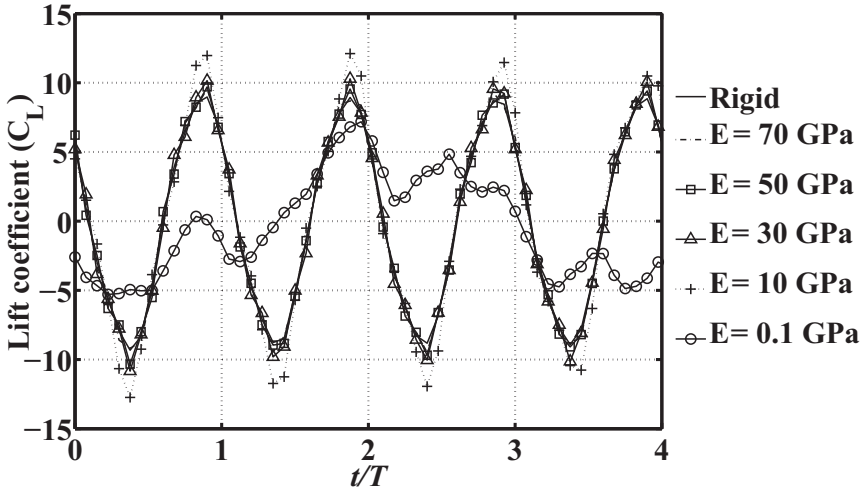

Figure 5.52: Lift coefficient response on the Zimmerman flapping wing with varying Young's modulus.

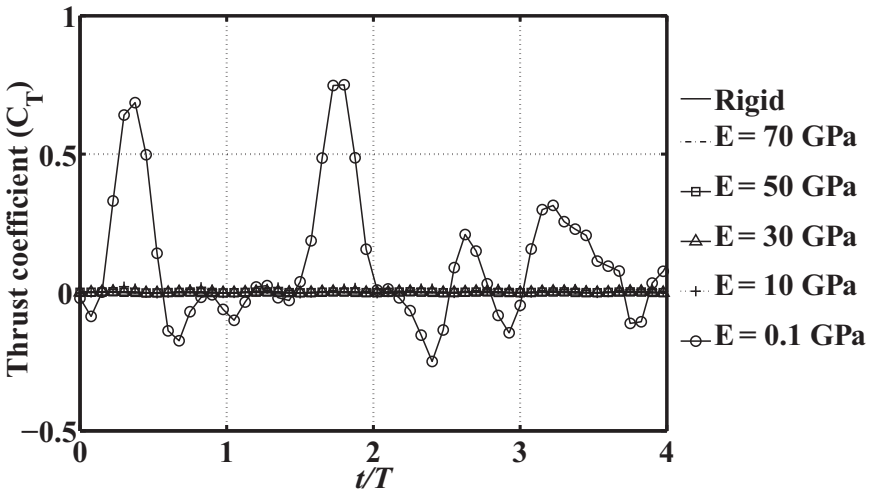

Figure 5.53: Thrust coefficient response on the Zimmerman flapping wing with varying Young's modulus.

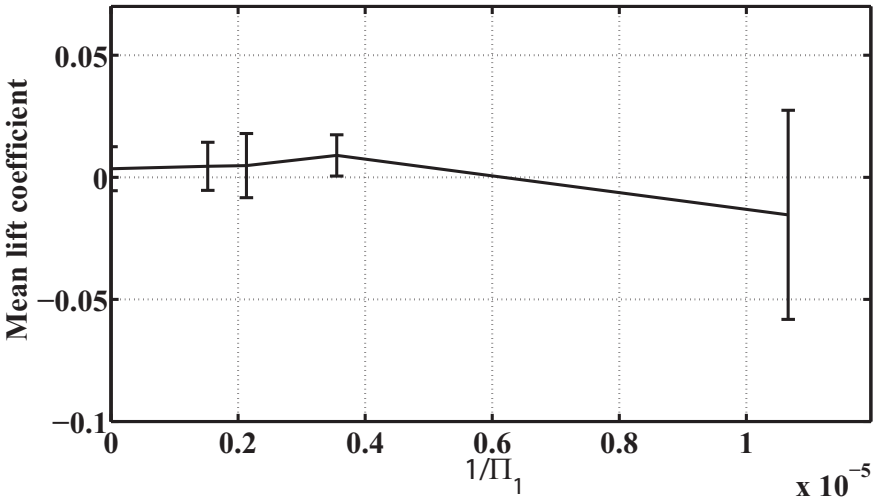

Figure 5.54: Mean and standard deviation of the mean lift coefficient of the hypothetical Zimmerman flapping wing configurations (standard deviation for Π_1 = 938 case is 2.08).

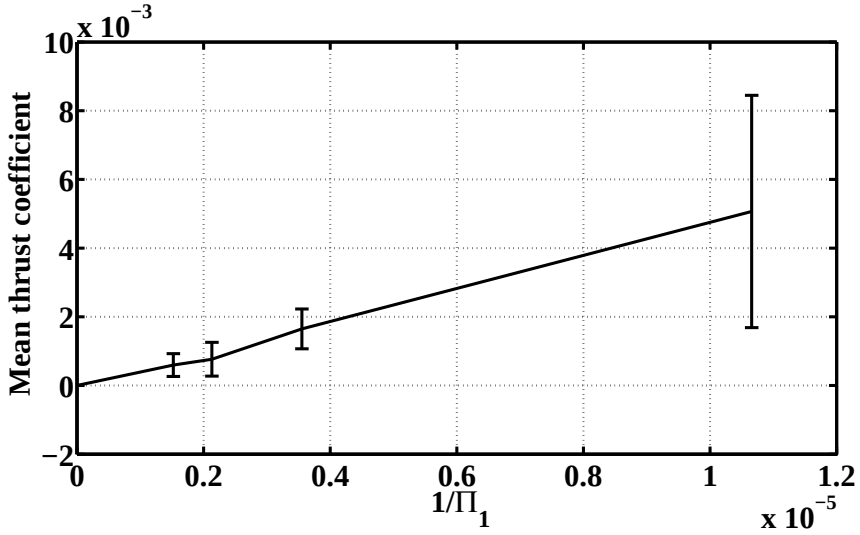

Figure 5.55: Mean and standard deviation of the mean thrust coefficient of the hypothetical Zimmerman flapping wing configurations (standard deviation for Π_1 = 938 case is 0.06).

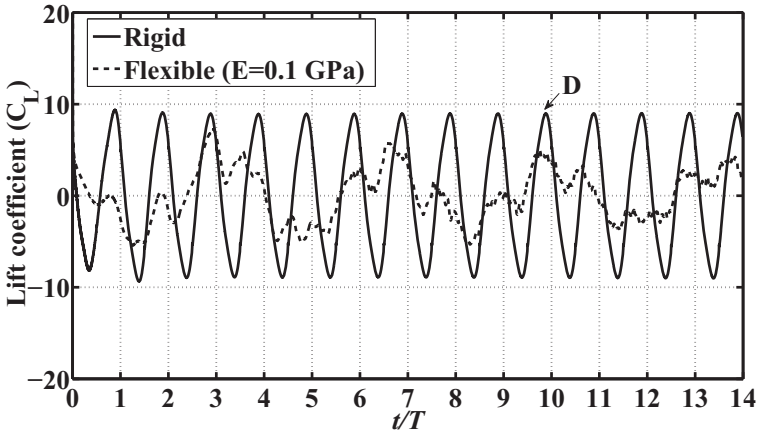

Figure 5.56: Lift coefficient response on the Zimmerman flapping wing for the "Rigid" and "E = 0.1 GPa" cases.

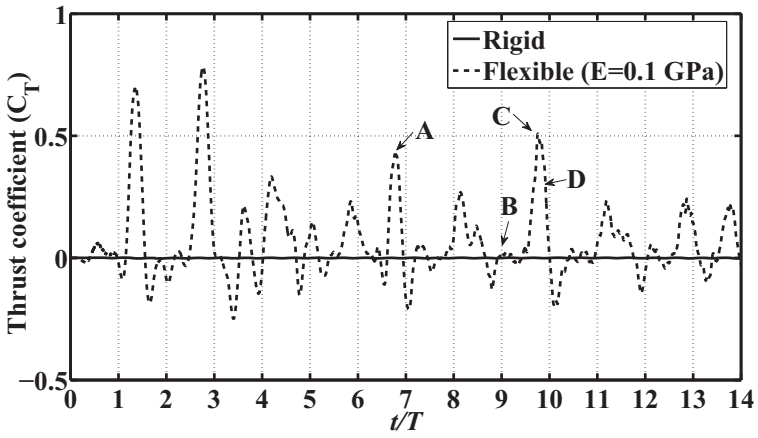

Figure 5.57: Thrust coefficient response on the Zimmerman flapping wing for the "Rigid" and "E = 0.1 GPa" cases.

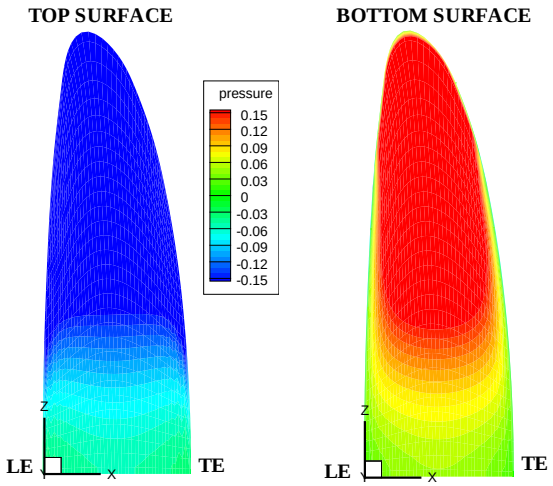

Figure 5.58: Pressure distribution on the top and bottom surfaces of the "Rigid" Zimmerman flapping wing at time instant D indicated in Fig. 5.56.

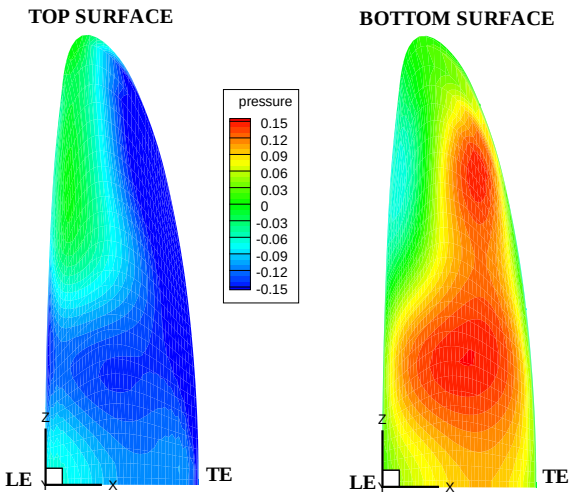

Figure 5.59: Pressure distribution on the top and bottom surfaces of the "E = 0.1 GPa" Zimmerman flapping wing at time instant D indicated in Fig. 5.56.

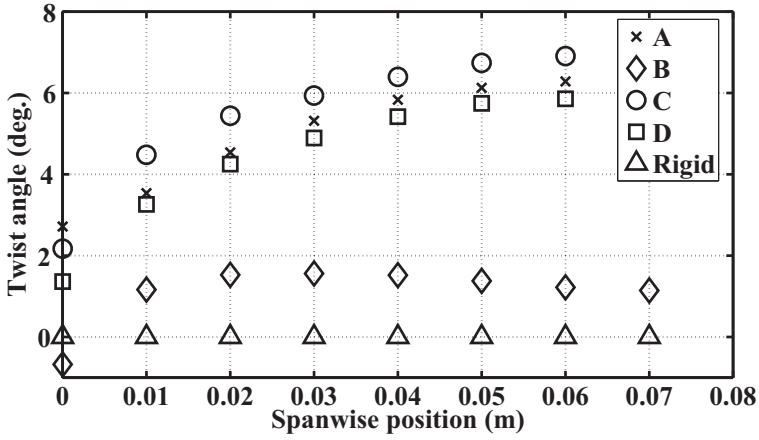

Figure 5.60: Geometric twist angle along the span for the "Rigid" and "E = 0.1 GPa" Zimmerman flapping wing configurations at time instants A, B, C, and D indicated in Fig. 5.57.

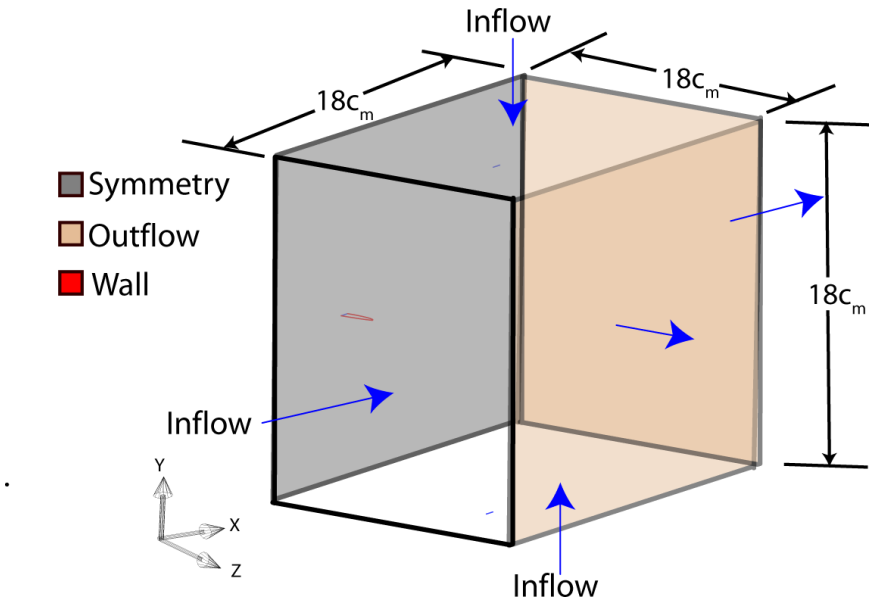

Figure 5.61: CFD computational model setup for the flapping rectangular wing.

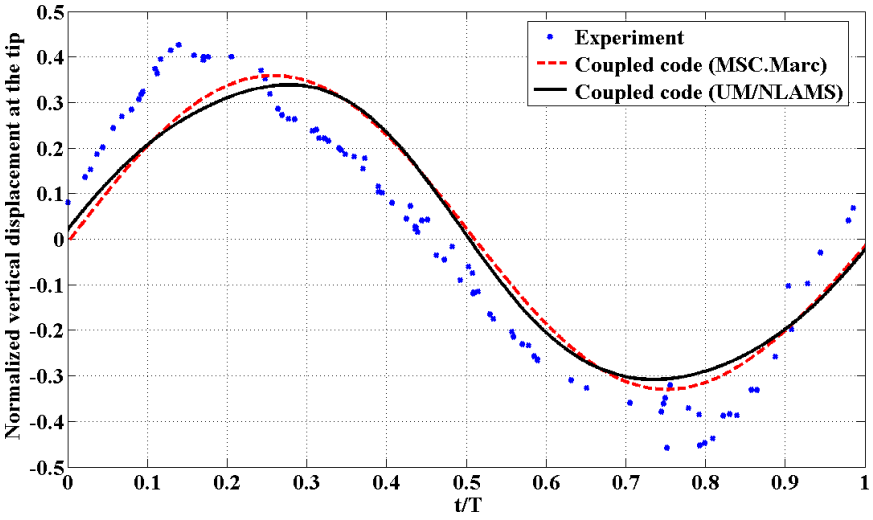

Figure 5.62: Tip displacement response of the flexible rectangular flapping wing configuration (displacement is normalized with respect to the wing length).

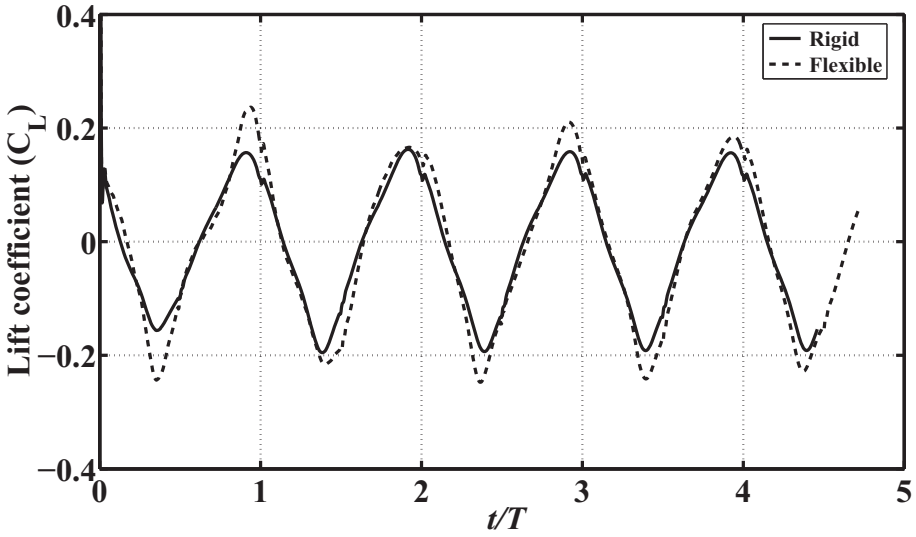

Figure 5.63: Lift coefficient response of the rigid and flexible rectangular flapping wing configurations.

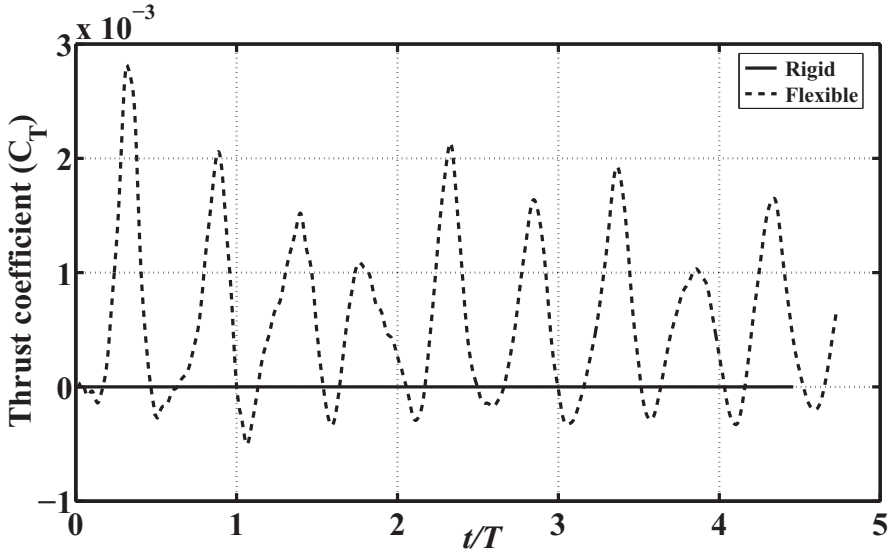

Figure 5.64: Thrust coefficient response of the rigid and flexible rectangular flapping wing configurations.

Chapter VI

CONCLUSIONS AND RECOMMENDATIONS

This chapter reviews the research done as part of this dissertation and provides concluding remarks which summarize all aspects of the work. Next, the key contributions made in this dissertation are presented. Lastly, based on the experience gained as part of this dissertation effort, certain recommendations are made for future work in the area.

6.1 Concluding Remarks

A substantial literature review in the computational aeroelasticity of flapping wings revealed that "CFD-based aeroelastic analyses" are rare. A key portion of this work therefore focused on the development of a suite of computational aeroelastic solutions of variable fidelity, all involving nonlinear structural dynamics and CFD tools and suitable for the analysis of flapping wing Micro Air Vehicle problems. Another portion of the work focused on the development of a nonlinear structural dynamics solver suitable for the analysis of structures prescribed with time-dependent boundary conditions. Verification and partial validation of the aeroelastic solutions against available experimental data were shown by analyzing simple isotropic plunging/flapping wing configurations in different media. Furthermore, numerical investigations performed on them provided valuable insight into the

impact of flexibility on aerodynamics. In addition to that, observations from experimental investigations were substantiated further with the help of the detailed computational analyses developed here.

The nonlinear structural dynamics solution UM/NLAMS developed in this work is based on a co-rotational formulation used in conjunction with a flexible multi-body type formulation to handle prescribed time-dependent boundary conditions. The application of a co-rotational frame in the finite element analysis enables the use of existing linear finite elements to be used in a nonlinear context. The structural dynamics equations of motions were integrated with the generalized-α method (allowing the classic Newmark as a sub-case of it). Several numerical studies conducted with UM/NLAMS were presented and verified against results from the commercial finite element solver MSC.Marc. In addition to UM/NLAMS, two structural formulations with different modeling capabilities were used. First, the UM/NLABS, which is capable of handling geometrically nonlinear beam-like deformations and linear plate-like motions [62, 64]. The other is MSC.Marc, a commercial finite element solver capable of modeling geometrically/materially nonlinear shell/plate built-up structures [2]. The Navier-Stokes flow solver used for the CFD analysis employs a well tested pressure-based algorithm and it was previously implemented in "UM/STREAM" [76, 83]. Assuming geometric similarity, several scaling parameters previously presented in other efforts [79] and certain additional ones useful for the aeroelastic simulations have been identified during the non-dimensionalization of the CSD and CFD formulations presented in this work. The importance of using such parameters was emphasized and they were quantified for selected low Reynolds flyers.

Each of the three stand-alone structural models were independently coupled to the CFD solver which resulted in three different coupled simulation codes with distinct capabilities. Two different coupling approaches ("explicit" and "implicit") were used within a partitioned solution framework to produce the coupled simulations codes. While the solvers involved in the "explicit" approach exchange solution once every coupled time step, subiterations are involved during the exchange of solution between fluid and the structural codes coupled via the "implicit" approach. The specific approach adopted for each coupled code was motivated by the limitation of the individual CSD solver. For example, MSC.Marc could not be used in an "implicit" context in its coupling with UM/STREAM due to its inability to exchange data with an external solver more than once per coupled time-step. In this work, the importance of using fluid-structure subiterations within a time-step and, therefore, the "implicit" scheme was emphasized and illustrated with sample results. A comprehensive discussion of the methodology for building the aeroelastic simulation codes was provided and, furthermore, illustrated via detailed flow charts.

Computational aeroelastic investigations were conducted on different wing configurations prescribed with time-dependent plunging/flapping boundary conditions. Based on Heathcote *et al.*'s experiment [41], numerical simulations were conducted on a rectangular NACA 0012 wing oscillating in pure heave. Four variations in spanwise flexibility of the plunging wing were considered. Quantitatively good agreement with the experimental results was obtained in some cases and only qualitative agreement in others. Several important conclusions stemmed from the numerical studies in this case as highlighted next:

- Within the range of non-dimensional parameters considered, spanwise flexibility was

shown to have a favorable impact on the thrust generation.

- Leading-edge suction was shown to be important for thrust generation in plunging wings with leading edge curvature.

- In the range of reduced frequencies considered (0.4 to 1.82), increasing reduced frequency increased the thrust generated by the wings considered for this study. In a similar fashion, the tip displacement increased with increasing reduced frequency.

- The role of instantaneous angle of attack and phase lag in the aerodynamic force generation of plunging wings was investigated in detail. It was found that in the case of the most flexible plunging configuration, the instantaneous angle of attack seen at most sections along the wing span decreased relative to the rigid and other wing configurations of lower flexibility. This was identified as responsible for the decrease in leading-edge suction effect and subsequently of the thrust in that case.

Based on the experiments conducted at the University of Florida on an elliptic and a rectangular Aluminium isotropic wing configurations prescribed with large amplitude single degree-of-freedom flapping motion, computational studies have been conducted to perform additional validation of the aeroelastic solutions and also to better understand the impact of flexibility on aerodynamics. While the experimental data was available only in one case, several variations in flexibility (via changes in Young's modulus) were considered in the computations. Within the range of parameters considered, the results from them showed that aerodynamic force generation could be enhanced due to wing flexibility. In particular, in the most flexible elliptic flapping wing case, the elastic twisting of the

wing was shown to produce larger mean and instantaneous thrust that is several orders of magnitude larger than that produced in other relatively rigid configurations.

6.2 Key Contributions

The following are the key contributions made in this dissertation:

1. Proposed, developed, and partially validated high-fidelity nonlinear aeroelastic formulations that enable the analysis of future MAV configurations and support the design of MAV aeroelastic experiments.

2. Characterized the role of instantaneous angle of attack and phase lag on the aerodynamic force generation of flexible plunging wings.

3. Proposed and developed a co-rotational structural dynamics solution to analyze shell-like flapping wing structures.

4. Derived scaling parameters for the different formulations involved in the aeroelastic solution of flapping wings.

5. Proposed and developed a generic code coupling procedure to couple external aerodynamics solvers with in-house/commercial FE solvers (specially with the latter).

6. Characterized the need of particular coupling strategies (explicit v/s implicit, convergence criterion) for flapping wing simulations.

This thesis presented a suite of high-fidelity computational aeroelasticity solutions suitable for the analysis of flexible flapping wings. Three nonlinear structural dynamics solu-

tions of variable fidelity (including two in-house and a commercial one) and an in-house incompressible Navier-Stokes solution were used to develop three different combinations of partitioned aeroelastic solutions. They were partially validated with available experimental data corresponding to flexible plunging/flapping wings. Further, such a multi-fidelity approach was shown to be useful in the cross-validation of computational aeroelastic solutions which is especially critical in the absence of experimental data. As part of the validation and the numerical investigation efforts, a series of flexible plunging wings were studied amongst others. It was found from the computations that only a degree of spanwise flexibility is desirable for thrust generation and that the variation of aerodynamic force coefficients with respect to spanwise flexibility is non-monotonic. In particular, the thrust generated in the most flexible wing was found to be the smallest. Even though this was one of the conclusions from the experimental effort of Heathcote *et al.* [41] too, this work supported and explained it further with the help of a rigorous analysis of flow structures, pressure distributions, aeroelastic deformation, and phase lag.

On the structural dynamics modeling side of the work, a methodology for the nonlinear structural dynamics analysis of shell-like flapping wings was proposed and developed. Time-dependent boundary conditions have been implemented using a body-fixed floating frame of reference and a co-rotational form of the total Lagrangian approach was used to account for geometric nonlinearities of the structure with respect to the floating frame. The procedure to apply the generalized-α method to nonlinear governing equations of motion was clearly highlighted. Structural dynamics solutions obtained from this approach were verified against those from the commercial finite element solver MSC.Marc.

Including the new shell element formulation described above, two "plate/shell" formulations were presented in this dissertation along with the one for a "beam". Nondimensionalizing each of those equations in conjunction with the "incompressible Navier-Stokes" equations resulted in two different sets of scaling parameters. The use of these parameters for aeroelastic simulations was emphasized in this work. Sensitivity studies were conducted with one of those parameters in the numerical investigations presented in this dissertation.

Apart from the above, the development of coupling interfaces for each of the three partitioned solutions was a key component in this dissertation. While the coupling procedures for the in-house structural solvers UM/NLABS and UM/NLAMS with CFD is not uncommon in existing literature, the proposed use of the code coupling interface provided by MSC.Marc to build an aeroelastic solution framework is a relatively novel approach. The process involved in the linking of such an interface with a generic external aerodynamics/CFD solver is possibly known to others working in this research area but was never published or presented in any setting to the best knowledge of the author. It is therefore presented in this dissertation in some detail.

Further, in this dissertation, the various coupling strategies involved in the development of an aeroelastic solution are summarized. In particular, two different approaches ("explicit" and "implicit") were emphasized in the aeroelastic simulations performed and the need of the latter was emphasized with examples. Subsequently, issues related to the use of a suitable convergence criterion for the implicit aeroelastic convergence within a coupled time-step were also discussed.

Overall, in this work, a foundation has been laid to enable a high-fidelity aeroelastic analysis of flapping wings and to help in the understanding of complex flow physics and deformation patterns that they present. The developed framework can be used to guide design of experiments and as an analysis tool for flapping wing concepts of future MAVs.

6.3 Recommendations for Future Work

Since the research activity in the computational aeroelasticity of flapping wings is an ongoing process just like in many other areas of research, several pending problems have been identified as part of this dissertation work that could be pursued as part of a future effort in this area. Further, a number of improvements could be made to the work already done here. These are highlighted next focusing on UM/NLAMS and UM/STREAM solvers along with the aeroelastic interface.

6.3.1 CSD solver UM/NLAMS

1. The existing solution framework for isotropic configurations could be extended to analyze composite wings. The formulation required was mostly incorporated as part of the current effort, but there are missing items in the implementation of certain transformations needed to convert elasticity matrices from one coordinate system to the other and in suitable input options to pre-process data related to general composite wing configurations. The formulation for the composite shell element is described in detail in Ref. [50].

2. Long term stability issues were encountered in the Newmark and generalized-α solutions for flapping frequencies above 25 Hz. Existing literature in this area points to energy conservation algorithms as a possible solution to such problems. Notwithstanding the possibility of the presence of implementation error in the current implementation of the generalized-α solution in UM/NLAMS, an energy conserving algorithm such as the one described in Ref. [68] is recommended for implementation in UM/NLAMS.

3. Membrane elements should be introduced in the solution to achieve the capability to perform analysis of membrane-batten flapping wings (e.g., Ref. [103]). Alternatively, the existing co-rotational formulation could be adapted so as to accommodate large strains as in Ref. [93] and then the membrane portions of the membrane-batten flapping wings could be discretized with shell elements too.

4. The total Lagrangian form of the co-rotational approach assumes small strains within each finite-element. The validity of the approach then becomes naturally dependent on the level of mesh refinement since it is important that the deformation in each finite-element is small relative to its dimensions. A systematic mesh refinement study could be done to understand the convergence and accuracy characteristics of the current implementation of the total Lagrangian co-rotational approach in different loading scenarios and try to mark off the boundaries in the level of strains that can be handled. The co-rotational form of the updated Lagrangian formulation which was previously found to help in the analysis of problems involving moderate strains (e.g., Ref. [46]) could be implemented in UM/NLAMS and compared to the existing

total Lagrangian form.

5. A significant reduction in pre-processing time could be achieved by developing and integrating an unstructured finite element mesh generator within the existing code. In the development of the finite element models for the current implementation of UM/NLAMS, MSC.Marc is being used.

6.3.2 CFD solver UM/STREAM

1. The grid deformation algorithm should be significantly improved to accommodate moderate to large plate/shell-like deformations (e.g., greater than 15% bending displacements and/or 10 deg elastic twist) particularly in the presence of mesh refinements near the wall. In such cases, the existing master-slave approach in the solver was not robust enough to prevent negative jacobian problems, which result due to crossing of grid lines in the re-meshing process.

2. A significant saving in the total time spent on running a simulation could be achieved if both code restart and parallel capabilities are introduced. Both of these issues have been major obstacles in the current effort to conduct more detailed aeroelastic analyses.

6.3.3 Aeroelastic interface

1. In this work, interpolation of data between the CFD and the CSD grids was done at each iteration by projecting the current configurations on to the horizontal plane. In

the case of problems where large rotations are involved, this could lead to singularities. For example, in the case of a wing that is rotated by 90 deg from the horizontal, the projection of points on a plane will cause points to coincide. Such a problem may be avoided by taking the third dimension into account in the interpolation. There are 3D methods available for that as in Ref. [87].

2. The coupled codes involving UM/NLAMS, UM/NLABS, and MSC.Marc could be integrated so that there is one unified framework in which different options are available for the user.

The aeroelastic solutions developed as part of this dissertation have a huge potential to analyze a variety of flapping wing problems. Since only simplified wing kinematics (single degree of freedom plunge or flap) have been studied in this work, problems involving more complex prescribed motions could be used to validate the aeroelastic solutions further and a better understanding of the physics of flapping wings could be gained.

Appendix A

Accuracy Assessment for Fluid-Structure Interpolation Schemes

The objective of this appendix is to assess the order of accuracy of the thin plate spline (TPS) and the bilinear interpolation schemes, used in this work. In order to do this, two arbitrary pressure distributions (given in Eqns. A.1 and A.2) considered separately were sampled on and prescribed to a "source CFD grid" and were then interpolated on to a "receiver CSD grid" using both types of interpolation schemes one after the other. The grids considered are two-dimensional and are of unit length in each direction. Four successive refinements of the CFD grid were considered in the study.

$$f_1(x, y) = sin(\pi x)cos(\frac{\pi}{2}y) \tag{A.1}$$

$$f_2(x, y) = 2x(1 - x) \tag{A.2}$$

Table A.1 provides details of the four CFD mesh configurations and a fixed CSD mesh configuration along with the RMS errors obtained for each case for pressure distribution function f_1 of Eq. A.1. Similarly, Table A.2 provides details of the four CFD mesh configurations and a fixed CSD mesh configuration along with the RMS errors obtained for each

case for pressure distribution function f_2 of Eq. A.2. The RMS errors in all the cases were computed using the interpolated solution obtained on the CSD grid and the exact solution calculated by sampling the corresponding analytical function on the same grid. Figs. A.1 and A.2 are plots showing the asymptotic convergence of error in the interpolated solution with increasing mesh refinement for the functions f_1 and f_2, respectively. With this information, the order of accuracy of the individual interpolation schemes may be estimated using the procedure discussed next [54].

Table A.1: RMS errors associated with interpolation schemes for function f_1 for different mesh configurations

CFD source grid	CSD receiver grid	RMS error (TPS)	RMS error (Bilinear)
12 x 12	11 x 11	0.0024	0.056
24 x 24	11 x 11	3.5 x 10^{-4}	0.0108
48 x 48	11 x 11	6.3 x 10^{-5}	0.0026
96 x 96	11 x 11	1.6 x 10^{-5}	5.7 x 10^{-4}

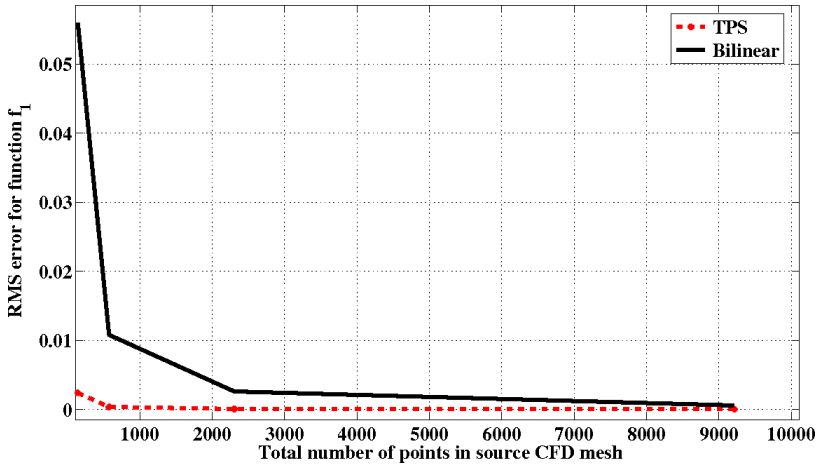

Figure A.1: RMS error convergence for function f_1 based on different interpolation schemes

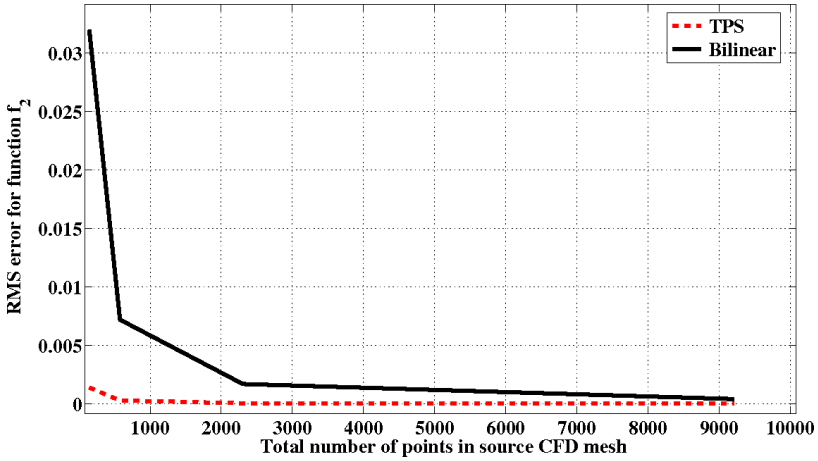

Figure A.2: RMS error convergence for function f_2 based on different interpolation schemes

Table A.2: RMS error associated with interpolation schemes for function f_2

CFD source grid	CSD receiver grid	RMS error (TPS)	RMS error (Bilinear)
12 x 12	11 x 11	0.0014	0.032
24 x 24	11 x 11	2.88 x 10^{-4}	0.0072
48 x 48	11 x 11	5.5 x 10^{-5}	0.0017
96 x 96	11 x 11	1.4 x 10^{-5}	4.1 x 10^{-4}

If the interpolation method is p^{th} order accurate, then, it can be expected that (as h$\rightarrow$0):

$$E(h) = Ch^p + o(h^p), \tag{A.3}$$

where E is the error metric, h is the discretized grid spacing, C is an arbitrary constant, and p is the order of accuracy. If h is sufficiently small, then,

$$E(h) \approx Ch^p \tag{A.4}$$

If the grid is refined by a factor of 2, then, it can be expected that,

$$E(h) \approx C(\frac{h}{2})^p \tag{A.5}$$

An error ratio can then be defined as:

$$R(h) \approx 2^p \tag{A.6}$$

and hence, the order of accuracy p is given as:

$$p \approx log_2(R(h)) \tag{A.7}$$

Using the data in Tables A.1 and A.2, the order of accuracy p was computed using the last two rows of data in both the tables, and the values of it for both types of interpolation and for both the functions are included in Table A.3. It is clear from this analysis that the order of accuracy associated with both TPS and bilinear interpolation methods is close to two. Repeating the analysis with much more refined discretization will improve the estimated orders. As samples, Fig. A.3 shows a mesh configuration (both CFD and CSD included) and Fig. A.4 shows the interpolated pressures on the CSD mesh plotted on top of the CFD pressure distribution for the case of function f_1. Similarly, Figs. A.5 and A.6 correspond to those for the case of function f_2.

Table A.3: Order of accuracy associated with interpolation schemes

TPS (f_1)	TPS (f_2)	Bilinear (f_1)	Bilinear (f_2)
1.97	1.97	2.18	2.05

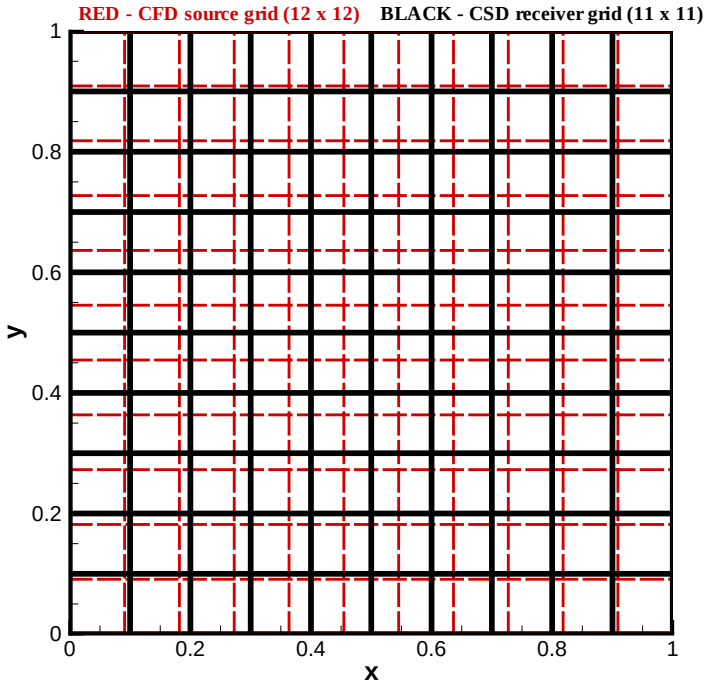

Figure A.3: Sample mesh configuration for TPS interpolation test with function f_1.

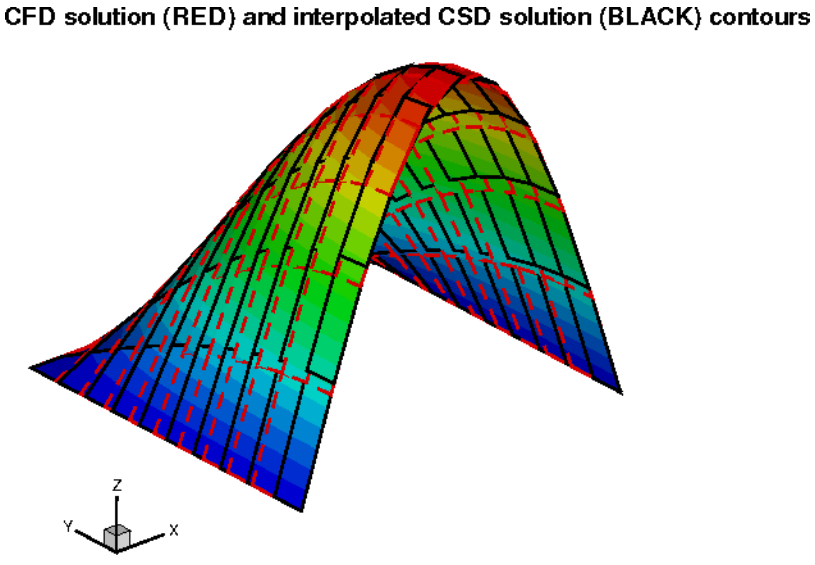

Figure A.4: Interpolated CSD solution superimposed on top of the source CFD solution for function f_1.

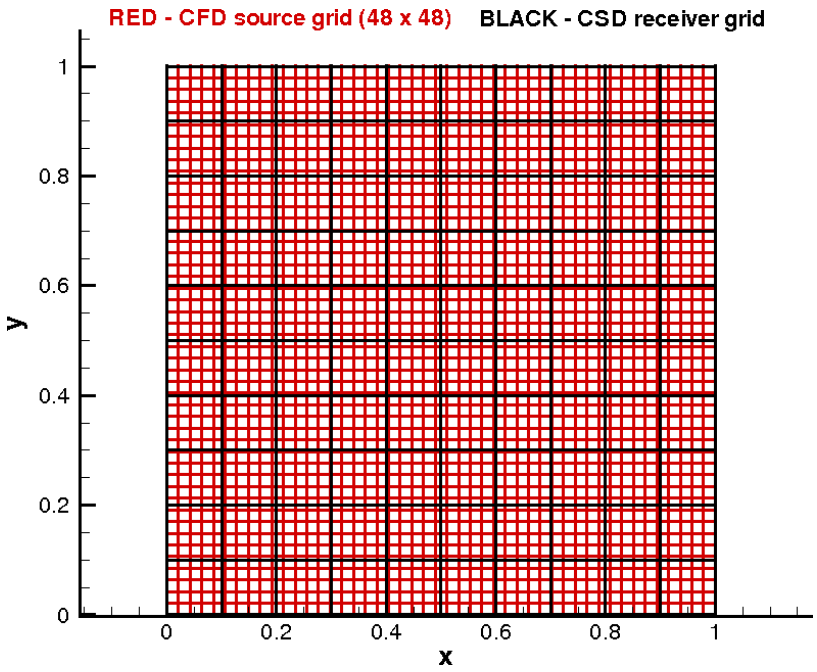

Figure A.5: Sample mesh configuration for TPS interpolation test with function f_2.

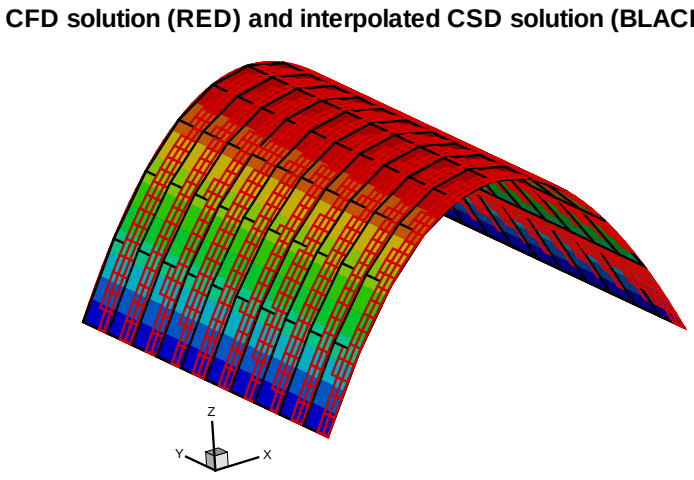

Figure A.6: Interpolated CSD solution superimposed on top of the source CFD solution for function f_2.

Appendix B

Cross-Sectional Stiffness and Inertia Matrices Corresponding to Plunging Wing Configurations

In this appendix, the cross-sectional stiffness and inertia matrices (defined in Eqs. 2.75 and 2.76 respectively but excluding the rows and columns corresponding to the finite section modes) computed in UM/NLABS for the "Flexible-1", "Flexible-2", and "Flexible-3" wing configurations are furnished.

B.1 "Flexible-1" Wing

B.1.1 Stiffness matrix

$$\begin{pmatrix} 2.1\text{x}10^{7} & 0 & 0 & 0 & 0 & -1.05\text{x}10^{6} \\ 0 & 6.73\text{x}10^{6} & -1.65\text{x}10^{-2} & -8.24\text{x}10^{-4} & 0 & 0 \\ 0 & -1.65\text{x}10^{-2} & 1.588\text{x}10^{4} & 7.94\text{x}10^{2} & 0 & 0 \\ 0 & -8.24\text{x}10^{-4} & 7.94\text{x}10^{2} & 42.3 & 0 & 0 \\ 0 & 0 & 0 & 0 & 1.783 & 6.0\text{x}10^{-6} \\ -1.05\text{x}10^{6} & 0 & 0 & 0 & 6.06\text{x}10^{-6} & 7.00\text{x}10^{4} \end{pmatrix}$$

B.1.2 Inertia matrix

$$\begin{pmatrix} 0.78 & 0 & 0 & 0 & 0 & -3.9\text{x}10^{-2} \\ 0 & 0.78 & 0 & 0 & 0 & 0 \\ 0 & 0 & 0.78 & 3.9\text{x}10^{-2} & 0 & 0 \\ 0 & 0 & 3.9\text{x}10^{-2} & 2.6\text{x}10^{-3} & 0 & 0 \\ 0 & 0 & 0 & 0 & 6.5\text{x}10^{-8} & 0 \\ -3.9\text{x}10^{-2} & 0 & 0 & 0 & 0 & 2.6\text{x}10^{-3} \end{pmatrix}$$

B.2 "Flexible-2" Wing

B.2.1 Stiffness matrix

$$\begin{pmatrix} 7\text{x}10^{6} & 0 & 0 & 0 & 0 & -3.5\text{x}10^{5} \\ 0 & 2.24\text{x}10^{6} & -5.5\text{x}10^{-3} & -2.74\text{x}10^{-4} & 0 & 0 \\ 0 & -5.5\text{x}10^{-3} & 5.29\text{x}10^{3} & 2.64\text{x}10^{2} & 0 & 0 \\ 0 & -2.74\text{x}10^{-4} & 2.64\text{x}10^{2} & 14.13 & 0 & 0 \\ 0 & 0 & 0 & 0 & 0.594 & 2.02\text{x}10^{-6} \\ -3.5\text{x}10^{5} & 0 & 0 & 0 & 2.02\text{x}10^{-6} & 2.33\text{x}10^{4} \end{pmatrix}$$

B.2.2 Inertia matrix

$$\begin{pmatrix} 0.27 & 0 & 0 & 0 & 0 & -1.35\text{x}10^{-2} \\ 0 & 0.27 & 0 & 0 & 0 & 0 \\ 0 & 0 & 0.27 & 1.35\text{x}10^{-2} & 0 & 0 \\ 0 & 0 & 1.35\text{x}10^{-2} & 9\text{x}10^{-4} & 0 & 0 \\ 0 & 0 & 0 & 0 & 2.25\text{x}10^{-8} & 0 \\ -1.35\text{x}10^{-2} & 0 & 0 & 0 & 0 & 9\text{x}10^{-4} \end{pmatrix}$$

B.3 "Flexible-3" Wing

B.3.1 Stiffness matrix

$$\begin{pmatrix} 4\text{x}10^{6} & 0 & 0 & 0 & 0 & -3.5\text{x}10^{5} \\ 0 & 1.28\text{x}10^{6} & -3.14\text{x}10^{-3} & -1.57\text{x}10^{-4} & 0 & 0 \\ 0 & -3.14\text{x}10^{-3} & 3.02\text{x}10^{3} & 1.51\text{x}10^{2} & 0 & 0 \\ 0 & -1.57\text{x}10^{-4} & 1.51\text{x}10^{2} & 8.07 & 0 & 0 \\ 0 & 0 & 0 & 0 & 0.34 & 1.15\text{x}10^{-6} \\ -2\text{x}10^{5} & 0 & 0 & 0 & 1.15\text{x}10^{-6} & 1.33\text{x}10^{4} \end{pmatrix}$$

B.3.2 Inertia matrix

$$\begin{pmatrix} 0.27 & 0 & 0 & 0 & 0 & -1.35\text{x}10^{-2} \\ 0 & 0.27 & 0 & 0 & 0 & 0 \\ 0 & 0 & 0.27 & 1.35\text{x}10^{-2} & 0 & 0 \\ 0 & 0 & 1.35\text{x}10^{-2} & 9\text{x}10^{-4} & 0 & 0 \\ 0 & 0 & 0 & 0 & 2.25\text{x}10^{-8} & 0 \\ -1.35\text{x}10^{-2} & 0 & 0 & 0 & 0 & 9\text{x}10^{-4} \end{pmatrix}$$

Appendix C

Generic Procedure to Couple Commercial FE and External (Third-Party) CFD solvers

The purpose of this appendix is to describe a process to couple commercial finite element codes to external CFD solvers. Figure C.1 highlights a generic procedure that is used in this dissertation, to couple an external (third-party) CFD solver to a typical commercial finite element solver that supports "custom" program execution. While the process of linking a commercial finite element code to an existing in-house CFD solver may be known to others, it was not published or presented in detail in any setting to the best knowledge of the author.

While the important steps involved in the coupling process are highlighted in Fig. C.1, a brief introduction to each step is given next:

1. The first step in the process is to check if the commercial FE solver can support "custom" program execution and has provided extensive API (which includes user and/or utility subroutines). Sample FE solvers that support these are ABAQUS, ANSYS, and MSC.Marc. In the case there is no such support and only user subroutine features are available, then they can be used to directly link the solver to a CFD solver.

2. The second step is to write an interface program which controls the CFD-based aeroelastic simulation. It should contain calls to the FE API, the external CFD solver, and the interface routines. All of these together will perform the tasks needed to run an aeroelastic simulation that include setting up of the individual FE and CFD models, i.e., the pre-processing, fluid-structure interpolation, CFD grid re-meshing, and the post-processing. In a custom setting like this, the procedure to set up the FE model could be different in each solver. For example, in the case of MSC.Marc, the inputs are read from an input file (which is supplied as an argument at the time of execution of the coupled code). However, in the case of ANSYS, each command has to be piped into the program through an intrinsic function from the interface program itself.

3. As part of the third and fourth steps described in Fig. C.1, the shell script that generates the stand-alone FE solver executable should be identified and the environment variables defined in it be extracted. The script generally comes bundled with the distribution files of the commercial solver. The variables defined in that script will provide paths to various object (*.o) and archive (*.a files, each of which is generally a combination of several *.o files) files that make up the FE solver's library.

4. In the next step, a "Makefile" (a special format file that together with the Unix "make" utility helps in automatically building and managing a project involving several source files) should then be created incorporating the FE solver's variable definitions extracted in the previous step along with those corresponding to the external CFD solver. This file should contain all the rules to be able to compile and link the

objects and the archives corresponding to the CFD, CSD, interpolation, CFD grid re-meshing routines along with the interface program prepared as part of the second step. While these objects and archives constitute the dependencies, the "target" (the executable that is created by "making" the file) will be the custom version of the FE solver which includes the functionality of the CFD and the interface routines.

5. The custom version of the FE solver should be executed by specific commands which are generally included in the manuals.

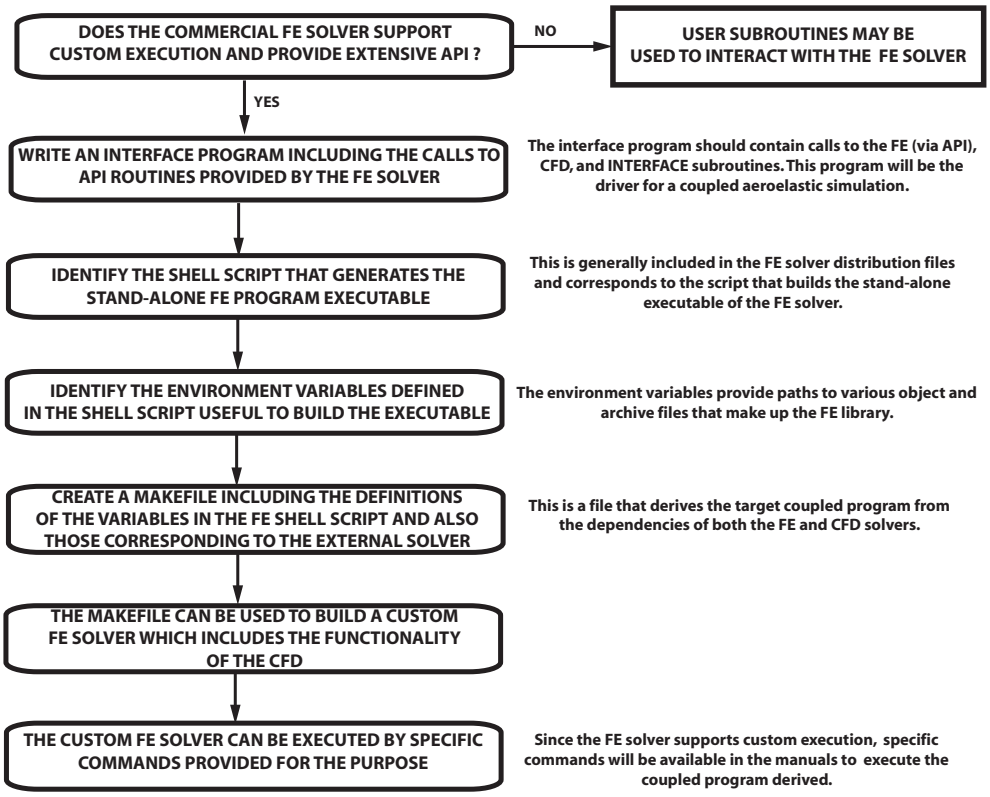

Figure C.1: Proposed generic code coupling procedure using commercial FE and external CFD solvers

Bibliography

[1] A. Agrawal and S.K. Agrawal. "Design of Bio-inspired Flexible Wings for Flapping-Wing Micro-sized Air Vehicle Applications," *Advanced Robotics*, 23:979–1002, 2009.

[2] Annon. *MSC.Marc Documentation Volumes A-E*, MSC Corporation, Santa Ana, California, 2005.

[3] S.A. Ansari, R. Zbikowski, and K. Knowles. "Aerodynamic Modelling of Insect-Like Flapping Flight for Micro Air Vehicles," *Progress in Aerospace Sciences*, 42:129–172, 2006.

[4] S.A. Ansari, R. Zbikowski, and K. Knowles. "Non-linear Unsteady Aerodynamic Model for Insect-Like Flapping Wings in Hover. Part 1: Methodology and Analysis,". *Progress in Aerospace Sciences*, 220:61–83, 2006.

[5] H. Aono, S.K. Chimakurthi, C.E.S. Cesnik, H. Liu, and W. Shyy. "Computational Modeling of Spanwise Flexibility Effects on Flapping Wing Aerodynamics," In *AIAA Aerospace Sciences Meeting*, Orlando, FL, January 2009. AIAA Paper Number 2009-1270.

[6] H. Aono and H. Liu. "Vortical Structure and Aerodynamics of Hawkmoth Hovering," *Journal of Biomedical Science and Engineering*, 1(1):234–245, 2006.

[7] J. Argyris. "An Excursion into Large Rotations," *Computer Methods in Applied Mechanics and Engineering*, 32(1-3):85–155, 1982.

[8] P.J. Attar and R.E. Gordnier. "High Fidelity Computational Aeroelastic Analysis of a Plunging Membrane Airfoil," In 50^{th} *AIAA/ASME/ASCE/AHS/ASC Structures, Structural Dynamics, and Materials Conference*, Palm Springs, CA, May 2009. AIAA Paper Number 2009-2472.

[9] A. Barut, M. Das, and E. Madenci. "Nonlinear Deformations of Flapping Wings on a Micro Air Vehicle," In 47^{th} *AIAA/ASME/ASCE/AHS/ASC Structures, Structural Dynamics, and Materials Conference*, Newport, RI, May 2006. AIAA Paper Number 2006-1662.

[10] K.J. Bathe, E. Ramm, and E.L. Wilson. "Finite Element Formulations for Large Deformation Dynamic Analysis," *International Journal of Numerical Methods in Engineering*, 9:353–386, 1975.

[11] J.L. Batoz, K.J. Bathe, and L.W. Ho. "A Study of Three-Node Triangular Plate Bending Elements," *International Journal for Numerical Methods in Engineering*, 15(12):1771–1812, 1980.

[12] J.M. Battini. "A Modified Co-rotational Framework for Triangular Shell Elements," *Computer Methods for Applied Mechanics and Engineering*, 196:1905–1914, 2007.

[13] J.M. Battini and C. Pacoste. "On the Choice of Local Element Frame for Co-rotational Triangular Shell Elements," *Communications in Numerical Methods in Engineering*, 20:819–825, 2004.

[14] J.M. Battini and C. Pacoste. "On the Choice of the Linear Element for Corotational Triangular Shells," *Computer Methods for Applied Mechanics in Engineering*, 195:6362–6377, 2006.

[15] L.P. Bernal, M. Ol, D.P. Szczublewski, and C.A. Cox. "Unsteady Force Measurements in Pitching-Plunging Airfoils," In 39^{th} *AIAA Fluid Dynamics Conference*, San Antonio, Texas, June 2009. AIAA Paper Number 2009-4031.

[16] J.M. Birch and M.H. Dickinson. "Spanwise Flow and the Attachment of the Leading-Edge Vortex on Insect Wings," *Nature*, 412:729–732, 2001.

[17] P. Causin, J.F. Gerbeau, and F. Nobile. "Added-mass Effects in the Design of Partitioned Algorithms for Fluid-Structure Problems," *Computer Methods in Applied Mechanics and Engineering*, 194:4506–4527, 2005.

[18] C.E.S. Cesnik and D.H. Hodges. "VABS: A New Concept for Composite Rotor Blade Cross-Sectional Modeling," *Journal of the American Helicopter Society*, 42(1):27–38, 1997.

[19] D.D.J. Chandar and M. Damodaran. "Computational Fluid-Structure Interaction of a Flapping Wing in Free Flight Using Overlapping Grids," In 27^{th} *AIAA Applied Aerodynamics Conference*, San Antonio, Texas, June 2009. AIAA Paper Number 2009-3849.

[20] S. K. Chimakurthi, J. Tang, R. Palacios, C. Cesnik, and W. Shyy. "Computational Aeroelasticity Framework for Analyzing Flapping Wing Micro Air Vehicles," In 49^{th} *AIAA/ASME/ASCE/AHS/ASC Structures, Structural Dynamics, and Materials Conference*, Schaumburg,IL, April 2008. AIAA Paper Number 2008-1814.

[21] J. Chung and G. Hulbert. "A Time Integration Algorithm for Structural Dynamics With Improved Numerical Dissipation," *Journal of Applied Mechanics*, 60(2):371–375, June 1993.

[22] L.J. Clancy. *Aerodynamics*, Pitman Publishing Limited, London, 1975.

[23] S. Combes and T. Daniel. "Flexural Stiffness in Insect Wings I.Scaling and the Influence of Wing Venation," *Journal of Experimental Biology*, 206:2979–2987, 2003.

[24] S.A. Combes and T.L. Daniel. "Into Thin Air: Contributions of Aerodynamic and Inertial-Elastic Forces to Wing Bending in the Hawkmoth *Manduca Sexta*," *The Journal of Experimental Biology*, 206:2999–3006, 2003.

[25] R.D. Cook, D.S. Malkus, M.E. Plesha, and R.J. Witt. *Concepts and Applications of Finite Element Analysis*, John Wiley and Sons, 2002.

[26] J. Cubo and A. Casinos. "Mechanical Properties and Chemical Composition of Avian Long Bones," *European Journal of Morphology*, 38(2):112–121, 2000.

[27] B. de Veubeke. "The Dynamics of Flexible Bodies," *International Journal of Engineering Science*, 14:895–913, 1976.

[28] J.D. DeLaurier and J.M. Harris. "Experimental Study of Oscillating-Wing Propulsion," *Journal of Aircraft*, 19(5):368–373, 1982.

[29] M.H. Dickinson, F.O. Lehmann, and S.P. Sane. "Wing Rotation and the Aerodynamic Basis of Insect Flight," *Science*, 284:1954–1960, 1999.

[30] H. Doi. *Fluid/Structure Coupled Aeroelastic Computations for Transonic Flows in Turbomachinery*. PhD Dissertation, Department of Aeronautics and Astronautics, Stanford University, Stanford, California, 2002.

[31] C.P. Ellington, C. Van den Berg, A.P. Willmott, and A.L.R. Thomas. "Leading-Edge Vortices in Insect Flight," *Nature*, 384:19–26, 1996.

[32] C.A. Felippa. "A Study of Optimal Membrane Triangles with Drilling Freedoms," *Computer Methods in Applied Mechanics and Engineering*, 192(16-18):2125–2168, 2003.

[33] K. Frampton, M. Goldfarb, D. Monopoli, and D. Cveticanin. "Passive Aeroelastic Tailoring for Optimal Flapping Wings," In T.J.Mueller, editor, *Fixed and Flapping Wing Aerodynamics for Micro Air Vehicle Applications*, volume 195, pages 473–482, New York, 2001. Progress in Astronautics and Aeronautics,AIAA.

[34] M. Geradin and A. Cardona. *Flexible Multibody Dynamics: A Finite Element Approach*, Wiley, March 2001.

[35] A. Gogulapati, P.P. Friedmann, and W. Shyy. "Nonlinear Aeroelastic Effects in Flapping Wing Micro Air Vehicles," In 49^{th} *AIAA/ASME/ASCE/AHS/ASC Structures, Structural Dynamics, and Materials Conference*, Schaumburge, Illionois, April 2008. AIAA Paper Number 2008-1817.

[36] A. Gogulapati, P.P. Friedmann, and W. Shyy. "Approximate Aeroelastic Analysis of Flapping Wings in Hover," In *International Forum for Aeroelasticity and Structural Dynamics Conference*, Seattle, Washington, June 2009. IFASD Paper Number 2009-143.

[37] P. Gopalakrishnan. *Unsteady Aerodynamic and Aeroelastic Analysis of Flapping Flight*. PhD Dissertation, Department of Mechanical Engineering, Virginia Polytechnic Institute and State University, Blacksburg, Virginia, 2008.

[38] M. Hamamoto, Y. Ohta, K. Hara, and T. Hisada. "Application of Fluid-Structure Interaction Analysis to Flapping Flight of Insects With Deformable Wings," *Advanced Robotics*, 21(1-2):1–21, 2007.

[39] P.M. Hartwich and S. Agrawal. "Method for Perturbing Multiblock Patched Grids in Aeroelastic and Design Optimization Applications," In *AIAA Computational Fluid Dynamics Conference*, Snowmass Village, Colorado, 1997. AIAA Paper Number 97-2038.

[40] S. Heathcote, D. Martin, and I. Gursul. "Flexible Flapping Airfoil Propulsion at Zero Freestream Velocity," *AIAA Journal*, 42(11):2196–2204, 2004.

[41] S. Heathcote, Z. Wang, and I. Gursul. "Effect of Spanwise Flexibility on Flapping Wing Propulsion," *Journal of Fluids and Structures*, 24(2):183–199, 2008.

[42] S. Ho, H. Nassef, N. Pornsinsirirak, Y.C. Tai, and C.H. Ho. "Unsteady Aerodynamics and Flow Control for Flapping Wing Flyers," *Progress in Aerospace Sciences*, 39:653–681, 2003.

[43] K.M. Hsiao. "Nonlinear Analysis of General Shell Structures by Flat Triangular Shell Elements," *Computers and Structures*, 25(5):665–675, 1987.

[44] D. Ishihara, T. Horie, and M. Denda. "A Two-Dimensional Computational Study on the Fluid-Structure Interaction Cause of Wing Pitch Changes in Dipteran Flapping Flight," *Journal of Experimental Biology*, 212:1–10, 2009.

[45] K.E. Jansen, C.H. Whiting, and G.M. Hulbert. "A Generalized-α Method for Integrating the Filtered Navier-Stokes Equations With a Stabilized Finite Element Method," *Computer Methods in Applied Mechanics and Engineering*, 190(3-4):305–319, 2000.

[46] L. Jiang, M.W. Chernuka, and N.G. Pegg. "A Co-rotational, Updated Lagrangian Formulation for Geometrically Nonlinear Finite Element Analysis of Shell Structures," *Finite Elements in Analysis and Design*, 18:129–140, 1994.

[47] R.M. Jones. *Mechanics of Composite Materials*, Taylor and Francis, 1999.

[48] R. Kamakoti and W. Shyy. "Evaluation of Geometric Conservation Law using Pressure-based Fluid Solver and Moving Grid Technique," *International Journal of Numerical Methods for Heat and Fluid Flow*, 14(7):851–865, 2004.

[49] P. Khosravi, R. Ganesan, and R. Sedaghati. "Co-rotational Nonlinear Analysis of Thin Plates and Shells," *International Journal of Numerical Methods in Engineering*, 69:859–885, 2007.

[50] P. Khosravi, R. Ganesan, and R. Sedaghati. "An Efficient Facet Shell Element for Co-rotational Nonlinear Analysis of Thin and Moderately Thick Laminated Composite Structures," *Computers and Structures*, 86:850–858, 2008.

[51] D.K. Kim, J.S. Lee, J.Y. Lee, and J.H. Han. "An Aeroelastic Analysis of a Flexible Flapping wing Using Modified Strip Theory," *Active and Passive Smart Structures and Integrated Systems*, 6928:1–8, 2008.

[52] G.V. Lauder. "Flight of the Robofly," *Nature*, 412:688 – 689, 2001.

[53] F.O. Lehmann. "The Mechanisms of Lift Enhancement in Insect Flight," *Nature*, 91:101–122, 2004.

[54] R.J. LeVeque. *Finite Difference Methods for Ordinary and Partial Differential Equations (Steady State and Time Dependent Problems)*, Society for Industrial and Applied Mathematics (SIAM), Philadelphia, 2007.

[55] Y. Lian. *Membrane and Adaptively-Shaped Wings for Micro Air Vehicles*. PhD Dissertation, Department of Mechanical and Aerospace Engineering, University of Florida,Gainsville,Florida, 2003.

[56] E. Liani, S. Guo, and G. Allegri. "Aeroelastic Effect on Flapping Wing Performance,". In 48^{th} *AIAA/ASME/ASCE/AHS/ASC Structures, Structural Dynamics, and Materials Conference*, Honololu,Hawaii, April 2007. AIAA Paper Number 2007-2412.

[57] H. Liu and K. Kawachi. "A Numerical Study of Insect Flight," *Journal of Computational Physics*, 146:124–156, 1998.

[58] K. Mattiasson and A. Samuelson. "Total and Updated Lagrangian Forms of the Co-rotational Finite Element Formulation in Geometrically and Materially Nonlinear Analysis," In *Numerical Methods for Nonlinear Problems*, April, 1984.

[59] J.L. Meek and Y. Wang. "Nonlinear Static and Dynamic Analysis of Shell Structures with Finite Rotations," *Computer Methods for Applied Mechanics and Engineering*, 162(1-4):301–315, 1998.

[60] B. Nour-Omid and C. Rankin. "Finite Rotation Analysis and Consistent Linearization Using Projectors," *Computer Methods for Applied Mechanics and Engineering*, 93, 1991.

[61] M. Nygard. "The Free Formulation for Nonlinear Finite Elements with Applications to Shells," *Structural Mechanics*, 1986.

[62] R. Palacios. *Asymptotic Models of Integrally-Strained Slender Structures for High-Fidelity Nonlinear Aeroelastic Analysis*. PhD Dissertation, Department of Aerospace Engineering, Ann Arbor, Michigan, 2005.

[63] R. Palacios and C.E.S. Cesnik. "Cross-Sectional Analysis of Non-Homogeneous Anisotropic Active Slender Structures," *AIAA Journal*, 43(12):2624–2638, 2005.

[64] R. Palacios and C.E.S. Cesnik. "Geometrically Nonlinear Theory of Composite Beams with Deformable Cross Sections," *AIAA Journal*, 46(2):439–450, 2008.

[65] W. T. Vetterling, S.A. Teukolsky, W.H. Press, and B.P. Flannery. *Numerical Recipes in Fortran: The Art of Scientific Computing*, Cambridge University Press, 2007.

[66] R. Ramamurti and W.C. Sandberg. "A Three-Dimensional Computational Study of the Aerodynamic Mechanisms of Insect Flight," *The Journal of Experimental Biology*, 205:1507–1518, 2002.

[67] C.C. Rankin and F.A. Brogan. "An Element Independent Co-rotational Procedure for the Treatment of Large Rotations," *ASME Journal of Pressure Vessel Technology*, 108:165–174, 1991.

[68] A. Relvas and A. Suleman. "Fluid Structure Interaction Modelling of Nonlinear Aeroelastic Structures Using the Finite Element Corotational Theory," *Journal of Fluids and Structures*, 22(1):59–75, 2006.

[69] A. Relvas and A. Suleman. "Application of the Co-rotational Structural Kinematics and Euler Flow to Two Dimensional Nonlinear Aeroelasticity," *Computers and Structures*, 85(17-18):1372–1381, 2007.

[70] E. Sallstrom and L. Ukeiley. "Three-Dimensional Averaged Flow Around Rigid Flapping Wings," In 38^{th} *Fluid Dynamics Conference and Exhibit*, Seattle, Washington, June 2008. AIAA Paper Number 2008-3721.

[71] E. Sallstrom, L. Ukeiley, P. Wu, and P. Ifju. "Three-Dimensional Averaged Flow and Wing Deformation Around Flexible Flapping Wings," In 39^{th} *AIAA Fluid Dynamics Conference*, San Antonio, Texas, June 2009. AIAA Paper Number 2009-3813.

[72] S.P. Sane. "The Aerodynamics of Insect Flight," *The Journal of Experimental Biology*, 206:4191–4208, 2003.

[73] A.A. Shabana. *Dynamics of Multibody Systems*, Cambridge University Press, 2005.

[74] C.M. Shearer and C.E.S. Cesnik. "Modified Generalized-α Method for Integrating Governing Equations of Very Flexible Aircraft," In 47^{th} *AIAA/ASME/ASCE/AHS/ASC Structures, Structural Dynamics, and Materials Conference*, Newport, RI, May 2006. AIAA Paper Number 2006-1747.

[75] J. Shimanuki and K. Machida. "Structure Analysis of the Wing of a Dragonfly," *Proceedings of the SPIE*, 5852:671–676, 2005.

[76] W. Shyy. *Computational Modeling for Fluid Flow and Interfacial Transport*, Elsevier, 1994.

[77] W. Shyy, M. Berg, and D. Ljungqvist. "Flapping and Flexible Wings for Biological and Micro Air Vehicles," *Progress in Aerospace Sciences*, 35(5):455–505, 1999.

[78] W. Shyy, Y. Lian, S.K. Chimakurthi, C.E.S. Cesnik, B. Stanford, and P. Ifju. "Flexible Wings and Fluid-Structure Interactions for Micro Air Vehicles," In D. Floreano, C.J. Zufferey, M.V. Srinivasan, and C. Ellington, editors, *Flying Insects and Robots (to be published)*, Switzerland, 2009. Springer Verlag.

[79] W. Shyy, Y. Lian, J. Tang, H. Liu, B. Trizila, B. Stanford, L. Bernal, C. Cesnik, P. Friedmann, and P. Ifju. "Computational Aerodynamics of Low Reynolds Number Plunging, Pitching and Flexible Wings for MAV Applications," In 46^{th} *AIAA Aerospace Sciences Meeting and Exhibit*, Reno, Nevada, January 2008. AIAA Paper Number 2008-523.

[80] W. Shyy, Y. Lian, J. Tang, D. Viieru, and H. Liu. *Aerodynamics of Low Reynolds Number Flyers*, Cambridge University Press, 2008.

[81] W. Shyy and H. Liu. "Flapping Wings and Aerodynamic Lift: The Role of Leading-Edge Vortices," *AIAA Journal*, 45(12):2817–2819, 2007.

[82] W. Shyy, P. Trizila, C.K. Kang, and H. Aono. "Can Tip Vortices Enhance Lift of a Flapping Wing ?," *AIAA Journal*, 47(2):289–293, 2009.

[83] W. Shyy, H. Udaykumar, M.R. Madhukar, and Richard W. Smith. *Computational Fluid Dynamics With Moving Boundaries*, Dover Publications, New York, 2007.

[84] B. Singh. *Dynamics and Aeroelasticity of Hover Capable Flapping Wings: Experiments and Analysis*. PhD Dissertation, Department of Aerospace Engineering, University of Maryland,College Park, Maryland, 2006.

[85] B. Singh and I. Chopra. "Insect-Based Flapping Wings for Micro Hovering Air Vehicles: Experimental Investigations," In *American Helicopter Society International Specialists Meeting on Unmanned Rotorcraft*, Arizona, January 2004.

[86] B. Singh and I. Chopra. "Dynamics of Insect-Based Flapping Wings: Loads and Validation," In 47^{th} *AIAA/ASME/ASCE/AHS/ASC Structures, Structural Dynamics, and Materials Conference*, Newport,Rhode Island, May 2006. AIAA Paper Number 2006-1663.

[87] M.J. Smith, D.H. Hodges, and C.E.S. Cesnik. "Evaluation of Computational Algorithms Suitable for Fluid-Structure Interactions," *Journal of Aircraft*, 37(2):282–294, 2000.

[88] R.B. Srygley and A.L.R. Thomas. "Unconventional Lift-Generating Mechanisms in Free-Flying Butterflies," *Nature*, 420:660–664, 2002.

[89] K. Subbaraj and M.A.A. Dokainish. "Survey of Direct Time-Integration Methods in Computational Structural Dynamics: II. Implicit Methods," *Computers and Structures*, 32(6):1387–1401, 1989.

[90] J. Tang, D. Viieru, and W. Shyy. "A Study of Aerodynamics of Low Reynolds Number Flexible Airfoils," In 37^{th} *AIAA Fluid Dynamics Conference and Exhibit*, Miami,Florida, June 2007. AIAA Paper Number 2007-4212.

[91] G.K. Taylor, R.L. Nudds, and A.L.R. Thomas. "Flying and Swimming Animals Cruise at a Strouhal Number Tuned for High Power Efficiency," *Nature*, 425:707 – 710, 2003.

[92] T.J. Mueller, editor. *Fixed and Flapping Wing Aerodynamics for Micro Air Vehicle Applications*, volume 195, New York, 2001. Progress in Astronautics and Aeronautics, AIAA.

[93] T. Tsang. *Dynamic Analysis of Highly Deformable Bodies Undergoing Large Rotations*. PhD Dissertation, The University of Arizona, 1993.

[94] R. Unger, M.C. Haupt, and P. Horst. "Structural Design and Aeroelastic Analysis of an Oscillating Airfoil for Flapping Wing Propulsion," In 46^{th} *AIAA Aerospace Sciences Meeting and Exhibit*, Reno, Nevada, January 2008. AIAA Paper Number 2008-306.

[95] C. Van Den Berg and C.P. Ellington. "The Three-Dimensional Leading-Edge Vortex of a "hovering," *Philosophical Transactions of the Royal Society of London*, pages 329 – 340.

[96] V.G.J. Vazquez. *Fluid-Structure Interaction Analysis: Development with Finite Elements*, VDM Verlag, 2008.

[97] Z.J. Wang. "Dissecting Insect Flight," *Annual Review of Fluid Mechanics*, 37:183–210, 2005.

[98] T. Wasfy. "Modeling Continuum Multibody Systems Using the Finite Element Method and Element Convected Frames, Machine Elements, and Machine Dynamics," In *23rd ASME Mechanisms Conference*, pages 327–336, 1994.

[99] T. Wasfy. "Computational Strategies for Flexible Multibody Systems," *Applied Mechanics Review*, 56(6):553–613, 2003.

[100] T. Weis-Fogh. "Quick Estimate of Flight Fitness in Hovering Animals, Including Novel Mechanisms for Lift Production," *The Journal of Experimental Biology*, 59:169–230, 1973.

[101] D. Willis, E. Israeli, P. Persson, M. Drela, J. Peraire, S. M. Swartz, and K. S. Breuer. "A Computational Framework for Fluid Structure Interaction in Biologically Inspired Flapping Flight," In 25^{th} *AIAA Applied Aerodynamics Conference*, Miami,Florida, June 2007. AIAA Paper Number 2007-3803.

[102] J. Wootton. "Support and Deformability in Insect Wings," *Journal of Zoology*, 193:447–468, 1981.

[103] P. Wu, P. Ifju, B. Stanford, E. Sallstrom, L. Ukeiley, R. Love, and R. Lind. "A Multidisciplinary Experimental Study of Flapping Wing Aeroelasticity in Thrust Production," In 50^{th} *AIAA/ASME/ASCE/AHS/ASC Structures, Structural Dynamics, and Materials Conference*, Palm Springs, CA, May 2009. AIAA Paper Number 2009-2413.

[104] P. Wu, B. Stanford, and P. Ifju. "Passive Bending and Twisting Motion during the Flapping Stroke of a Micro Elastic Wing for Thrust Production," In *AIAA Aerospace Sciences Meeting*, Orlando, FL, January 2009. AIAA Paper Number 2009-879.

[105] L. Zheng, X. Wang, A. Khan, R.R. Vallance, and R. Mittal. "A Combined Experimental-Numerical Study of the Role of Wing Flexibility in Insect Flight," In 47^{th} *AIAA Aerospace Sciences Meeting and Exhibit*, Orlando, Florida, January 2009. AIAA Paper Number 2009-382.

[106] Q. Zhu. "Numerical Simulation of a Flapping Foil with Chordwise or Spanwise Flexibility," *AIAA Journal*, 45(10):2448–2457, 2007.

[107] O.C. Zienkiewicz and R.L. Taylor. *The Finite Element Method*, Elselvier Butterworth-Heinemann, 2005.